Component-based modelling of the thermal abuse in lithium-ion batteries

Zur Erlangung des akademischen Grades eines
Doktors der Ingenieurwissenschaften (Dr.-Ing.)
von der KIT-Fakultät für Elektrotechnik und Informationstechnik des
Karlsruher Instituts für Technologie (KIT)

angenommene
Dissertation
von

Florian Baakes, M.Sc.
geboren in Dinslaken

Tag der mündlichen Prüfung:	2. Juli 2024
Hauptreferentin:	Prof. Dr.-Ing. Ulrike Krewer
Korreferentin:	Prof. Dr. Claire S. Adjiman

Kurzfassung

Die hohe Nachfrage nach geeigneten Energiespeicher-Systemen für mobile wie auch stationäre Anwendungen führte zum massiven Einsatz von Li-Ionen-Batterien. Diese sind zwar die derzeit beste Wahl in Bezug auf Energiedichte und Leistung. Jedoch macht ihr inhärentes Risiko des thermischen Durchgehens eine angemessene Sicherheitsbewertung zwingend erforderlich. Moderne Methoden verwenden eine Kombination aus experimenteller Analyse und Modellierung. Die bislang meist semi-empirischen Modelle erlauben jedoch keine direkte Ableitung der Wechselwirkungen zwischen den auftretenden Phänomenen und zugrundeliegenden Wirkmechanismen innerhalb der Zelle.

Um diese offene Herausforderung zu bewältigen, wurde in der vorliegenden Arbeit ein Modellierungsansatz entwickelt, der die verschiedenen Spezies sowie deren Interaktion innerhalb einer Zelle berücksichtigt. Dieser Ansatz beinhaltet die explizite Darstellung von 20 Spezies, in bis zu 12 Reaktionen, welche von 60 °C bis zum thermischen Durchgehen ablaufen. Ein weiterer Schwerpunkt wurde auf Dampf-Flüssig-Phasengleichgewichte und deren Zusammenspiel mit den entstehenden Reaktionen gelegt. Die Analyse einer Acclerating Rate Calorimetry Messung mittels dieses Modellierungsansatzes konnte zeigen, dass aus chemischen Reaktionen entstehende Gase das Sieden des Elektrolyten bis zum Öffnen des Sicherheitsventils unterdrücken. Zudem wurde eine detaillierte Sensitivitätsanalyse durchgeführt. Hier wurde, die Menge von Wasser als Verunreinigung sowie die Eigenschaften der Solid-Electrolyte-Interphase (SEI) variiert. Diese zeigte, dass eine sichere Batterie eine dicke, anorganische SEI und kaum Wasser enthält. Im Falle einer Wasserkontamination konnte ein wesentlicher Einfluss auf das thermische Durchgehen nur in Verbindung mit sehr hoher Kontamination gefunden werden. Daher ist eine starke Trocknung der Elektroden im Sinne der Betriebssicherheit nicht notwendig, da sie keinen nennenswerten Sicherheitsvorteil bietet und die Leistung der Elektroden verringert. Schließlich wurde die statistische Theorie der assoziierten Fluide verwendet, um die Druckentwicklung in Li-Ionen Batterien verwendeten Elektrolyten zu analysieren. Es zeigte sich, dass das Edelgas Argon und Stickstoff gute Wahlen als Inertgas für die Lösungsmittellagerung und den Zellbau sind. Dies ist darauf zurückzuführen, dass beide eine

geringe Löslichkeit in den verwendeten Lösemitteln aufweisen und sich diese, im Fall von Argon, bei Temperaturanstieg erhöht. Weitere Simulationen machen deutlich, dass das Lösungsmittel optimiert werden muss, um die Löslichkeit der Gase aus den Abbaureaktionen zu maximieren. Dies deutet darauf hin, dass, obwohl kontraintuitiv, niedrig siedende Lösungsmittelkomponenten wie Dimethylcarbonat oder Ethylmethylcarbonat zu diesem Zweck bevorzugt werden sollten.

Zusammenfassend verdeutlicht der hier entwickelte komponentenbasierte Ansatz den entscheidenden Einfluss von ablaufenden Reaktionen auf die entstehenden Phasengleichgewichte und vice versa während des Durchgehens von Batterien. Der präsentierte Modellierungsansatz ist ein vielversprechendes Werkzeug für das Verständnis und die Minimierung von Sicherheitsrisiken bei Li-Ionen Batterien.

Abstract

The high demand for suitable energy storage systems for mobile and stationary applications led to the mass deployment of Li-ion batteries. While they are currently the best choice regarding energy density and rate performance, their inherent risk for thermal runaway makes a proper safety assessment mandatory. State-of-the-art methods use a combination of experimental analysis and modelling approaches. However, up until now, most of the employed models are semi-empirical and do not allow a direct deduction of interdependencies of occurring phenomena with chemical species within the battery.

To tackle this open challenge a component-based modelling approach was developed in the presented work. This approach explicitly represents 20 species participating in up to 12 reactions from around 60 °C up to the thermal runaway. Further focus has been laid on vapour-liquid phase equilibria and their interplay with emerging reactions. Employing this novel modelling approach in the analysis of an accelerating rate calorimetry measurement showed that evolving gases from degradation reactions will suppress electrolyte boiling until the venting of the battery. A detailed sensitivity analysis of the impact of the contaminant water and solid electrolyte interphase (SEI) properties revealed that a safe battery would constitute a thick inorganic SEI and have low water content. In the case of water contamination, a substantial effect could only be observed for severe contamination. Thus, massive electrode drying can be avoided as it has no significant safety benefit while decreasing electrode performance. Eventually, an exhaustive analysis of factors influencing the pressure evolution during a thermal event was conducted utilising the statistical associating fluid theory. The findings show that argon or nitrogen are good choices as the inert gas employed during solvent storage and cell assembly. This is a consequence of their low solubility in the electrolyte systems and, in the case of argon, an increasing solubility with higher temperatures. Further simulations highlight the need for optimising the solvent to maximise the solubility of gases from degradation reactions. This indicates that, counterintuitively, low boiling solvent components like dimethyl carbonate or ethyl methyl carbonate should be favoured for this purpose.

In summary, the component-based approach developed here illustrates the decisive influence of chemical reactions on the phase equilibria and vice versa. The presented modelling approach is a promising tool for understanding and minimising safety risks in Li-ion batteries.

Publications within the scope of this thesis

Journal publications

First author

1. F. Baakes, R. Song, T. Bernet, G. Jackson, C. S. Adjiman, A. Galindo, U. Krewer, “Understanding pressure evolution during thermal abuse of Li-ion batteries,” submitted to Applied Energy, 2024.
2. F. Baakes, D. Witt, U. Krewer, “Impact of electrolyte impurities and SEI composition on battery safety,” Chemical science, 14, 47, 13783–13798, 2023.
3. F. Baakes, M. Lüthe, M. Gerasimov, V. Laue, F. Röder, P. B. Balbuena, U. Krewer, “Unveiling the interaction of reactions and phase transition during thermal abuse of Li-ion,” Journal of Power Sources, 522, 230881, 2022.

Co-author

1. D. Witt, L. Bläubaum, **F. Baakes**, and U. Krewer, ”Origin of Performance Improvements in Lithium-Ion Cells after Fast Formation,” Batteries & Supercaps, e202400023, 2024.
2. L. Bläubaum, P. Röse, **F. Baakes**, U. Krewer, “Impact of Lithium-Ion Battery Separators on Gas Evolution during Temperature Abuse,” Batteries & Supercaps, e202300534, 2024.
3. M. Gerasimov, F. A. Soto, J. Wagner, **F. Baakes**, N. Guo, F. Ospina-Acevedo, F. Röder, P. B. Balbuena, U. Krewer, “Species distribution during solid electrolyte interphase formation on lithium using MD/DFT-parameterized kinetic Monte Carlo simulations,” The Journal of Physical Chemistry C, 127, 10, 4872–4886, 2023.

4. S. Toghyani, W. Cistjakov, **F. Baakes**, U. Krewer, “Conceptual Design of Solid-State Li-Battery for Urban Air Mobility,” Journal of The Electrochemical Society, 170, 10, 103510, 2023.

5. S. Toghyani, **F. Baakes**, N. Zhang, H. Kühnelt, W. Cistjakov, U. Krewer, “Model-Based Design of High Energy All-Solid-State Li Batteries with Hybrid Electrolytes,” Journal of The Electrochemical Society, 169, 4, 040550, 2022.

6. B. Horstmann, J. Shi, R. Amine, M. Werres, X. He, H. Jia, F. Hausen, I. Cekic-Laskovic, S. Wiemers-Meyer, J. Lopez, D. Galvez-Aranda, **F. Baakes**, D. Bresser, C. Su, Y. Xu, W. Xu, P. Jakes, R. Eichel, E. Figgemeier, U. Krewer, J. M. Seminario, P. B. Balbuena, C. Wang, S. Passerini, Y. Shao-Horn, M. Winter, K. Amine, R. Kostecki, A. Latz, “Strategies towards enabling lithium metal in batteries: interphases and electrodes,” Energy & Environmental Science, 14, 10, 5289–5314, 2021.

7. X. He, D. Bresser, S. Passerini, **F. Baakes**, U. Krewer, J. Lopez, C. T. Mallia, Y. Shao-Horn, I. Cekic-Laskovic, S. Wiemers-Meyer, F. A Soto, V. Ponce, J. M. Seminario, P. B. Balbuena, H. Jia, W. Xu, Y. Xu, C. Wang, B. Horstmann, R. Amine, C. Su, J. Shi, K. Amine, M. Winter, A. Latz, R. Kostecki, “The passivity of lithium electrodes in liquid electrolytes for secondary batteries,” Nature Reviews Materials, 6, 11, 1036–1052, 2021.

8. D. Witt, D. Wilde, **F. Baakes**, F. Belkhir, F. Röder, U. Krewer, “Myth and Reality of a Universal Lithium-Ion Battery Electrode Design Optimum: A Perspective and Case Study,” Energy Technology, 9, 6, 2000989, 2021.

9. Y. E. Durmus, H. Zhang, **F. Baakes**, G. Desmaizieres, H. Hayun, L. Yang, M. Kolek, V. Küpers, J. Janek, D. Mandler, S. Passerini, Y. Ein-Eli, ”Side by side battery technologies with lithium-ion based batteries,” Advanced Energy Materials, 10, 24, 2000089, 2020.

Conference contributions

First author

1. F. Baakes, L. Bläubaum, U. Krewer, ”Battery Safety Simulation and Experimental Investigations: The Undefeatable Team,” poster presentation at the BACCARA Power Day in Münster, Germany (May 19., 2022).

2. F. Baakes, U. Krewer, “Model-based Assessment of Species Contributions to the Thermal Runaway in Lithium-ion Batteries,” oral presentation at the 31st Topical Meeting of the International Society of Electrochemistry in Aachen, Germany (May 15–19, 2022).

3. F. Baakes, U. Krewer, ”Illuminating Catalytic Species During the Thermal Runaway of Lithium-ion Batteries,” oral presentation at the Annual Meeting on Reaction Engineering (May 10–21, 2021, online).

4. F. Baakes, F. Röder, U. Krewer, ”The influence of electrolyte phase transition on the thermal runaway in Lithium-ion batteries,” oral presentation at the 70th Annual Meeting of the International Society of Electrochemistry in Durban, South Africa, (August 4–9, 2019).

5. F. Baakes, F. Röder, U. Krewer, ”Incorporating phase transition phenomena into a thermal runaway model of lithium-ion batteries,” short oral presentation at the 4th German Israeli Battery School in Berlin, Germany (May 12–16, 2019).

Co-author (selected)

1. D. Witt, L. Bläubaum, **F. Baakes**, U. Krewer, “In-Depth Analysis of the Substantial Effect of Fast Formation on Lithium-Ion Cell Characteristics,” oral presentation at the 242nd ECS meeting in Atlanta, Georgia, USA (October 9–13, 2022).

2. S. Toghyani, **F. Baakes**, N. Zhang, H. Kühnelt, W. Cistjakov, U. Krewer, “Model-Assisted Design of Oxide-Based All-Solid-State Li-Batteries with Hybrid Electrolytes for Aviation,” oral presentation at the 242nd ECS meeting in Atlanta, Georgia, USA (October 9–13, 2022).

3. D. Wilde, D. Witt, M. Sgroib, S. Hein, T. Danner, **F. Baakes**, A. Latz, U. Krewer, “Toward realistic battery design: drive cycle vs. constant current,” oral presentation at the Regional Meeting of the International Society of Electrochemistry in Prague, Czech Republic (August 15–19, 2022).

4. U. Krewer, F. Röder, **F. Baakes**, D. Witt, “Modelling of Li-Ion Batteries – From Cradle to Grave,” oral presentation at the 72nd Annual Meeting of the International Society of Electrochemistry (August 29 – September 3, 2021, online).

5. U. Krewer, **F. Baakes**, D. Witt, “Insight into Li-ion Battery Changes during Aging and Thermal Runaway,” poster presentation at the 21st International Meeting on Lithium Batteries Exhibition in Sydney (June 26 – July 1, 2022).

6. L. Bläubaum, **F. Baakes**, C. Nowak, A. Kwade, U. Krewer, “Particle Size Effects on Gas Evolution during Formation and Temperature Abuse,” oral presentation at the 29th Topical Meeting of the International Society of Electrochemistry (April 18–21, 2021, online).

„On the shoulders of giants.“

- Unknown Author

Acknowledgements

Science operates as a self-improving entity, a concept that the quote from the previous page encapsulates perfectly. We continually build upon the work of those who preceded us. Without the dedication of the countless scientific pioneers before us, progress to the extent we are now experiencing would be impossible. At this juncture, I would like to extend my heartfelt gratitude to the giants in my personal journey — those who, with their varied yet equally essential and supportive roles, have helped me stand tall.

At the outset, I am immensely grateful to my supervisor, Prof. Dr.-Ing. Ulrike Krewer, for allowing me to delve into this captivating and demanding topic. Her open-mindedness, trust, and meticulous attention to detail have been an indispensable guidance. This gratitude undeniably includes the trust and mentorship for the sometimes burdensome but fulfilling task as the group leader of the battery group at the Institute for Applied Materials-Electrochemical Technologies at Karlsruhe Institute of Technology.

I want to take this opportunity to express my deep gratitude towards my leading colleagues, Janika Wagner, Dr. rer. nat. Philipp Röse, Dr.-Ing. Wolfgang Menesklou, and Dr.-Ing. habil. PD. André Weber. The numerous yet productive meetings we held to shape the institute as it stands today have provided me with lessons of immeasurable value.

I sincerely thank Thomas Bernet, Prof. Amparo Galindo, Prof. Claire Adjiman and Prof. George Jackson from Imperial College London. Their engaging discussions sharpened my understanding of the physical world around us. This research stay was sponsored by the Karlsruhe House of Young Scientists (KHYS).

A big thank you to my colleagues at the InES and the IAM-ET for sparking numerous enlightening and thought-provoking scientific and non-scientific conversations.

I owe a particular debt of gratitude to the members of the battery group: Walter Cistjakov, Lars Bläubaum, Dion Wilde, Somayeh Toghyani, Michael Gerasimov, Leon Schmidt, Michelle Allion, Kie Hankins, Jorge Valenzuela and Jakub Jambrich. The last three years have undeniably been the most demanding period of my entire life. Yet, you helped me to step into the role of a group leader and thus provided me with the opportunity for significant learning and personal development.

I am particularly grateful to Daniel Witt for his critical review and proofreading of this manuscript and to all my co-authors for our fruitful scientific discussions and collaborative research efforts.

I also want to express my genuine appreciation to all the dedicated students who supported me during my time as a Ph.D. candidate. A special nod to Maximilian Lüthe, whose relentless work in establishing and validating species properties was unparalleled.

Lastly, but by no means the least, I wish to thank my partner Luisa Ropelato, whose constant support and encouragement have been an invaluable source of strength throughout this journey.

London, 6th August 2024 *Florian Baakes*

Contents

1 Motivation

Harnessing the energy conserved in fossil fuels is what powered the industrial revolution. It helped humanity to increase its population size from 1 billion to 8 billion in only 200 years. At the same time, the average life expectancy rose from around 30 years to 72 years, and extreme poverty decreased below 10% [1]. Yet, nothing comes without a prize. Extreme weather conditions like floodings, storms, and droughts have increased substantially. All of this is brought about by a group of molecules called greenhouse gases. Figure 1.1 presents the enormous amount of 51.000.000.000 t $CO_{2,eq}$ annual human-made greenhouse gas emissions and its distribution among the energy sector, industry, waste management, and agriculture [2]. Without massive change, the continued emissions will put a third to half of the human population outside our habitable niche until the end of this century [3]. To prevent the worst, the quest for our and coming generations is to find and establish ways to bring this number below zero.

A huge contributor to these emissions is CO_2, released from burning fossil fuels in transport of all forms, making up 16.2% of the total emissions [2]. Fortunately, solutions already exist. These range from hydrogen-fueled cars over more intensive use of bicycles and public transport to electric vehicles (EV) using batteries or H_2 as mobile energy storage systems. Here, the Li-ion battery, with its superior energy storage and power capabilities, already makes up 50% of the whole electrical energy storage market. When only considering the mobile sector this increases to remarkable 99% [1] [4]. Besides the properties mentioned above, safety is among the most essential requirements for mass deployment of Li-ion batteries. During their development, Li-ion batteries have been the promising safer alternative to lithium metal-based secondary batteries [5–7]. Still, potential safety hazards under high-temperature abuse exist and have already been known during and before commercialisation [6, 8, 9]. Ongoing integration into electric mobility and the constantly increasing energy densities made consideration of safety an omnipresent accompanying issue [9–11]. Even though EVs are far from being as distributed as classical internal combustion engine vehicles (ICEV), an increasing number of safety incidents are reported [12]. The most dangerous safety hazard is the thermal runaway, caused by a cascade of exothermic reactions.

[1] Lead acid batteries are excluded as they are almost exclusively used for starting, lighting, and ignition processes.

Despite extensive analysis, there are still a lot of unanswered questions. The following Chapter 2 will introduce Li-ion batteries in general, explain the general progression of a thermal event and present the current state of technology regarding experimental and model-based safety assessment. This literature survey highlights open research questions which are answered in the thesis. Subsequently, the thesis structure is outlined.

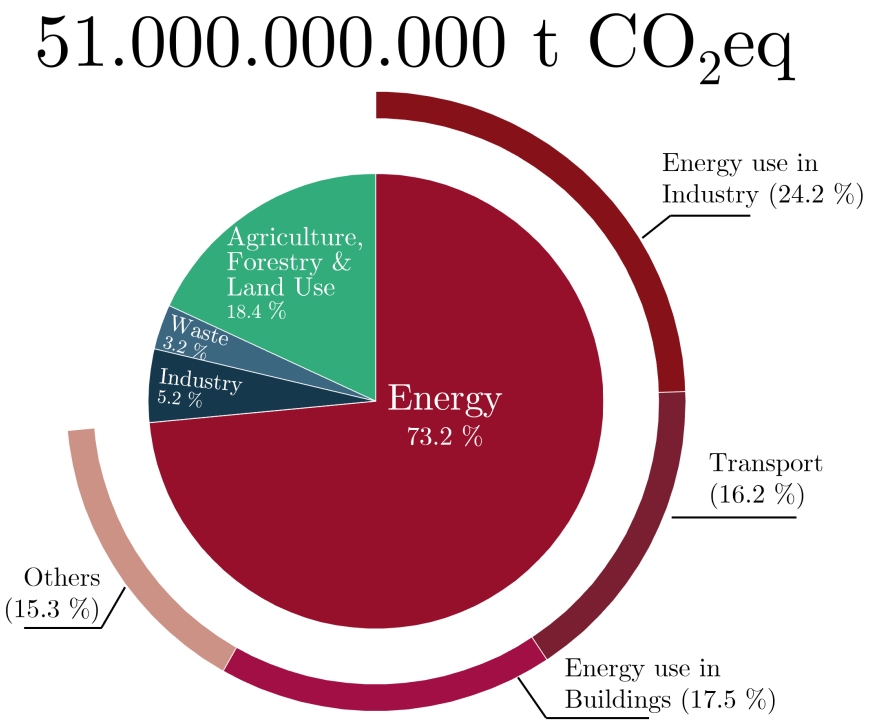

Figure 1.1: Distribution of annual human-made greenhouse gas emissions among the energy sector, industry, waste management, and agriculture. Adapted from [2].

2 Fundamentals — Safety in Li-ion batteries

This chapter introduces the fundamentals for assessing the safety of Li-ion batteries. First, the principles and constitutive components of Li-ion batteries are covered. This is followed by a general description of thermal events in the same. After this first introduction, measurement methods to evaluate battery safety are shown. Further, existing modelling approaches within the scope of battery safety assessment are summarised. In this context, special emphasis is placed on equations of state. At the end of this chapter, open research questions are deduced from the literature review. Lastly, the layout of the remaining parts of the thesis is presented.

2.1 State of the art Li-ion batteries in thermal abuse

After their development in the late 1980s, Li-ion batteries have become an integral part of our everyday lives. Their applications range from mobile phones over their mass deployment in EVs to stationary energy storage. Owing to this tremendous attention from academia and industry, the gravimetric energy density tripled in the last three decades [5]. And while the physical limits of higher energy densities are approached, the search for ever-better alternatives is extensive. These superior alternatives, surfacing in the shapes of Li-metal [13, 14], silicon-based anodes [15], Li-sulphur [16] or Na-ion batteries [17] promise to solve some of the open obstacles. But still, huge challenges such as safety requirements, short lifespan, unstable surface films, electrode passivation or ion shuttles exist. Thus, the Li-ion battery has come to stay [18]. In the following, the individual components and the underlying processes will be presented shortly.

2.1.1 Li-ion battery fundamentals

A Li-ion battery comprises four key parts: the negative electrode, also commonly referred to as the anode, the separator, the positive electrode, also widely referred to as the cathode,

and the electrolyte. The negative and positive electrodes are usually coated onto copper and aluminium current collectors, respectively, enabling the movement of electrons through an external electric circuit. The electrolyte, on the other hand, allows Li-ions to move from electrode to electrode. The separator prevents an electric short circuit between the electrodes while simultaneously permitting the transportation of Li-ions.

Li-ion batteries work with a ”rocking chair” mechanism [19, 20]. This means that the ions move from the negative to the positive electrode without ever converting to their metallic form. Graphite is commonly used as the active material for the anode due to its ability to intercalate Li-ions within its layered structure [21]. Materials employed as the positive active material are transition metal oxides such as $LiMn_2O_4$, $LiNiO_2$, $LiCoO_2$ or a stoichiometric combination of the former such as in $LiNi_{0.8}Mn_{0.1}Co_{0.1}O_2$ [21].

The governing electrochemical reactions at the active material particle surfaces are given by

$$LiC_6 \rightleftharpoons Li_{1-x}C_6 + xe^- + xLi^+ \tag{2.1}$$

for a graphite-based anode and by

$$LiCoO_2 \rightleftharpoons Li_{1-x}CoO_2 + xe^- + xLi^+ \tag{2.2}$$

for a Co-based cathode.

Typical liquid electrolytes in Li-ion batteries consist of a combination of linear carbonates such as dimethyl carbonate (DMC), diethyl carbonate (DEC), ethyl methyl carbonate (EMC), the cyclic carbonate ethylene carbonate (EC) and lithium hexafluorophosphate ($LiPF_6$) as the conductive salt [22]. Even though this solvent mixture is not stable over the whole electrochemical window of Li-ion batteries, a protective surface layer called the solid electrolyte interphase (SEI) is formed in the first cycles. This mitigates further side reactions and allows for the continuous operation of the battery. Due to its uttermost importance not only for the stability of Li-ion batteries under regular operation but also during thermal abuse, an in-depth explanation of the SEI will be given below.

2.1.2 Solid electrolyte interphase[1]

After the SEI model was proposed by Peled et al. [23], its pivotal role in determining Li-ion battery performance and stability became clear [24]. Thus, the past three decades have been filled with ever more accurate analysis of this critical surface layer [13, 14]. However, the fact that it forms within the first cycles, is merely a few nanometer thick and mostly unstable at atmospheric conditions made this task extraordinarily difficult. Therefore, even after more than a quarter of a century of research, some of the most fundamental questions about its growth, Li-ion transport processes, and exact quantitative composition remain at least partially unanswered [13, 14, 25].

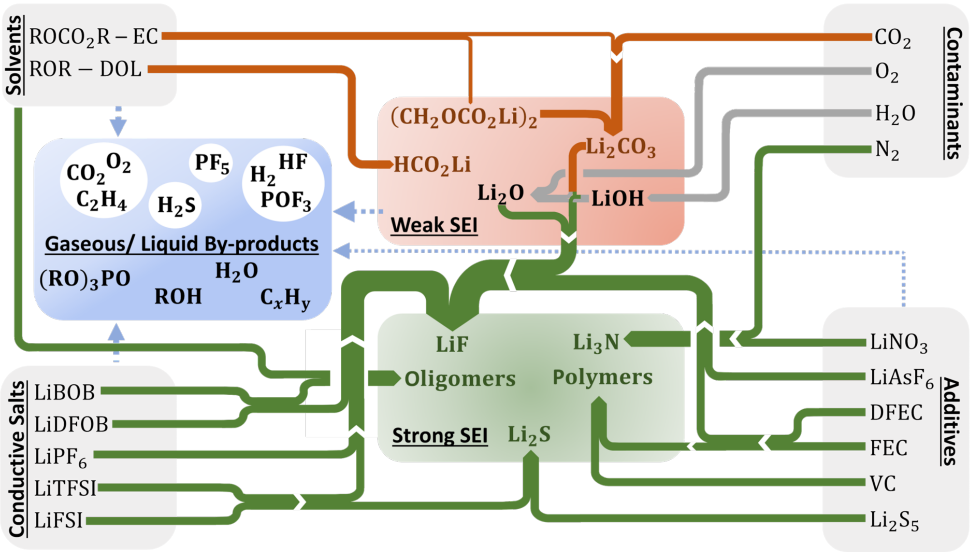

Figure 2.1: Formation of the most common SEI components and gaseous or liquid degradation products from electrolyte components in Li-based batteries. The SEI components are clustered into those considered to exhibit favourable or weak SEI properties. Reactions of products from the electrolyte components are taken from literature for additives [26–34], conducting salts [26, 35–38], contaminants [39–42] and solvents [31, 35, 43, 44]. The thickness of the arrows corresponds to the number of reactants producing a specific SEI component.

The SEI is formed within the very first cycles of operation. Therefore, these cycles are also called formation cycles and due to their time-consuming nature, they pose a great potential for optimisation [45]. The composition of the SEI is known to contain a vast number of species,

[1] Parts of this subsection have been published as own contributions in Horstmann et al., "Strategies towards enabling lithium metal in batteries: interphases and electrodes", Energy and Environmental Sciences, DOI:10.1039/D1EE00767J, CC BY NC 3.0 [14].

which are highly dependent on the electrolyte mixture and contaminants present during cell assembly. Figure 2.1 displays the relationship between solvents, conductive salts, additives and contaminants. The cyclic carbonate component EC leads to the formation of rather unwanted species. The organic SEI component lithium ethylene dicarbonate[2] (LEDC) is identified as one of its major decomposition products [13, 48]. Another main constituent of the SEI is lithium carbonate (Li_2CO_3), which may be formed either from solvent components, LEDC decomposition, or CO_2 as an impurity. Further reported species are LiF, Li_2O and LiOH, which stem from the decomposition of the used conductive salt or contaminants. Given the crucial role of SEI properties, additives designed to alter them were already developed in the late 1990s [49, 50]. Here, the polymer-forming additives vinylene carbonate (VC) and fluoroethylene carbonate (FEC) are most commonly used in conventional Li-ion batteries. The reaction pathways of film formation based on these substances are intricate, and even two decades after their development still need to be fully understood. Further additives such as $LiNO_3$ or Li_2S_5 produce a rigid SEI, which is almost exclusively of use in Li-metal batteries. The architecture of the SEI features a multilayered-mosaic configuration. Primarily, the inner dense layer is composed of inorganic SEI species such as LiF, Li_2O, LiOH, and Li_2CO_3. In comparison, the outer porous layer consists of organic species such as LEDC and oligo- or polymers [51, 52].

The SEI forms due to the instability of the electrolyte components in the low potential region of pure lithium or almost entirely lithiated graphite. Due to its formation, the battery loses lithium inventory and, thus, the capacity is reduced. The question arises, why does this layer promote battery performance? This intriguing surface layer has the distinct feature that it is electronically insulating yet ionically conducting. Therefore, once this layer is stably formed, it mainly inhibits its further growth while ensuring the battery operates normally. However, there are still certain aspects that remain predominantly unexplored, given its electronically insulating property. How are film thicknesses up to 100 nm possible [53–55]? Even considering quantum effects such as electron tunnelling, a film that perfectly covers the electrode should not extend about 10 nm. Here, several theories to answer this question exist, ranging from a not perfectly insulating porous initial SEI layer [56, 57] over particle expansion and contraction and consequent SEI cracking [51, 58] to dissolved SEI species which only form the known surface layer after agglomeration [59]. Despite these open questions about how growth happens, it is known that the SEI steadily grows, even if slowly, over the lifetime of a battery. What is also known is that the outermost layer of organic SEI species increasingly decomposes to form inorganic species during ageing [25, 51]. These aspects will play a significant role in determining the impact of the SEI on battery safety.

[2] Please note that doubts about the stability of LEDC have evolved suggesting lithium ethylene mono-carbonate to be the main organic species instead [46]. However, the decomposition mechanisms involved seem to need high amounts of water [47]. Thus, this thesis will stick to LEDC as the major organic SEI component.

Now that we[3] have discussed the SEI's components, structure, and features, we will shift our focus in the next section to explore the general progression of thermal events in Li-ion batteries, where the SEI plays a central role.

2.1.3 Thermal events in Li-ion batteries[4]

The way Li-ion batteries behave during thermal events that lead to thermal runaway is intricate. From an initially safe battery state, a range of different phenomena can cause the battery to heat itself, eventually culminating in a thermal runaway with temperature gradients up to 1000 °C/min, venting of toxic gases, and in the worst case explosion of the battery [12, 61].

As Li-ion batteries are, fortunately, stable and safe at room temperature, rather only an abuse of the battery will start the chain reaction depicted in Figure 2.2. These abuse cases can be classified as mechanical, electrical or thermal abuse [62]. Different abuse scenarios will cause a different pathway the battery may take to thermal runaway. Mechanical abuse is almost exclusively connected to an accident of some kind. The following deformation of the battery's interior leads to short circuits, which introduce massive heat, elevating the battery's temperature in regions where degradation reactions readily occur. These reactions will then culminate into a thermal runaway when not actively cooled. Here, the connection between the incident and thermal runaway is obvious and almost immediate. A prime example of electrical abuse is overcharging caused by a malfunctioning charging unit and battery management system. Depending on the quantity of overcharging, this may cause direct battery explosion or merely elevated temperatures. Hence, it may either be directly evident or, like thermal abuse, more subtle. Thermal abuse is caused by extensive exposure to the sun or some other heat source, e.g., over/fast charging. As the resulting temperatures are comparably low, around 80 °C, the occurring reactions are also slow compared to the processes initiated by mechanical abuse. The started self-heating of the battery might stay unobserved, and e.g. a parked car might catch fire overnight without a direct connection to the incident [61].

Conventional Li-ion batteries have a safe operating window up to 60 °C. At this point, the decomposition of the conductive salt initiates the degradation reactions [63]. This is followed by the decomposition of the SEI starting in a range of 80 °C to 120 °C with subsequent reformation reactions [64]. Based on the boiling temperature of commonly employed electrolyte mixtures, these can change phases around 100 °C to 130 °C. This phenomenon, however, has

[3] The inclusive "we" is used during this thesis, referring to the author and the reader.

[4] Parts of this chapter have been published as own contributions in Baakes, F., Lüthe M., Gerasimov, M., Laue, V., Röder, F., Balbuena, P., Krewer, U., "Unveiling the interaction of reactions and phase transition during thermal abuse of Li-ion batteries", Journal of Power Sources, DOI:10.1016/j.jpowsour.2021.230881, CC BY 4.0 [60].

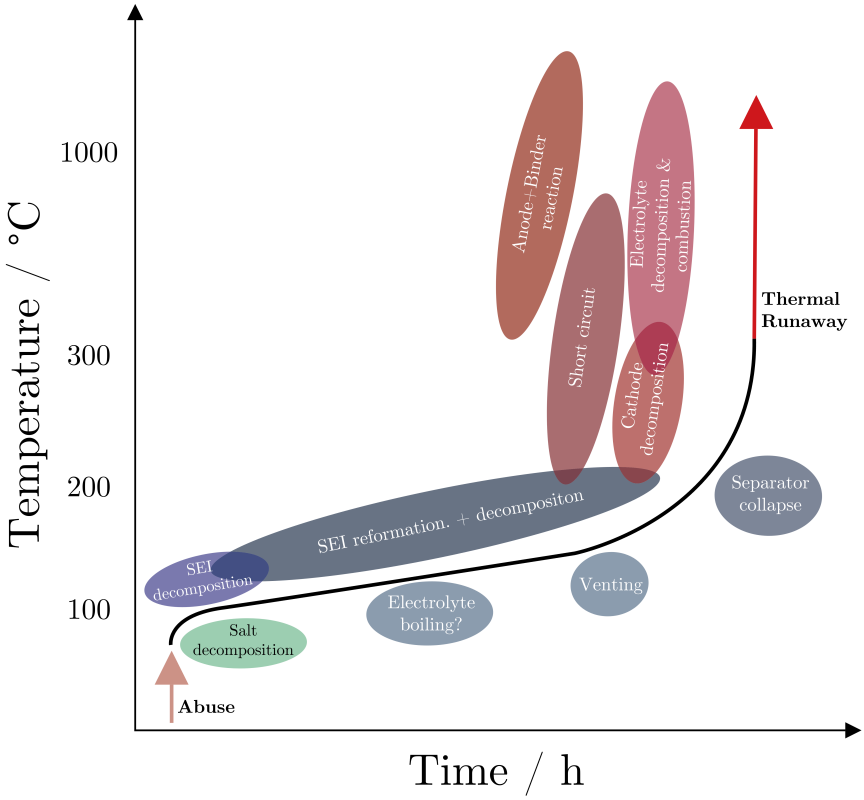

Figure 2.2: Sequential representation of occurring phenomena during the thermal abuse of Li-ion batteries. Adapted from Feng et al. [62].

not yet been subject to any rigorous investigation, even though the cooling potential caused by this phase transition is substantial. In the temperature range between 130 °C and 150 °C the so-called venting of the battery occurs. Here, the pressure build-up from degradation gases causes the cell to open. In order to reach equilibrium, the vapour phase within the cell will spread out to the environment until the internal cell pressure and the pressure in its immediate environment are even [65]. This phenomenon is known to be endothermic and can also cause a visible drop in cell temperature. The SEI re-formation and simultaneous decomposition bridge the temperature range from 120 °C to 150–200 °C, where the cathode active material will start to decompose [66]. This combination of processes signals the start of the rapid thermal runaway itself due to the reaction of O_2 released from this decomposition with the solvent components and its substantial heat release [64]. At around this temperature, ceramic

separators can collapse, leading to an internal short circuit that massively accelerates the high-temperature gradient. Any earlier mechanical abuse or defects could have already led to a short circuit at lower temperatures [61, 64]. Further high-temperature reactions include the self-decomposition of the solvents as well as the reaction of the Na-CMC binder in the anode.

Further, it should be noted that Li-ion batteries, especially in automotive applications, are built-in packs constituting a series of smaller batteries. An important aspect within these packs is the thermal runaway propagation which describes the spreading of thermal runaway through the battery pack caused by one initially malfunctioning cell. In this case, the venting of gases plays a critical role since the ejected gases carry and distribute a high amount of heat and are, thus, a significant driver in increasing the temperature of neighbouring cells to a critical level [67, 68].

After this general introduction to the progression of thermal events in Li-ion batteries, the following section will cover experimental and modelling approaches for their safety assessment.

2.2 Analysis techniques for thermal abuse[5]

Several analysis techniques have been developed to examine the safety characteristics of Li-ion batteries. The first part of this section will introduce the main experimental approaches, while the second half will show how modelling supports our understanding of this complex topic.

2.2.1 Experimental approaches

Various experiments are used to gain deeper insight into batteries and their safety. The most common ones are Accelerating Rate Calorimetry (ARC) and Differential Scanning Calorimetry (DSC) [69–72]. In both methods, the battery cell is heated, and the released energy is observed. Yet, the way of observation differs.

In an ARC measurement, a sample is preheated to a given temperature. Then an equilibration period is performed. This is followed by a seek period in which it is repeatedly checked if a certain threshold of self-heating is exceeded. This is called Heat-Wait-Seek (HWS) mode. In the case of self-heating, the method switches to adiabatic operation, i.e. no additional external heating and cooling. In this so-called exotherm mode, the setup tracks and follows the

[5] Parts of this chapter have been published as own contributions in Baakes, F., Lüthe M., Gerasimov, M., Laue, V., Röder, F., Balbuena, P., Krewer, U., ”Unveiling the interaction of reactions and phase transition during thermal abuse of Li-ion batteries”, Journal of Power Sources, DOI:10.1016/j.jpowsour.2021.230881, CC BY 4.0 [60].

temperature evolution of the sample until reaching a set temperature, e.g. several 100 °C for thermal runaway studies. Figure 2.3 a) shows the described progression of an ARC measurement. Here, the three different stages have been marked in green (Heat-Wait-Seek), yellow (Exotherm) and red (Thermal runaway). Note that the second phase has different names assigned to it in the literature. The most common ones are exotherm mode, adiabatic mode and self-heating phase [73–75]. In this dissertation, exotherm mode is used when referring to the experimental set-up, and the term self-heating phase when describing the behaviour of the investigated battery. However, all terms describe the same stage and could be used interchangeably. Additionally, two essential temperatures are marked. These are the on-set temperature of self-heating, denoted as T_{SH}, and the on-set temperature of thermal runaway, denoted as T_{TR}. The latter is defined as the point where the temperature gradient exceeds $\frac{dT}{dt} = 10\,K\,s^{-1}$ [76]. Further, the critical time window between the on-set of sustainable self-heating, T_{SH} and thermal runaway, T_{TR}, Δt_{TR} is depicted. Apart from this basic procedure, several extensions to ARC measurements exist. A typical modification is an additional measurement of evolving pressure in the test chamber or even of the battery itself [73, 77]. This can further be adjusted such that the test chamber will follow the pressure evolution in the battery [78]. Also, adapted testing procedures, including pressure evolution, are reported. Additionally, a gas analysis method can be coupled to the ARC, allowing analysis of the reactive gases and thus giving further insight into the occurring reactions [79]. ARC measurements can be considered the standard method to assess the safety behaviour of Li-ion batteries. They have been applied to, e.g. study the impact of different positive active materials and ageing conditions. Feinhauer et al. [79] just recently used ARC measurements in combination with ultrasonic measurements, a strain sensor and gas analysis. With this unique combination, they built on previous work [80] and ought to uncover the effects of either low or medium-temperature ageing conditions. They found that low temperature ageing at 15 °C leads to Li plating, which will reduce the self-heating temperature of the battery by about 13 °C. Moderate temperatures of 35 °C, on the other hand, lead to an increase in self-heating temperature of up to 15 °C. This is assumed to be connected to a thicker, more inorganic SEI. These results are further underscored by the thermal analysis databank by Feng et al. [81], where the same trend can be observed for various differently aged cells.

In a DSC measurement, on the other hand, a fixed heating rate is applied to the probe and a reference. The difference in heat flow to the sample and reference is measured as a function of temperature or time. Figure 2.3 b) shows this curve schematically. Here, the baseline refers to the heat flow to the reference and reaction heat to the sample. The sample's exothermic or endothermic heat flow is concluded by subtracting the baseline from the reaction heat curve. This is mainly utilised to analyse singular battery materials with respect to temperature ranges of reactions and the heat released of the same [82, 83]. A frequent modification of a DSC is the combination with a scale to measure the mass loss during operation. This apparatus also

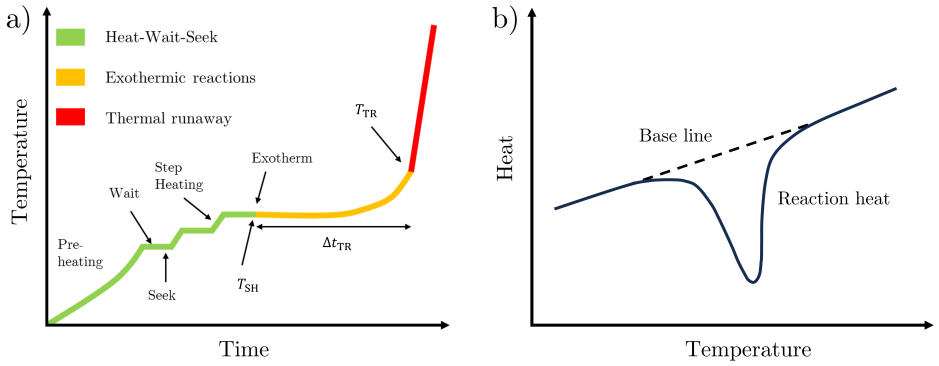

Figure 2.3: Schematic representation of a) an ARC measurement and b) a DSC measurement. Adapted from [60].

exists without a DSC and is called a thermo gravimetric analysis (TGA). This combination can be coupled with a gas analysis, such as a mass spectrometer (MS), to obtain even more information. The works of Kriston et al. [84] should be named here specifically. In their set-up, they combined a DSC-TGA with gas analysis. This combination revealed that the SEI will not decompose in a single step. It will simultaneously form a secondary layer which will decompose further.

Another frequently employed analysis method for electrochemical systems is online electrochemical mass spectrometry (OEMS). Here, a functioning electrochemical cell is connected to a MS [85]. Depending on the experimental set-up, the cell is only opened in specific time intervals or remains open for the whole measurement [63, 86, 87]. This method has been successfully used to investigate the gas evolution of formation gases and reactions at temperatures up to 60 °C [85]. Just recently, an in-operando high-temperature OEMS was used by Bläubaum et al. [88] to investigate the behaviour of different separator materials at elevated temperatures of up to 132 °C. Here, we could show that even though all separators in the study are considered safe in the investigated temperature region, this is not true in a real battery environment. The PET separator shows harsh signs of degradation after a performed heating step, rendering the battery unsuited for further operation.

Further experiments used for safety assessment of whole cells or battery packs are nail penetration, crush, and oven tests [89–91]. The goal of these tests is to emulate conditions during an accident or abuse of the battery. In a nail penetration test, either one cell or whole stacks are placed in a test chamber. Then a nail penetrates the cell either entirely or to a specified degree. The resulting short circuits will produce massive heat release and subsequent thermal runaway [92]. Crush tests are commonly employed to gain information about the mechanical resilience of the battery casing. Here, a test body with varying possible geometries is used to

crush the cell with either a specified force or to a limited extent [93]. The resulting deformation and forces are precisely measured. While the nail and crush test mimics sharp and blunt impacts during accidents, oven tests reproduce thermal abuse conditions. The cell or pack is placed in an oven, and a specified heating rate is applied during the measurement. Following, the temperature evolution of the cell is tracked [11]. The deviation of the temperature curve of the cell from the oven then indicates the start of exothermic reactions. The above methods can also be coupled with additional analysis methods such as gas analysis or video recording.

2.2.2 Modelling approaches

Experiments do not allow for a direct conclusion on the occurring processes inside the battery. Here, the coupling of experiments and mathematical battery models is a highly potent approach that provides insight into the underlying processes [64, 91, 94–97]. Due to the complexity and variety of phenomena during the thermal runaway, building a comprehensive model that covers all occurring effects is an ongoing effort [98, 99]. As a clear division between the models is challenging, the presentation of modelling approaches in this complex area will follow the historical development.

The first approach to assess battery safety with the help of mathematical models has been performed by Richard et al. [100]. Through a substitute reaction, this pioneering work was the first to suggest the initial decay of the SEI as the primary cause of initial self-heating in an ARC measurement. Hatchard et al. [91] extended the approach by Richard et al. to three substitute reactions, further incorporating SEI reformation and positive active material decomposition. This enabled them to replicate an oven test for a whole Li-ion cell. This approach of separating the heat contributions within the battery into distinct parts such as:

$$Q_{\text{tot}} = Q_{\text{SEI Decomposition}} + Q_{\text{SEI Reformation}} + Q_{\text{Cathode Decomposition}}, \tag{2.3}$$

has subsequently been adopted widely. Developing this idea further, Kim et al. [96] also included solvent decomposition and combined this approach with a three-dimensional battery model for heat distribution. More recently, Ren et al. [70] parameterised a Hatchard-type model including six exothermic reactions based on DSC data and subsequently predicted the thermal runaway measured within an adiabatic type measurement. Apart from these purely reactive approaches, models incorporating internal and external short circuits have also been developed. Zhang et al. [101] merged internal short circuit experimental data and a computational model incorporating heat transfer and Joule heating. By this means, they determined that high temperatures initially disrupt the short circuit path by inducing melting. In another

study, Coman et al. [102] implemented a simplified thermal-electrochemical model encompassing three Arrhenius-type reactions and a heat term based on short circuits. Using this model, they revealed that the heat released during a thermal runaway is comparable if it is triggered by an internal short circuit or overheating. A further inclusion of heat-related terms arises from venting. Here, the goal was to describe and predict the timing of venting and its impact on battery temperature. In their early work, Coman et al. [103] introduced three additional heat terms in the venting model: electrolyte boiling, ejection and Joule-Thomson effects[6]. With this, they could get a qualitatively sound description of the measured venting in a cylindrical cell. By combining this approach with the gas generation rate of a pre-venting reaction, they could reproduce the pressure profile up to the cell venting [65]. In both studies, however, the cooling effect produced from the venting was severely overestimated. Another model by Bugryniec et al. [105] considered a mixture of the CO_2 released from reactions and the solvent DMC, applying the ideal gas law to estimate the pressure rise until venting. Using this approach, the accuracy in predicting the venting pressure was increased. Kim et al. [106] focused on describing the gas flow in combination with gas-phase reactions after the venting. By employing a momentum balance, they found that the gas flow within the cell can be best described by Darcy-Forchheimer's law[7] and the flow outside of the cell with a Reynolds-Averaged Navier Stokes equation. They also found that the initial venting, before thermal runaway, does not contribute significantly to gas-induced heat propagation. Here, the gas released during the thermal runaway plays a key role. In a comprehensive study, Wang et al. [107] incorporated Euler-Lagrange-based CFD methods for continuous flow simulations with a discrete phase model to cover particle behaviour. This allowed to reproduce the critical venting phase including particle ejection.

When considering battery packs or whole stacks, the described gas venting is also a central part of thermal runaway propagation. Thus, this intricate phenomenon is also part of simulational and modelling studies. Recently, Wang et al. [68] integrated a computational fluid dynamics simulation with a thermal resistance network. This fusion allowed them to assess how pack ventilation affects explosion risk, demonstrating that unventilated gas mixtures can reach saturation and become explosion-prone. Ventilation on the other hand prevents saturation but also introduces concentration fluctuations in the gas phase. Further considering model-based studies for propagation, Coman et al. [108] expanded on their previous work and investigated the propagation behaviour of 18650 cells in a specially designed aluminium heat sink. Here, they could show that the designed heat sink significantly aids in fast distributing the evolving heat and, thus, mitigates the thermal runaway propagation.

[6] This effect describes the temperature change of a real gas with an isenthalpic pressure reduction, which for most gases leads to a cooling of the gas. Noble gases are the exception [104].

[7] This law describes the pressure loss of a viscous fluid at high velocities in porous media.

The approaches mentioned above could be classified as semi-empirical. The presented heat terms refer to an existing component of the battery, and the decline of a given substance is monitored with a mass balance, considering the exact measured mass or an estimate. There is, however, no connection to any chemical species and their physical properties. This is especially true when considering the released heat in these approaches derived from DSC peaks attributed to the decay of a given part of the battery. Besides this reaction model, most of the described procedures include actual physical processes such as joule heating, evaporation heat, heat propagation, and multi-phase flow. Yet, the sheer complexity of a thermal event in Li-ion batteries prevented a fully physical-based model entailing all occurring phenomena until now.

The first known reaction model with a more physical basis was developed by Tanaka et al. [109]. They simulated the SEI decomposition based on the chemistry of LEDC as the central SEI component. Here, the released heat is calculated based on species properties, such as the heat of formation and the resulting heat of reaction. Kupper et al. [110] extended the work of Tanaka et al. by including SEI-specific calendaric ageing mechanisms at various temperatures into a pseudo-3D electrochemical model. Besides complex electrochemical charge transfer and ageing reactions, heat and mass transport processes are implemented in their framework. Thereby, they were able to capture the nonlinear relationship between calendar ageing, performance and temperature. Based on their previous results, Kupper et al. [111] investigated the influence of an external short-circuit in combination with ARC and DSC simulations. They found that the external short-circuit experiment could be reproduced assuming an insulating secondary SEI consisting of Li_2CO_3. However, none of these approaches included gas solubilities or phase equilibria and their interplay with occurring reactions.

Apart from the above semi-empirical and physical-based models, data-based modelling approaches are used to assess battery safety more frequently. Kriston et al. [112] combined a physical model with machine learning techniques such as principal vector analysis and clustering to assess the severity of thermal runaway based on the initial conditions. Another relevant data-based approach is the time sequence map introduced by Feng et al. [113]. Here, the heats measured with DSC are transferred to a vector-based representation which can subsequently be aligned in a diagram. In this approach, the complex reaction network is uncoupled, and each heat is individually addressed. In this way, a simple method to interpret the intricate thermal runaway evolution is proposed.

Considering that semi-empirical models are almost exclusively utilised for addressing thermal runaway behaviour, it is evident that species-dependent interactions between reactions are mostly not taken into account. One crucial aspect of this is the solubility of gases, which also significantly impacts the pressure inside the battery cell. The conventional approach in chemical engineering to address this issue employs equations of state (EoS). Utilising an EoS

can effectively model the solubility of gases from degradation reactions and the ensuing pressure increase caused by the same. Recognising their significance to the field, the following section briefly introduces EoS and provides an overview of existing strategies.

2.3 Equations of state

An EoS relates pressure, volume, and temperature and, thus, describes the state of matter for a given substance. The most basic form of this equation is the ideal gas law:

$$pV = nRT, \tag{2.4}$$

where p, V, n, R, and T describe the pressure, volume, molar amount, gas constant and absolute temperature, respectively. It was introduced by Claperyon in 1834 and is effectively a summary of the empirical works of Boyle's law, Charles's law, Avogadro's law, and Gay-Lussac's law [114]. This description does not take into account any species-specific properties. Therefore, it falls short of accurately portraying the diverse behaviours that arise from their unique features. At the end of the 19$^{\text{th}}$ century, Van der Waals (VdW) [8] introduced his famous cubic equation of state that takes into account an attraction term, a, between the molecules as well as their occupied volume b, which are specific for individual species [115]. With this extension, it was for the first time possible to describe the vapour-liquid phase transition of a pure compound. However, as with every EoS up until now, it fails in accurately predicting the compressibility factor Z at the critical point, which is $Z_{\text{VdW}} = 0.375$, whereas measured Z values most often range around 0.29 [116]. Thus, expanded descriptions such as of Soave-Redlich-Kwong (SRK) [117] and Peng-Robinson (PR) [118] included further terms to accurately describe the Z value and increase their precision. All three EoS can be described in the same form:

$$p = \frac{RT}{v-b} - \frac{a\alpha(T_{\text{r}})}{v^2 + c_1 bv + c_2 b^2}, \tag{2.5}$$

with v being the molar volume, b a constant described as the co-volume, $\alpha(T_{\text{r}})$ a term describing the temperature dependence of the attractive term a, and $T_{\text{r}} = T/T_{\text{c}}$ the reduced temperature with respect to the critical temperature T_{c}. c_1 and c_2 are constants, which are both 0 for the VdW EoS, 1 and 0 for SRK and 2 and -1 for PR. Rearranging Equation 2.5 gives:

[8] Van der Waals based his approach on the idea of distinct atoms. Which is especially remarkable as then the scientific community still struggled with the acceptance of existence of atoms.

$$0 = v^3 + \left[(c_1 - 1)b - \frac{RT}{p}\right] v^2 + \left[(c_2 - c_1)b^2 - c_1\frac{RT}{p}b + \frac{a\alpha(T_\mathrm{r})}{p}\right] v - \left[c_2 b^2 + c_2\frac{RT}{p}b + \frac{a\alpha(T_\mathrm{r})}{p}\right] b, \tag{2.6}$$

in its cubic form [116].

Since their development, the pure EoS forms PR and SRK have been modified in various ways. Two hundred modifications are available for the PR EoS for pure components and one hundred for mixtures [119]. To estimate and predict the phase behaviour of mixtures, so-called mixing rules have been developed, of which Wong-Sandler [120] and the Huron-Vidal [121] are among the most prominent. Most commonly, the applied mixing rules rely on the EoS/G_E relation, which states that G_E, the excess Gibbs energy, usually calculated from activity models such as the Universal Quasichemical (UNIQUAC) approach and its group contribution extension UNIQUAC Functional-group Activity Coefficients (UNIFAC), must be the same as the excess Gibbs energy of the EoS. This allows to solve for the high-pressure and high-temperature phase equilibrium based on low-pressure G_E models [122].

Combined with mixing rules, cubic EoS are in their various forms and modifications widely applied in the chemical industry to describe the phase transition of mixtures and pure compounds, e.g. in separation units. However, during the second half of the 20$^{\mathrm{th}}$ century, the quest for a more physical-based EoS that would also accurately describe the phase behaviour of polar species has led to the development of a variety of new EoS. Most have been rejected by industry and academia as they do not allow for a better description than the classical and straightforward cubic EoS [123].

An exception is the statistical associating fluid theory (SAFT) EoS developed in the late 1980s by Chapman et al. [124, 125]. By adopting the first-order thermodynamic perturbation theory treatment for associating fluids of Wertheim [126–129], it was the first EoS that accounted for association and non-sphericity. Through this novelty, it was able to describe an unprecedented number of fluids with an accuracy surpassing classical cubic EoS[9]. In light of this achievement, the theory has been adapted and developed further such that now a variety of SAFT theories exists, some of which are pertubated chain-SAFT [131, 132], soft-SAFT [133], SAFT-variable range [134]. A recent extension of the original framework is introducing a group-contribution aspect. Group-contribution (GC) as a means to derive predictive models has already been

[9] Cubic EoS are still seen as competitive in industry as well as academia [123]. Especially the development of cubic plus association models helped to close the gap [130]. Here, the simplicity of classical cubic EoS and the association term from the SAFT framework are combined.

developed in the 1950s by Lydersen [135] and further improved by Joback and Reid [136]. GC extensions exist for all kinds of EoS, classically, in the form of the above-introduced mixing rules. As molecules within the SAFT framework are composed of segments, it delivers an almost natural starting point for this approach [137]. A class of GC SAFT approaches, that will also be utilised in this dissertation, is called SAFT-γ and was introduced in [138]. Compared to other approaches that employ a homonuclear chain approach with mixing rules, SAFT-γ composes the molecules of heteronuclear chains. This enables the prediction of binary and multi-component mixtures from pure component data alone as long as all relevant groups are part of the pure components. Since its development, the SAFT-γ approach has been applied to a range of different fields, such as in a computer-aided molecular design framework to design solvents for separation and carbon capture processes [139, 140]. Most recently, Wehbe et al. employed the SAFT-γ Mie[10] approach to predict the solubility of ibuprofen in different aqueous electrolyte solutions [141]. The same approach was also recently applied to predict the CO_2 absorption capabilities of differing amine mixtures [142].

However, the field of liquid electrolytes for state-of-the-art Li-ion batteries still remains untouched by classical EoS as well as SAFT EoS until now. This lack of research likely originated from the complexity and vast number of used solvent combinations. Here, the GC aspect of SAFT-γ poses the perfect solution. Once the core solvent groups' parameters are identified, different molecules and compositions can be studied.

2.4 Scope and structure

The majority of employed models in literature make use of the same structure which was initially introduced by Hatchard et al. [91]. Here, the thermal runaway is partitioned into heat sources which can be classified as exothermic reactions, internal short-circuits and heat sinks from electrolyte venting. While this approach has proven to be a powerful tool in describing the evolution of the thermal runaway, more insight and explanation of occurring phenomena are needed. This is mainly owed to the missing connection to chemical species. To address this open challenge, this thesis aims to develop a component-based model for the safety assessment of Li-ion batteries. Herein, the focus will be on the rigorous estimation of initial conditions and proper representation of physical properties. Moreover, the effect of phase equilibria will be studied in detail. Few literature sources considered the boiling of the electrolyte [65, 84, 105] and in all studies, the solvent was a pure component. Since industry and academia almost exclusively use binary and higher-order electrolyte mixtures, this thesis

[10] This is a special form of the SAFT-γ EoS, which is also used in this thesis and will be introduced in detail in Section 3.3.1.

will encompass these combinations. Hence, an approach utilising EoS to incorporate binary and, subsequently, multi-component mixtures is presented. This allows to study the intricate interplay between evolving reaction gases and vapour-liquid equilibria of Li-ion batteries. Furthermore, most of the above-described work primarily concentrates on thermal runaway and the corresponding alterations influenced by changing conditions or parts of the battery, such as the electrode active materials. But at this point, it is too late. To understand the underlying mechanisms leading to this catastrophic event, this thesis will elucidate the transition from safe operation to self-heating and to thermal runaway.

This thesis is structured into 7 chapters. The following Chapter 3 introduces the underlying methodology. First, the reaction network is presented and discussed. Further, the model equations are introduced.

In Chapter 4, this framework is employed to simulate an ARC measurement, and the first conclusions about the interplay of reactions and phase equilibria will be presented.

Based on these findings, Chapter 5 will investigate the influence of H_2O as an impurity and SEI properties on the crucial self-heating temperature and subsequent temperature progression.

Chapter 6 describes the implementation of a group-contribution EoS to perform a detailed analysis of factors that affect the pressure progression in Li-ion battery electrolyte systems during a thermal event.

The dissertation is completed with Chapter 7, which assesses the impact of the presented findings and provides an outlook for future work.

3 Methodology and models

This chapter outlines the methods utilised in this thesis. Initially, the fundamental reaction network is presented and examined in relation to the existing body of literature. This is followed by a detailed description of the mathematical model equations used to simulate the thermal event in Li-ion batteries. The chapter concludes with an introduction to the SAFT-γ Mie EoS, which is used to analyse the pressure changes inside the battery during a thermal event.

3.1 Reaction network[1]

A proper analysis of the underlying reaction network is mandatory to obtain the degree of physical accuracy needed for a better understanding of the thermal runaway. The network depends on the used cell chemistry. In this thesis, an ARC measurement of Maleki et al. [69] is utilised, which will be described in more detail in Section 4.1.2. The cell chemistry is a graphite anode, $LiCoO_2$ cathode combined with an EMC/EC $LiPF_6$ electrolyte. The resulting reaction network is summarised in Table 3.1.

Considering battery safety, the first reactions that occur at notable rates are the conductive salt decomposition (CSD) and the subsequent decomposition to POF_3 (PFD) and HPO_2F_2 (POFD) at elevated temperatures between 60 °C to 80 °C. They also take place at room temperature but only slowly in the range of days. During thermal abuse, they are accelerated and occur within hours or minutes. Following the publication of Stich et al. [144], the decomposition of $LiPF_6$ to PF_5 and LiF (CSD) and the subsequent decomposition of PF_5 with H_2O to POF_3 and HF (PFD) are considered as equilibrium reactions. In the original publication by Stich et al. [144], PF_5 directly reacts with two H_2O to form three HF and HPO_2F_2. However, in a study by Solchenbach et al. [85] POF_3, an intermediate is detected by gas analysis techniques such as OEMS. This detection implies that the lifespan of POF_3 is sufficiently long to be considered

[1] Parts of this chapter have been published as own contributions in Baakes, F., Lüthe M., Gerasimov, M., Laue, V., Röder, F., Balbuena, P., Krewer, U., "Unveiling the interaction of reactions and phase transition during thermal abuse of Li-ion batteries", Journal of Power Sources, DOI:10.1016/j.jpowsour.2021.230881, CC BY 4.0 [60] and Baakes, F., Witt, D., Krewer, U., "Impact of electrolyte impurities and SEI composition on battery safety", Chemical Science, DOI:10.1039/D3SC04186G, CC BY 3.0 [143].

Table 3.1: Degradation reactions, their reaction enthalpy (blue = endothermic, red = exothermic), the Gibbs free energy of reaction (blue = endergonic, red = exergonic) and their temperature range in which they are observed in differential scanning calorimetry, accelerated rate calorimetry or electrochemical measurements. Products that also act as reactants are highlighted in bold.

Name	Abbr.	Equation	$\Delta H_r^{\ominus}$ kJ mol^{-1}	$\Delta G_r^{\ominus}$ kJ mol^{-1}	T_{Start} °C
$LiPF_6$ decomposition [43, 144–146]	CSD	$LiPF_6 \rightleftharpoons LiF + \mathbf{PF_5}$	82.07	29.69	25/60–80*
PF_5 decomposition [144, 147, 148]	PFD	$PF_5 + H_2O \rightleftharpoons 2\,\mathbf{HF} + \mathbf{POF_3}$	80.09	2.71	25/60–80*
POF_3 decomposition [147]	POFD	$POF_3 + H_2O \longrightarrow \mathbf{HF} + HPO_2F_2$	296.53	293.12	25/60–80*
LEDC production [35, 149]	OSP	$2\,LiC_6 + 2\,C_3H_4O_3(EC) \longrightarrow (\mathbf{CH_2OCO_2Li})_2 + C_2H_4 + 2\,C_6$	-135.73	-131.22	25/80–120**
Li_2CO_3 production [43, 149]	ISP	$2\,LiC_6 + C_3H_4O_3(EC) \longrightarrow \mathbf{Li_2CO_3} + C_2H_4 + 2\,C_6$	-572.62	-608.08	25/80–120**
LiOH production [150]	LSP	$LiC_6 + H_2O \longrightarrow \mathbf{LiOH} + 0.5\,H_2 + C_6$	-199.11	-198.40	25/80–120**
LEDC decomposition [94, 151]	OSD	$(CH_2OCO_2Li)_2 \longrightarrow \mathbf{Li_2CO_3} + C_2H_4 + CO_2 + 0.5\,\mathbf{O_2}$	-187.05	-347.21	60–120
Li_2CO_3 decomposition [152, 153]	ISD	$Li_2CO_3 + 2\,HF \longrightarrow 2\,LiF + \mathbf{H_2O} + CO_2$	-152.09	-127.44	25/60–120
LiOH decomposition [150, 154]	LSD	$LiC_6 + LiOH \longrightarrow Li_2O + 0.5\,H_2 + C_6$	-113.82	-119.72	100–120
$LiCoO_2$ decomposition [66, 69, 82, 155]	CD	$Li_xCoO_2 \longrightarrow xLiCoO_2 + (1\text{-}x)/3\,\mathbf{O_2} + (1\text{-}x)/3\,Co_3O_4$	-240.10	—***	150–220
EMC decomposition [66, 156]	EMCD	$3.5\,O_2 + C_4H_8O_3(EMC) \longrightarrow 4\,CO_2 + 4\,\mathbf{H_2O}$	-2071.7	—***	180–350
EC decomposition [66, 156]	ECD	$2.5\,O_2 + C_3H_4O_3(EC) \longrightarrow 3\,CO_2 + 2\,\mathbf{H_2O}$	-1161.3	-1201.8	180–350

* Slow process, considered during cell assembly, see Appendix Figure C.2.
** Higher temperature considered for re-formation.
*** Not possible to calculate due to lack of entropic data of at least one participating species.

significant and cannot be disregarded in our analysis. Thus, the first decomposition of PF_5 with H_2O to form POF_3 and HF (PFD) and the subsequent decomposition of POF_3 with H_2O to form HF and HPO_2F_2 (POFD) are considered as individual reactions[2]. The decomposition of the conductive salt initiates the release of HF, which causes the breakdown of Li_2CO_3 by reacting with HF to form LiF, H_2O, and CO_2 (ISD). Freiberg et al. [152] investigated Li_2CO_3 coated on a carbon electrode which reacted immediately with protons to CO_2. From this, it is concluded that the decomposition reaction of Li_2CO_3 with HF/H^+ is not rate-limiting. This implies that this reaction is directly connected to the decomposition of PF_5 and POF_3 and the corresponding release of HF. The decomposition of organic SEI (OSD) is reported to start somewhere in a wide temperature range from 60 °C to 120 °C [69, 70, 94, 157, 158]. It is responsible for the transition into the self-heating phase of an ARC [64, 94]. The decomposition of LiOH with

[2] Chapter 4 does only account for the first step, i.e. the decomposition of PF_5 to POF_3. In addition, this first approach has only considered forward reactions.

lithium to form H_2 and Li_2O (LSD)[3] is reported in literature [150]. However, no information on the temperature range for this reaction could be found. Therefore, this work relies on a study of the decomposition of LiOH with LiH into Li_2O and H_2, which reported a decomposition temperature of about 120 °C [154].

The initial decomposition of SEI compounds, including Li_2CO_3, LEDC, and LiOH, exposes the bare electrode surface. Given the solvent's instability against the anode's low potential, subsequent reactions occur between them. These re-formation reactions (OSP, ISP, LSP[4]) are direct results of the preceding decomposition. They are linked to the battery's self-heating [64]. Notably, the temperature range for these reactions aligns with the decomposition reactions. Self-heating is strongly accelerated as soon as the decomposition of $LiCoO_2$ (CD) starts. The released O_2 leads to the massively exothermic combustion of solvent molecules (ECD, EMCD) [91, 156].

Aside from these reactions, electrolyte boiling may occur during cell heating. While this effect is usually ignored in other scientific works, its potential role as a heat sink, capable of stabilising the cell temperature, makes it an essential part of the analysis in this work. The boiling temperature of the mixture depends on the assumed electrolyte composition and the pressure, which here are considered to be a 1/1 (v/v) EC/EMC mixture under isobaric atmospheric pressure. For this initial composition, the boiling temperature is given with $T_{\mathrm{b,\ mixture}} = 122.45\,^{\circ}\mathrm{C}$ [5].

Besides these reactions and phase transitions, the following processes are briefly described but will not be considered in this work. The reaction of active material with the binder polyvinylidene fluoride is attributed to reactions happening around 300 °C, which is outside the relevant temperature range before the inevitable thermal runaway. Also, reactions involving materials like conductive agents and the current collectors are not considered. Whereas they may play a role in long-term battery ageing due to overcharging or high current operation, to the best of my knowledge, there are no reactions reported for high-temperature abuse [159]. Additionally, the separator is not considered as for the employed polypropylene/polyethylene separators in this work, aside from melting [62], no reactions are reported in the context of thermal runaway [88]. However, some reactions are reported for polyethyleneterephthalate separators at elevated temperatures up to 132 °C [88]. Further, electrolyte degradation with glass fibre separators has been found [88, 160]. Neither aspect is included in this work. However, they might be of interest for future investigations.

[3] This reaction was not accounted for in the study in Chapter 4.
[4] This reaction was also not accounted for in the study in Chapter 4.

Deviations in underlying system

As this thesis is the cumulative work of 5 and a half years, it is natural that the underlying model and reaction network also evolved during this time. Therefore, the reaction networks and models of Chapter 4 and Chapter 5 differ slightly. Here, the latter has been extended to better account for the intricate interplay of the conductive salt decomposition and SEI species. These differences also lead to deviations in reaction progressions, even though both models are ultimately parameterised against the same ARC experiment by Maleki et al. [69]. These deviations and their implications on the validity of the results from Chapter 4 will be discussed in Chapter 5. To avoid a repeated description of most model parts, the following chapter will give the complete model and reaction network utilised in Chapter 5. It will be noted whenever parts are omitted or have not yet been included in Chapter 4. Further, the introduction of each chapter will summarise the individual set of considered reactions.

3.2 Models for thermal abuse[6]

The following section will describe the mathematical equations employed for the used approach. First, a brief overview of the model and underlying conditions and assumptions is given. This is followed by the implemented species balances according to reaction rate equations. Subsequently, the energy balance and calculation of heat capacity, reaction heat and heat of phase transition are introduced. After that, concentrations, partial pressures and solubility models are explained. This section closes with a description of a simple pressure calculation.

3.2.1 Model overview

The modelled scenario is the ARC measurement of Maleki et al. [69], conducted at 4.15 V cell voltage, corresponding to a SOC of 100%. Adiabatic conditions during the self-heating period are assumed. The system is closed. Self-heating and thermal runaway are driven by the heat of reaction released or consumed. Thus, a crucial component of the presented modelling approach is the calculation of reaction heats from the enthalpies of formation of participating components by Hess's law [161]. All modelled species and their physical parameters can be

[6] Parts of this chapter have been published as own contributions in Baakes, F., Lüthe M., Gerasimov, M., Laue, V., Röder, F., Balbuena, P., Krewer, U., "Unveiling the interaction of reactions and phase transition during thermal abuse of Li-ion batteries", Journal of Power Sources, DOI:10.1016/j.jpowsour.2021.230881, CC BY 4.0 [60] and Baakes, F., Witt, D., Krewer, U., "Impact of electrolyte impurities and SEI composition on battery safety", Chemical Science, DOI:10.1039/D3SC04186G, CC BY 3.0 [143].

found in the Appendix in Table B.2. Furthermore, an approach for calculating the heat of boiling of a binary electrolyte mixture based on an EoS is proposed. Finally, the individual contribution of each reaction or phase change to the overall produced heat can be calculated, and a correlation between the balance of the species and the heat sinks and sources can be drawn. To allow a first investigation of the principle interaction of reaction and phase change during thermal abuse of a Li-ion battery, diffusion and thermal conductivity are not implemented. The different phases inside a battery are distinguished by four reference phases: the anode, including the SEI, the liquid electrolyte, the cathode and the gas phase. The following additional assumptions are underlying this modelling approach:

- Ideal mixed solution - no spatial discretisation. Since the time constant for diffusion and thermal conductivity is in seconds and the ARC measurement takes hours, this assumption of a perfectly mixed system is deemed a sound approach for this work.
- No pressure increase due to gas evolution. This assumption corresponds to the initial stages of a highly inflatable pouch cell.
- Within each time step, the solvent is in vapour-liquid equilibrium.
- Salt and its degradation products do not impact the vapour-liquid equilibrium.
- Reactions are pseudo-homogeneous.
- The electrolyte consists of a 50/50 (v/v) mixture of EC and EMC with $1200\,\mathrm{mol\,m^{-3}}$ $LiPF_6$.
- The geometry of the cell is taken from a commercially available one with a capacity and cell chemistry comparable to the cell used in the study by Maleki et al. [162].
- The electrode geometry is similar to other published electrodes of the same chemistry [163, 164].

3.2.1.1 Set notation

In the following model description, the set notation is used to unambiguously state, e.g. reaction rates and participating species. The used sets are Ω_{RE} with the subset $\Omega_{\mathrm{SEI,\ form}}$, referring to the modelled reactions and SEI formation reactions, respectively. Further, Ω_{SP} with the subsets of Ω_{Solv}, Ω_{SEI}, Ω_{S}, Ω_{L} and Ω_{G} related to the modelled species, solvent components, SEI, solid, liquid and gaseous species, respectively. Another subset of Ω_{SP} is Ω_{U} which encompasses all species u taking part in reaction j. Given the example reaction of $LiPF_6 \longrightarrow LiF + PF_5$ this would translate to the species $LiPF_6$, LiF and PF_5. The set Ω_{U} is then further divided

into subsets of forward $\Omega_{\mathrm{U_f}}$ and backwards reactions $\Omega_{\mathrm{U_b}}$. In the given example $\Omega_{\mathrm{U_f}}$ contains $LiPF_6$ and $\Omega_{\mathrm{U_b}}$ contains LiF and PF_5.

As the sets differ between Chapter 4 and 5, the exact composition will be given at the beginning of each chapter.

3.2.2 Species balances and reaction kinetics

Since the battery is modelled as a closed system, there is no molar flux in or out of the battery. This yields the following species balance for all species i and respective reactions j:

$$\frac{\mathrm{d}n_i}{\mathrm{d}t} = \sum_{j \in \Omega_{\mathrm{RE}}} \nu_{ji} r_j, \forall\, i \in \Omega_{\mathrm{SP}}. \tag{3.1}$$

Here, n_i is the molar amount of species i, ν_{ji} refers to the stoichiometric coefficient of component i in reaction j and r_j refers to the reaction rate of reaction j. If not mentioned otherwise, the reaction kinetics are modelled as power law kinetics combined with Arrhenius law to describe the temperature dependency [165]:

$$r_j = k_{0,\,j} \exp\left(\frac{-E_{\mathrm{A},\,j}}{RT}\right) \prod_{u \in \Omega_{\mathrm{U_f}}} a_u^{\nu_{uj}}, \forall\, j \in \Omega_{\mathrm{RE}} \backslash \{\Omega_{\mathrm{SEI}}, CSD\}. \tag{3.2}$$

Here, $k_{0,\,j}$ refers to the pre-exponential factor for reaction j and $E_{\mathrm{A},\,j}$ the respective activation energy. The dimensionless activity of each participating component is written as a_k, and their definition is given in Section 3.2.4.

Equation 3.3 represents a special case for reactions of intercalated lithium with the solvent that also takes the thickness of the SEI-layer d_{SEI} into account since SEI growth is known to depend on SEI thickness [110]:

$$r_j = k_{0,\,j} \frac{1}{d_{\mathrm{SEI}}} \exp\left(\frac{-E_{\mathrm{A},\,j}}{RT}\right) \prod_{u \in \Omega_{\mathrm{U_f}}} a_u^{\nu_{uj}}, \forall\, j \in \Omega_{\mathrm{SEI}} \tag{3.3}$$

Given its simplicity, the introduced dependency of SEI forming reactions on the SEI thickness is better understood as a dependency on the capability of the SEI to form an electron-insulating layer. This capability is first and foremost reduced by its decomposition due to reactions. However, crack formation induced by particle swelling [166–168] and SEI dissolution [169] could also lead to new SEI formation.

Furthermore, it is widely assumed that for the decomposition of the conductive salt $LiPF_6$, only the non-dissociated part, as in the left-hand side of $LiPF_6 \rightleftharpoons Li^+ + PF_6{}^-$ is decomposed [144]. Therefore, the dissociation constant[7] α is introduced in the salt decomposition rate to describe this phenomenon [147]. The constant is set to $\alpha = 0.7$ as already described by Stich et al. [144].

$$r_j = k_{0,j}(1-\alpha)\exp\left(\frac{-E_{A,j}}{RT}\right)\prod_{u\in\Omega_{U_f}} a_u^{\nu_{uj}}, \forall\, j \in \{CSD\} \tag{3.4}$$

As the ARC is conducted at OCV, no electrochemical reactions are implemented.

3.2.2.1 Reversible reactions

Further reversible reactions are introduced for the decomposition of $LiPF_6$ and PF_5. As the Gibbs free energy $\Delta\underline{G}_{r,j}$ of only these reactions allows for reasonable backward reactions[8], see Table 3.1. The equations then change to [170]:

$$r_j = k_{f,j}(1-\alpha)\prod_{u\in\Omega_{U_f}} a_u^{\nu_{uj}} - k_{b,j}\prod_{u\in\Omega_{U_b}} a_u^{\nu_{uj}}, \quad \forall j \in \text{CSD}, \tag{3.5}$$

$$r_j = k_{f,j}\prod_{u\in\Omega_{U_f}} a_u^{\nu_{uj}} - k_{b,j}\prod_{u\in\Omega_{U_b}} a_u^{\nu_{uj}}, \quad \forall j \in \text{PFD}. \tag{3.6}$$

Here, $k_{b,j}$ represents the reaction constant for the backward reactions computed as:

$$k_{b,j} = \frac{k_{f,j}}{K_j} \quad \text{and} \quad K_j = \exp\left(-\frac{\Delta\underline{G}_{r,j}(T)}{RT}\right), \quad \forall j \in \text{CSD, PFD}, \tag{3.7}$$

where the Gibbs free energy of reactions is given with:

$$\Delta\underline{G}_{r,j}(T) = \Delta\underline{H}_{r,j}(T) - T\Delta\underline{S}_{r,j}(T), \quad \forall j \in \text{CSD, PFD}. \tag{3.8}$$

Here, $\Delta\underline{S}_{r,j}(T)$ refers to the entropy of reaction.

[7] This phenomenon will be discussed more deeply in Section 3.3.3 and Chapter 6

[8] In Chapter 4, both reactions have been modelled as irreversible. Thus, Equations 3.2 and 3.4 are used instead.

3.2.3 Energy balance, heat of reaction, and phase change

The model for the temperature evolution is divided into three parts, where the first part, the pre-heating[9], is performed with a constant heating rate as:

$$\frac{\mathrm{d}T}{\mathrm{d}t} = 1\,\mathrm{K\,min^{-1}}. \tag{3.9}$$

The following step-wise heating is modelled using a simple P controller with one constant as follows:

$$\frac{\mathrm{d}T}{\mathrm{d}t} = \frac{T_{\mathrm{Setpoint}} - T}{\kappa}. \tag{3.10}$$

Here, T_{Setpoint} corresponds to the temperature set by the ARC algorithm, which increases by 10 °C after each HWS step. κ is a time constant chosen to reproduce the step-heating accurately. In this simplified approach, the Heat period, where the temperature step is performed, and the Wait period, where the cell is given time to equilibrate with the temperature of the device in the experiment, are joined together. This is done since, in our simulation, only the cell temperature is simulated, and the cell is not discretised. Thus, the cell is always in equilibrium. After the Heat-Wait period, the temperature evolution is calculated as follows within the Seek period:

$$\frac{\mathrm{d}T}{\mathrm{d}t} = \frac{\sum_{j\in\Omega_{\mathrm{RE}}} Q_j + Q_{\mathrm{PT}}}{C_{\mathrm{p,\,bat}}}, \tag{3.11}$$

where Q_j and Q_{PT} refer to the rate of production of heat from reaction j and the heat from phase transition[10] of the electrolyte, respectively. If at the end of the seek period, the self-heating rate of the battery exceeds the threshold[11] $\frac{\mathrm{d}T}{\mathrm{d}t} = 0.02\,\mathrm{K\,min^{-1}}$, the temperature evolution is further calculated as in Equation 3.11 corresponding to the exothermic mode of the ARC. Otherwise, another Heat and Wait period is performed as in Equation 3.10. For the calculation of the self-heating phase, quasi-adiabatic conditions are assumed for the energy balance due to the ARC set-up explained in Section 2.2.1. Thus, the balance equation reduces to the form above, containing only heat sinks or sources due to reaction or phase change.

[9] This part of the experiment is only introduced for the work in Chapter 5.
[10] Heat from phase transition has been excluded for the work in Chapter 5 based on the results from Chapter 4.
[11] Please note that due to lack of data in the original publication of Maleki et al. [69] this threshold was taken from another publication of the same author [171].

The isobaric heat capacity of the battery $C_{\mathrm{p,bat}}$ is calculated from the individual components as follows:

$$C_{\mathrm{p,bat}} = \sum_{i \in \Omega_{\mathrm{SP}}} \underline{C}_{\mathrm{p},i} n_i + C_{\mathrm{p,Al}} + C_{\mathrm{p,Cu}} + C_{\mathrm{p,Casing}}. \tag{3.12}$$

The parameters $\underline{C}_{\mathrm{p},i}$, $C_{\mathrm{p,Al}}$, $C_{\mathrm{p,Cu}}$ and $C_{\mathrm{p,Casing}}$ represent the molar heat capacity of component i, the heat capacity of the aluminium and copper current collector and the casing (in this case pouch-cell foil), respectively (see Table A.10 in the Appendix for more information).

The rate of heat produced or consumed in each reaction j is the product of their respective reaction rate r_j and the molar enthalpy of reaction $\Delta\underline{H}_{\mathrm{r},\,j}$:

$$Q_j = -r_j \Delta\underline{H}_{\mathrm{r},\,j}(T), \forall\, j \in \Omega_{\mathrm{RE}}. \tag{3.13}$$

The heat consumption rate resulting from the transition of the liquid solvents of the electrolyte from liquid state to their gaseous state is calculated as:

$$Q_{\mathrm{PT}} = \sum_{\sigma \in \Omega_{\mathrm{Solv}}} \frac{\mathrm{d}n''_{\sigma}(T,p,x_{\mathrm{EC}})}{\mathrm{d}t} \cdot \Delta\underline{H}_{\mathrm{vap},\,\sigma}(T), \tag{3.14}$$

where $\Delta\underline{H}_{\mathrm{vap},\,\sigma}$ represents the vaporisation enthalpy of solvent σ and $\frac{\mathrm{d}n''_{\sigma}(T,p,x_{\mathrm{EC}})}{\mathrm{d}t}$ is the boiling rate of solvent σ which is calculated based on equilibrium data for T, p and compositions x_{EC}. Please note that prime notation refers to liquid or gaseous molar amounts, with $'$ and $''$ signalling the liquid and gas phases, respectively. The exact procedure is explained in Appendix A.3.2.10.

3.2.4 Solubility model — Concentration, partial pressure and activity

The calculations of concentrations and partial pressures are based on the four different phases where the reactions occur. Therefore, the concentration C_i is calculated as:

$$C_s, = \frac{n_s}{V_{\text{An+SEI/Cat}}}, \forall s \in \Omega_{\text{S}}, \tag{3.15}$$

$$C_l, = \frac{n_l^{'}}{V_{\text{El}}}, \forall l \in \Omega_{\text{L}}, \tag{3.16}$$

$$C_g, = \frac{n_g^{'}}{V_{\text{El}}}, \forall g \in \Omega_{\text{G}}. \tag{3.17}$$

here, the subscripts l, g, and s denote the state of a particular substance under standard conditions, with $T^{\ominus} = 298.15K$ and $p^{\ominus} = 100$ kPa, where l represents liquid, g stands for gas, and s signifies solid. V_{El} refers to the electrolyte volume, and $V_{\text{An+SEI/Cat}}$ to either the anode+SEI or cathode depending on the species. A detailed description of how the volumes are calculated is provided in A.1. Considering molar fractions, the notations x, y, and z represent the liquid, gas, and overall compositions, respectively.

The partial pressure p_g of gas g is given as the product of the mole fraction of the component in the gas phase y_g and the given system pressure as stated by Dalton's law [172]

$$p_g = p \cdot y_g, \forall g \in \Omega_{\text{G}}. \tag{3.18}$$

The system pressure is set to $p = 101\,325\,\text{Pa}$. Isobaric conditions are assumed. Thus, the value is kept constant during the whole simulation. The mole fraction of each species within the gas phase is calculated as follows:

$$y_g = \frac{n_g^{''}}{\sum_{\gamma \in \Omega_{\text{G}}} n_\gamma^{''}}, \forall g \in \Omega_{\text{G}}. \tag{3.19}$$

Activities are then defined as:

$$a_s = \frac{C_s}{C^{\ominus}}, \forall s \in \Omega_{\text{S}} \text{ and} \tag{3.20}$$

$$a_l = \frac{C_l}{C^{\ominus}}, \forall l \in \Omega_{\text{L}} \text{ and} \tag{3.21}$$

$$a_g = \frac{p_g}{p^{\ominus}}, \forall g \in \Omega_{\text{G}}, \tag{3.22}$$

depending on the state of the modelled species. The reference concentration for both active materials is set to their respective maximal concentration of lithium in their solid phase $C^{\ominus} = C_{\max}$. In all other cases, the reference pressure and reference concentration is the standard thermodynamic reference state defined by the IUPAC as $p^{\ominus} = 100\,000\,\mathrm{Pa}$ and $C^{\ominus} = 1000\,\mathrm{mol\,m^{-3}}$, respectively [173]. Non-idealities, usually expressed by the activity or fugacity coefficient, may be present for the species. However, they are mostly not known yet, and we thus neglect them in the work presented here.

The phase transition of the electrolytes' solvent components EC and EMC, and thus the molar amount of each solvent in both phases, is calculated using a phase equilibrium model of the binary mixture. A detailed explanation is given in the Appendix A.3.4.2. For all other gaseous species, such as CO_2 or C_2H_4, the solubility is modelled via Henry's law [174]. Here, the solubility in both solvents is considered separately. The Henry coefficient $H_{g\sigma}$ is hence used to obtain the mole fraction $x_{g\sigma}$ of the gaseous species g within the solvent σ as follows :

$$x_{g\sigma} = \frac{p_g}{H_{g\sigma}}, \forall g \in \Omega_{\mathrm{G}} \backslash \Omega_{\mathrm{Solv}} \wedge \forall \sigma \in \Omega_{\mathrm{Solv}}. \tag{3.23}$$

by rearranging Equations 3.19 and 3.23, the total maximal amount $n_g^{',\max}$ of a gaseous species g in both solvents can be calculated as:

$$n_g^{',\max} = \sum_{\sigma}^{|\Omega_{\mathrm{Solv}}|} \frac{\frac{n'_\sigma \cdot p \cdot n_g}{H_{g\sigma} \cdot \sum_{\gamma}^{|\Omega_{\mathrm{G}}|} n_\gamma}}{\frac{1-(n'_\sigma \cdot p \cdot n_g)}{H_{g\sigma} \cdot \sum_{\gamma}^{|\Omega_{\mathrm{G}}|} n_\gamma}}, \forall g \in \Omega_G \backslash \Omega_{\mathrm{Solv}} \tag{3.24}$$

Since the gases are produced due to degradation reactions and are not present within the system from the start, we assume that they will stay dissolved until their respective solubility limit, expressed by the Henry coefficient, is reached. Thus, the calculation of the molar amount of each species in the liquid and gas phases needs to be divided into two cases, as shown below:

$$n_g^{'}, n_g^{''} = \begin{cases} n_g^{'} = n_g, n_g^{''} = 0 & \text{for } n_g \leq n_g^{',\max} \\ n_g^{'} = n_g^{',\max}, n_g^{''} = n_g - n_g^{',\max} & \text{for } n_g > n_g^{',\max} \end{cases}, \forall g \in \Omega_G \backslash \Omega_{\mathrm{Solv}} \tag{3.25}$$

3.2.5 Changes in cell volume and pressure

In general, no pressure increase is assumed in the model due to the use of an inflatable pouch cell. However, a pressure increase is expected as there is a limit in the maximal pouch volume

above this value. The total gas volume is analysed to monitor if and where this threshold is reached. For this and further analysis regarding the rise in pressure due to evolving reaction gases, two phases need to be considered. First is the isobaric period, during which the pouch cell volume increases due to the decomposition of gases. Second is the isochoric phase, in which the pouch cell reaches its maximum volume, and the gases contribute to a rise in pressure. For this, the cell volume is calculated as

$$V_{\mathrm{Cell}} = \begin{cases} V_{\mathrm{Cell},0} + \sum_{g \in \Omega_{\mathrm{G}} \setminus \Omega_{\mathrm{Solv}}} \frac{n_g'' \cdot M_g}{\rho_g} & \text{for } V_{\mathrm{Cell}} < V_{\mathrm{Cell},0} \cdot 10, \\ V_{\mathrm{Cell},0} \cdot 10 & \text{for } V_{\mathrm{Cell}} \geq V_{\mathrm{Cell},0} \cdot 10. \end{cases} \tag{3.26}$$

Where $V_{\mathrm{Cell},0}$ is the volume of the cell at the beginning of the experiment/simulation, ρ_g refers to the density of gaseous species g, which is either calculated with Helmholtz models implemented in the CoolProp library or a version of the Peng-Robinson equation of state, see A.3.3 for more information. The maximum cell volume is assumed to be ten times the initial cell volume. This approximation is based on the measurement of Lee et al., who reported a sixfold increase of the pouch cell volume for cathode-only NMC pouch cells stored at 90 °C for 4 h [175]. The tenfold increase in volume is chosen to prevent a too-conservative assumption leading to a mistakenly high-pressure rise, thus resulting in a shift in the boiling temperature of the mixture. Therefore, the calculation of the pressure follows:

$$p = \begin{cases} 101\,325\,\mathrm{Pa} = \mathrm{const.} & \text{for } V_{\mathrm{Cell}} < V_{\mathrm{cell},0} \cdot 10, \\ 101\,325\,\mathrm{Pa} + \frac{\sum_{g}^{|\Omega_{\mathrm{G}} \setminus \{\mathrm{EC,EMC}\}|} n_g'' \cdot R \cdot T}{10 \cdot V_{\mathrm{Cell},0}} & \text{for } V_{\mathrm{Cell}} \geq V_{\mathrm{Cell},0} \cdot 10. \end{cases} \tag{3.27}$$

The gas volume of the vaporised solvent compounds is not considered. This is done to isolate the influence of emerging degradation gases on the pressure and, thus, the possibility of vaporisation. These calculations are, in combination with the binary phase equilibrium of EC and EMC, used to analyse if, due to the rise in pressure caused by evolving reaction gases, a phase transition would occur in such a system. Note that these considerations are not implemented in the model and are only analytical calculations performed on the gained results.

3.3 Detailed pressure model

After introducing the thermal runaway model as the basis for the studies in Chapters 4 and 5, this section will cover the SAFT-γ Mie model as an advanced method to study the pressure evolution in Li-ion electrolyte systems. The first part covers the underlying principles of the

SAFT-γ Mie EoS. The second part summarises methods used to estimate, unlike interaction parameters, from like interaction parameters without suitable experimental data. This is followed by a brief description of variables needed for phase equilibrium calculations and how they can be obtained from SAFT-γ Mie. The section closes by introducing a model extension to SAFT-γ Mie that allows to solve systems with low Dielectric constants, where ion association is prevalent.

3.3.1 SAFT-γ Mie[12]

As noted in Section 2.3, there is still a severe lack of research in representing vapour-liquid equilibria of conventional liquid electrolytes for Li-ion batteries. Therefore, this dissertation will address this open challenge. To do so, the SAFT-γ Mie EoS will be utilised, and the missing group interactions will be developed. This allows for an unprecedented in-depth analysis of various factors, such as electrolyte composition, gas solubility and conductive salt concentration, on the pressure evolution during thermal abuse in Li-ion batteries. Since the original model's development was not part of this thesis and is described elsewhere [137], only a brief analysis of the model's key aspects will be given.

This particular form of the SAFT EoS uses the segmental structure of the underlying theory. A given molecule is divided into constitutive groups such as the methyl group, CH_3, or the carboxyl group, COOH, in an acetic acid molecule, see Figure 3.1 a).

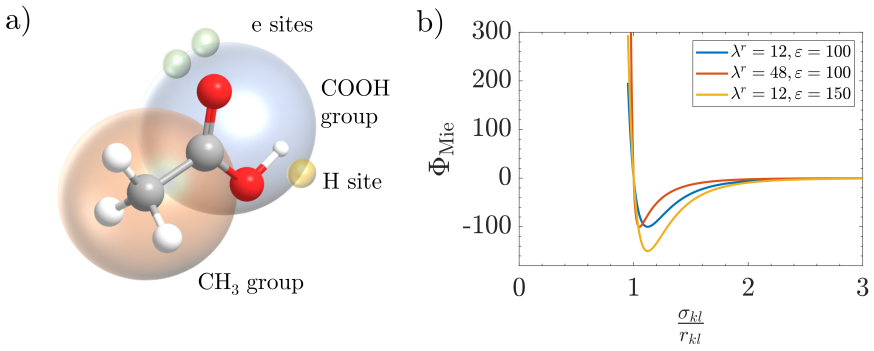

Figure 3.1: Schematic of the underlying principles of SAFT-γ-Mie with a) the group structure of acetic acid and b) the impact of varying repulsive exponent λ_{kl}^{r} and the depth of potential well ε_{kl} on the Mie potential.

[12] The following model description has mostly been adapted from Haslam et al. [137].

Describing the interaction between two distinct groups using a radial potential is roughly accurate for mostly spherical groups such as the abovementioned ones. However, this is not true for non-spherical groups, like the aromatic aCCOOH group, e.g. in benzoic acid. To account for this deviation, the groups are subdivided into several spherical segments with equal diameters. ν_k^* describes the number of segments for group k and S_k refers to its sphericity. Since every group consists of at least one segment, all interactions are described in segment interactions. The interaction between segments k and l is then calculated based on a Mie potential, which is a generalised Lennard-Jones potential:

$$\Phi_{kl}^{\mathrm{Mie}}(r_{kl}) = C_{kl} \cdot \varepsilon_{kl} \left(\left(\frac{\sigma_{kl}}{r_{kl}} \right)^{\lambda_{kl}^{\mathrm{r}}} - \left(\frac{\sigma_{kl}}{r_{kl}} \right)^{\lambda_{kl}^{\mathrm{a}}} \right), \tag{3.28}$$

where $\lambda_{kl}^{\mathrm{a}}$ and $\lambda_{kl}^{\mathrm{r}}$ describe the variable attractive and repulsive exponents between the segments k and l, respectively. ε_{kl} is the depth of the potential well, r_{kl} represents the centre-centre distance of two given segments k and l, and σ_{kl} is a size parameter which for a like-like interaction, i.e. $k = l$, is the segment diameter. Also,

$$C_{kl} = \left(\frac{\lambda_{kl}^{\mathrm{r}}}{\lambda_{kl}^{\mathrm{r}} - \lambda_{kl}^{\mathrm{a}}} \right) \left(\frac{\lambda_{kl}^{\mathrm{r}}}{\lambda_{kl}^{\mathrm{a}}} \right)^{\frac{\lambda_{kl}^{\mathrm{a}}}{\lambda_{kl}^{\mathrm{r}} - \lambda_{kl}^{\mathrm{a}}}}, \tag{3.29}$$

is a prefactor that ensures that the minimum of the potential well is always ε_{kl}, independent of the chosen $\lambda_{kl}^{\mathrm{a}}$ and $\lambda_{kl}^{\mathrm{r}}$.

Figure 3.1 b) shows the form of the Mie potential over increasing distance between two segments of equal diameter, where a distance of 1 refers to the radius of a given group, i.e. representing direct contact, this yields a potential of 0. Also, a variation of the repulsive exponent λ^r and the depth of the potential well ε is shown. Increasing the repulsive part will shorten the interaction distance while the depth of the potential well stays constant. On the other hand, increasing the depth of the potential well will increase the interaction distance.

To account for association-type interactions present in polar substances, a square-well potential interaction is implemented such that an association site[13] of type a on segment k interacts with another site of type b on segment l like:

$$\Phi_{kl,ab}^{\mathrm{HB}}(r_{kl,ab}) = \begin{cases} -\varepsilon_{kl,ab}^{\mathrm{HB}} & \text{if} \quad r_{kl,ab} \leq r_{kl,ab}^{\mathrm{c}}, \\ 0 & \text{if} \quad r_{kl,ab} > r_{kl,ab}^{c}. \end{cases} \tag{3.30}$$

[13] The types of the site refer to Lewis-base Lewis-acid interactions. This can be explained as partial electron-proton interactions and will be denoted e and H, respectively.

Where $r_{kl,ab}$ is the distance between the centres of sites a and b, $\varepsilon^{\mathrm{HB}}_{kl,ab}$ [14] is the association energy, and $r^{\mathrm{c}}_{kl,ab}$ is the cutoff range of the interaction between the two sites.

The SAFT-γ Mie EoS is based on the Helmholtz free energy A. A is obtained from the addition of individual contributions as:

$$\begin{aligned} A =& A^{\mathrm{ideal}} + A^{\mathrm{monomer}}(S_k, \nu^*_k, \sigma_{kl}, \varepsilon_{kl}, \lambda^{\mathrm{a}}_{kl}, \lambda^{\mathrm{r}}_{kl}) \\ &+ A^{\mathrm{chain}}(S_k, \nu^*_k, \sigma_{kl}, \varepsilon_{kl}, \lambda^{\mathrm{a}}_{kl}, \lambda^{\mathrm{r}}_{kl}) \\ &+ A^{\mathrm{association}}(S_k, \nu^*_k, \sigma_{kl}, \varepsilon_{kl}, \lambda^{\mathrm{a}}_{kl}, \lambda^{\mathrm{r}}_{kl}, K^{\mathrm{HB}}_{kl,ab}, \varepsilon^{\mathrm{HB}}_{kl,ab}) \\ &+ A^{\mathrm{Born}}(\sigma^{\mathrm{Born}}_{kk}) + A^{\mathrm{ion}}(\sigma_{kk}), \end{aligned} \tag{3.31}$$

where A^{ideal} denotes the free energy of an ideal gas, A^{monomer} represents the interaction of monomeric segments via Mie potentials, A^{chain} is the free energy contribution resulting from the formation of molecular chains from the combined Mie segments, and $A^{\mathrm{association}}$ signifies the molecular association through short-range directional interactions. These initial four terms encapsulate the non-ionic contributions [176–178]. The influence of charged species is considered in the final two terms [179–181], which are formulated within a primitive-model framework which implicitly accounts for the electrostatic character of the solvent depicted within a uniform dielectric medium. The A^{ion} term embodies the Coulombic ion-ion interactions, derived using the unrestricted Mean Spherical Approximation (MSA) model [182, 183], while the A^{Born} term accounts for the ion-solvent electrostatic interactions in accordance with the Born model [184]. The adjustable model parameters are shown in brackets for each contribution. In the case of ionic contributions, the adjustable model parameters are extended by the Born diameter of a given ion indicated by $\sigma^{\mathrm{Born}}_{kk}$.

The Van der Waals equation of state and each subsequently developed EoS describe the phase behaviour based on two features. The SAFT-γ Mie EoS is no exception. The first feature is the volume occupied by a molecule or segment structure, which in the SAFT-γ Mie EoS is mainly influenced by the segment (or molecule) diameter, σ_{kl}. The second is the attractive forces, primarily influenced by the form of the Mie potential and, for some groups, the association interactions. Both are described by the attractive and repulsive exponents, $\lambda^{\mathrm{a}}_{kl}$ and $\lambda^{\mathrm{r}}_{kl}$, as well as the depth of the potential wells, ε_{kl} and $\varepsilon^{\mathrm{HB}}_{kl,ab}$. What does this mean for physical properties such as the density or the vapour pressure? The density is, to a high degree, influenced by the shape of the molecules and, thus, the volume they occupy. The more volume a given

[14] The superscript of HB stands for hydrogen bond as this is the primary example of the described association interactions. This superscript has developed historically to describe the association interactions.

molecule takes, the fewer molecules fit in a container volume. On the other hand, the vapour pressure is highly influenced by attractive forces. Vapour pressure is the force molecules in the vapour phase exhibit on the walls of a closed container normalised to the area of the container walls. Fewer molecules will have enough kinetic energy to escape the liquid phase if the molecules are more attracted or bound to each other. Thus, fewer molecules will be present in the vapour phase, meaning less impact and force on the container walls. It should be noted that cross interactions exist, i.e., the density is also influenced by the potential form as well as the vapour pressure by the occupied volume. However, this short explanation is given to aid in understanding the underlying principles.

A more detailed description of the model equations would hinder the reading flow and does not contribute to the basic understanding of dependencies necessary in this thesis. Thus, the individual contributions are in the Appendix A.4.

3.3.2 Combining rules

Due to the scarcity of data, it is often impracticable to obtain all necessary, unlike interaction parameters from experiments. An established approach is the use of so-called combining rules. Here, the parameters of identical group interactions, e.g. $\varepsilon_{CH_3-CH_3}$ are obtained from pure substance data. These parameters are typically referred to as like interaction parameters. To obtain parameters of non-identical group interactions, e.g. ε_{CH_3-COOH}, referred to as unlike interaction parameters, two possibilities exist. The first choice is always to estimate these parameters from experimental data. However, if no suitable experimental data exists, the go-to strategy is to use averages of the like interaction parameters, in this case, $\varepsilon_{CH_3-CH_3}$ and $\varepsilon_{COOH-COOH}$. The set of equations to obtain these are called combining rules. Since combining rules are an estimate, they are only used when the corresponding unlike interaction parameters can not be estimated from experimental data. The following paragraph will summarise the combining rules used in this thesis.

To obtain the unlike segment diameter, the Lorentz rule [185] is used:

$$\sigma_{kl} = \frac{\sigma_{kk} + \sigma_{ll}}{2}, \tag{3.32}$$

while the unlike depth of the potential well is calculated based on an augmented geometric-mean rule accounting for the different segment sizes [176]:

$$\varepsilon_{kl} = \frac{\sigma_{kk}^3 \sigma_{ll}^3}{\sigma_{kl}^3} \sqrt{\varepsilon_{kk} \varepsilon_{ll}}. \tag{3.33}$$

Further, the geometric-mean criterion is applied to estimate the unlike attractive and repulsive exponents [176, 186]:

$$\lambda_{kl}^{y} = 3 + \sqrt{\left(\lambda_{kk}^{y} - 3\right)\left(\lambda_{ll}^{y} - 3\right)}, \quad y = \mathrm{a}, \mathrm{r}. \tag{3.34}$$

The unlike association energy $\varepsilon_{kl,ab}^{\mathrm{HB}}$ for interactions involving uncharged associating groups is calculated with a geometric mean as [177]:

$$\varepsilon_{kl,ab}^{\mathrm{HB}} = \sqrt{\varepsilon_{kk,aa}^{\mathrm{HB}} \varepsilon_{ll,bb}^{\mathrm{HB}}}, \tag{3.35}$$

while the unlike bonding volume $K_{kl,ab}^{\mathrm{HB}}$ is calculated as [177]:

$$K_{kl,ab}^{\mathrm{HB}} = \left(\frac{\left(\sqrt[3]{K_{kk,ab}^{\mathrm{HB}}} + \sqrt[3]{K_{ll,ab}^{\mathrm{HB}}} \right)}{2} \right)^{3}. \tag{3.36}$$

In case of charged group interactions, combing rules based on the work of Hudson and McCoubrey [187] are used to estimate the dispersion energy between like or unlike ions:

$$\varepsilon_{kl} = \left(\lambda_{kl}^{\mathrm{r}} - 3\right)\left(\lambda_{kl}^{\mathrm{a}} - 3\right)^{2} C_{kl} \frac{\left(\lambda_{kl}^{\mathrm{r}} - \lambda_{kl}^{\mathrm{a}}\right) \alpha_{k}^{0} \alpha_{l}^{0}}{(4\pi\varepsilon_{0})^{2} \sigma_{kl}^{6}} \frac{I_{k} I_{l}}{I_{k} + I_{l}}, \tag{39}$$

where α^{0} and I are the ion's electronic polarisability and ionisation potential, respectively. These can be found in Table D.1 in the Appendix for the Li^{+} and PF_{6}^{-} ions utilised in the current work.

3.3.3 Ion association

In general, the SAFT-γ Mie model is capable of representing solvent-ion mixtures. As stated in Section 3.3.1, aside from the ions' charge and Born diameter, the Dielectric constant D has to be known for involved solvents. The parameters needed for the calculation of D are listed in Appendix A.4.1. The original publication that extended the SAFT-γ Mie model to electrolyte solutions [180] states that a complete dissociation of the chosen salt is assumed. This assumption renders invalid for solvents with low Dielectric constants; see Figure 3.2. Here, a good example is DMC with a Dielectric constant of 3.13 at room temperature [188], compared to 73.4 for water [189]. Even mixtures of salt with EC and PC, both having Dielectric constants above 90 and 60, respectively, do not exhibit complete dissociation of the salt. The mixture of EC/DEC has a measured dissociation degree of around 60%, and even for PC, with a Dielectric

constant of above 60 [190], the dissociation degree of $LiPF_6$ is measured around 80% [191]. The formation of neutral ion pairs can explain the phenomenon of not fully dissociated salt [192]: some dissolved ions remain bonded due to electrostatic forces. In this state, they do not contribute to the conductivity of the electrolyte [193].

Ion association or ion-pairing is a phenomenon that puzzled physicists already more than 100 years ago [192]. Its effect on transport properties, such as the ion diffusivity in conventional Li-ion electrolyte mixtures, has been discussed widely [194–198]. Further examination has revealed that a high level of ion association results in the rapid deterioration of the conductive salt when exposed to water [147]. In thermodynamic modelling, ion association has also been a matter of broad discussion. Within the last decades, several models accounted for it [181, 199–201]. All approaches lead to a sufficiently good representation of the specific system under study. Yet, only Olsen et al. [201] investigated non-aqueous systems. In the current work, an association model will be implemented that is based on the same fundamental assumptions as the electrolyte expansion used in the commercially available SAFT framework [179, 180], namely a mean sphere approximation combined with a so-called primitive model for asymmetric ion sizes. The model has been adapted from Krienke et al. [202] and is implemented in MATLAB [203]. In the following, the model will be summarised.

The dissociation degree α can be calculated as a function of the association constant K_A, the mean ionic activity coefficient ${\gamma_\pm}'$ and the activity coefficient of the formed ion-pair ${\gamma_0}'$ as in:

$$\frac{1-\alpha}{\alpha^2} = \frac{C K_\mathrm{A} ({\gamma_\pm}')^2}{{\gamma_0}'}. \tag{3.37}$$

The association constant K_A is given with:

$$K_\mathrm{A} = 8\pi N_\mathrm{A} \sum_k^{N^\mathrm{ion}} \sum_l^{N^\mathrm{ion}} \tilde{x}_k \tilde{x}_l r_{kl}^3 B(b_{kl}), \tag{3.38}$$

where $N_\mathrm{A} = 6.022 \cdot 10^{23}$ denotes the Avogadro constant and N^ion the total number of ions. $\tilde{x}_k$ and $\tilde{x}_l$ are the molar fractions of both ions. r_{kl} is the arithmetic mean of interacting ion radii, where the radius is calculated from the ion diameter as $r_k = \sigma_k/2$. $B(b_{kl})$ is a solution to the ion-ion correlation function and b_{kl} is the so called Bjerrum length q_{kl} divided by r_{kl}. The Bjerrum length denotes the length at which the electrostatic forces of two elementary charges $\frac{e^2}{4\pi\varepsilon_0 D}$, is equal to the thermal energy given with $k_\mathrm{B}T$ [204]. The mathematical expressions to describe these and some further definitions are listed below:

$$B(b_{kl}) = \sum_{m\geq 4} \frac{b^{m-3}}{m!(m-3)!}, \qquad b_{kl} = \frac{q_{kl}}{r_{kl}} = \frac{z_k z_l e^2}{4\pi\varepsilon_0 D k_\mathrm{B} T r_{kl}}, \qquad \tilde{x}_k = \frac{\rho_k}{\rho}, \tag{3.39}$$

$$\rho_i = C_k N_\mathrm{A}, \qquad C_k = C\alpha. \tag{3.40}$$

Here, z_k and z_l are the charges, $e = 1.602176634 \cdot 10^{-19}\,\mathrm{C}$ is the elemental charge of an electron, $\varepsilon_0 = 8.8541878128 \cdot 10^{-12}\,\mathrm{F\,m^{-1}}$ is the permittivity of the vacuum, D is the dielectric constant, $k_\mathrm{B} = 1.380649 \cdot 10^{-23}\mathrm{JK^{-1}}$ the Boltzmann constant, T is the temperature, ρ is the number density, and C is the salt concentration.

The mean ionic activity coefficient can be calculated as follows:

$$\ln(\gamma_\pm') = \frac{\Gamma e^2}{4\pi\varepsilon_0 D k_\mathrm{B} T \rho} \sum_k^{N_\mathrm{ion}} \left(\frac{z_k^2 \rho_k}{1+\Gamma r_k^3} \right) + \frac{\pi\Omega P_\mathrm{n}^2}{2\Delta}, \tag{3.41}$$

with Δ, Ω and P_n being described as:

$$\Delta = 1 - \frac{\pi\rho}{6} \sum_{k=1}^{N_\mathrm{ion}} x_k r_k^3, \quad \Omega = \frac{\pi\rho\Delta}{2} \sum_{k=1}^{N_\mathrm{ion}} \frac{x_k r_k^3}{1+\Gamma r_k}, \quad P_\mathrm{n} = \frac{\rho}{\Omega} \sum_{k=1}^{N_\mathrm{ion}} \frac{x_k r_k^3 z_k}{1+\Gamma r_k}. \tag{3.42}$$

Here, Δ refers to the ion packing fraction, whereas Ω and P_n are coupling parameters. Ω relates to the ion packing fraction and P_n to the ionic charge. Both are functions of the screening length Γ[15], which is computed as:

$$4\Gamma^2 = \kappa^2 \sum_k^{N_\mathrm{ion}} \frac{\rho_k}{(1+\Gamma r_k)^2} \left(z_k - \frac{\pi P_\mathrm{n} r_k}{2\Delta} \right)^2 \frac{1}{\sum_k^{N_\mathrm{ion}} \rho_k z_k^2}. \tag{3.43}$$

where, $\kappa = \sqrt{16\pi q N_\mathrm{A} \alpha C}$ is the Debye shielding factor. As Γ has to be computed iteratively, a first initial guess has to be introduced as Γ_0. This is computed from the restricted primitive model, which further states that both ions must have the same radius.

[15] Electrostatic screening describes the dampening of an electric field of a given elementary charge in a medium with mobile charges. Consider a positive charge in a vacuum. The electric field will spread out evenly. If now mobile electrons are introduced, they will cluster around the charge, which will "shield" or dampen the electric field of the positive charge to someone or something in the range of the electrons. This range is called the screening length.

$$\Gamma_0 = \frac{1}{r'}\left(\sqrt{1+\kappa r'}-1\right), \quad r' = \frac{\sum_k^{N_{\text{ion}}} \rho_k r_k}{\rho}. \tag{3.44}$$

The activity coefficient of the ion-pair is calculated as:

$$\ln(\gamma_0') = \frac{2bx^2}{6\zeta(1+x+\sqrt{1+2x})+3(1+\sqrt{1+2x})(2+\zeta^2 x)+x^2\zeta^3} \tag{3.45}$$

with ζ and x defined as:

$$\zeta = 2^{1/3}, \quad x = r_{+-}\kappa. \tag{3.46}$$

For known ionic radii, this gives a parameter-free model for ion association. Inserting r_{--} with the ionic radius of PF_6^- as 2.54 Å and r_{++} with the ionic radius of Li^+ as 0.9 Å, see Table D.1, allows to calculate the following relationship between the degree of dissociation α, the salt concentration C_{LiPF_6} and the dielectric constant D shown in Figure 3.2.

It is readily apparent that a dissociation degree of 100% only exists for $C_{LiPF_6} \rightarrow 0$, even for high dielectric constants of 90, which would relate to pure EC as a solvent. This highlights the necessity to include ion association in the context of Li-ion batteries, where typical salt concentrations range from 1 to 2 mol dm^{-3} and depending on the used solvent mixture, Dielectric constants can vary from below 20 to around 40 [196, 197]. The applied numerical procedures to solve for the screening length Γ and the dissociation degree α are the Direct Substitution and Euler-Tschebyschow procedures, respectively. These procedures are briefly described in the Appendix A.5.

3.3.4 Phase-equilibrium calculations

The Helmholtz free energy of a fluid mixture is given as a function of temperature T, volume V, and the vector of moles $\mathbf{n}$ of i components. Knowledge of the pressure p, a chemical potential μ_i and fugacity coefficient ϕ_i of a given component i allows for calculating fluid-phase behaviour and solution properties. These can be obtained from the Helmholtz free energy following standard thermodynamic relations [205].

The pressure is obtained as:

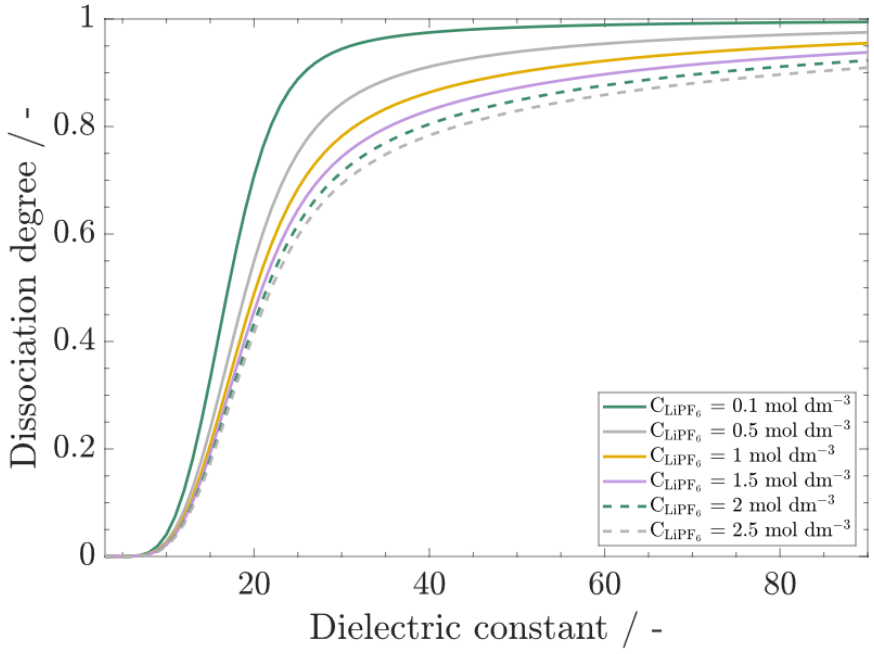

Figure 3.2: Dependency of dissociation degree on Dielectric constant D and salt concentration $C_{\mathrm{LiPF_6}}$ according to the implemented mean sphere approximation primitive model for salt dissociation.

$$p = -\left(\frac{\partial A(T,V,\mathbf{n})}{\partial V}\right)_{T,\mathbf{n}}, \tag{3.47}$$

the residual chemical potential as:

$$\mu_i^{\mathrm{Res}}(T,p,\mathbf{n}) = \left(\frac{\partial A^{\mathrm{Res}}(T,V,\mathbf{n})}{\partial n_i}\right)_{T,V,n_{j\neq i}} - RT\ln Z(T,p,\mathbf{n}), \tag{3.48}$$

and the fugacity coefficient via:

$$\ln\phi_i(T,p,\mathbf{n}) = \frac{\mu_i^{\mathrm{Res}}(T,p,\mathbf{n})}{RT}. \tag{3.49}$$

Here, μ_i^{Res} is the residual chemical potential of component i, $A^{\mathrm{Res}} = A - A^{\mathrm{Ideal}}$ is the residual free energy, $Z = \frac{pv_p}{RT}$ is the compressibility factor, with $v_p = \frac{V_p}{N_{\mathrm{tot}}}$ as the molar volume at the

specified pressure, N_{tot} is the total number of moles. For a given T, p, and $\mathbf{n}$, fluid-phase-equilibria calculations are performed using Tp-flash or TV-flash[16] algorithms implemented in gPROMS® [206]. Hereafter, the phase equilibrium calculations will be referred to by the respective names of the algorithms used, i.e. Tp-flash and TV-flash. Alternative open-source software packages to reproduce these results are SGTPy [207] and Claperoyn.jl [208].

3.3.4.1 Solving systems with ion association

By solving Equation 3.37 for α, the free ion and ion-pair concentrations can be computed as $C^{\pm}_{\text{LiPF}_6} = C_{\text{LiPF}_6}\alpha$ and $C^{0}_{\text{LiPF}_6} = C_{\text{LiPF}_6}(1-\alpha)$, respectively. The ion concentration is effectively reduced compared to the assumption of fully dissociated ions currently incorporated in the SAFT-γ Mie framework [180]. The ion pair has to be introduced as an additional group within the SAFT-γ Mie framework. Also, two more phenomena must be considered to get a sound representation of the studied system. First, the ion pairs act as a dielectric medium, increasing the mixture's dielectric constant [209, 210]. This will lead to a higher degree of dissociation, effectively reducing the dielectric constant and, thus, the dissociation again. The second phenomenon is that free ions will fix solvent molecules, rendering them inactive as a dielectric medium [198]. This effect will reduce the dielectric constant and, thus, the degree of dissociation. The reduced dielectric constant will lead to more ion pairs, increasing the dielectric constant. Therefore, both effects have to be solved iteratively, which is done using an Euler-Tschebyschow procedure. This initial approach assumes that every ion will bind to three polar molecules, e.g. EC, PC or $LiPF_6$. This aligns with the range of solvation numbers reported for EC and PC [54, 195, 211, 212], and yields the following total number of fixed molecules:

$$n^{\text{fix}}_{\text{tot}} = 3n_{\text{ions}}, \tag{3.50}$$

with $n_{\text{ions}} = n_{\text{Li}^+} + n_{\text{PF}_6^-}$. The amount of fixed molecules is calculated as follows:

$$n^{\text{fix}}_{i} = n^{\text{fix}}_{\text{tot}} x^{\text{polar}}_{i} \quad \forall\, i \in \{\text{EC}, \text{PC}, \text{LiPF}_6\}, \tag{3.51}$$

[16] Flash algorithms are used to calculate how a global mixture $\mathbf{z} = \frac{\mathbf{n}}{N_{\text{tot}}}$ distributes among the liquid $\mathbf{x}$ and vapour phase $\mathbf{y}$. Different variations exist, where Tp refers to constant temperature and pressure and TV refers to constant temperature and volume. In order to solve for a full phase diagram, these algorithms have to be calculated in the whole composition, temperature and pressure/volume domain.

with $x_i^{\text{polar}} = \frac{n_i^{\text{polar}}}{\sum_{i=1} n_i^{\text{polar}}}$. To obtain the same effect within the SAFT framework, each polar species has a twin with the same physical properties, except for a temperature-independent dielectric constant of 1. To estimate the parameters for the newly introduced groups of $PF_6{}^-$ and $LiPF_6$ as well as the cross-interactions of the salts groups with carbonate groups and CO_2, the combined model is compared to experimental data.

3.4 Error quantification

To evaluate the accuracy of the developed interaction parameters of the SAFT-γ Mie model, simulated data is compared to experimental data or simulated data against other simulated data. The metrics used to compare the deviations will be introduced here to give a common ground for quantification.

If only singular experimental or reference points X and simulated points Y are considered, the absolute deviation AD is calculated as:

$$AD = |X - Y| = \sqrt{(X - Y)^2}. \tag{3.52}$$

The percentage absolute deviation %AD, also commonly referred to as relative deviation, is calculated as:

$$\%AD = \frac{AD}{X} \cdot 100. \tag{3.53}$$

When contemplating a whole experiment or a range of data points, the average absolute deviation AAD and percentage average absolute deviation %AAD are given with:

$$AAD = \frac{\sum_{i=1}^{N_X} AD_i}{N_X}, \tag{3.54}$$

$$\%AAD = \frac{\sum_{i=1}^{N_X} \%AD_i}{N_X}, \tag{3.55}$$

where N_X refers to the number of data points.

4 Interaction of reactions and phase transition during thermal abuse[1]

The scope of this thesis is derived from the literature review presented in Chapter 2. It aims to tackle the unresolved challenge of examining the interaction between vapour-liquid equilibria and occurring reactions during thermal events of Li-ion batteries. This will be achieved by meticulously integrating chemical species and their physical properties. This chapter will deal with this demanding task by performing the simulation of thermal abuse in Li-ion batteries utilising the component-based modelling approach introduced in Chapter 3 emulating an ARC measurement.

As mentioned in the previous chapters, the thermal runaway, like most reaction-related phenomena in batteries, e.g. SEI formation [213] or LiS chemistry [214], consists of a complex reaction network including degradation of all battery components, see Figure 2.2. Additionally, phase transitions of the liquid electrolyte components are induced due to the rapid temperature increase caused by the thermal runaway. Phase transition has, up until now, mainly been studied in connection to the venting of cells [65, 103, 105]. However, boiling is an endothermic process, and its interaction with exothermic degradation reactions as well as their influence on the self-heating behaviour during thermal abuse, have not yet been studied. Thus the following open questions are identified:

- How do occurring reactions during the thermal runaway interact, and how would boiling of the electrolytes' solvent components influence this interaction?
- To what extent does the pressure build-up through the evolution of gaseous degradation products influence the phase transition behaviour?

To address these questions, the developed model is put into practice to analyse the complex course of events during an ARC measurement of a Li-ion battery. Particular focus is laid on studying the primary stages during the self-heating phase, between 90 °C and 130 °C, where a

[1] Parts of this chapter have been published as own contributions in Baakes, F., Lüthe M., Gerasimov, M., Laue, V., Röder, F., Balbuena, P., Krewer, U., "Unveiling the interaction of reactions and phase transition during thermal abuse of Li-ion batteries", Journal of Power Sources, DOI:10.1016/j.jpowsour.2021.230881, CC BY 4.0 [60].

fragile equilibrium between exothermic events such as degradation reactions and endothermic processes such as boiling is present. Ultimately, the influence of evolving reaction gases on the phase transition behaviour is illuminated.

4.1 Procedure

The following section summarises the procedure employed in this first approach to simulate the thermal abuse in Li-ion batteries. First, the modelled system is presented in the form of mathematical sets. This is followed by a brief description of the underlying experimental work of Maleki et al. [69]. Subsequently, the initial conditions are provided, accompanied by some explanatory remarks. The section finishes with a description of the parameter estimation procedure.

4.1.1 Modelled system

The model incorporates energy and species balances, including phase equilibria as described in Section 3.2. Phase changes are considered because the model is isobaric. The set notation below contains the complete sets of species and reactions used to model the system in the present chapter are given.

The first set Ω_{SP} contains the chemical species included in the selected system:

$$\begin{aligned}\Omega_{\mathrm{SP}} = \{&\mathrm{LEDC}, \mathrm{Li_2CO_3}, \mathrm{LiF}, \mathrm{LiPF_6}, \mathrm{LiC_6}, \mathrm{C_6}, \mathrm{Li}_x\mathrm{CoO_2}, \mathrm{Co_3O_4},\\ &\mathrm{C_2H_4}, \mathrm{CO_2}, \mathrm{O_2}, \mathrm{HF}, \mathrm{PF_5}, \mathrm{POF_3}, \mathrm{H_2O}, \mathrm{EC}, \mathrm{EMC}\}.\end{aligned}$$

The subsets Ω_{Solv} and Ω_{SEI} describe the components of the solvent and the SEI, respectively.

$$\begin{aligned}\Omega_{\mathrm{Solv}} &= \{\mathrm{EC}, \mathrm{EMC}\} \subseteq \Omega_{\mathrm{SP}},\\ \Omega_{\mathrm{SEI}} &= \{\mathrm{LEDC}, \mathrm{Li_2CO_3}, \mathrm{LiF}\} \subseteq \Omega_{\mathrm{SP}}.\end{aligned}$$

Moreover, the set Ω_{RE} lists all considered reactions, with abbreviations added in brackets:

$$\begin{aligned}\Omega_{\mathrm{RE}} = \{&\mathrm{LiPF_6\,decomposition\,(CSD)},\ \mathrm{PF_5\,decomposition\,(PFD)},\\ &\text{LEDC decomposition (OSD)},\ \mathrm{Li_2CO_3\,decomposition\,(ISD)},\\ &\text{LEDC production (OSP)},\ \mathrm{Li_2CO_3\,production\,(ISP)},\\ &\mathrm{LiCoO_2\,decomposition\,(CD)},\ \text{EC decomposition (ECD)},\ \text{EMC decomposition (EMCD)}\}.\end{aligned}$$

The reaction equations are summarised in Tab. 3.1. The subset of SEI-forming reactions is then given with the following:

$$\Omega_{\mathrm{SEI\,form}} = \{\mathrm{OSP,\,ISP}\} \subseteq \Omega_{\mathrm{RE}}.$$

4.1.2 Underlying experimental work

Experimental data from Maleki et al. [69] was chosen because the chemistry is close to the ones used today. In addition, since the experiments were carried out with a commercial cell in 1999, it is safe to assume that no SEI-forming additives like vinylene carbonate (VC) have been added. This is due to the fact that the first patent covering the usage of VC as an additive for Li-ion batteries has only been filed in 1998, and first research articles investigating the effects of VC have not been published before 2002 [49, 50]. Malekis experiments are thus also assumed not to contain any formation and degradation of polymeric SEI components resulting from VC degradation. The cell used for the experiments had a capacity of 550 mAh. The chemistry was reported to be a carbon-based anode, an $LiCoO_2$ cathode, polyvinylidene fluoride as a binder in both electrodes and an EC/EMC mixture with $LiPF_6$ as the conductive salt. Yet, since the original publication lacks additional data, some assumptions have to be made to achieve a proper set of initial and boundary conditions for the simulation, see Section 3.2.1.

4.1.3 Initial conditions

Table 4.1 lists the initial values of all modelled species and their respective reference volumes for calculating their concentrations. Underlying assumptions are marked with asterisks and added as footnotes. The initial temperature is given with $T_{t=0} = 40\,^{\circ}\mathrm{C}$ and the pressure is hold constant at $p = 101\,325\,\mathrm{Pa}$.

The initial composition of the SEI is defined based on the knowledge that a pristine SEI mostly consists of organic species like LEDC and will change its composition during ageing to a more inorganic one. However, it is also known that a layer of LiF builds up very close to the

Table 4.1: All species listed with their possible states, their respective initial amount and definition of the reference volume

Species	States	$n_i(t=0)$ in mmol	Reference Volume
$(CH_2OCO_2Li)_2$ (LEDC)	solid	0.723**	$V_{SEI} + V_{AM,An}$
Li_2CO_3	solid	1.178**	$V_{SEI} + V_{AM,An}$
LiF	solid	3.356**	$V_{SEI} + V_{AM,An}$
$LiPF_6$	liquid	2.655***	V_{El}
LiC_6	solid	24.605***	$V_{AM,An}$
Li_xCoO_2	solid	21.670***	$V_{AM,Cat}$
Co_3O_4	solid	0*	$V_{AM,Cat}$
C_2H_4	liquid, gas	0*	V_{El}
CO_2	liquid, gas	0*	V_{El}
O_2	liquid, gas	0*	V_{El}
H_2O	liquid, gas	0.0061**	V_{El}
HF	liquid, gas	0*	V_{El}
PF_5	liquid, gas	0*	V_{El}
POF_3	liquid, gas	0*	V_{El}
$C_3H_4O_3$ (EC)	liquid, gas	16.581****	V_{El}
$C_4H_8O_3$ (EMC)	liquid, gas	10.095****	V_{El}

* Assumed
** Calculated based on assumptions given in the text below.
*** Calculated from structural data given in Table B.1.
**** Calculated based on assumption of EMC/EC 50/50 v/v mixture.

surface of the anode. Thus it also takes up a certain volume of the pristine SEI. From this the following composition of the SEI given in volume fraction is assumed for the simulation, $\varepsilon_{(CH_2OCO_2Li)_2} = 55$ vol-%, $\varepsilon_{Li_2CO_3} = 25$ vol-% and $\varepsilon_{LiF} = 20$ vol-%. Furthermore, the SEI thickness is assumed to be 50 nm, which is in the range of measured SEI thicknesses formed without VC as an additive. [55, 215, 216]

No data on the amount of water in whole battery cells, neither for freshly assembled nor for aged ones, could be found in literature. It is known that electrolyte solutions contain a small amount of usually nowadays 20 ppm water. For our simulations, this value is further increased because of possible diffusion of water through the casing and the hygroscopic properties of the cathode material[2]. 50 ppm H_2O are chosen under the assumption of a slightly aged cell [150, 217].

[2] Chapter 5 will analyse the initial water content and SEI composition in more detail.

The complete set of calculations used to obtain the initial conditions can be found in A.2 along with structural in Table B.1 as well as component-specific physical parameters in Table B.2.

4.1.4 Parameter estimation

Based on the assumptions listed in this section and the considerations regarding the general progression of all reactions discussed in Section 3.1, the kinetic parameters, k_0 and E_A, have been adjusted such that two constraints are met: The first one is that the reactions take place within the reported temperature interval for each given reaction. The second constraint is that the simulation can reproduce the experimental data from Maleki et al. [69] as best as possible. Note that data points after the cell opening, marked as grey stars in Figure 4.1, are excluded from the parameterisation since the model, for now, can not reproduce this phenomenon. Due to the difference in reported start temperatures for all reactions, a step-wise parameterisation had to be performed. This has, for reasons of complexity, been performed by hand. Since two cases have been considered, one which assumed a battery case design which is highly inflatable (isobaric) and one that limits the inflation at ten times the initial volume (isochoric), the parameterisation has been performed twice. The kinetic parameters derived by parameterising both cases against the available data can be found in Table B.3.

All presented model equations, parameters, and submodels are implemented in MATLAB, and the simulation was performed using the ode15s solver for stiff systems. All calculations have been performed with MATLAB Version 2020b, or higher [203], i7-9750H processor, 16 GB RAM. The average simulation time was between one to fifteen minutes.

4.2 Results and discussion

The upcoming section first compares temperature abuse simulations with experiments and analyses the predicted progression of reactions, their interplay and their contribution to temperature evolution during the abuse test. Here particular focus is given to the transition from the HWS to exotherm mode. Thereafter, the pressure evolution and its impact on solvent boiling is analysed.

4.2.1 Process interplay and temperature evolution during thermal abuse

Figure 4.1 shows the experimental and simulated temperature change during the ARC test. The filled green and empty circles illustrate the experimental data points before and after the cell opening, respectively.

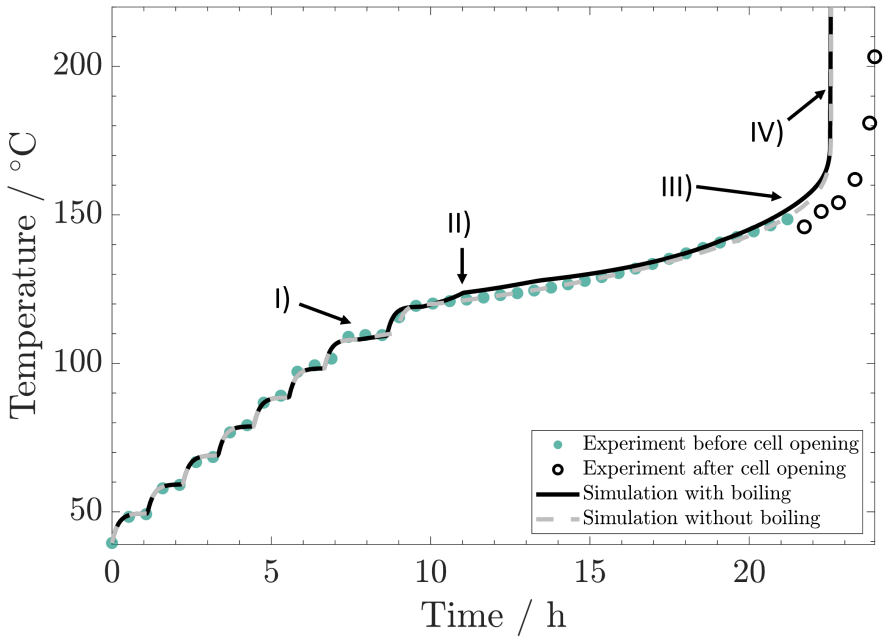

Figure 4.1: Accelerated Rate Calorimetry measurement taken from Maleki et al. [69] and the parameterised model with (solid black line) and without (dashed grey line) boiling of electrolyte. Here, I) marks the first transition from HWS to exotherm mode, II) the deviation between simulation and experiment, III) accelerated temperature increase IV) the thermal runaway, respectively.

The analysis starts at $T_0 = 40\,°C$, directly followed by a 10 °C heating step which in turn is followed by a 15-minute wait period, and a 35 minute seek period. This HWS pattern proceeds in the experiments until at 108 °C, marked by I) in Figure 4.1, an exothermic event leads to exothermic mode where the ARC follows the battery cell temperature. Due to insufficient heat production, the HWS modus starts again and at 110 °C, an additional heating step is performed. After that, other exothermic events lead to a steady but slow temperature increase from 119 °C until the experimental cell opening is marked by a change in markers from filled green to empty circles at 148 °C. Cell opening leads to venting of the electrolyte and thus cooling of the battery

[65, 157, 218]. This is assumed to occur here also, even though the temperature decrease and its correlation to cell opening were not discussed in the original publication. At this point, the experiment shows a temperature decrease to 145 °C. This is followed by a further temperature increase leading to thermal runaway around 177 °C, marked with a IV).

The isobaric simulation, i.e. represented by the solid black line, is in excellent agreement with the experiments until around 119 °C, marked by a II). Here, the simulation has a higher temperature gradient, and thus temperature, than the experiment. In the following, the simulation's gradient decreases while the experiment's gradient increases again. Therefore, the simulative curve is again in very good agreement with the experiment until the drop caused by cell opening. Since the here presented model is isobaric and can, thus, not reproduce cell opening, temperature deviation between experiment and simulation after cell opening is expected.

Evolution of the heat sources and sinks from individual processes that lead to the observed temperature progression. Here, the transition from HWS to exotherm mode gives crucial insight into why cells run into thermal runaway and how this can be prevented. In Figure 4.2 a), the endothermic (blue colours) and exothermic heats (red colours) and their sums are shown with respect to temperature, and the self-heating threshold that needs to be surpassed such that the ARC switches to exothermic mode. For better illustration, reactions and solvent boiling have been clustered, respectively. Individual contributions are given in the Appendix B.1. The temperature horizon represents the temperature span where the transition to the exothermic region occurs. Non-monotonous progression of heat evolution with local maxima and minima is observable throughout the simulation. These can be attributed to unsteady heating: The heating steps increase the system's temperature and, thus, the reaction rate of all reactions. In the following Wait and Seek period, the occurring reactions consume the reactants, leading to a reduction in reaction rates and, with it, the produced heat. The corresponding reactants for each reaction are shown in Figure 4.2 b).

The first endothermic reaction taking place is the salt decomposition of $LiPF_6$ to PF_5 and LiF. The reaction rate exhibited in our simulation at 70 °C is comparable to one reported in experiments by Sloop et al. [145]. However, in our simulation, this reaction is, to a small extent, already present at around 40 °C. Thus, our results differ slightly from the reported temperature interval for the onset of this reaction between 60 °C–80 °C. Considering additional side reactions, such as the produced PF_5 with linear solvent components, could help reduce this observed difference between experiments and simulation. The first exothermic reaction is the organic SEI decomposition, where LEDC decomposes to Li_2CO_3 and gases at temperatures above 80 °C. In the beginning, the heat consumption due to salt decomposition prevails, and the sum of heat sinks and sources is endothermic. At around 105 °C, LEDC decomposition

increases drastically, leading to an exothermic sum of heats. LEDC decomposition is thus identified as the reason for the first change from HWS to exothermic mode that was observed in experiments and simulation, confirming the theory of Richard et al. [94, 100]. The subsequent steep decline in produced heat is due to slowed LEDC decomposition due to the depletion of LEDC within the system, represented as a solid black line in Figure 4.2 b) at I). This causes the sum of heats to approach the self-heating threshold around 110 °C, triggering a further heating step that can be observed in the experiment and simulation.

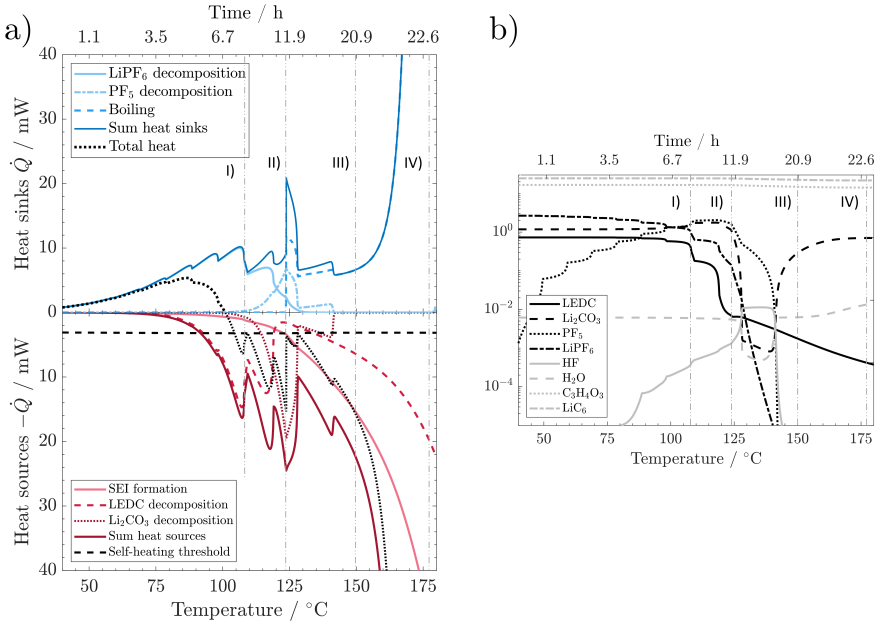

Figure 4.2: a) Isobaric simulation: produced endothermic and exothermic heats during the experiment leading to thermal runaway. Endothermic heats are presented in different shades of blue. Exothermic heats are shown in different shades of red. The sum of heat sinks and heat sources is shown in a solid line of blue and red, respectively. The sum of both together is represented by the dotted line. The dashed line visualises the self-heating threshold of the ARC. Inorganic and organic SEI formation and boiling of both solvents are lumped into SEI formation and boiling, respectively. b) Evolution of molar amount of all reactants participating in reactions illustrated in a).

In the temperature region after the heating step around 120 °C, PF_5 and H_2O react to POF_3 and HF, and HF triggers inorganic SEI decomposition with Li_2CO_3 and HF reacting to LiF and H_2O. These reactions form an auto-catalytic cycle where PF_5 decomposition is endothermic, and Li_2CO_3 decomposition is exothermic. The sum of both, however, is exothermic. This leads, in combination with fast kinetics in both reactions, to a peak in the sum of heats, causing the observable deviation of isobaric simulation (i.e. with boiling) and experiment at II) in Figure 4.1 (see also discussion in next section). At 123 °C, the endothermic boiling of EC

and EMC sets in. The immediate jump in endothermic heat leads to a drop of released heats without passing the self-heating threshold. Therefore, no further heating step is performed. The exothermic formation of inorganic and organic SEI that sets in due to the primary decomposition of SEI leads to an increase in the sum of exothermic heats. Li_2CO_3 decomposition and HF production, then both exhibit first a rapid decline and a slow rise in produced heat until at 142 °C both heats vanish. The underlying complex processes can be explained as follows. The reason for the sharp decline in inorganic SEI decomposition and PF_5 decomposition at 128 °C is that the concentration of Li_2CO_3 almost reached zero, see the dashed black line in Figure 4.2 b) at II). Note that PF_5 decomposition depends on water production, which in turn is produced from Li_2CO_3. Further, both are limited by the production of Li_2CO_3. Until at 142 °C the amount of PF_5, represented as a dotted black line in Figure 4.2 b), in the system is used up and the auto-catalytic cycle stops. This leads to a small dip in the sum of exothermic and endothermic heats. From then on, the steady formation of both the inorganic as well as organic SEI and the subsequent re-decomposition of the organic SEI leads to a continuous increase in produced exothermic heat. The boiling solvent partly counterweights this. However, the sum of both heats also increases steadily, leading to the temperature increase observed in the measurement.

Kupper et al. [111] already revealed that two reactions, primary formation and decomposition of the SEI, do not release sufficient heat to sustain the thermal runaway. They suggested that further side reactions must be considered to simulate an ARC measurement. With the addition of conductive salt decomposition and subsequent side reactions such as PF_5 decomposition and Li_2CO_3 decomposition, we achieved this goal for the first time.

For better illustration, the solvent decomposition and cathode decomposition are not shown in Figure 4.2. However, they are, also in this study, responsible for the thermal runaway occurring around 177 °C as already reported in literature [69, 70, 84] (see Appendix B.1 for individual reaction rates over the whole simulated temperature). Therefore, the general behaviour of all considered reactions, introduced and discussed in Section 3.1, could successfully be reproduced. This makes this model the first to reproduce an ARC measurement solely based on chemical reactions, it's participating species and their physical and chemical properties, such as the heat of formation or heat capacity. Enabling us to in-depth analyse the interaction among them and draw the following conclusions.

The above description of occurring effects allows to reveal two competing phenomena. On the one hand, the rising temperature accelerates the dominating exothermic reactions. On the other hand, the acceleration of their underlying reactions leads to a decline in reactants concentration. Hence, it becomes evident how the concentration of the primary reactants, such as LEDC, can drastically influence the progression of thermal runaway in actual accidents. This adds to the

list of effects, such as gas venting and localisation of internal short circuits, that make the thermal runaway and its propagation such an unpredictable phenomenon [62, 219].

Additionally, the processes occurring in the analysed region can be classified into two groups, one which may be limited by reactant availability and the other where sufficient reactant is available. The first group contains the organic and inorganic SEI decomposition, conductive salt decomposition, and the PF_5 decomposition. This first group includes all reactions with a relatively low amount of reactants within the system and can therefore deplete early, leading to the fluctuating behaviour of the temperature gradient. Additionally, the reactants of these reactions can vary among different systems as well as between different cells of the same chemistry. For example, LEDC, as the main SEI component, or H_2O as a contaminant can vary from cell to cell depending on different production environments and procedures or the age of the cell. They make the thermal runaway particularly unpredictable. Owing to this intriguing correlation, the upcoming chapter will delve deeper into the analysis of SEI properties, such as composition and thickness, as well as H_2O contamination. The second group contains the organic and inorganic formation of the SEI. Here, the reservoir of reactants is up to two orders of magnitudes higher, see Figure 4.2 b), which means that these will not be used up during the early stages of thermal abuse and will, in turn, lead to a monotonously increasing temperature gradient. Therefore, once these reactions are the main contributors to released heat, at temperatures 130 °C, and above, only rapid cooling can prevent the thermal runaway of the battery. The reactants, LiC_6 and EC, are among the components that differ the least among conventional Li-ion chemistries. Thus they do not, percentage-wise, vary as significantly between systems or even from cell to cell as the reactants of the first group. Therefore, if activated by high temperatures, these reactions will occur to more or less the same extent in all systems.

Eventually, the electrolyte boiling at 123 °C uses up such a significant amount of heat that the temperature gradient changes noticeably. Thus, the occurring reactions are slowed down, and the thermal runaway is delayed. On the other hand, the reactions and their released gases might, in return, also influence the solvent boiling. This aspect is analysed in more detail in the upcoming section.

4.2.2 Pressure build-up and solvent boiling

While the model, for now, has been isobaric due to the assumption of an infinitely inflatable pouch cell, evolving reaction gases in the real cell may have influenced the pressure and, thus, the boiling point of the solvent mixture EC/EMC and the resulting contribution on the heat balance. To shed light on the impact of pressure, we here analyse in-depth a possible pressure increase and its effect on phase equilibrium and evaporative cooling during the heat abuse test.

The model used for this assessment is described in Section 3.2.5 and the used equilibrium model in the Appendix A.3.4.

Figure 4.3 a) shows the progression of the relative volume increase and pressure during the temperature abuse test. Following our assumptions of a ten times inflatable pouch cell, the evolving gases will first lead to a volume increase of the pouch cell up to a maximum of 10 times its initial volume (region I). From then on, the system is assumed to be isochoric, and the following evolving gases increase the system pressure (region II). It can be observed that until 1.25 h, neither the volume ratio nor the pressure is increasing since no significant amount of gases is produced. Then, the volume rises continuously until it reaches the threshold of 10 times inflation at 7.3 h. The main contributing reactions are the decomposition of $LiPF_6$ and LEDC since, as discussed above, they mainly occur at this time. The system pressure starts to rise with a steep gradient until 13.2 h. This is the timespan where most gas-producing reactions are happening simultaneously, namely the conductive salt decomposition, PF_5 decomposition and the organic as well as inorganic SEI decomposition and production. The depletion of PF_5 and the subsequent decline of gas-producing reactions such as PF_5 decomposition and the inorganic SEI decomposition leads to a more flat gradient until shortly before the end at 23 h, an almost vertical increase in pressure can be observed. This is correlated to the release of O_2 due to cathode decomposition and the subsequent decomposition of the solvent species EC and EMC to CO_2 and H_2O.

The pressure evolution is taken as input for the binary phase equilibrium model to calculate the solvent's boiling point. The evolution of the battery temperature relative to the boiling point of the solvent is shown in Figure 4.3 b). The solvent composition of EC/EMC 50/50 (v/v), which was assumed in the experiment and used in the simulation, is indicated by a black line. The threshold in relative temperature above which boiling occurs, i.e. $\frac{T}{T_b} > 1$, is visualised with a dashed line.

The step-wise temperature rise caused by the HWS mode of the ARC increases the relative temperature significantly from 0.3 to its first maximum of 0.85 at 7.3 h. This first maximum corresponds to the moment at which the maximum volume of the pouch cell is reached. Subsequently, the curve first declines to 0.8 due to the pressure increase, followed by a slight increase to 0.82 at 9 h. Which is caused by the last heating step that occurs after the first minor exothermic event, see Figure 4.1 I). The pressure increase then leads to a continuous decline to 0.75 at 17 h. At around 13 h, the point where due to depletion of PF_5, PF_5 decomposition, as well as the inorganic SEI decomposition, fade, the direction of the slope changes. Reactions such as PF_5 decomposition here take a special role: they are endothermic and thus slow down the temperature rise. At the same time, they produce a significant amount of gases that contribute to the suppression of solvent boiling by a pressure increase. Thus, due to their decline and, in general, the reduction of simultaneously occurring reactions, the temperature

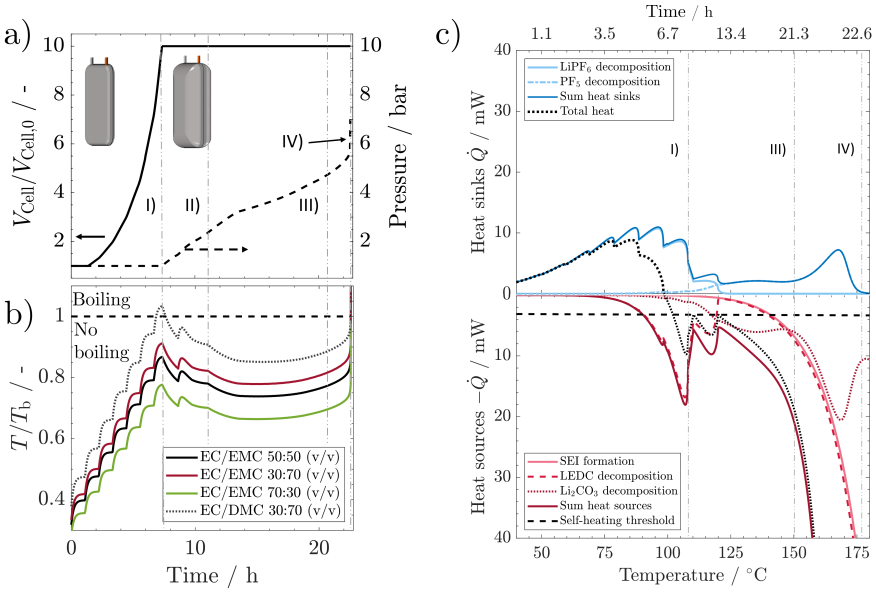

Figure 4.3: a) Evolution of the cell volume vs. its initial volume (solid line) and cell pressure with EC/EMC 30/70 (v/v)b) Corresponding evolution of temperature relative to boiling temperature for various solvent compositions c) Heat evolution over temperature for the re-parameterized case without solvent boiling with EC/EMC 30/70 (v/v)

rise dominates over the increase in boiling point. Hereafter, the relative temperature increases sharply, corresponding to the thermal runaway, where the boiling point of the binary mixture is reached.

From this analysis, it can be concluded that the investigated solvent mixture would not reach its boiling point before the thermal runaway. Thus, assuming a maximum inflatability of 10 times the initial pouch cell volume, phase transition does not occur and thus does not influence the processes occurring during the HWS and self-heating phase of the thermal abuse test.

Solvent boiling is unlikely to occur before the final thermal runaway, even if the pouch cell can inflate. The absence of boiling in the experimental system could explain the deviations to the simulated temperature evolution in Fig 4.1. The simulation shows a clear change in the gradient of the temperature evolution caused by the onset of boiling. To evaluate how the reactant and reaction evolution would be in the case without boiling and if a simulation without boiling can reproduce the experimental temperature evolution better, the presented model has been re-parameterised to the experimental data without solvent boiling. All kinetic parameters of both scenarios can be found in Table B.3. The results can be seen in Figure 4.1

represented by the grey dashed line. In contrast to the model with boiling, the model without boiling almost perfectly reproduces the experimental data points. Compared to the scenario with boiling, the reaction kinetics of PF_5 decomposition, inorganic SEI decomposition and SEI formation are significantly slower, see Figure 4.3. Here, the inorganic SEI decomposition and PF_5 decomposition even reach up to temperatures around 180 °C and higher. This results from the missing endothermic heat of solvent boiling, which in the first scenario outweighed the faster kinetics. Note that even though it seems that more heat is released by those two reactions without solvent boiling, this is not the case. The time it takes to change from 120 °C to 140 °C is around 8.7 h but to reach from 140 °C to 180 °C only 3.7 h.

Other solvent ratios of EC/EMC are also commonly used for batteries [220]. The boiling point evolution has also been performed for EC/EMC 30/70 (v/v) and EC/EMC 70/30 (v/v) to check whether boiling would be expected for these compositions. As EC is still in excess in those cases, not many changes in the gas evolution were assumed, and the same gas evolution was used for the calculations. Since EMC is the lower boiling component of the mixture, the system with EC/EMC 30/70 (v/v) experiences an upwards shift, and the EC/EMC 70/30 (v/v) shows a lower relative temperature. For both solvent compositions, the boiling point is also not reached before the thermal runaway. Therefore, it can be concluded that it is improbable that a mixture of these two solvents would start to boil before the rapid thermal runaway sets in if pressure is allowed to build up.

Besides the investigated solvent mixture, other types of linear carbonates, such as DMC are frequently used as co-solvents [220] instead of EMC. DMC has a lower boiling point than EMC. The same calculation has been performed with a binary equilibrium model of EC/DMC 30/70 (v/v) to evaluate whether boiling is expected for such systems. The result is shown in Figure 4.3 b) as a dotted line. It can be observed that due to the lower boiling point of DMC, the boiling point of EC/DMC 30/70 (v/v) is reached before the maximum cell volume and, thus, before the pressure starts to rise. What this would mean for the further progression of temperature evolution is complex. Boiling would, due to its endothermic nature, on the one hand, have a cooling effect which would delay thermal runaway. On the other hand, the comparably high amounts of gases released from solvent boiling would increase the pressure to an extent that would most probably suppress further boiling. All of the above shows that the electrolyte system used in this study, EC/EMC, is improbable to reach the boiling point before the thermal runaway.

Concluding, a pressure build-up during thermal abuse may prevent phase transition. As the cooling effect of boiling is missing, this may accelerate the transition to thermal runaway. Whether boiling occurs depends strongly on battery composition, especially the solvent, and particular reactants such as LEDC. The quantitative prediction will require further research

to assess the salts' impact on the boiling point. Thus, the SAFT-γ Mie approach is utilised to address this open challenge. An in-depth analysis of pressure progression during a thermal event in Li-ion batteries is presented in Chapter 6.

4.3 Concluding remarks

This chapter revealed the impact and interplay of exothermic reactions and solvent boiling during the thermal abuse of Li-ion batteries. The first successful model approach to reproduce an ARC measurement rigorously based on the chemical components of a battery and their thermodynamic properties is presented. Here, especially in the early stages of self-heating, a fragile equilibrium between simultaneously occurring endothermic reactions, exothermic reactions and phenomena, such as solvent boiling, could be identified.

Occurring reactions could further be divided into two groups. Those whose reactants are only present in small amounts. Prominent members of this group are reactions involving the SEI component LEDC and the contaminant H_2O. Due to the variance in their initial quantity, for example, caused by fluctuations during production and formation, these reactants are among the causes that make the thermal runaway unpredictable. The other group contains the formation of SEI after its primary decay and repeated decomposition. From the comparably high amount of the involved reactants, it follows that only active cooling will prevent thermal runaway once higher temperatures activate these reactions. Further, we shed light upon the probability of a possible phase transition and its impact on temperature evolution during the self-heating phase. For the isobaric case, the phase transition influences the course of the thermal runaway of a Li-ion battery, as its endothermic nature slows down self-heating.

Gases released by degradation reactions may lead to rising pressure in the system and thus influence the phase transition behaviour. Assuming a ten times inflatable pouch cell, the rising pressure completely suppressed solvent boiling until the final rapid thermal runaway phase for all EC/EMC solvent compositions of 30/70 to 70/30 volume ratio. However, for a lower boiling EC/DMC 30/70 (v/v) mixture, boiling of the electrolyte could be shown to occur shortly before surpassing the self-heating threshold of the ARC. Therefore, we suggest to evaluate the behaviour of each electrolyte system individually. It could be shown that the complex interaction between gassing reactions, phase transition and eventually their impact on battery safety is an intricate phenomenon.

Based on the findings of this chapter, two new research questions are identified, which will be addressed in the upcoming chapters:

1. How do highly fluctuating properties such as SEI composition, SEI thickness and H_2O impurities affect a thermal event in Li-ion batteries? — Chapter 5
2. What are the impacts of differing solvents, gas solubilities, reactions and conductive salt on the pressure evolution during a thermal event? — Chapter 6

5 Sensitivity to SEI properties and impurities[1]

The simulation performed in the previous chapter showed that the initial stages of thermal abuse are dominated by reactions dependent on highly fluctuating properties such as the SEI thickness, composition and H_2O impurities. Thus, this chapter investigates those critical factors in a thermal event in Li-ion batteries. This is of special importance because the initial period of self-heating poses an opportunity to apply counteracting measures to prevent thermal runaway. Yet, this demands a thorough understanding of the processes triggering and occurring during this critical initial period. Not much is known about the effects of SEI properties and highly reactive impurities like water on the self-heating behaviour of Li-ion batteries.

As mentioned, it was already 20 years ago when the first experiments by Richard et al. connected the self-heating behaviour of Li-ion cells to SEI decomposition [94, 100]. Other experimental studies of cells aged at elevated temperatures revealed an increase in the self-heating temperature of about 15–20 °C with increased ageing temperature [76, 79–81]. This has been connected to a thicker and more inorganic SEI. However, neither detailed experimental nor simulation-based studies have been performed on the influence of the SEI composition or thickness on battery safety. Thus, this chapter aims to tackle this open challenge.

H_2O is a known impurity during battery manufacturing[221]. Hygroscopy of electrodes is the most often referenced origin of water in cells [150, 222]. Several studies showed the detrimental effect of water on battery performance [39, 223]. However, also positive impacts of H_2O addition for Li-metal batteries have been reported [224]: LiF is formed from the reaction of H_2O with $LiPF_6$, and it is a stable and highly conducting SEI component leading to better performance. In contrast, worse performance is usually connected to formation of the phosphorous decomposition products PF_5 and POF_3. These reactions are known to occur at room temperature and are inherently linked to battery ageing. Weber et al.[225] investigated the ageing of an electrolyte mixture stored at 95 °C and identified 12 different organo-phosphoric

[1] Parts of this chapter have been published as own contributions in Baakes, F., Witt, D., Krewer, U., "Impact of electrolyte impurities and SEI composition on battery safety", Chemical Science, DOI:10.1039/D3SC04186G, CC BY 3.0 [143].

decomposition products. They suggested that a detailed analysis of the formation of these products during ageing could be used to identify "ageing stages" for $LiPF_6$-based electrolyte composition. Stich et al. [144] investigated the kinetics of these decomposition reactions by purposely contaminating an electrolyte solution with 1000 ppm water and measuring the concentrations of H_2O, HF and HPO_2F_2. They found that hydrolysis is not following a simple rate law and thus developed a kinetic model to describe their experiments. Huttner et al. [226] studied the influence of different drying strategies for water removal on battery performance. They found that extensive drying can decrease performance. This is due to the extreme conditions the battery materials are subjected to during drying. In general, H_2O contamination and follow-up reactions might not immediately influence battery performance, as Zheng et al. showed [223]. They found that after 100 cycles, the capacity retention for batteries contaminated with H_2O and without contamination was in the same range, with around 95% remaining capacity for water-free and 90% remaining capacity for water-containing batteries. However, after 300 cycles, increased H_2O content drastically reduced capacity retention. The results show 90% remaining capacity for water-free batteries and 55% for water-contaminated ones. The water-containing battery had 14 mg water added to a 18650 battery. Despite these efforts to qualitatively and quantitatively correlate H_2O contamination and battery performance, no reports in literature on tests to investigate the effect of water on battery safety, especially during the crucial self-heating phase have been found. Therefore, this chapter will contribute to shed light on the extent of H_2O contamination influences on battery safety.

The component-based Li-ion battery degradation model from Chapter 4 is slightly extended to address the sensitivity of water impurities and SEI composition on thermal self-heating and thermal runaway. The complete model encompasses 12 decomposition reactions and 20 participating species, which will be parameterised through two separate experiments. First, the experiments conducted by Stich et al. [144] will be used for the conductive salt decomposition. Thereafter, the complete set of reactions is parameterised against the ARC measurement Maleki et al. [69]. In-depth case studies will be conducted on the impact of LEDC content, the SEI thickness, and the H_2O contamination on Li-ion battery safety. Eventually, a broader parameter study that combines all three effects will be presented, examining potential interdependencies between them and illuminating dominating processes and properties.

5.1 Procedure

The following section summarises the procedure employed to perform the sensitivity analysis for the thermal abuse in Li-ion batteries in the context of SEI thickness and composition as well as H_2O impurities. First, the modelled system is presented in the form of mathematical sets. This is followed by a brief description of the underlying experimental work of Stich et al.

[144], which is used to parameterise the reactions among the conductive salt decomposition. Subsequently, the reference case conditions are outlined with an extensive discussion on the initial conditions of SEI composition, thickness and H_2O content. Thereafter, the variation in each of those properties is presented. The section finishes with a brief description of the parameter estimation procedure and compares the model against the experimental data for model validation.

5.1.1 Modelled system

To better account the impact of H_2O content, the preliminary reaction network of Chapter 4 has been extended. As presented in Chapter 3, a set notation is used to unambiguously illustrate the occurring processes concisely. Thus, in the following, the complete sets of species and reactions used to model the system in the present chapter are given. For better illustration, species and processes added in comparison to Chapter 4 are expressed in bold font.

The first set Ω_{SP} contains all modelled chemical species:

$$\begin{aligned}\Omega_{\mathrm{SP}} = \{&(CH_2OCO_2Li)_2\,(\mathrm{LEDC}), Li_2CO_3, \mathbf{LiOH}, \mathbf{Li_2O}, LiF, LiPF_6, LiC_6, C_6, Li_xCoO_2, Co_3O_4,\\ &C_2H_4, CO_2, O_2, HF, PF_5, POF_3, \mathbf{HPO_2F_2}, H_2O, C_3H_4O_3\,(\mathrm{EC}), C_4H_8O_3\,(\mathrm{EMC})\}.\end{aligned}$$

Thus the Ω_{SEI} adjusts to:

$$\begin{aligned}\Omega_{\mathrm{Solv}} &= \{C_3H_4O_3, C_4H_8O_3\} \subseteq \Omega_{\mathrm{SP}},\\ \Omega_{\mathrm{SEI}} &= \{(CH_2OCO_2Li)_2, Li_2CO_3, \mathbf{LiOH}, \mathbf{Li_2O}, LiF\} \subseteq \Omega_{\mathrm{SP}}.\end{aligned}$$

The set Ω_{RE} is extended to:

$$\begin{aligned}\Omega_{\mathrm{RE}} = \{&\mathrm{LiPF_6}\,\text{decomposition(CSD)}, \mathrm{PF_5}\,\text{decomposition (PFD)},\\ &\textbf{POF}_\mathbf{3}\,\textbf{decomposition (PFD)}, \text{LEDC decomposition (OSD)},\\ &\mathrm{Li_2CO_3}\,\text{decomposition(ISD)}, \textbf{LiOH decomposition (LSD)}\\ &\text{LEDC production (OSP)}, \mathrm{Li_2CO_3}\,\text{production(ISP)},\\ &\textbf{LiOH production (LSP)}, \mathrm{LiCoO_2}\,\text{decomposition(CD)}\\ &\text{EC decomposition (ECD)}, \text{EMC decomposition (EMCD)}\}.\end{aligned}$$

The subset of SEI-forming reactions is then given with the following:

$$\Omega_{\mathrm{SEI\,form}} = \{\text{OSP, ISP, } \mathbf{LSP}\} \subseteq \Omega_{\mathrm{RE}}.$$

5.1.2 Underlying experimental work

This part of the thesis aims to extensively probe the influence of H_2O impurities and SEI composition on high-temperature battery safety. Two distinct experiments from literature are referenced to obtain kinetic parameters, k_0 and E_A. One experiment will again be the ARC measurement conducted by Maleki et al. [69]. For a more detailed description, see Section 4.1.2. This will be extended by the experiment by Stich et al. [144], who focused on the decomposition of $LiPF_6$ with H_2O as an impurity. The latter provides an isolated study of $LiPF_6$, PF_5 and POF_3 decomposition allowing for better identification of the kinetic parameters connected to these reactions. In their study, Stich et al. [144] used a EC/DEC 50/50 v/v 1 M $LiPF_6$ electrolyte with an initial concentration of <= 15 ppm H_2O and <= 50 ppm HF. They then added 1000 ppm of water. The concentrations of H_2O, HF, and HPO_2F_2 have been monitored for 15 days at room temperature by Coulometric Karl Fischer titration, acid-base titration, and ion chromatography.

5.1.3 Reference case conditions

With their intricate internal decomposition mechanisms during formation, operation and thermal abuse, Li-ion batteries present a complexity that hinders the precise determination of amount of species present at the beginning of a thermal decomposition study. Due to these restrictions, educated estimates for some components are necessary, a challenge addressed in the following section. First, the procedure to estimate values for conductive salt decomposition products, namely PF_5, POF_3, HPO_2F_2, HF, and H_2O, is explained. Afterwards, the assumptions for

estimating the initial amount of the SEI components, Li_2O, LEDC, LiOH, LiF, and Li_2CO_3, as well as the initial SEI thickness, are discussed.

Using the reactions connected to conductive salt decomposition, namely CSD, PFD and POFD, allows to estimate the initial values for their reactants. Here, the initial mixing of the electrolyte is emulated by a simulation of the reaction of electrolyte species with 40 ppm H_2O impurities. At equilibrium, most of the water has been converted, and the electrolyte contains eight ppm H_2O and 50 ppm HF, which is in excellent agreement with the recorded < 10 ppm H_2O and < 50 ppm HF by electrolyte suppliers [227]. Further, H_2O is introduced into the system during cell assembly, originating from the separator and cathode. Values for water contamination for the anode, cathode, and separator are based on the medium drying procedure reported in the publication by Huttner et al. [226]. This is estimated to result in an additional 334 ppm of water in the electrolyte for the reference case. The water contained in the anode is assumed to react to LiOH fully. After cell assembly, the formation procedure is conducted. Li_2CO_3, in turn, reacts swiftly already at room temperature with HF to form H_2O (ISD). The H_2O is then used up by the reactions of PF_5 (PFD) and POF_3 (POFD), which occur steadily but slowly at room temperature. Therefore, the last step to get realistic initial conditions for the simulation of the ARC measurement is estimating the time between cell formation and testing. This study assumes direct testing, and the initial values after a formation period of three days with C/10 are considered. The whole procedure and intermediate results are described in Appendix C.1. From this procedure, the initial values for PF_5, POF_3, HPO_2F_2, HF, and H_2O are calculated as 992 ppm, 46 ppm, 1306 ppm, 0 ppm, and 260 ppm, respectively.

Initial values for the SEI composition are challenging to obtain as most literature does not report quantitative values. Thus, the assumptions here are based on the study of Liu et al. [53]. Using a electrochemical quartz crystal microbalance,hey measured the mass increase on a graphite anode during formation. In combination with electrochemical data, OEMS measurements, and XPS, they were able to provide a reasonable estimate of the corresponding mass attributed to individual SEI species. As the introduced Li_2CO_3 reacts with the present HF to form LiF, as described above, the composition changes slightly during the applied ageing procedure. From this, the volumetric SEI composition is deducted as follows (details see Appendix C.1):

Li_2O: Liu et al. found that the anode lost weight within the first discharge after formation. Based on the measured weight loss, they assume the following oxidation to occur: $(CH_2OCOLi)_2) \longrightarrow Li_2O + 2\,CO_2 + C_2H_4 + O_2$. Following this, the Li_2O content is estimated as 10 vol-%.

LEDC: The content is estimated to be 45 vol-%

LiOH : It is assumed that all residual water in the anode reacts to form LiOH during cell formation. This accounts for 0.6 vol-% for the reference case.

LiF : Since Liu et al. could not distinguish between LiOH and LiF, we assume that both substances add up to 10 vol-% of the SEI. Combined with the additional production of LiF by decomposition of Li_2CO_3 (ISD) during the applied ageing procedure, this accounts for 10.4 vol-% for LiF.

Li_2CO_3: The last 34 vol-% of the SEI is assumed to be composed of Li_2CO_3.

The SEI is assumed to be 50 nm thick. This is in the range of reported thicknesses [53–55]. The initial and maximum temperatures are 25 °C and 220 °C, respectively. The pressure is constant at p = 101325 Pa. All modelled species and their physical parameters and data on the electrode structure can be found in Table B.1 and B.2. From this, the complete set of initial conditions for the reference case can be deducted and presented as molar quantities in Table C.1.

5.1.4 Variation in water content and SEI properties

H_2O impurities, SEI compositions and SEI thickness can be influenced during manufacturing processes such as electrode drying or formation current adjustments, as well as through battery ageing. At present, it is unfeasible to model and incorporate all these processes. Nevertheless, to implicitly investigate their effects during thermal abuse, a case study is designed that uses varied initial values for these three properties, see Table 5.1.

Table 5.1: Changes in initial parameters for water content and SEI to study the effect of different manufacturing and ageing conditions: reference scenario, organic or inorganic SEI, thick or thin SEI, wet or dry electrode.

Parameter	Reference	Thick SEI	Thin SEI	Organic SEI	Inorganic SEI	Wet Electrode	Dry Electrode
d_{SEI} / nm	**50**	**75**	**25**	50	50	50	50
ε_{LEDC} / vol-%	**45**	45	45	**90**	**0**	46	45
$\varepsilon_{Li_2CO_3}$ / vol-%	**34**	34	33	**8.4**	**39**	30	34
ε_{LiF} / vol-%	**10.4**	10.4	11.4	**1**	**30.4**	9	10.6
ε_{Li_2O} / vol-%	**10**	10	10	**0**	**30**	10	10
ε_{LiOH} / vol-%	**0.6**	0.6	0.6	0.6	0.6	**5**	**0.4**
C_{H_2O} / ppm	**260**	260	260	260	260	**505**	**168**
C_{HF} / ppm	**0**	0	0	0	0	**0**	**0**
C_{PF_5} / ppm	**992**	992	992	992	992	**880**	**1017**
C_{POF_3} / ppm	**46**	46	46	46	46	**95**	**31**
$C_{HPO_2F_2}$ / ppm	**1306**	1306	1306	1306	1306	**5332**	**536**

The variation in H_2O content is based on a study of different drying procedures from Huttner et al. The H_2O content will change due to different water contents in the electrodes following Huttner's results for the undried "wet", the medium dried, and the highly dried electrodes. The different values in the anode of 2422 ppm, 286 ppm, and 214 ppm translate into 5 vol-%, 0.6 vol-% and 0.4 vol-% of LiOH content within the SEI. The reported values of 2644 ppm, 500 ppm and 464 ppm in the separator and 313 ppm, 156 ppm, and 63 ppm for the cathode translate to an H_2O increment in the electrolyte of 930 ppm, 334 ppm, and 172 ppm, respectively. In the early 2000's it was revealed that LEDC is the primary decomposition product of EC [48]. A recent study by Wang et al.[46], however, questions the stability of LEDC and proposed that lithium ethylene mono-carbonate (LEMC) is the stable alternative. Following this, Xie et al. [47] investigated the formation pathways of LEMC, including the decomposition of LEDC and found that all kinetically favourable pathways need water as a reactant. It is apparent that there is still a lively discussion on the exact composition of the SEI. Thus, a wide range of differing compositions is considered and LEDC as the major organic compound is assumed: Here, 90 vol-%, 45 vol-% and 0 vol-% LEDC are investigated. The pure LEDC content is not chosen since LiOH has to be part of the SEI to account for water impurities. Further, the complete lack of Li_2CO_3 would lead to an accumulation of HF according to the above-described behaviour, which is deemed very improbable. Thus, the remaining volume percentages are Li_2CO_3. The SEI thickness has been varied as 25 nm, 50 nm, and 75 nm, which are within reported values for SEI thicknesses [53–55]. All variations undergo the same formation and conditioning procedure described in the previous section. From this, the initial values listed in Table 5.1 are calculated. An extensive parameter variation, including all possible 27 variations (3x3x3), has been simulated to investigate the interdependence. The additional 18 initial values, apart from the 9 already listed in Table 5.1, can be found in Table C.2.

5.1.5 Parameter estimation

The kinetic parameters for the decomposition of $LiPF_6$ and subsequent reactions of PF_5 and POF_3, namely CSD, PFD, and POFD, have been parameterised such that two constraints are met. The first is that the experimental data of Stich et al. [144] on room-temperature electrolyte changes could be reproduced. The second is that the reactions notably accelerate within the reported temperature interval, see Table 3.1. For the decomposition of Li_2CO_3, the kinetic constants are set such that this reaction is not limiting. For the other reactions, the kinetic parameters have been adjusted to meet two constraints: The first one is that the reactions occur within the reported temperature interval for each given reaction. The second constraint is that the simulation can reproduce the experimental data from Maleki et al. [69]. Exceptions to

this are the SEI forming reactions, OSP, ISP, and LSP. Given that they are, in nature, electrochemical reactions, they should notably occur even at room temperature with an unprotected electrode. Reported energy barriers for these reactions are very low, if not 0 [44, 228, 229]. The term introduced to account for the inhibition effect of the SEI, see Equation 3.3, does not prevent notable reactions even at low temperatures with these low barriers. Therefore, the energy barriers are adjusted such that these reactions occur in a temperature range concurrently with the decomposition of the existing SEI.

Model equations and parameters were implemented in MATLAB, and the simulation was performed using the ode15s solver. All calculations have been performed with MATLAB Version 2022a, or higher [203], using an i7-9750H processor with 16 GB RAM. The average simulation time was six minutes.

5.1.6 Model accuracy

Figure 5.1 compares the model with the experiments of a) Stich et al. [144] and b) Maleki et al. [69]. The agreement between simulation and experiment is excellent in both cases. Please note that in the case of the experiment by Maleki et al. the data points after cell opening have not been considered for the parameterisation. Due to the adjustments to the model, the simulated curve extends slightly farther in the direction of these points when compared to the first parameterisation performed in Chapter 4. The outstanding agreement of simulated and experimental data now allows for further investigation. Thus, the coming section will present the results of the performed sensitivity analysis.

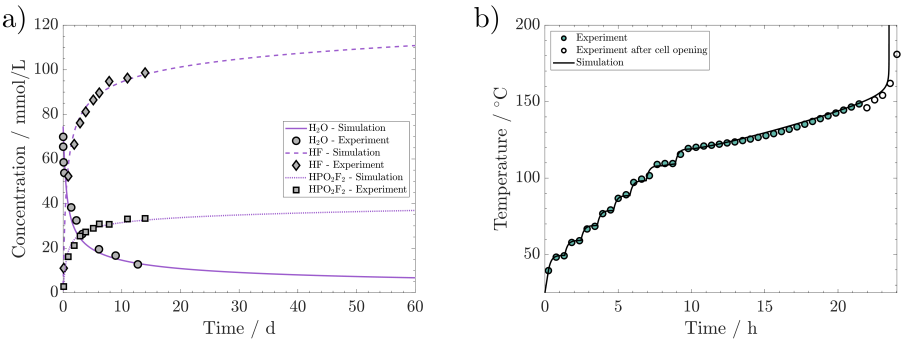

Figure 5.1: Comparison of the model against experimental data for a) the conductive salt decomposition against the data of Stich et al. [144] and b) the whole model against the ARC measurement of Maleki et al. [69].

5.2 Results and discussion

The upcoming section evaluates the propagation and characteristics of the thermal runaway during thermal abuse of the given Li-ion battery for the various manufacturing and ageing scenarios. First a high level discussion of sensitivities of ARC measurements to water content, SEI composition and SEI thickness are identified and quantified. This is followed by an in-depth analysis of this behaviour and the underlying causes based on the progression of reactions, their interplay, and their contribution to the temperature evolution during the abuse test. Particular focus is given to the transition from the heat-wait-seek to the exothermal self-heating mode, as this is the crucial point determining a battery's safety range. Then the effects of different water content and initial SEI properties on the state of the battery and their consequences in an ARC measurement are elucidated.

5.2.1 Impact of SEI state and H_2O on temperature evolution

In Figure 5.2, the simulated temperature evolution is displayed for a variation in a) SEI composition, b) SEI thickness, and c) H_2O content. The preheating procedure (1 °C/min) can be observed up to 40 °C. From then on, the ARC switches to the Heat-Wait-Seek phase and performs 10 °C heating steps, including wait-and-seek periods. This is repeated until the first self-heating is detected. This happens for the reference scenario (black line) at 108 °C and 7.8 h, marked by SH-II). Then, the ARC switches to the self-heating mode and starts to follow the cell temperature. For the reference scenario, self-heating at this stage is not sustained, and after a period of 1 h at 110 °C, an additional heating step is performed. At 119 °C and 10.1 h, marked by SH-III), another self-heating of the cell leads to switching to the exothermic mode of the ARC again. The temperature monotonically increases throughout the subsequent 13 h until the thermal runaway is triggered at 174 °C and 23 h marked by TR).

Figure 5.2 a) shows the effect of variation of SEI composition to 90 vol-% LEDC (dashed line) and 0 vol-% (dash-dotted line). No significant difference between the scenarios can be observed during the preheating phase and in the first six heating steps. At 98 °C and 6.9 h, marked by SH-I), significant self-heating is observed for the 90 vol-% LEDCcase, which is 11 °C earlier compared to the reference case. Temperature increases monotonically without a further heating step, and the cell reaches the thermal runaway at 173 °C and 24.5 For the inorganic SEI without LEDC, one additional heating step compared to the reference case is needed, with self-heating starting only at 127 °C and 10 h. This makes a difference of +9 °C compared to the reference case. Yet, the cell goes faster into the thermal runaway. It can be concluded that SEI composition has a notable effect on thermal safety of a battery, with cells

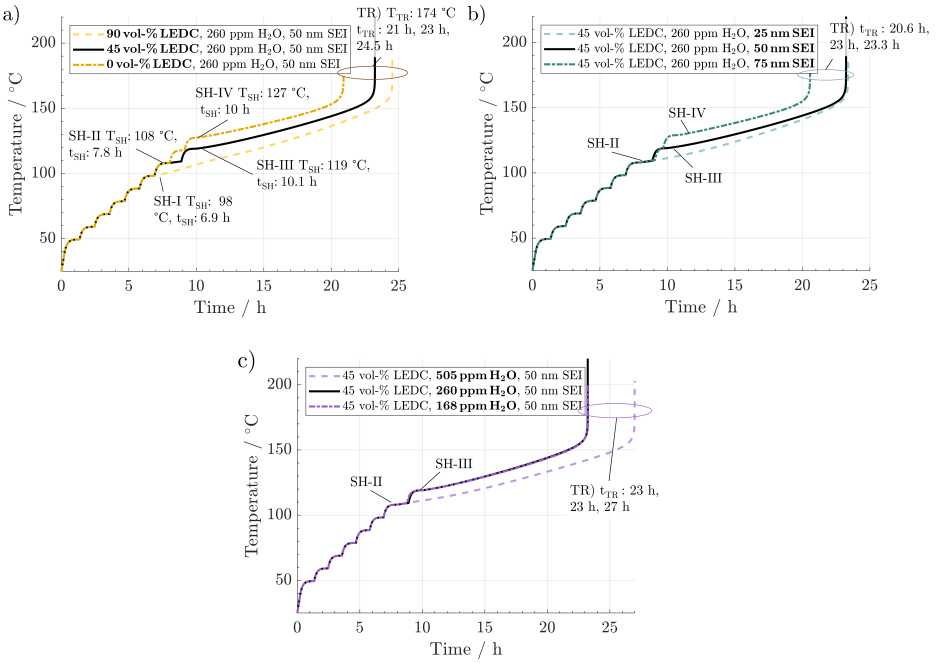

Figure 5.2: ARC simulations with variations of a) SEI composition, b) SEI thickness, and c) water content originating from the electrodes. The solid black line refers to the reference case in all subfigures. The lighter dashed line refers to the scenario featuring the lower self-heating temperature. The dash-dotted darker line indicates the scenario with the higher self-heating temperature T_{SH}. Characteristic self- heating temperatures, self-heating times, t_{SH}, and runaway times, t_{TR}, are indicated in the graphs.

with more LEDC, e.g. due to less ageing, being more likely to enter a thermal event, leading finally to thermal runaway.

In Figure 5.2 b), the effect of SEI thickness on thermal runaway is presented. The behaviour during the preheating and first heating steps shows no deviation from that of the reference case. The thin SEI enters one heating step earlier into the self-heating phase than the reference case. Self-heating progresses and causes a rapid thermal runaway at 174 °C and 23.3 h. In contrast, the thick SEI case reaches the self-heating only after a further heating step, at around 127 °C and 10 h, and enters the final runaway phase earlier, at 74 °C and 20.6 h. According to this analysis, SEI thickness also significantly impacts battery safety, with thicker SEI leading less quickly to self-heating. It should be noted that the results presented here are specific for the investigated system of a graphite anode combined with EC/EMC 1.2 M $LiPF_6$ liquid electrolyte. For example, in case of Li metal and all solid state batteries, a decrease in safety with increasing SEI thickness was found [230, 231].

Finally Figure 5.2 c) shows the impact of H_2O impurities. As in the variations before, no difference is observed until 108 °C and 7.8 h. Then, the cell with high H_2O amounts enters one heating-step earlier into the sustained self-heating phase. The thermal runaway is reached at 174 °C and 27 h. In contrast, the curves for low and medium water amounts are identical. Thus, high amounts of H_2O seem to be detrimental to thermal safety of Li-ion batteries.

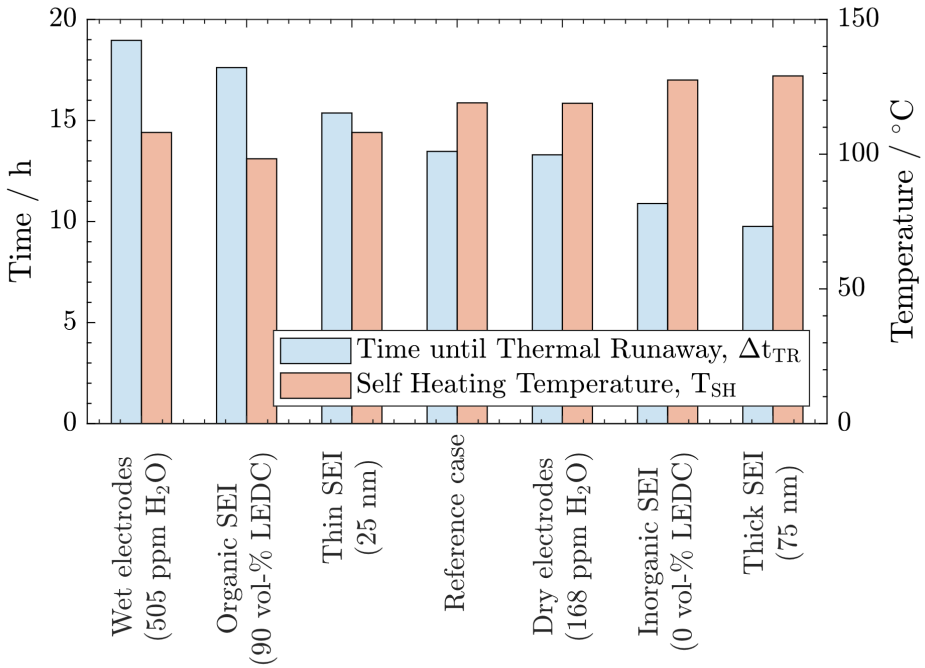

Figure 5.3: Comparison of self-heating temperature T_{SH} and time until the thermal runaway is reached after the first exothermic phase Δt_{TR} as key indicators for all cases.

From the above-described results, it can be concluded that all three parameters significantly impact thermal safety. The most apparent difference between all cases is the change in self-heating temperature and the time until the thermal runaway is reached. For a better comparison, these key parameters are summarised in Figure 5.3. Here, a clear trend can be observed. A lower self-heating temperature corresponds to a longer time until the cell reaches the thermal runaway eventually. These opposing trends of earlier self-heating but later thermal runaway pose a fundamental question as to how to produce inherently safer batteries: While higher self-heating temperatures can be interpreted as safer, a shorter time until reaching the thermal runaway, and with this, a virtually unstoppable thermal event could be considered unsafe. Manufacturers must perform a risk analysis to make a good trade-off for these safety-critical

parameters. While discussing the case study, including 27 variations, in Section 5.2.3 an alternative metric is offered to include both characteristics in the safety assessment of Li-ion batteries. Note that the temperature for the start of the thermal runaway is identical for all cases. Similarly, as reported in literature, this is almost exclusively caused by the onset of the cathode active material decomposition. In this study, the cathode material was not varied. Thus, this behaviour was expected. In the following section, a deeper analysis of processes during the thermal abuse tests is performed to reveal the origin of the manufacturing- and ageing-specific differences in safety behaviour.

5.2.2 Analysis of produced heats and concentration progression

To understand the main reactions impacting the self-heating and their sensitivity to SEI state and water impurities, here the progression of reactions, related species concentrations and produced or consumed heat during the thermal misuse are analysed. For better readability, the figures display only those reactions that are substantially influenced by SEI composition or water content. For the same reason, all SEI-forming reactions, namely OSP, ISP, and LSP, are summed up. For individual contributions, see the Appendix Figure C.4. Analysis starts at 40 °C, where the first degradation reactions are observed (Figure 5.4): The initial decomposition of the conductive salt is triggered by a shift of the equilibrium towards the decomposition product with increasing temperature. Further, the decomposition of PF_5 (PFD) and POF_3 (POFD) start at 60 °C, peak around 75 °C, and end for the first time around 110 °C (SH-II). The HF released from these reactions initiates the decomposition of Li_2CO_3 (ISD), which, thus, happens simultaneously to PFD and POFD. Note that the concentration of Li_2CO_3 is only slightly declining due to the only small amounts of H_2O, and thus reactant HF, whereas it is produced in significant rates also from LEDC decomposition. Decomposition of PF_5, POF_3 and Li_2CO_3 happen simultaneously, and the ratio of produced heat by Li_2CO_3 decomposition vs. the consumed heat by PF_5 and POF_3 decomposition is always below 1 and decreases with temperature. Thus, the reactions caused by salt decomposition products, i.e. PFD, POFD, and ISD, act as heat sinks. The cause for the extinction of these reactions is the depletion of the necessary reactant H_2O. As the reaction rates and, therefore, their interplay is strongly dependent on water availability, we continue the discussion when analysing the wet and dry case scenario. Reactions connected to salt decomposition are complemented by the exothermic decomposition of LEDC with notable reaction rates occurring above 80 °C. Eventually, by increased decomposition of LEDC and already decreasing endothermic heats due to H_2O depletion, the first self-heating starts at 108 °C (SH-II). This phase is, however, not self-sustaining because the exothermic LEDC decomposition slows down when much of the available LEDC has been

consumed, so that a further heating step is required to trigger a thermal event. The transition to continuous self-heating of the battery at 118 °C (SH-III) is caused by the almost complete decomposition of $LiPF_6$, which reduces the endothermic heats to nearly 0. The self-heating phase until the rapid thermal runaway is dominated by the re-formation of organic SEI, i.e. LEDC, and inorganic SEI, i.e. Li_2CO_3, and further decomposition of LEDC. The declining concentration of LiOH denotes its decomposition to Li_2O (LSD) around 120 °C. The amount of LiOH introduced into the system by H_2O in the anode after drying is too small to produce notable amounts of exothermic heats. The thermal runaway is eventually set in motion by the decomposition of the cathode active material (CSD) starting around 150 °C. The thus produced O_2 triggers the subsequent solvent combustion, first of EC (ECD), then of EMC (EMCD); see Apendix Figure C.4. The combustion product H_2O, in turn, triggers an exponential increase of PF_5 (PFD) and POF_3 (POFD) decomposition reactions; despite being endothermic, they cannot compensate for the strongly exothermic reactions. Simultaneously, the exothermic decomposition of Li_2CO_3 is also re-initiated by HF produced from the PF_5 and POF_3 decomposition. Finally, it should be noted that above 130 °C, LEDC concentration is kept at around zero, as any generated LEDC is directly consumed. In contrast, LiF concentration rises until all $LiPF_6$ is decomposed and then stays constant. The SEI is therefore completely inorganic at higher temperatures. Concentrations of HF, $LiPF_6$ and Li_2O are either 0 (HF) or can be deduced from LiF ($LiPF_6$) or LiOH (Li_2O) progressions. For the sake of clarity, they are shown in the Appendix Figure C.4.

The combustion product H_2O, in turn, triggers an exponential increase of PF_5 (PFD) and POF_3 (POFD) decomposition reactions; despite being endothermic, they cannot compensate for the strongly exothermic reactions. Simultaneously, the exothermic decomposition of Li_2CO_3 is also re-initiated by HF produced from the PF_5 and POF_3 decomposition. Finally, it should be noted that above 130 °C, LEDC concentration is kept at around zero, as any generated LEDC is directly consumed. In contrast, LiF concentration rises until all $LiPF_6$ is decomposed and then stays constant. Concentrations of HF, $LiPF_6$ and Li_2O are either 0 (HF) or can be deduced from LiF ($LiPF_6$) or LiOH (Li_2O) progressions.

Having understood the process interplay for the reference case, it is further evaluated how their dependence on SEI composition and water content can explain the observed change in thermal self-heating and runaway behaviour.

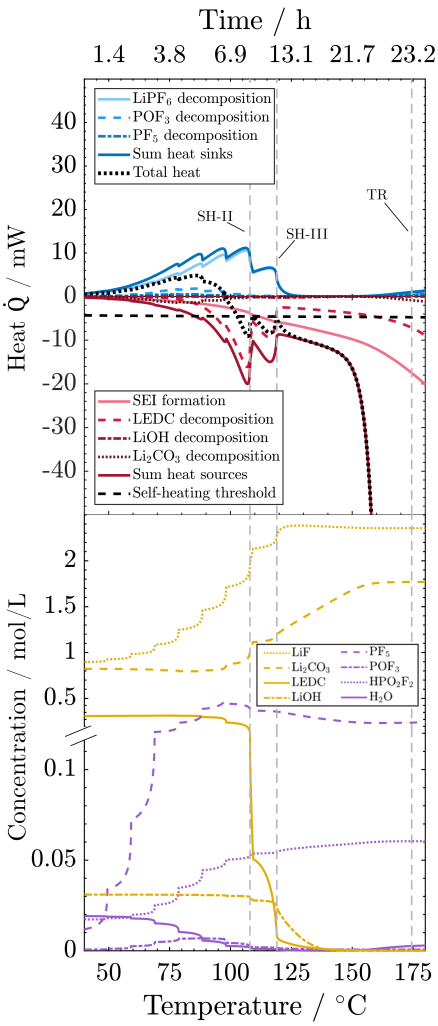

Figure 5.4: Reference case: evolution of heat sinks (blue) and heat sources (red) and related concentrations, as well as the total heat (black) and the self-heating threshold (horizontal dashed line). Vertical dashed lines indicate events marked in Figure 5.2. The y-axis break is at 0.12 mol/m^3.

Deviations in underlying system

The following box discusses the deviations between the results obtained in Chapter 4 and this chapter. As discussed in the box on page 22, the model and reaction network have been extended when moving from the basic simulation in Chapter 4 to this more detailed analysis. The major differences are the addition of the decomposition of POF_3 with H_2O to form HPO_2F_2 and HF as well as the formation of LiOH and its decomposition at higher temperatures. In this study, the decomposition of $LiPF_6$ and PF_5 are also modelled as reversible reactions. Further, based on the works of Solchenbach et al. [85], the decomposition of Li_2CO_3 with HF is now assumed not to be rate limiting.

These differences show a slight deviation in the progression of evolving heats and, thus, reactions. This majorly affects the cycle of Li_2CO_3 decomposition with HF producing H_2O and the reaction of PF_5 with this water to form HF again. In Chapter 4, this decomposition only set in above 100 °C and was kept up until around 170 °C, see Figure 4.3. From the above assumption of a not rate-limiting reaction of Li_2CO_3 with HF and the joint parameterisation of reaction CSD, PFD and POFD along with the experiment of Stich et al. [144] it follows that the decomposition of Li_2CO_3 happens at lower temperatures as previously assumed. Another major difference between both modelled networks is the temperature range in which the decomposition of Li_2CO_3 can happen. These are 100 °C to 170 °C for Chapter 4 and 60 °C to 100 °C in this study. The reason for this phenomenon is the newly considered subsequent reaction of POF_3 with H_2O to form HF and HPO_2F_2. Compared to the decomposition of PF_5, only one HF is formed for each molecule of H_2O involved. Since no other reaction generates H_2O in this temperature range, the progress of these reactions leads to water depletion, affecting all reactions directly or indirectly dependent on it.

What does this imply for the validity of conclusions from the last chapter? Even though the exact progression of events is different, general statements remain true. The on-set of self-heating is still governed by highly fluctuating properties such as SEI thickness, composition and H_2O as is the content of this chapter. Also, is the amount of released gases not substantially different from the previous chapter's results. Thus, it is still highly likely that no solvent boiling occurs during the initial phase of self-heating. This will also be addressed in Chapter 6.

As SEI composition impacts mainly the SEI formation and SEI decomposition reactions, their corresponding heats are presented in Figure 5.5 a). Li_2CO_3 decomposition is only marginally affected by changes in the SEI composition and is thus displayed together with other reactions in the Appendix C.4. A higher LEDC volume fraction leads to notably earlier on-set of LEDC decomposition. This leads to the earlier self-heating on-set at 98 °C (SH-I) for the 90 vol-% LEDC case compared to the reference case (45 vol-% LEDC). For 90 vol-% LEDC, heat production from this reaction decreases much slower after reaching the self-heating because there is still a significant amount of LEDC in the SEI (see Appendix Figure C.5). Together with the higher SEI formation reaction, this can explain that the 90 vol-% LEDC case needs no further heating step to proceed to thermal runaway. The large fraction of LEDC in the initial SEI and its rapid but not complete consumption leads to a significant drop of SEI thickness to 60% before SEI formation sets in and rebuilds the SEI. The decline is much more significant than for the reference case, where ca. 80% of the SEI, mostly inorganic, remains and is subsequently rebuilt. For the inorganic case, i.e. 0 vol-% LEDC in the initial SEI, the missing exothermic heat from the decomposition of the initial LEDC and the slow exothermic SEI formation lead to additional heating steps. At around 128 °C, marked by SH-IV), eventually, self-heating of the battery sets in due to higher exothermic SEI formation rates at this temperature. As no LEDC is present in the initial SEI in this case, and as Li_2CO_3 decomposition is negligible and compensated by its production, SEI thickness increases monotonously. In all three cases, during proceeding self-heating >120 °C, the heat from LEDC decomposition is smaller than from SEI formation. It can be concluded that LEDC content in the SEI is strongly impacting thermal safety, as the self-heating onset is strongly impacted by LEDC decomposition and formation rates, and thus by LEDC availability.

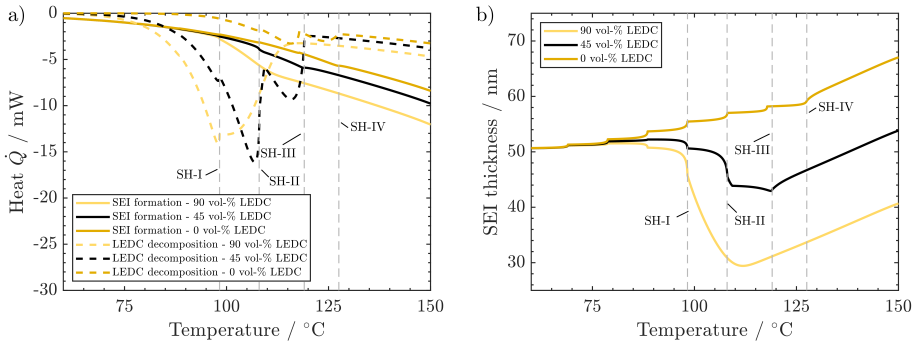

Figure 5.5: Effect of SEI composition on behaviour during ARC test: a) Produced heats from LEDC decomposition and SEI formation. b) Corresponding changes in SEI thickness. Conditions: 260 ppm water, 50 nm thick SEI.

Following, the impact of initial SEI thickness on heat evolution from LEDC decomposition and reformation (Figure 5.6 a) and on the resulting changes in SEI thickness (Figure 5.6 b) are discussed. From Figure 5.2 b), we know that a thicker initial SEI leads to a higher self-heating temperature. This is counterintuitive as more SEI, i.e., more LEDC, means more reactants for low-temperature decomposition. Indeed, more SEI leads to more LEDC decomposition (Figure 5.6 a); yet, during the seek period, LEDC decomposition heats decrease to similar values for all SEI thicknesses, whereas, for the thin SEI, exothermic SEI formation is almost double that of the thicker SEIs. The thickness-dependent SEI formation rate, Equation 3.3, is the key to explain why thin SEI still leads to lower self-heating temperatures. The thinner the SEI is, the higher the formation rate and thus produced heat from SEI formation reactions. SEI thickness can therefore be seen as a beneficial property of the SEI to prevent further formation and early thermal runaway.

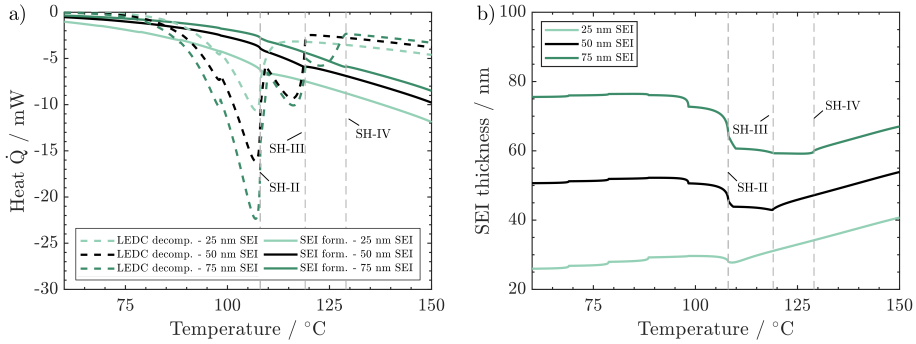

Figure 5.6: Effect of SEI thickness on behaviour during ARC test: a) Produced heats from LEDC decomposition and SEI formation. b) Corresponding changes in SEI thickness. Conditions: 45 vol-% LEDC, 260 ppm water.

These findings are also in good agreement with ARC tests of cycling-aged cells in the temperature range of 35–45 °C from literature by Feng et al. [81], Feinauer et al. [79], Börner et al. [76], and Waldmann et al. [80]. All studies independently found that these ageing procedures lead to an increase of the on-set temperature of self-heating by 15–20 °C when compared to their fresh reference. The here presented study now delivers an explanation for this increase: when cells age, SEI becomes thicker and more inorganic; both effects have been shown here to lead to a delayed self-heating temperature. Röder et al. [232] in contrast, found a lowered self-heating temperature for calendaric-aged cells at 60 °C. The model developed in this thesis may explain this behaviour also: either the SEI had much more total amount of LEDC, probably dissolved also in the electrolyte, or the LEDC had reacted at 60 °C and left a thin, less inhibiting SEI.

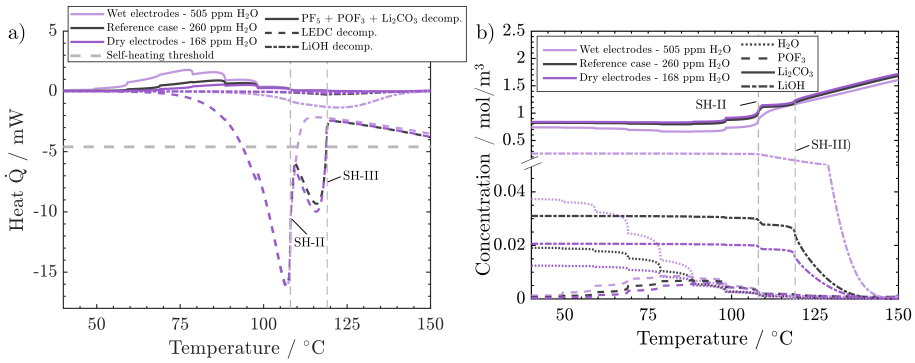

Figure 5.7: Effect of H_2O impurities on behaviour during ARC test: a) endothermic heats PF_5 + POF_3 +Li2CO3 and exothermic heats of LEDC and LiOH decomposition. b) concentrations of H_2O, POF_3, Li_2CO_3, and LiOH. Conditions: 45 vol-% LEDC, 50 nm SEI.

Finally, the processes during the ARC tests with different H_2O content are analysed to understand why low and medium water impurities lead to the same temperature evolution while high water content leads to earlier self-heating. PF_5, POF_3 and Li_2CO_3 decomposition reactions (PFD, POFD, ISD) happen almost simultaneously. Their added values are endothermic and increase with water content (Figure 5.7 a). It can also be observed that the higher the water content, the earlier the on-set of these reactions. In the case of dry and reference H_2O concentration, the released heats are almost identical and very small. From ca. 80 °C onwards, in the wet electrode case, most of the endothermic heat is still small and released in a temperature range where no exothermic counterpart exists. With increasing impurity concentration, the temperature gradient after sustained self-heating changes from 4.4 °C/h (dry case) to 4.65 °C/h (medium dried case) to 4.1 °C/h (wet case). These changes are connected to the increased concentration of LiOH, which decomposes exothermically, and the corresponding decrease in self-heating temperature (wet case). First, when moving from the dry case to the medium dry case, the temperature gradient only increases slightly which can be explained by an also only small increase of LiOH content from 0.4 vol-% to 0.6 vol-%. However, for the wet case the temperature gradient decreases, which is counterintuitive at first but is also connected to the higher LiOH content of 5 vol-%. The significantly higher concentration of LiOH in the wet electrode case leads to notable LiOH decomposition rates and exothermic heats in the self-heating critical temperature range of 100—130 °C. This leads to a transition into self-heating one temperature step earlier. The lower temperature in turn leads to a slower progression of all occurring reactions and, thus, a lower temperature gradient. This points to an important characteristic of an ARC measurement. As discrete temperature steps are used, more produced heat can either increase the temperature gradient (dry → medium dry), when self-heating starts during the same time step. Or it leads to a lower self-heating temperature, with subsequent lower temperature gradient. Thus, it is important to discuss both characteristics together. In order to

illustrate these impacts, the water variation case was simulated using a 2.5 °C temperature step instead of the 10 °C used before (see Appendix Figure C.8). Even though, the wet case also transitions into self-heating one step earlier, the gradients, 2.5210 °C/h (dry), 2.5459 °C/h (medium) and 2.6975 °C/h (wet), now better correspond to the produced heats as the temperatures are closer together.

In conclusion, H_2O impurities only play a significant role in battery safety when the electrodes have not been dried properly. The impact is negligible as soon as even a medium-intense drying procedure (260 ppm residual H_2O) is applied. Also, further drying (168 ppm residual H_2O) does not bring any noticeable benefit, because already at medium rates, LiOH decomposition rates are too low to give a significant heat contribution to tilt the balance towards sustained heating. As such, at least under the analysed circumstances and battery chemistry, extensive drying is unnecessary for a safer performance. This result aligns with the experimental findings of Huttner et al. [226], who found a negative impact on performance metrics for intense drying procedures. Two more points should be accounted for in a holistic analysis of battery safety, which may be followed in further studies: The acids produced from H_2O, such as HPO_2F_2, are present in higher concentrations, i.e., 0.175 mol/m^3 in the wet case compared to 0.078 mol/m^3 in the reference case. The acids were reported to lead to increased dissolution of transition metals from the cathode, which will then promote SEI decomposition [233]. Eventually, even though the energetic impact of these reactions is small, all are gassing reactions and will impact cell pressure. Here, the following chapter poses as a starting point to include this essential part of gassing degradation reactions into the herein developed battery safety model.

5.2.3 Impact of joint variation of SEI state and H_2O content

So far, we have analysed how the thermal safety behaviour changes when varying a single variable, SEI thickness, composition or water content. In reality, multiple factors change due to ageing or different manufacturing processes. In the following, the impact of the cross-influence of the three variables is analysed, and trends and generalisations are deduced.

Figure 5.8 a) shows the average temperature gradient in the region between self-heating on-set and thermal runaway, $\frac{T_{TR}-T_{SH}}{t_{TR}-t_{SH}}$, over the inverse self-heating temperature, $\frac{1000}{T_{SH}}$, for all 27 variations. Here, a high temperature gradient refers to a fast heating rate and, thus, lesser time to intervene. A low self-heating temperature indicates a lower resistance of the battery against thermal abuse. Thus, both characteristics can be considered indicators for battery safety and have therefore been chosen for this comparison. Cases that are located in the lower left corner of the figure can be considered rather safe, because it represents high self-heating temperatures and a low self-heating rate. Whereas, the cases closer to the upper right show the opposite

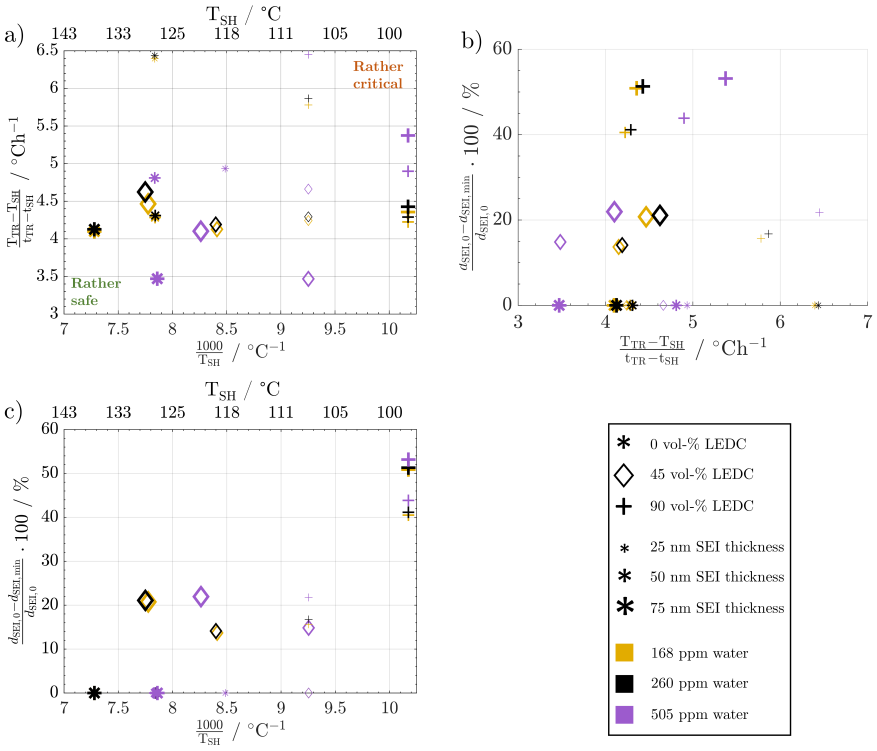

Figure 5.8: Impact of changes in water content and SEI properties on: a) temperature gradient over the inverse self-heating temperature scaled by 1000, b) the percentage of SEI thickness reduction over the temperature gradient, and c) the percentage of SEI thickness reduction over the inverse self-heating temperature scaled by 1000.

characteristics and, thus, can be considered rather critical. There are cases in all four quadrants of the figure, so no general correlation of the cases with fast self-heating and self-heating temperature can be found. The graph shows that the highly critical variations almost exclusively include high LEDC contents and a thin to medium thick SEI. The safe region on the other hand embodies almost exclusively all thick SEI variations with a big proportion of the inorganic cases. We can also observe that the thin SEI cases tend to have high temperature gradients probably due to the faster reformation at higher temperature. Higher LEDC content correlates with lower self-heating temperatures, as LEDC decomposition already occurs at low temperatures, whereas Li_2CO_3 decomposition is less strong at these temperatures. Variations of H_2O are scattered over the whole figure, which indicates that its influence is not as significant and straight-forward as the SEI properties even for high contaminations. This confirms the lower sensitivity to H_2O content than to SEI thickness and LEDC content.

The complex water effects warrant further analysis. For cells with thick inorganic SEI (large stars, Figure 5.8 a) the wet case (violet) has a lower self-heating temperature and a lower gradient compared to the dry and medium dry case. That means it enters the self-heating phase earlier but then heats up slower, i.e. one metric gets worse and the other better. In contrast, for the high LEDC contents (+) the higher water contamination value does not lead to lower self-heating temperature, and the temperature gradient shows the opposite behaviour to the inorganic case: it increases. The root causes lies in the onset of LiOH decomposition. Only in cases with high water contamination is the LiOH amount high enough to significantly impact the temperature progression, which we showed in Figure 5.7 a). The onset of this exothermic decomposition is around $>115\,°C$, which is higher than the self-heating temperature of all high LEDC cases. That means the LEDC cases are already in sustained self-heating when the LiOH decomposes; thus, water content does not impact the self-heating temperature for high LEDC content cases. Whereas, for all cases that have not transitioned to sustained self-heating before LiOH decomposes, the heat from LiOH decomposition impacts the self-heating temperature: the higher the water content and thus LiOH concentration, the more LiOH decomposition heat, thus the lower the self-heating temperature. The observed lower temperature gradient for the wet, inorganic and reference LEDC concentration cases is directly correlated with the lower temperature itself. The lower the temperature the slower all reactions progress, thus, the less heat is produced.

A low SEI thickness has been shown to accelerate the exothermic SEI reformation; thus, we analyse for the different cases how much the SEI is reduced, and how does this correlate to the temperature gradient (Figure 5.8 b) and the self-heating temperature (Figure 5.8 c). The high LEDC content cases (+) exhibit the highest decline in SEI thickness compared to the medium and inorganic cases. The low thicknesses for high LEDC contents in turn accelerate the reformation and, thus, contribute to higher temperature gradients. The high concentration of LEDC also leads to a low self-heating temperature. The pure inorganic cases, represented by stars, and most of the thin SEI cases, represented by small symbols, do not show any thickness reduction. Inorganic SEI cases do not show a decrease in SEI thickness because the decomposition of Li_2CO_3 is not substantial enough to compensate the SEI formation rates even for the thick SEI cases. Therefore, no decrease in SEI thickness can be observed. For the thin SEI cases, the thickness does not decrease substantially because the thin SEI accelerates SEI reformation, which counteracts SEI decomposition reactions. Most of the thin SEI and the inorganic SEI cases show a correlation of the temperature gradient, the self-heating temperature and the SEI thickness: the thinner the SEI the higher the temperature gradient and the lower the self-heating temperature. For the high LEDC content, thin SEI cases, the high amount of LEDC decomposes before substantial reformation starts. Thus, they show a slight SEI thickness reduction. Due to their anyway thin SEI thickness they also show the highest temperature gradient among all organic cases. Comparing the thin SEI cases with the medium thick SEI

cases it shows that the medium thick SEI cases exhibit lower temperature gradients and higher self-heating temperatures. This is explained by the accelerated reformation rates for the thin SEI cases. Whereas, the comparison of the medium thick SEI and thick SEI cases reveals that the thick SEI cases have a higher temperature gradient. This is explained by the higher self-heating temperature of the thick SEI cases. Since they transition at higher temperatures into self-heating phase, the reactions occur faster and more heat is produced.

From these extensive variations and their impact on thermal safety behaviour, it can be concluded that the SEI thickness and LEDC content are the dominating effects in terms of battery safety. A safer battery has an inorganic, thick SEI. Safety decreases with increasing LEDC content and reducing SEI thickness. Besides these two, H_2O impurities only play a role when severe contamination is present and generally contribute less than the SEI properties. The effect of water is also more challenging to address. High contamination does effect the self-heating temperature and the temperature gradient differently depending on the composition of the SEI.

5.3 Concluding remarks

This chapter has elucidated the impact of initial SEI state and water impurities on the thermal safety behaviour of Li-ion batteries with EC/EMC 1.2 M $LiPF_6$ and a graphite anode, including when and why self-heating occurs and the subsequent progression to the rapid thermal runaway. Initial concentrations of SEI components, impurities and conductive salt decomposition products were rigorously derived from assessing manufacturing, production and ageing effects.

Dominating detrimental effects are high LEDC concentrations and thin SEI, such as those found in rather fresh cells. Here, a high LEDC content could be connected to an earlier onset of self-heating. In contrast, a thinner SEI relates to faster SEI reformation and thus to a higher temperature gradient. The experimentally observed increase in self-heating temperature for aged cells [76, 79–81] is thus attributed to an ageing-induced change from foremost organic SEI to inorganic SEI and a thicker SEI, which delays exothermic SEI reformation processes. The impact of H_2O impurities on battery safety is found to be marginal as long as a moderate drying procedure is applied to the electrodes during manufacturing. Thus, it could be shown that extreme electrode drying does not benefit battery safety. However, high H_2O contaminations during production should be avoided as this will have a substantial negative impact. Here, the effect of high contamination was found to be depending on the SEI composition. For inorganic and mixed SEI, the contamination will reduce the self-heating temperature due to

decomposition of LiOH. High LEDC content cases, on the other hand, exhibit a higher temperature gradient, because here the self-heating already starts before LiOH decomposition sets in.

The here gained insights contribute significantly to understanding and controlling Li-ion battery behaviour during thermal abuse. The trends for impact of water as an electrolyte impurity, the complexities of SEI properties, and their combined battery safety have been shown, and that they cross influence each other. The presented degradation reactions and kinetics are suitable for integration into full cell models to evaluate the impact of local hotspots and heat removal, and thus to reveal battery runaway and propagation on cell and pack level. The studies may be further extended to include the effect of different active materials and electrolytes, as reactions, reactivity and mechanical stability may change. Different experimental behaviour was reported here, especially for the highly reactive Li metal, and solid state electrolytes. Also, of special importance is the interaction of the cathode with water impurities and of metal dissolution on the reaction network and the thermal safety behaviour.

Thus, the first set of questions raised at the end of the last chapter could be answered. The next chapter will delve into a detailed analysis of pressure evolution during the thermal abuse of Li-ion cells and how it is affected by different factors such as solvent composition, reactions and the conductive salt.

6 In-depth analysis of pressure evolution

After having assessed the general relationship between reactions and phase transitions in Chapter 4 and the impact of impurities and SEI properties in Chapter 5, this chapter will delve into a detailed exploration of the pressure dynamics resulting from thermal abuse in Li-ion batteries.

Despite the significant amount of published research in the field of Li-ion battery safety, the pressure increase is outside the focus of most published articles. Even though, pressure increase exceeding a specific value, can result in venting of the battery, ejecting toxic reaction gases, such as HF, and flammable solvent molecules, or in the worst case explosion of the battery [12]. Therefore, quantifying pressure evolution and how it is affected by battery components such as the active materials and the electrolyte is crucial to design mitigation strategies.

The following gives a brief literature review of existing studies about the impact of battery materials on pressure evolution. Golubkov et al. [234] measured the pressure during thermal runaway within the ARC testing chamber and utilised the ideal gas law to convert the pressure into the amount of ejected gases. In their study, 18650 cells with three different cathode active materials, namely $LiFePO_4$ (LFP), $LiNi_{0.45}Mn_{0.45}Co_{0.10}O_2$ (NMC-type) and a blend of $LiCoO_2$ (LCO) and $LiNi_{0.50}Mn_{0.25}Co_{0.25}O_2$ (NMC) have been investigated. They found that, with 265 mmol, the $LiCoO_2$/$LiNi_{0.50}Mn_{0.25}Co_{0.25}O_2$-blend released the highest amount of gases. The pure NMC-type batteries came second with 149 mmol, and the LFP produced the least amount of gases with 50 mmol. They also found that for the investigated batteries, the amount of gases, i.e. the pressure increase and the highest temperature reached during the ARC test are directly correlated. Subsequently, they studied the impact of the state of charge and overcharge on commercial 18650 LFP and Nickel Cobalt Aluminum (NCA) batteries [235]. For both battery types, the self-heating temperature decreases with an increasing state of charge, whereas the temperature maximum increases. The LFP-type batteries produced less gas and reached lower maximum temperatures than their NCA counterparts over the investigated charges. Interestingly, the observed correlation of produced gases and temperature maxima could only be reproduced for the NCA-type batteries, not the LFP ones. Lei et al. [73] used a similar technique to investigate Li-ion cells with $LiMnO_2$ active material and found that

the amount of released gas, and thus the pressure increase, is with 76.5 mmol substantially lower than the reported values for NMC and LCO/NMC blends from [234]. Jhu et al. [236] used a vent sizing package 2 calorimeter to study four commercially available LCO cells at different states of charge. In this type of measurement, the overpressure in the cell is compensated by the testing chamber so that the Li-ion battery remains intact. They also found that charged batteries are thermally more hazardous, with a pressure maximum of up to 5.5 times higher than that of an uncharged cell. They further reported significant differences in pressure increase between the various commercial cells, indicating that other components, apart from the active material, also play a major role in the pressure evolution during thermal abuse of Li-ion batteries. In a subsequent study, Jhu et al. [78] compared Li-ion batteries with LCO and NMC active materials. They found that LCO-type batteries are generally more reactive, leading to an earlier thermal runaway and a higher pressure.

Even though the reported pressure of the testing chamber gives some hindsight of the reactivity of active materials, no direct correlation to the internal pressure evolution before cell venting can be drawn. Therefore, some studies tried to implement a pressure sensor directly into the Li-ion cell [65, 73]. However, as summarised by Vendra et al. [77], such sensors are challenging to construct, and no two identical experiments are reported to yield comparable pressure curves.

It becomes evident that obtaining a pressure evolution from inside a Li-ion cell during thermal abuse is challenging. Thus, mathematical models are employed to aid in this matter. Coman et al. [65] used a combination of a representative gassing reaction and the vapour pressure curve of DMC as solvent to simulate the venting behaviour of a cylindrical 18650 cell. They could successfully reproduce the measured venting behaviour. Kim et al. [106] used a three-dimensional CFD simulation to investigate the venting behaviour of 18650 cells. They found that most gases measured in the vent gases are produced during the rapid heating phase of the thermal runaway. Vendra et al. [77] measured the pressure in the ARC testing chamber and used this reported pressure with an analytical equation to set initial conditions for their computational fluid dynamics simulation of fire dynamics.

The presented studies focused on the total pressure and gases produced or the venting behaviour of a Li-ion cell. Also, the cathode active material is the most studied subject. To the author's best knowledge, a systematic analysis of the impact of solvent components, atmospheric or degradation gases, and the conductive salt on the pressure evolution before cell venting has not been performed.

To close this gap, this chapter employs the SAFT-γ Mie EoS, introduced in Chapter 3.3.1, to perform a structured analysis of the electrolytes' effects on the pressure evolution in Li-ion batteries. A graphical overview of the study performed within this chapter is given in Figure 6.1. First, the necessary model parameters are estimated. Next, the study of pressure

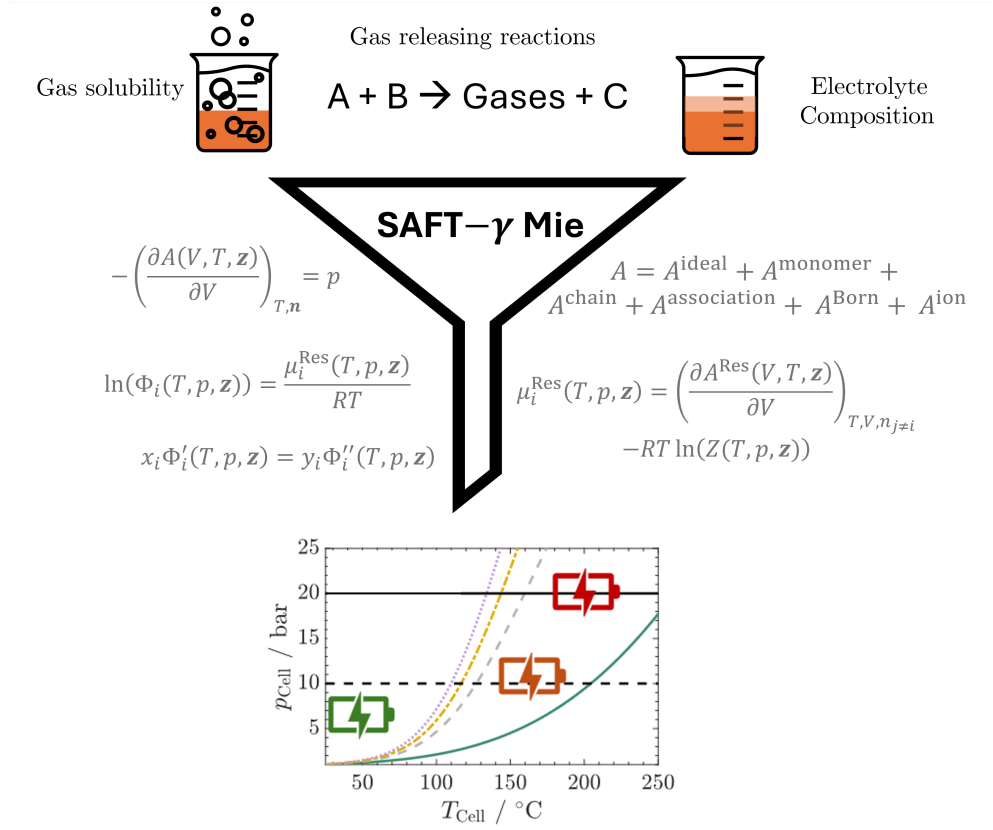

Figure 6.1: Graphical summary of the pressure evolution study performed in this chapter.

evolution within Li-ion batteries is addressed by investigating the influence of different solvent compositions in a specified temperature range. This part is followed by an in-depth analysis of the effects of saturation of the electrolyte with argon and CO_2. Further, the influence exerted by different concentrations of the conductive salt $LiPF_6$ on the pressure evolution is investigated. Eventually, a pseudo-reaction producing CO_2 is introduced, and its impact is examined. By understanding the impact of solvent, salt, and gases on pressure evolution, this endeavour offers a unique and comprehensive insight into the pressure evolution in Li-ion batteries before cell venting occurs. The insights and model will aid in exploring mitigation strategies.

6.1 Procedure

The following section summarises the methodology employed in this chapter. First, the modelled liquid electrolyte system is described, and the given species are divided into their respective SAFT groups. Subsequently, the parameter estimation procedure is described to identify unknown group interaction parameters from experimental data. The section closes by comparing the parameterised model against experimental data to evaluate the model's accuracy.

6.1.1 Modelled electrolyte system

As introduced in Chapter 2.1, liquid electrolyte systems for conventional Li-ion batteries consist of a mixture of linear and cyclic carbonates and a conductive salt, most commonly $LiPF_6$. Unfortunately, the range of mixtures used in academia and industry is vast. Even though all consist of almost identical base molecules, their exact composition varies widely and often seems to be arbitrarily chosen. As the pressure evolution in a closed system depends on the liquid phase, this poses some hurdles in setting up an appropriate model for estimating the pressure as a function of temperature, volume and global composition. Fortunately, the group contribution Helmholtz free energy EoS SAFT-γ Mie, introduced in Section 3.3.1, entails the capability to tackle this problem. Figure 6.2 summarises the modelled electrolyte species and presents the groups in which they are divided by differently coloured spheres.

The linear carbonates, namely DMC, EMC, DEC and dipropyl carbonate (DPC), all consist of the groups CH_3 and the newly introduced linear carbonate group OCOO. Additional CH_2 groups are added depending on the chain length. In the case of the cyclic carbonates, EC, PC and butylene carbonate (BC), all molecules include the $cyCH_2$ and the new cyclic carbonate group cyOCOO. For PC and BC, which also contain a side-chain, the groups cyCH, CH_2 and CH_3 need to be considered. Since $LiPF_6$ is the most commonly used conductive salt for state-of-the-art Li-ion batteries, it is also included in this study. The ions Li^+, $PF_6{}^-$ and the ion-pair $LiPF_6$ are analysed. In terms of gases, CO_2, one of the major degradation gases measured in thermal abuse of Li-ion batteries, and argon, the most frequently used inert gas in glove boxes of academia, are assessed.

The group interaction parameters marked with a blue colour (A) in Table 6.1 are taken from literature Haslam et al. [137] and Dufal et al. [237]. The interaction parameters marked with red (N) and grey (CR) have been developed in this study or are calculated based on combining rules, respectively. Even though they are not used as liquid battery electrolytes, DPC and BC were integrated into the parameter estimation and model comparison to investigate possible trends and enhance the parameters' generality and applicability.

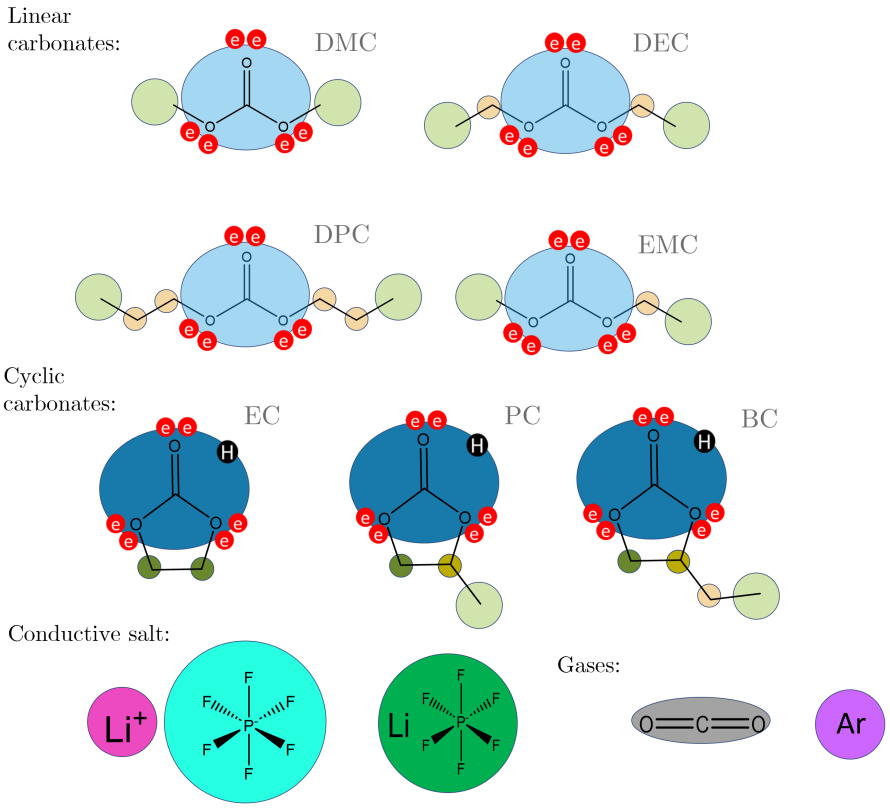

Figure 6.2: Molecular presentation of the modelled electrolyte species including separation in their SAFT-γ Mie groups (coloured circles). Shown are the linear carbonates, dimethyl carbonate (DMC), diethyl carbonate (DEC), dipropyl carbonate (DPC), ethyl methyl carbonate (EMC), the cyclic carbonates, ethylene carbonate (EC), propylene carbonate (PC), butylene carbonate (BC), the ions, Li^+ and $PF_6{}^-$ and the ion pair $LiPF_6$ as well as the gases argon and CO_2.

6.1.2 Parameter estimation

The following explains the parameter estimation of the group interactions highlighted in red in Table 6.1. This is the precondition to using the SAFT-γ Mie approach to calculate the vapour-liquid equilibrium for the electrolyte mixture. Subsequently, the necessary parameters within the SAFT-γ Mie approach are shortly discussed. This is followed by comparing the model with chosen suitable experiments to obtain these parameters. An exception to the standard group interactions, the modelling of $LiPF_6$'s influence necessitates expanding the existing model, which was introduced in Section 3.3.3.

Table 6.1: Matrix representation of the modelled SAFT-γ-Mie group interaction parameters. A blue (A) background corresponds to group interaction parameters available from previous works [137, 237], backgrounds shaded red (N) are developed in this work and grey (CR) backgrounds correspond to interaction parameters calculated with combining rules.

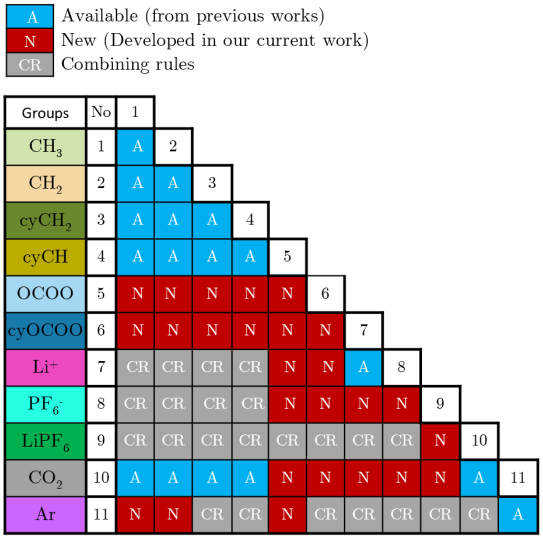

To recapitulate: The model parameters can be derived from the description of the SAFT-γ Mie model. They can be divided into a set that deals with the geometrical representation of the modelled groups and a set that contemplates the interaction potentials. The geometrical set includes S, the form factor, quantifying the group's sphericity, ν^*, the number of group segments and σ, the segment diameter. The interaction set consists of λ^r and λ^a as the attractive and repulsive exponents of the Mie potential. ε represents the interaction energy or the depth of the potential well. Moreover, the interaction set also encompasses n_H and n_e which represent the number of association sites, along with ε^HB and K, symbolising the association energy and bonding volume, respectively. The complete set of parameters employed for the simulation of the electrolyte system using the SAFT-γ Mie model is detailed in the Appendix in Tables D.1, D.2, and D.3. The parameters developed in this thesis by the subsequently described parameter estimation procedure are highlighted within these tables.

The liquid density [238–240], vapour pressure [241–246] and enthalpy of vaporisation [241, 245, 246] in pure compound data are suitable experimental values to extract good like and unlike interaction parameters for those groups and group interactions, where the parameters are not available. The like-interaction parameters of the linear and cyclic carbonate groups are

determined from the experiments, and the unlike-interaction parameters for the interactions of groups in the pure compounds. Binary mixture data such as vapour-liquid curves [247, 247] and mixture densities [248] are utilised to obtain further unknown unlike-interaction parameters. Interaction parameters for the gaseous and solvent groups are extracted from solubility data [249–251]. Additionally, mixture data including the conductive salt $LiPF_6$ [210, 252–254] is utilised to obtain like-interaction parameters for the ion-pair group, the $PF_6{}^-$ group as well as unlike-interaction parameters where experimental data was available.

Apart from the salt interactions, all other parameters have been obtained numerically. The estimation procedure uses the numerical solvers of the commercial software package gPROMS® [206]. The objective function employed is based on the maximum likelihood formulation:

$$\Phi = \frac{N_p}{2}\ln(2\pi) + \frac{1}{2}\min_{\mathbf{v}}\left[\sum_{u=1}^{N_E}\sum_{v=1}^{N_{V_u}}\sum_{w=1}^{N_{M_{uv}}}\left(\ln\left(\sigma_{uvw}^2\right) + \frac{(X_{uvw} - Y_{uvw}(\mathbf{v}))^2}{\sigma_{uvw}^2}\right)\right]. \tag{6.1}$$

Here, $\mathbf{v}$ denotes the parameters to be identified. X_{uvw} and Y_{uvw} are the experimental and calculated property values, respectively. N_P, N_E, N_{V_u} and $N_{M_{uv}}$ describe the total number of points, the number of performed experiments, the number of variables in experiment u and the number of measurements of variable v in experiment u, respectively. To reflect the uncertainty in experimental measurements, the constant relative variance is always included with $\sigma_{uvw} = 0.01X_{uvw}$ [255].

6.1.3 Model accuracy

This section compares the deviation between experimental data and data obtained from the SAFT-γ Mie model. The obtained percentage average absolute deviations (% AADs) of each property used for parameter estimation are briefly discussed for brevity. A more thorough analysis, including accompanying figures and tables, can be found in the Appendix D.

Pure-compound properties for all carbonate species, i.e. EC, PC, BC, DMC, EMC, DEC and DPC, are reproduced with an outstanding accuracy of an %AAD of 0.3% for liquid density, 7.36% for vapour pressure, and 0.8% for enthalpy of vaporisation. Outliers are the vapour pressures of DEC and DPC, with a deviation of around 15%. Given that the vapour pressures of these solvents have comparably low values, minor absolute errors result in high relative errors. Thus, the high numbers for %AAD are expected.

Binary mixture data in the form of vapour-liquid equilibrium data for EMC/DMC, EC/DMC and mixture liquid densities for EC/PC and EC/DMC could also be reproduced with an excellent overall %AAD of 1.38%. In the case of gas solubility (CO_2 and Ar) in single solvents and

solvent mixtures, the overall %AAD is 16.03%. Even though this appears to be a high deviation, the cause lies exclusively in the characteristics of how the %AAD is calculated. Using the solute as the denominator inherently leads to high relative deviations. The visual agreement between the data and model is still excellent, as can be seen in Appendix D Figure D.3.

The employed ion association model allows us to reproduce vapour pressure, liquid densities and CO_2 solubilities of a mixture of carbonates and $LiPF_6$ with an overall of %AAD 2.23%.

In summary, 26 interaction parameters are obtained from 623 experimental points with an %AAD 5.10%. Hence, a valid parameter set to study phase equilibria and the resulting pressure for given temperature, volume and electrolyte compositions in Li-ion batteries due to electrolyte heating has been successfully obtained.

6.1.4 Further assumptions and testing procedure

Before analysing the electrolyte system's thermodynamic behaviour during thermal abuse, the procedure to obtain a system close to actual Li-ion batteries is described. The following assumptions are made:

- The system is perfectly closed.
- The cell casing is rigid, as in prismatic and round cells.
- Active material, current collector and separator are assumed to be incompressible solids.
- They are further assumed not to undergo thermal expansion and be non-reactive.
- Vapour-liquid equilibrium is always assured.

A system volume, subsequently referred to as cell volume, of $V_{\text{cell}} = 1.55$ mL is considered. This corresponds to the electrolyte volume from the system used in the previous Chapters 4 and 5. Unlike in the earlier chapters, where the pore space in the electrodes and separator are assumed to be fully liquid, a gas phase is introduced. The exact liquid vol-% in batteries is uncertain. Thus, its effects will be analysed in a sensitivity study. Further, a pad gas that mimics the atmospheric conditions during cell assembly and storage is included. The procedure for reproducing the cell assembly and storage effect on the initial battery state is illustrated in Figure 6.3: It starts with calculating the amount of liquid electrolyte based on the desired liquid vol-%. This is followed by an initial calculation of the pad-gas amount from the cell and liquid volume difference. After that, an initial phase equilibrium calculation at constant temperature and pressure (Tp-flash) is performed for equilibration of the liquid and vapour phases at room temperature. This leads to the dissolution of the pad gas and will effectively reduce the

volume. The cell volume is then iteratively replenished with pad gas, performing a Tp-flash calculation in each step and applying the Euler-Tschebyschow procedure (see Appendix A.5) for numerical efficiency.

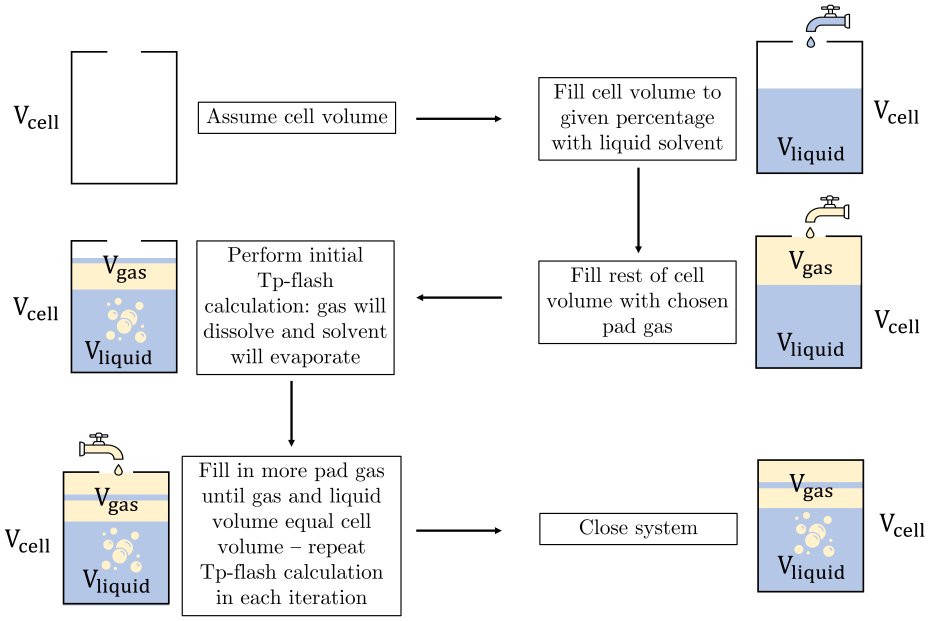

Figure 6.3: Sketch of modelling the cell's filling procedure and the final state of the cell.

Using this initial system state at room temperature as a starting condition, the cell is then exposed to heating. The pressure evolution is then calculated as a function of cell temperature and global composition by evaluating a phase equilibrium at a constant volume of 1.55 ml (TV-flash) across a temperature range of 25 °C to 250 °C. For 25 °C, the obtained pressure is close to the atmospheric pressure of 101.1 kPa.

6.1.4.1 Constant volume vs. constant pressure

In Chapter 4, we investigated the effect of evolving gases on the vapour-liquid equilibrium in Li-ion cells during thermal abuse. This resulted in gases increasing system pressure, which suppressed phase change of the liquid electrolyte. The herein developed SAFT-γ Mie model is utilised to study the difference between systems at constant volume vs. constant pressure to obtain a more thorough picture. The constant volume case refers to battery cells with a closed

rigid cell casing. The constant pressure case estimates open cells, and the vapour volume can expand infinitely. The systems are studied regarding phase change and the resulting endothermic heat of vaporisation. The latter is especially interesting as it would have a cooling effect during the self-heating of the battery.

It is important to note that, following exact thermodynamic definitions, both systems are closed, as only energy but no matter can be exchanged. In reality, an open battery cell would also be an open system by thermodynamic definition and exchange both energy and matter. Therefore, the presented calculations are a first estimate of how open systems would behave.

The following calculation will help to get a quantitative understanding of what effect the vaporisation heat might have on the self-heating of a Li-ion battery. Assuming a constant heating rate and employing the heat capacity of the cell, see Appendix Table B.1, the difference in heat of vaporisation and heat introduced into the system to obtain the desired temperature rise can be estimated as:

$$Q_{\mathrm{Vap}} = \sum_{\sigma}^{|\Omega_{\mathrm{Solv}}|} \frac{\Delta n_{\sigma}''}{\Delta T} \cdot \Delta \underline{H}_{\mathrm{Vap},\,\sigma}, \tag{6.2}$$

and

$$Q_{\mathrm{Heating}} = \Delta T C_{\mathrm{p,bat}}. \tag{6.3}$$

$\Delta n_{\sigma}''$ and ΔT are calculated as the differences of n_{σ}'' and T of two equilibrium calculations. The ratio of both heats $\frac{Q_{\mathrm{Vap}}}{Q_{\mathrm{Heating}}}$ is utilised as a characteristic to rate the potential cooling effects through the vaporisation of solvent species.

6.1.4.2 Reactive systems

In previous chapters, the central aspect was the impact of reactions on the safety aspects of Li-ion batteries during thermal abuse. The analysis of a complete reaction model, as employed in the previous chapters, is not yet possible due to missing interaction parameters of degradation gases. Therefore, a pseudo-reaction that converts the reactive cyclic carbonate EC to a pseudo-solid product, which does not affect the pressure, and CO_2 in a one-step reaction EC $\longrightarrow$ Solid + CO_2 will be considered as a starting point. As we know from previous chapters, the occurring reactions involving several evolving degradation gases are more complex. Therefore, this simplification should be seen as a first estimate of how reactions could impact the pressure in a Li-ion battery during thermal abuse. To achieve the desired change in molar amounts of EC

and CO_2, a Gaussian distribution function is utilised as a substitute model because it mimics a chemical reaction[1]. This way, the composition used as an input for the phase equilibrium calculations is altered over the temperature. The change in molar amounts of EC and CO_2 are calculated as follows:

$$n_{\mathrm{EC}}(T) = n_{\mathrm{EC},0} - \frac{\mathrm{d}n}{\mathrm{d}T} \text{ and} \tag{6.4}$$

$$n_{\mathrm{CO_2}}(T) = n_{\mathrm{CO_2},0} + \frac{\mathrm{d}n}{\mathrm{d}T}, \tag{6.5}$$

with

$$\frac{\mathrm{d}n}{\mathrm{d}T} = \left(\frac{A}{2}\right) \cdot \left(1 + \mathrm{erf}\left(\frac{\alpha \cdot (T-\mu)}{\sigma \cdot \sqrt{2}}\right)\right). \tag{6.6}$$

A represents the total quantity of EC converted to CO_2, α displays the skewness and is set as $\alpha = 1$ to obtain a symmetrical distribution. μ is the mean value of the distribution, which in this case refers to the temperature where the reaction rate exhibits its peak. It is set to 140 °C. This way, the reaction is simulated to occur in the early phases of self-heating. σ indicates the standard deviation of the distribution shaping the pseudo-reaction to be more or less narrow and has been set to 0.1μ.

6.2 Results and discussion

Now that the model is established and missing group interaction parameters have been obtained from experimental data, the relationship between temperature and pressure at equilibrium in Li-ion batteries will be studied. The first part will analyse non-reactive electrolyte systems, including the influence of the conductive salt $LiPF_6$. This is followed by investigating the effects of a pseudo-reaction involving the evolution of the known reactive gas CO_2.

[1] This approach of emulating chemical reactions via a Gaussian distribution, was also used by Feng et al. [256] as a substitute model that allows quick parameter estimation based on heat release curves from DSC measurements.

6.2.1 Non-reactive systems

First, different aspects of non-reactive electrolyte systems such as liquid-to-void volume ratio, solvent composition, gas solubilities, open and closed systems, as well as the influence of the conductive salt $LiPF_6$ are analysed.

6.2.1.1 Influence of liquid volume percentage

Given that the primary design goal for Li-ion batteries is to maximise gravimetric and volumetric energy density, one could anticipate that the gas phase within these batteries would be minimised to reduce overall cell volume and boost energy density. However, the studies from Kupper et al. [110] and Coman et al. [65] estimated the liquid volume percentage ($\frac{V_{\text{Liquid}}}{V_{\text{Void}}+V_{\text{Liquid}}}$) as 70 and 50 vol-% from imaging data. Thus, commercial Li-ion cells contain such a considerable safety buffer that there might still be space for optimisation. Therefore, the first part of this study investigates the effects of different volumetric gas/liquid ratios on the pressure evolution in Li-ion cells. In Figure 6.4 a), the dependence of pressure on cell temperature for a cell with a DMC/EC 50/50 v/v mixture with argon as pad gas at initial liquid vol-% of 98, 95, 90 and 85 (at 25 °C) is presented. If not stated otherwise, Ar is used as the pad gas, and the mixtures are always given in volume percentages. In this and all subsequent figures, dashed and solid black lines indicate safety measures typically included in commercial batteries. The first, typically activating at 10 bar (dashed black line) [257], is called a current-interruption device (CID). When activated, it disrupts the connection between the pole and the current collector, halting further current flow and, thus, effectively reducing electrochemical reactions. The second, typically activating around 20 bar (solid black line) [257], is a safety valve that opens to release gases so that the pressure is reduced to safe levels.

A cell that is optimised for volumetric energy density, with 98 vol-% of liquid phase (solid green line in Figure 6.4 a)), would activate the safety valve at just 87 °C, even without accounting for any side reactions. This phenomenon can be traced back to the expansion of the liquid volume. At lower temperatures, where $V_{\text{cell}} > V_{\text{liq}}$, the liquid volume expands into the gas phase. This only has negligible effects. At the point where $V_{\text{cell}} = V_{\text{liq}}$ (subsequently referred to as volume parity), all gas molecules have to be submerged in the liquid phase. For each further increase in temperature afterwards, the liquid tries to expand further but is hindered by the cell wall. Thus, it is compressed. Since liquids are known to be more or less incompressible, this results in the build-up of extreme pressures. The pressure massively increases from just under 2 bar to around 100 bar within a 5 °C change.

For the lower liquid vol-%, this effect shifts towards higher temperatures. This is explained by the additional gas volume into which the liquid phase can expand before reaching volume

parity. It becomes nearly negligible at 85 vol-% liquid volume, where volume parity is reached at 235 °C. These findings suggest that batteries should maintain a minimum free volume as a safety buffer to avoid explosion at temperatures below 100 °C, which could be reached, e.g. due to fast charging. However, compared to the 70 vol-% [110] and 50 vol-% [65] liquid volume obtained from imaging data, the here presented findings further suggest that the liquid volume percentage could be increased to 85 vol-% without risk of early venting below 200 °C, caused by the liquid phase alone. Later in this chapter, this study is revisited and extended to account for gases evolving from degradation reactions. However, to exclude this effect from further analysis, the initial liquid vol-% is set to 70 vol-% for all other cases. This translates to the void volume reported by Kupper et al. [110].

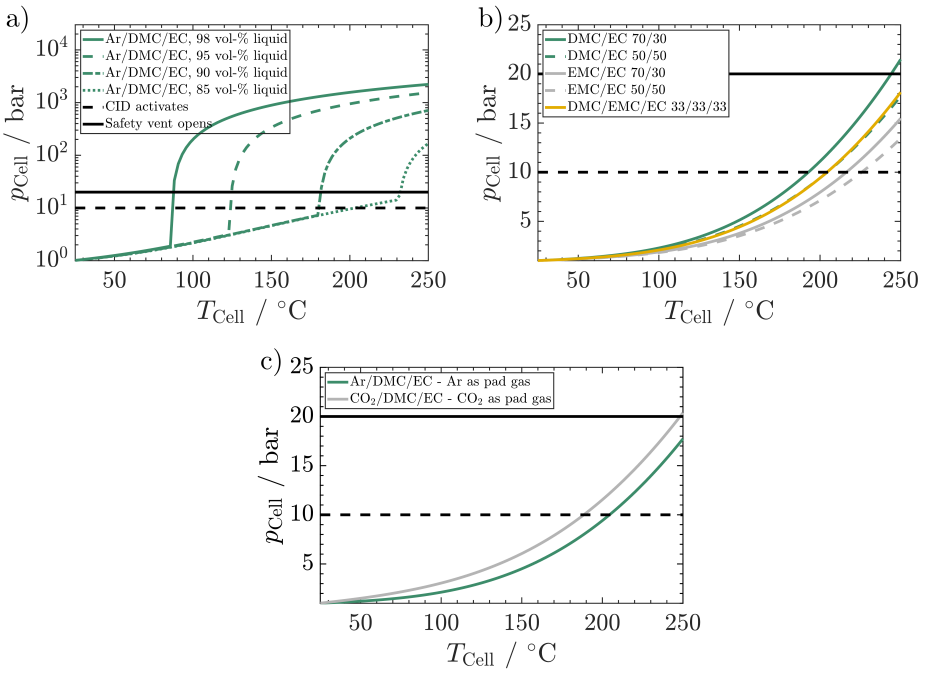

Figure 6.4: Pressure change for a cell heated to different T_{Cell} from room temperature depending on a) initial liquid volume percentage, b) global solvent composition, c) used pad gas. For the studies in b) and c), the initial liquid vol-% is set to 70 vol-%.

6.2.1.2 Influence of solvent composition

In Figure 6.4 b), a comparison between commonly applied liquid electrolyte solvent compositions is performed. The investigated cases include DMC/EC with 70/30 and 50/50 vol-% and EMC/EC governing the identical vol-% distributions. A ternary mixture of 33/33/33 DMC/EMC/EC is also investigated. The deviations between the different solvents in pressure are not significant at temperatures below 50 °C. Then, the curves start to deviate: the 70/30 DMC/EC mixture (solid green line) has the most significant pressure increase and the 50/50 EMC/EC mixture (dashed grey line) the least. The other compositions lie in between both. The 70/30 DMC/EC mixture reaches the activation pressure of CID, 10 bar, at 190 °C compared to the high boiling EMC/EC 50/50 mixture at 225 °C. The low boiling 70/30 DMC/EC mixture is the only one that reaches the safety valve opening pressure of 20 bar within the investigated temperature range, precisely at 240 °C. DMC/EC mixtures containing more EC, e.g. DMC/EC 50/50, show a lower pressure over the whole temperature range. The 33/33/33 DMC/EMC/EC mixture shows an almost identical pressure evolution as the DMC/EC 50/50 mixture.

This behaviour can be explained by the different boiling points of DMC (108 °C), EMC (115 °C), and EC (240 °C), values calculated using the developed SAFT-γ Mie model. The mixtures, including the lower boiling DMC, have a higher pressure increase since the number of molecules in the gas phase increases more rapidly than in the higher boiling EMC-containing mixtures. The same logic applies to mixtures containing more EC: the higher boiling point compared to the linear carbonates leads to fewer molecules in the gas phase at lower temperatures, thus a smaller pressure. For the investigated solvent compositions, the solvent choice can make a difference of up to 50% in pressure evolution. The deviations between the pressure evolutions of all cases are shown in Appendix D Figure D.5.

From this analysis, it is advisable to minimise linear carbonates in the electrolyte mixture. As is covered shortly, this is not generally true when considering gassing degradation reactions. However, higher boiling alternatives like EMC over DMC are always advisable when battery performance and costs permit it.

6.2.1.3 Influence of pad gas

In the next step a comparison between two different pad gases CO_2 and Ar, is performed using a DMC/EC 50/50 mixture. Ar is chosen as a pad gas because it is a common gas used to obtain an inert atmosphere for cell assembly in academia. CO_2 is chosen because it is reported, among CO and H_2, for having the highest concentrations after a thermal runaway [234, 258, 259]. Ar further has a 96% lower solubility in the given mixture (calculated using the established SAFT-γ Mie model at 25 °C and 101.1 bar) than CO_2. The comparison, thus,

provides a good impression of how using different inert gases with differing solubilities during assembly and storage impacts the safety behaviour of Li-ion cells.

The mixture containing CO_2 as pad gas, Figure 6.4 c), has up to 20% higher pressure compared to Ar, shown as a solid green line. This might seem surprising as CO_2 has a higher solubility, which should lead to fewer molecules in the gas phase and, thus, lower pressure. The culprit, however, lies in the storage or assembly conditions mimicked using the above-described filling procedure. In these procedures, gas is added to the mixture until the cell volume is reached. That means that a gas with a higher solubility results in more gas molecules in the mixture. When the mixture is heated up, the CO_2 solubility will decline, and, thus, the number of molecules in the gas phase increases more rapidly compared to argon since more molecules are present.

Two optimal properties for pad or inert gases can be derived from this behaviour. First, it should have a low solubility in the used solvent mixture to reduce the number of molecules in the system. Second, it should have endothermic dissolution enthalpy such that the solubility of the gas rises with increasing temperature. As a matter of fact, argon does exhibit both properties. However, as it is a noble gas that must be produced significantly, it might not be economically feasible as an inert gas during solvent storage or cell assembly, especially on an industrial scale. Nitrogen is even 38 % less soluble in linear carbonates [260] than argon, at room temperature. Therefore, it is more likely to be used on an industrial scale, as e.g. shown by [261].

6.2.1.4 Constant volume vs. constant pressure

The following section will contemplate the difference between constant volume and constant pressure electrolyte systems in terms of changes in the vapour phase amount and the resulting vaporisation heat. In the previous Chapter 4, the results suggested that due to evolving gases and, thus, increased pressure in a closed battery cell, the solvent boiling is suppressed until the thermal runaway is reached. This section will utilise the advanced phase equilibrium model and give a more specific answer to this question.

A mixture of Ar/DMC/EC with a liquid phase composition of DMC/EC v/v 70/30 is investigated under constant volume, i.e. resembling a closed battery cell, vs. constant pressure, estimating the behaviour of an open battery cell. Figure 6.5 a) shows the fraction of all molecules in the gas phase with respect to the total number of molecules over the temperature in both systems.

The constant volume system, represented by the solid green line, shows almost no phase change. The vapour phase fraction does not exceed 1%. It can be concluded that virtually

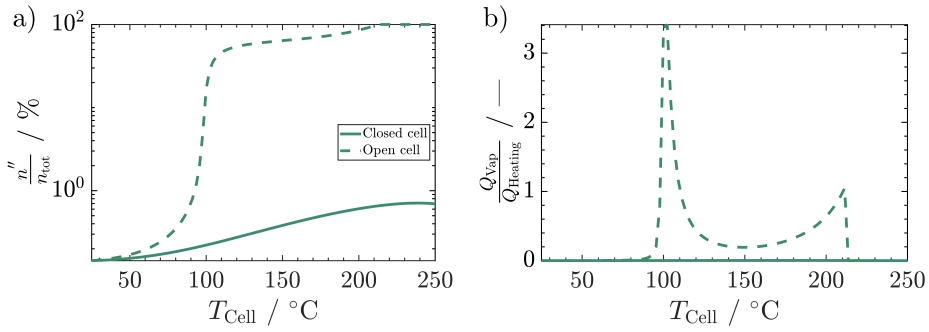

Figure 6.5: Difference between closed vs. open electrolyte systems in a cell with an Ar/DMC/EC mixture with 70/30 v/v of DMC and EC in a) vapour phase fraction and b) heat of vaporisation. For both cases, the initial liquid vol-% is set to 70 vol-%.

no solvent boiling occurs in the investigated temperature range for a closed battery cell. It also follows that the energy of vaporisation in a closed cell will be almost negligible. Figure 6.5 b) shows the heat ratio of the energy of vaporisation and energy introduced into the system to obtain a desired temperature, see Section 6.1.4. The ratio is close to 0 for the closed cell over the whole temperature range. Therefore, no cooling effect due to solvent boiling during the self-heating of a Li-ion battery can be expected for closed cells. In contrast to the results from Chapter 4, the current analysis proves that no degradation reactions are needed to suppress solvent boiling as none are considered in the presented study.

In contrast, the open cells, represented by the dashed green line, shows a first steep increase from 80–100 °C and a second smaller steep increase from 150–200 °C before reaching 100% vapour fraction at around 210 °C. These slopes are correlated to the boiling temperatures of the linear carbonate around 100 °C and cyclic carbonate around 200 °C, respectively. Therefore, in open cells, solvent boiling occurs as soon as the boiling point of the lower boiling linear carbonate is approached and continues until all solvents have changed phases. The ratio between the energy of vaporisation and energy needed to heat the system with a constant temperature gradient sharply increases around 90 °C. It reaches a maximum of 3.2 at 100 °C, see Figure 6.5. It then decreases to reach a local minimum of 0.2 at 150 °C before rising again to reach a ratio of 1 at temperature 210 °C. The ratio drops to 0 directly after this since a 100% vapour phase fraction is reached, and no further boiling can occur. It follows that solvent boiling would severely influence the temperature progression in an open cell. Especially since the ratio first peaks around 100–120 °C, where this cooling effect is opposed with a relatively small amount of produced heat from exothermic reactions, see Chapter 5.

6.2.1.5 Impact of conductive salt

The following section investigates the influence of the conductive salt $LiPF_6$ on the pressure at vapour-liquid equilibrium. The chosen solvent system is a DMC/EC v/v 50/50 mixture with CO_2 as pad gas. In this case, CO_2 is used as a pad gas instead of argon since, due to numerical problems, the systems could not be solved using argon.

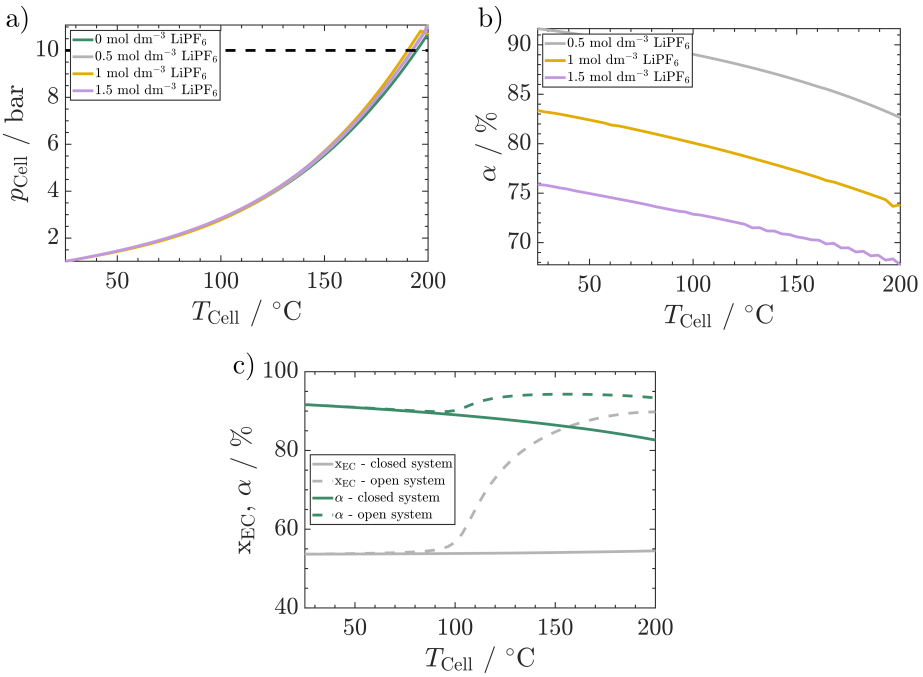

Figure 6.6: Influence of $LiPF_6$ on the pressure in the investigated temperature range and studied system of DMC/EC v/v 50/50 mixture with CO_2 as pad gas and 70 vol% initial liquid volume. a) a variation in $LiPF_6$ concentrations b) the effect on the dissociation degree and c) the difference between an open and closed system on the liquid molar fraction of EC and dissociation degree of $LiPF_6$.

In Figure 6.6 a), the pressure over the studied temperature range of the system with salt concentration ranging from 0 to 1.5 mol dm^{-3} is shown. The overall effect is relatively small, with a maximum relative deviation of 4% to the 0 mol dm^{-3} case compared to the 1 mol dm^{-3} case. The influence of $LiPF_6$ as the conductive salt is, thus, much smaller than different solvent compositions, showing deviations up to 50%, or pad gases, up to 20%. However, minor differences

between the studied cases exist. The pressure increases less strongly for the low and high salt concentrations 0.5 and 1.5 mol dm^{-3} compared to the 1 mol dm^{-3} case.

The reason for the even small increase in pressure due to introducing salt into the system warrants further exploration. Since both the influence of the salt on the present gases and the solvent could lead to this increase, both contributions are analysed separately.

The solubility of CO_2 decreases with increasing salt concentration, which is also known as the salting-out effect, see Appendix D Figure D.4. This would in theory explain the observed pressure increase for higher salt concentrations, see Figure 6.6 a), since more CO_2 in the gas phase leads to a higher pressure increase. However, this phenomenon already occurs during electrolyte mixing and cell assembly. Thus, less CO_2 will be in the system at the start compared to the no-salt case. As we know from previous discussions, fewer gas molecules lead to lower pressure increases. Therefore, this cannot be the reason for the increased pressure when introducing salt.

Considering the impact of the salt on the solvent, literature values of a DMC/$LiPF_6$ mixture, also used in our parameter estimation procedure (see Appendix D Figure D.4), show that introducing $LiPF_6$ into pure DMC increases its vapour pressure [252]. Even though this explains the observed pressure increase, it contradicts the generally recognised norm that introducing salt into a liquid mixture will result in an elevated boiling temperature. The higher boiling point for salt-containing mixtures is attributed to solvent molecules forming a solvation shell around the ions. They interact more strongly with the ions than with each other. Therefore, more energy must be introduced to break these interactions and transfer the solvent molecules in the gas phase. Thus, adding salts should decrease the pressure. However, if this would be true, the pressure should be lower for the investigated salt-containing mixtures. The influence of the conductive salt on the pressure increase in standard battery electrolyte systems appears to be a complex matter that needs more research.

Another intriguing effect that can be investigated with the employed model is the salt's dissociation degree during a thermal event. Figure 6.6 b) shows that the dissociation degree of the salt decreases with increased temperature and salt concentration. Both effects are similar, with around 10% change between concentrations or over the whole temperature range. This can be explained by the fact that apart from the salt concentration, the dissociation degree is mainly influenced by the dielectric constant of the solvent. As shown in Figure, A.4 does the Dielectric constant of high dielectric solvent such as EC decrease rapidly with increasing temperature. This explains the observed lower degree of dissociation. It should be noted that in a real battery environment, the conductive salt would start to degrade around 80 °C, see chapters 4 and 5. Therefore, the salt concentration would change at higher temperatures.

In the previous example, a closed battery, i.e. constant volume, is evaluated, and no phase change would occur. Solvents will change phases in open cells, i.e. under constant pressure. This will additionally impact the degree of dissociation as the phase change alters the solvent composition. The low-boiling linear carbonates, like DMC, will evaporate in open cells first. Hence, the composition will change to contain more cyclic carbonates with a higher dielectric constant. This effect is shown in Figure 6.6 c), where the molar fraction of EC in the liquid phase and dissociation degree are compared for an open and closed cell. Here, EC's liquid molar fraction increases steeply around 100 from 54% to 90% at 200. The mixture's increased dielectric constant leads to a 12% higher degree of dissociation. It is assumed that impurities such as H_2O react more readily with ion pairs than ions [147]. Therefore, the increased degree of dissociation will reduce the occurring degradation reactions of the conductive salt. It follows that even though open cells such as *in-operando* gas analysis allow for unprecedented insight into occurring reactions, the deviation from a real battery environment must be considered.

It should noted that the current model still shows an artefact. A kink in the graph of the 1 mol dm^{-3}, see solid yellow line, can be observed around 190 °C. This kink relates to a phase separation where two liquid phases are formed. One liquid phase mainly consists of the ions and the high dielectric ion pair. In contrast, the second phase mostly constitutes the solvents and CO_2. For the 1.5 mol dm^{-3} case, this phase separation is already present at the initial temperature of 25 °C. As this phase behaviour has, to my knowledge, never been observed in a laboratory, it appears to be an artefact of the model. Therefore, refining the model for future studies is advised.

6.2.1.6 Influence of electrolyte additives

State-of-the-art electrolyte formulations for Li-ion batteries contain several functional additives [220]. Thus, we will briefly discuss how they might influence the phase equilibria. Given the low concentrations in which additives are added to the electrolyte formulations, typically below 6 wt-% [262], their effect on the phase equilibrium can be expected to be relatively low. Film-forming additives, such as VC and FEC, should also not be present significantly after the formation cycles. Overcharge and flame-retardent additives are more challenging to assess as they are more different from the rest of the electrolyte formulation and should not react during a battery's regular operation. However, as they also should be added in relatively low concentrations, their impact should be negligible.

We can look at the boiling points of the respective pure compounds for a quick assessment of how any additive might impact the phase equilibrium. Boiling points higher than the low-boiling linear carbonates, i.e. above 108 °C for DMC or 115 °C for EMC, will potentially lower the pressure of the mixture. The film forming additives VC, $T_{b,VC} = 162$ °C [263],

FEC, $T_{b,FEC} = 212\,°C$ [264], the flame retardent additive dimethyl phosphate, $T_{b,DMP} = 171\,°C$ [265], all have higher boiling points. Thus, they should decrease the pressure. However, as will be shown in the next section, the solubility of degradation gases such as CO_2 is even more important for the system pressure. No solubility data for these substances is reported. Therefore, it can not be answered with certainty how they might influence the phase equilibria.

In summary, a quick assessment of the boiling points of common additives showed that they could, in theory, even lower the pressure of Li-ion batteries during a thermal event. Yet, as no solubility data is reported, this cannot be said with certainty. However, due to the low amount of commonly added electrolyte additives, they should not have substantial effects on the phase equilibria and, thus, the pressure.

6.2.2 Reactive systems

The following section will deal with the effect of gases stemming from degradation reactions on the pressure evolution during a thermal event of a Li-ion battery. The exemplary gas used is CO_2. Alongside H_2 and CO, CO_2 is the most measured degradation gas produced in a thermal event of a Li-ion battery [234, 258, 259]. From the previous chapters, we know that CO_2 producing reactions occur in the examined temperature range up to 250 °C. The CO_2 gas is supposed to be released in a Gaussian curve shape, i.e. with an increase and then decrease with temperature (see Section 6.1.4). The total amount of released CO_2 is chosen to reflect 10, 15 and 20 mol% of EC in the mixture, respectively. According to Chapter 5, these represent anodes with thick SEI (10 mol% EC reacted) up to thin SEI (20 mol% EC reacted). Please note that this analysis should only be considered as an initial impression. To get a holistic insight into the complex interdependency of gassing reactions, phase equilibria and, thus, pressure evolution, a comprehensive analysis including real reactions and a wider variety of evolving gases with their respective solubilities needs to be considered.

In Figure 6.7 a), the results for CO_2-releasing reactions with the three different CO_2 amounts are shown for a closed cell with a DMC/EC 50/50 mixture using argon as pad gas. They are compared to the system without a reaction. The evolving gas from degradation reactions tremendously amplifies the pressure evolution. The maximum deviation compared to the case with no reaction is 200% for the low intense reaction (dashed green line) and further increases to 500% in the severe reaction case (dotted green line). For all released CO_2 amounts, the cell reaches the CID activation in the range from 105 °C to 125 °C. Also, the safety valve will open in all cases in the temperature range from 142 °C to 175 °C. This is in the reported temperature range of venting in ARC experiments [73, 266].

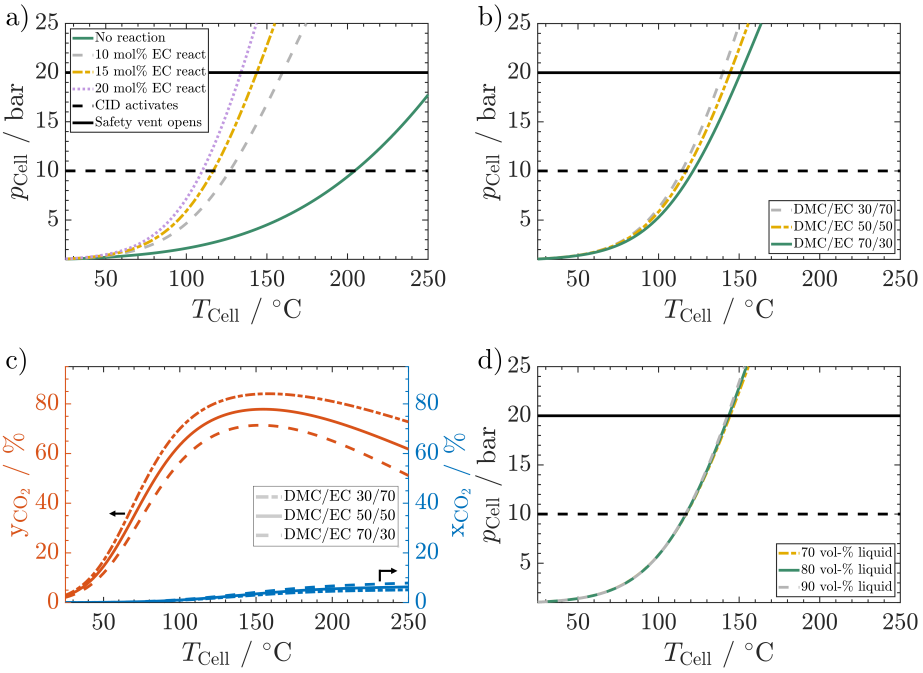

Figure 6.7: Influence of a CO_2 releasing reaction on pressure increase due to cell heating with: a) a variation in reacting EC in mol-% for a DMC/EC 50/50 mixture using argon as pad gas, b) the influence of solvent compositions with composition independent reactions (15-mol% of EC of the 50/50 v/v DMC/EC case) and c) CO_2 composition in gas and liquid phase for variations shown in b). The initial liquid vol-% is set to 70 vol-% for all cases in a)-c). d) shows the influence of a composition independent reactions (15-mol% of EC of the 50/50 v/v DMC/EC case) in a DMC/EC 50/50 v/v mixture with varying levels of liquid volume fraction.

Figure 6.7 b) analyses the impact of different solvent compositions in combination with a gas-releasing reaction. To do so, the amount of EC reacting to CO_2 will be fixed to 15 mol-% of EC in a DMC/EC 50/50 mixture. Then, three compositions, namely a DMC/EC 50/50 and DMC/EC 70/30 and DMC/EC 30/70, are studied. This analysis aims to gain a qualitative understanding of the impacts of different compositions on pressure evolution based on the change in gas solubility.

The highest pressure can be observed for the 30/70 DMC/EC mixture (dashed grey line). It reaches the safety valve pressure at 140 °C. The DMC/EC 50/50 mixture (dash-dotted yellow line) shows a slightly lower pressure evolution, with a maximum deviation to the DMC/EC 30/70 case of up to 10%. The lowest pressure in the investigated temperature range can be observed for the DMC/EC 70/30 mixture. Interestingly, higher amounts of low boiling linear

carbonate DMC do not lead to a higher pressure. This contrasts our findings for non-reactive systems, where increasing amounts of low-boiling linear carbonates led to increased pressure, see Section 6.2.1.2.

In Figure 6.7 c), the corresponding CO_2 fractions in the vapour phase and liquid phase are shown. The vapour phase fraction of CO_2 shows a steep increase around 50 °C for all cases. It peaks between 140 °C and 150 °C dependent on the studied case and then declines again. The first steep increase corresponds to the start of the modelled pseudo-reaction. The later decline can be explained by a reduction in CO_2 production and an increased amount of the solvent components in the gas phase. Generally, the CO_2 vapour phase fraction aligns with the pressure increase, showing the highest value for DMC/EC 30/70, followed by DMC/EC 50/50 and the lowest for DMC/EC 70/30.

The liquid phase, on the other hand, does not follow this pattern. The highest liquid phase fraction for CO_2 can be observed for DMC/EC 70/30, followed by the DMC/EC 50/50 reference and eventually the DMC/EC 30/70. The reason is the higher solubility of CO_2 in DMC over EC. The more linear carbonates are present in the mixture, the more CO_2 can dissolve in the liquid phase, thus mitigating the pressure increase. This indicates that the amount of reaction gases and their solubility in the solvent mixture define the pressure progression during a thermal event in Li-ion batteries.

Consequently, considering gas-releasing reactions prompts a comprehensive re-evaluation of our previous understanding; the safety of cyclic carbonates and the perceived risk of linear carbonates are reversed. From these findings, a general rule can be deduced: if gas-releasing reactions cannot be avoided, the solvents should be chosen or designed so that the evolving gases have high solubility in them. In this case, CO_2 is considered as a degradation gas with higher solubility in linear carbonates than cyclic carbonates. Therefore, from a safety perspective, linear carbonates are more favourable. However, this might change if gases with higher solubility in cyclic carbonates are added to this analysis.

Typical measured degradation gases, together with CO_2 making up above 90%, are H_2, CO, C_2H_4 [234, 258, 259]. For all mentioned gases the solubility is higher in linear than in cyclic carbonates [251, 267–270]. gases like PF_5 and POF_3, as degradation gases from $LiPF_6$ decomposition, are also measured to evolve in the early stages of a thermal event, alongside the above-mentioned ones [85, 88]. As for them, no solubility data is available. Their influence on the pressure increase during a thermal event can not be addressed in the presented work. However, since most gases from degradation reactions are proven to be more soluble in linear carbonates and due to the higher reactivity of cyclic carbonates with the negative electrode [271], it is doubtful that a higher concentration of cyclic carbonates will lead to lower pressures and, therefore, safer batteries.

Ultimately, we re-evaluate the liquid-to-void volume percentage and how a gas-releasing reaction impacts it. In Figure 6.7 d), a variation in liquid vol-% of 70 vol-%, 80 vol-% and 90 vol-% is shown for a 50/50 DMC/EC v/v mixture. A composition-independent reaction, based on 15 % of EC in a 50/50 DMC/EC v/v mixture with 70 vol-% liquid volume, is assumed. Compared to previous cases, the latter assumption has to be added since an increased liquid volume also raises the molar amount of EC. All cases follow a similar pressure increase over the shown temperature and pressure range. Until 100 °C, the curves are almost identical, showing a maximum deviation of below 2%, see Appendix Figure D.5. At this point, all cases reached the CID activation pressure of 10 bar. Above 100 °C, the cases with a higher vol-% show a slightly higher pressure than the 70 vol-% reference. However, the deviation is below 5% even for the 90 vol-% case. Due to the minimal differences in pressure increase, all cases reach the venting pressure of 20 bar in a temperature window of 142.5 °C–144.3 °C. This additional analysis reinforces our prior conclusions regarding the liquid-to-void volume ratio. It demonstrates that the ratio can be safely raised from the previously reported figures of 50 vol-% [65] and 70 vol-% [110], to at least 85 vol-% without significantly increasing safety risks, such as venting of the battery at lower temperatures.

6.3 Concluding remarks

Pressure evolution in Li-ion batteries is an essential factor when assessing battery safety. The wide variety of solvent compositions prevented an in-depth analysis of the former until now. The work presented in this chapter introduced an approach based on the group contribution SAFT-γ Mie framework. This allowed to investigate the influence of varying solvent compositions, gas solubilities, the conductive salt $LiPF_6$ and CO_2 releasing reactions on pressure at phase equilibrium.

This study revealed that a battery perfectly optimised for volumetric energy density with none or low gas volume left would have severe safety issues. The expanding liquid phase will lead to a dramatic pressure rise already below 100 °C. However, in commercially available cells, there is still room for optimisation. The presently employed liquid volume percentage of 70 to 50 vol-% could be increased to at least 85 vol-% without elevated safety risk below 200 °C. This could also be shown for systems considering gassing reactions.

Further, it was found that choosing the low-boiling linear carbonate, such as DMC and EMC, is crucial for non-reactive systems. It was found that selecting the higher-boiling EMC over the lower-boiling DMC can decrease the pressure by 20%. When considering different pad gases, a gas with high solubility increases pressure since more of the gas will be enclosed in the battery system. From this observation, the general rule could be derived that an optimal pad

gas should have a low solubility in the used solvent mixture and further increase its solubility with increasing temperature. Argon or other noble gases are good examples exhibiting both characteristics. However, as they must be produced with significant effort, nitrogen, which is even less soluble than argon, is an equally good alternative already used on an industrial scale.

A comparison of open and closed battery cells showed that almost no solvent boiling would occur in a closed cell. This supports the findings of Chapter 4 and extends to cells without gas-releasing reaction.

To achieve a holistic analysis of the system, the influence of the conductive salt on the system pressure was also investigated. The findings revealed that there was only a slight 4% deviation compared to the solvent system without added salt, indicating that it is not a significant factor. Analysing the difference between open and closed cells, including the conductive salt, revealed that the salt's dissociation degree can be up to 12% higher in open cells. Thus, it will change how the system reacts and should be considered when open cells, such as in online electrochemical mass spectrometry, are used to estimate reaction parameters.

Finally, the effects of reactions on pressure progression were explored. It was found that even mild reactions can trigger the safety valve opening in the analysed temperature range from 25 to 250 °C. When investigating the influence of solvent composition in combination with gassing reactions, results show that the higher solubility of CO_2 in linear carbonates has a higher impact on pressure evolution than their low boiling point. Thus, the general rule extends as follows: the solvent system should always be chosen such that the solubility of possible gases stemming from degradation reactions should be as high as possible. Comparing the solubilities of other common degradation gases in linear and cyclic carbonates showed that all gases with available solubility data are more soluble in linear carbonates than in cyclic carbonates. Therefore, from the current state of knowledge, it is advisable to maximize linear carbonates in the electrolyte mixture in order to mitigate pressure evolution during a thermal event in Li-ion batteries.

7 Summary and Outlook

With an ever-growing number of EVs and the co-currently deployed Li-ion batteries, the latter's safety gets increasingly important. Thermal runaway in Li-ion batteries and the preceding self-heating phase induced by thermal events pose the most crucial safety risk. The intricate interplay of mechanical strain, internal or external short circuits, and thermal degradation reactions drive catastrophic events. Aside from excessive experimental analysis ranging from material to pack level, simulations based on mathematical modelling have proven significant help. Most employed models use a semi-empirical approach when considering occurring reactions and their released heats. Even though this simplification allowed to include more phenomena, a correlation between occurring reactions and their respective components is impossible. This effectively reduces the obtainable insights and also possible mitigation strategies. To aid in the quest for a better understanding of the underlying processes during thermal abuse in Li-ion batteries, a component-based modelling approach to assess the interplay between reactions and phase transitions has been developed within this thesis.

In Chapter 4, the developed model constituting 10 reactions, 17 chemical species and the phase transition of the solvent was first employed. It was the first component-based model that was able to simulate a full ARC measurement successfully. Further analysis of the simulation results showed that an intricate equilibrium between endo- and exothermic processes exists at the beginning of the crucial first self-heating phase. Based on these findings, occurring reactions could be partitioned into two groups. The first group embodies reactions whose reactants are only present in small amounts. Prominent members of this group are reactions involving the SEI component LEDC and the contaminant H_2O. Due to the variance in their initial quantity, for example, caused by fluctuations during production and formation, these reactants are among the causes that make the thermal runaway unpredictable. The second group contains the formation of SEI after its primary decay and repeated decomposition. From the comparably high amount of the involved reactants, it follows that only active cooling will prevent thermal runaway once higher temperatures activate these reactions. Eventually, it was shown that the evolving gases stemming from degradation reactions would increase the cell pressure and suppress solvent boiling until the cell opens or the thermal runaway is reached.

Based on the findings from the previous chapter, the following Chapter 5 dealt with the sensitivity of temperature progression during thermal abuse on impurities such as H_2O and SEI

properties. The modelling approach was extended to 12 reactions and 20 chemical species. Also, equilibrium reactions of the conductive salt decomposition and follow-up reactions were implemented. With this, an extensive analysis of the impact of the initial conditions for H_2O impurities and SEI compositions has been performed. The results showed that a safe battery would feature a thick, inorganic SEI and a low H_2O content. This aligns perfectly with literature results showing an increased self-heating temperature for cells aged 35–45 °C. These ageing conditions are assumed to produce a thick inorganic SEI, also identified in the present study as beneficial for battery safety. In the case of H_2O contamination, a negative effect on battery safety could only be observed at very high contamination degrees. From this, it can be deduced that an extensive drying procedure will bring no benefit to Li-ion battery safety while having a negative impact on the performance due to the harsh conditions the electrodes are subjected to during this procedure.

The last Chapter 6 presented an in-depth analysis of pressure progression during a thermal event. Here, the influence of solvent compositions, gassing reactions and the conductive salt were investigated utilising the SAFT-γ Mie EoS. The model was extended to account for ion association, a phenomenon readily observed in Li-ion electrolyte mixtures. Results showed that compared to commercially available cells, the liquid volume percentage could be increased from 50–70 vol-% to 85 vol-% without any additional safety risk. Also, the following general rules could be derived for employed pad gases and solvent compositions: First, the pad gas should optimally be chosen to have a low solubility in the given solvent mixture and increase the solubility with increasing temperature. Argon and nitrogen are good examples as both embody a low solubility and even meet both qualities in the case of argon. Further, the solvent mixture should be chosen to maximise the solubility of any degradation gases. The mixture's boiling point only plays a secondary role as soon as gassing reactions are considered. Further, it could be shown that the conductive salt only has a minor effect on the pressure progression with a 4% deviation from the no-salt cases. Eventually, the results from Chapter 4 relating to the suppression of solvent boiling could be proven and even extended. This advanced analysis showed that no solvent boiling will occur in closed cells, even without any gassing reaction. Open cells, on the other hand, showed a substantial change in liquid composition, leading to an up to 12% higher dissociation degree of $LiPF_6$. Thus, these effects must be considered when using, e.g. online electrochemical mass spectrometry systems to obtain kinetic parameters.

This thesis is the starting point for a component-focused analysis of the thermal abuse of Li-ion batteries. As such, it provides unprecedented insights into underlying phenomena. Thus, these promising results allow for further development. Based on this, future work should extend the considered reaction network. The increased number of reactions and species will exacerbate the difficulty of obtaining proper kinetic parameters and physical properties. Thus, ab

initio methods, such as classical MD and QM-DFT, should aid this development. This approach has already been used to reveal possible reaction pathways and obtain reaction energies for SEI formation [228, 229]. Another promising approach to acquire the needed parameters is the development of physics-informed neural networks in chemical engineering, which already showed promising results in predicting thermodynamic consistent activity coefficients [272, 273]. Further, more experiments should be utilised to increase the models' accuracy and, thus, its predictive power. Continuous gas analysis using an online electrochemical mass spectrometer would suit the task. The open character of such systems should, however, be carefully evaluated. Another exciting way forward would be directly combining the SAFT-γ Mie EoS with the whole reaction model to better understand the impact and interplay of gas solubilities and pressure build-up in a closed battery cell. The implemented ion dissociation will play a significant role, as the conductive salt's degradation reactions directly depend on the degree of dissociation. Thus, optimally, the SAFT-γ Mie approach would be extended to consider ion dissociation directly as has already been done for other EoS [199, 201].

Bibliography

[1] Free Data from, "www.gapminder.org," 2023.

[2] H. Ritchie, M. Roser, and P. Rosado, "CO_2 and Greenhouse Gas Emissions," *Our World in Data*, 1 2020. [Online]. Available: https://ourworldindata.org/co2-and-other-greenhouse-gas-emissions

[3] T. M. Lenton, C. Xu, J. F. Abrams, A. Ghadiali, S. Loriani, B. Sakschewski, C. Zimm, K. L. Ebi, R. R. Dunn, J.-C. Svenning, and M. Scheffer, "Quantifying the human cost of global warming," *Nature Sustainability*, 5 2023.

[4] U.S. Department of Energy, "Energy Storage Grand Challenge: Energy Storage Market Report," U.S. Department of Energy, Tech. Rep., 2020. [Online]. Available: https://energy.gov/energy-storage-grand-challenge/downloads/energy-storage-

[5] M. Winter, B. Barnett, and K. Xu, "Before Li-ion batteries," *Chemical Reviews*, vol. 118, no. 23, pp. 11 433–11 456, 12 2018.

[6] J. Tarascon and D. Guyomard, "The $Li_{1+x}Mn_2O_4$/C rocking-chair system: A review," *Eletrochimica Acta*, vol. 38, no. 9, pp. 1221–1231, 1993.

[7] K. Brandt, "Historical development of secondary lithium batteries," *Solid State Ionics*, vol. 69, pp. 173–183, 1994.

[8] S. Passerini, J. M. Rosolen, and B. Scrosati, "Plasticized carbon electrodes of interest for lithium rocking chair batteries," *Journal of Power Sources*, vol. 45, pp. 333–341, 1993.

[9] P. Biensan, B. Simon, J. P. Peres, A. De Guibert, M. Broussely, J. M. Bodet, and . F. Perton, "On safety of lithium-ion cells," *Journal of Power Sources*, vol. 81-82, pp. 906–912, 1999.

[10] P. G. Balakrishnan, R. Ramesh, and T. Prem Kumar, "Safety mechanisms in lithium-ion batteries," *Journal of Power Sources*, vol. 155, no. 2, pp. 401–414, 4 2006.

[11] Y. Chen, Y. Kang, Y. Zhao, L. Wang, J. Liu, Y. Li, Z. Liang, X. He, X. Li, N. Tavajohi, and B. Li, "A review of lithium-ion battery safety concerns: The issues, strategies, and testing standards," *Journal of Energy Chemistry*, vol. 59, pp. 83–99, 8 2021.

[12] P. Sun, R. Bisschop, H. Niu, and X. Huang, "A review of battery fires in electric vehicles," *Fire Technology*, vol. 56, no. 4, pp. 1361–1410, 7 2020.

[13] X. He, D. Bresser, S. Passerini, F. Baakes, U. Krewer, J. Lopez, C. T. Mallia, Y. Shao-Horn, I. Cekic-Laskovic, S. Wiemers-Meyer, F. A. Soto, V. Ponce, J. M. Seminario, P. B. Balbuena, H. Jia, W. Xu, Y. Xu, C. Wang, B. Horstmann, R. Amine, C. C. Su, J. Shi, K. Amine, M. Winter, A. Latz, and R. Kostecki, "The passivity of lithium electrodes in liquid electrolytes for secondary batteries," *Nature Reviews Materials*, vol. 6, no. 11, pp. 1036–1052, 11 2021.

[14] B. Horstmann, J. Shi, R. Amine, M. Werres, X. He, H. Jia, F. Hausen, I. Cekic-Laskovic, S. Wiemers-Meyer, J. Lopez, D. Galvez-Aranda, F. Baakes, D. Bresser, C. C. Su, Y. Xu, W. Xu, P. Jakes, R. A. Eichel, E. Figgemeier, U. Krewer, J. M. Seminario, P. B. Balbuena, C. Wang, S. Passerini, Y. Shao-Horn, M. Winter, K. Amine, R. Kostecki, and A. Latz, "Strategies towards enabling lithium metal in batteries: Interphases and electrodes," *Energy and Environmental Science*, vol. 14, no. 10, pp. 5289–5314, 10 2021.

[15] Y. Zhang, B. Wu, G. Mu, C. Ma, D. Mu, and F. Wu, "Recent progress and perspectives on silicon anode: Synthesis and prelithiation for LIBs energy storage," *Journal of Energy Chemistry*, vol. 64, pp. 615–650, 1 2022.

[16] M. Zhao, B.-Q. Li, X.-Q. Zhang, J.-Q. Huang, and Q. Zhang, "A perspective toward practical lithium–sulfur batteries," *ACS Central Science*, vol. 6, no. 7, pp. 1095–1104, 7 2020.

[17] M. Sawicki and L. L. Shaw, "Advances and challenges of sodium ion batteries as post lithium-ion batteries," *RSC Advances*, vol. 5, no. 65, pp. 53 129–53 154, 2015.

[18] Y. E. Durmus, H. Zhang, F. Baakes, G. Desmaizieres, H. Hayun, L. Yang, M. Kolek, V. Küpers, J. Janek, D. Mandler, S. Passerini, and Y. Ein-Eli, "Side by side battery technologies with lithium-ion based batteries," *Advanced Energy Materials*, vol. 10, no. 24, 6 2020.

[19] B. Scrosati, "Lithium rocking chair batteries: An old concept?" *Journal of The Electrochemical Society*, vol. 139, no. 10, pp. 2776–2781, 10 1992.

[20] D. Guyomard and J.-M. Tarascon, "Rocking-chair or lithium-ion rechargeable lithium batteries," *Advanced Materials*, vol. 6, no. 5, pp. 408–412, 5 1994.

[21] M. Winter, J. O. Besenhard, M. E. Spahr, and P. Novμk, "Insertion electrode materials for rechargeable lithium batteries," *Advanced Materials*, vol. 10, no. 10, pp. 725–763, 1998.

[22] K. Xu, "Nonaqueous liquid electrolytes for lithium-based rechargeable batteries," *Chemical Reviews*, vol. 104, no. 10, pp. 4303–4418, 10 2004.

[23] E. Peled, D. Golodnitsky, G. Ardel, and V. Eshkenazy, "The SEI model-application to lithium-polymer electrolyte batteries," *Electrochimica Acta*, vol. 40, no. 13-14, pp. 2197–2204, 1995.

[24] E. Peled, D. Golodnttsky, G. Ardel, C. Menachem, D. Bar Tow, and V. Eshkenazy, "The role of SEI in lithium and lithium-ion batteries," *MRS Proceedings*, vol. 393, p. 209, 2 1995.

[25] B. Horstmann, F. Single, and A. Latz, "Review on multi-scale models of solid-electrolyte interphase formation," *Current Opinion in Electrochemistry*, vol. 13, pp. 61–69, 2 2019.

[26] H.-H. Sun, A. Dolocan, J. A. Weeks, R. Rodriguez, A. Heller, and C. B. Mullins, "In-situ formation of a multicomponent inorganic-rich SEI layer provides a fast charging and high specific energy Li-metal battery," *Journal of Materials Chemistry A*, vol. 7, no. 30, pp. 17 782–17 789, 2019.

[27] X. Ren, Y. Zhang, M. H. Engelhard, Q. Li, J.-G. Zhang, and W. Xu, "Guided lithium metal deposition and improved lithium coulombic efficiency through synergistic effects of $LiAsF_6$ and cyclic carbonate additives," *ACS Energy Letters*, vol. 3, no. 1, pp. 14–19, 1 2018.

[28] A. L. Michan, B. S. Parimalam, M. Leskes, R. N. Kerber, T. Yoon, C. P. Grey, and B. L. Lucht, "Fluoroethylene carbonate and vinylene carbonate reduction: Understanding lithium-ion battery electrolyte additives and solid electrolyte interphase formation," *Chemistry of Materials*, vol. 28, no. 22, pp. 8149–8159, 11 2016.

[29] I. A. Shkrob, J. F. Wishart, and D. P. Abraham, "What makes fluoroethylene carbonate different?" *The Journal of Physical Chemistry C*, vol. 119, no. 27, pp. 14 954–14 964, 7 2015.

[30] X.-B. Cheng, C. Yan, X. Chen, C. Guan, J.-Q. Huang, H.-J. Peng, R. Zhang, S.-T. Yang, and Q. Zhang, "Implantable solid electrolyte interphase in lithium-metal batteries," *Chem*, vol. 2, no. 2, pp. 258–270, 2 2017.

[31] B. Mercier-Guyon, B. Chavillon, E. Mayousse, A. Le Comte, Y. Reynier, and C. Barchasz, "Influence of electrolyte composition on high energy lithium-metal cells," *Solid State Ionics*, vol. 350, p. 115321, 7 2020.

[32] C.-Z. Zhao, X.-B. Cheng, R. Zhang, H.-J. Peng, J.-Q. Huang, R. Ran, Z.-H. Huang, F. Wei, and Q. Zhang, "Li_2S_5-based ternary-salt electrolyte for robust lithium-metal anode," *Energy Storage Materials*, vol. 3, pp. 77–84, 4 2016.

[33] X. Zhang, T. Li, B. Li, R. Zhang, P. Shi, C. Yan, J. Huang, and Q. Zhang, "A sustainable solid electrolyte interphase for high-energy-density lithium-metal batteries under practical conditions," *Angewandte Chemie International Edition*, vol. 59, no. 8, pp. 3252–3257, 2 2020.

[34] F. Liu, L. Wang, Z. Zhang, P. Shi, Y. Feng, Y. Yao, S. Ye, H. Wang, X. Wu, and Y. Yu, "A mixed lithium-ion conductive Li_2S/Li_2Se protection layer for stable lithium-metal anode," *Advanced Functional Materials*, vol. 30, no. 23, p. 2001607, 6 2020.

[35] D. Aurbach, A. Zaban, Y. Ein-Eli, I. Weissman, B. Markovsky, M. Levi, E. Levi, A. Schechter, and E. Granot, "Recent studies on the correlation between surface chemistry, morphology, three-dimensional structures and performance of Li and Li-C intercalation anodes in several important electrolyte systems," *Journal of Power Sources*, vol. 68, pp. 91–98, 1997.

[36] D. Aurbach, "A short review of failure mechanisms of lithium-metal and lithiated graphite anodes in liquid electrolyte solutions," *Solid State Ionics*, vol. 148, no. 3-4, pp. 405–416, 6 2002.

[37] S. Nowak and M. Winter, "Review—Chemical analysis for a better understanding of aging and degradation mechanisms of non-aqueous electrolytes for lithium-ion batteries: Method development, application and lessons learned," *Journal of The Electrochemical Society*, vol. 162, no. 14, pp. A2500–A2508, 2015.

[38] T. Schedlbauer, U. Rodehorst, C. Schreiner, H. Gores, and M. Winter, "Blends of lithium bis(oxalato)borate and lithium tetrafluoroborate: Useful substitutes for lithium difluoro(oxalato)borate in electrolytes for lithium metal based secondary batteries?" *Electrochimica Acta*, vol. 107, pp. 26–32, 9 2013.

[39] T. Osaka, T. Momma, T. Tajima, and Y. Matsumoto, "Enhancement of lithium anode cyclability in propylene carbonate electrolyte by CO_2 addition and its protective effect against H_2O impurity," *Journal of The Electrochemical Society*, vol. 142, no. 4, pp. 1057–1060, 4 1995.

[40] C. Shen, H. Yan, J. Gu, Y. Gao, J. Yang, and K. Xie, "Li_2O—Reinforced solid electrolyte interphase on three-dimensional sponges for dendrite-free lithium deposition," *Frontiers in Chemistry*, vol. 6, 11 2018.

[41] S. Shiraishi, K. Kanamura, and Z.-I. Takehara, "Influence of initial surface condition of lithium metal anodes on surface modification with HF," *Journal of Applied Electrochemistry*, vol. 29, no. 7, pp. 867–879, 1999.

[42] E. Wang, S. Dey, T. Liu, S. Menkin, and C. P. Grey, "Effects of atmospheric gases on lithium-metal cyclability and solid electrolyte interphase formation," *ACS Energy Letters*, vol. 5, no. 4, pp. 1088–1094, 4 2020.

[43] D. Aurbach, B. Markovsky, A. Shechter, Y. Ein-E1i, and H. Cohen, "A comparative study of synthetic graphite and lithium electrodes in electrolyte solutions based on ethylene carbonate-dimethyl carbonate mixtures," *Journal of the Electrochemical Society*, vol. 143, no. 12, pp. 3809–3820, 1996.

[44] Y. Wang, S. Nakamura, M. Ue, and P. B. Balbuena, "Theoretical studies to understand surface chemistry on carbon anodes for lithium-ion batteries: Reduction mechanisms of ethylene carbonate," *Journal of the American Chemical Society*, vol. 123, no. 47, pp. 11 708–11 718, 11 2001.

[45] D. Witt, F. Röder, and U. Krewer, "Analysis of lithium-ion battery state and degradation via physicochemical cell and SEI modeling," *Batteries & Supercaps*, vol. 5, no. 7, 7 2022.

[46] L. Wang, A. Menakath, F. Han, Y. Wang, P. Y. Zavalij, K. J. Gaskell, O. Borodin, D. Iuga, S. P. Brown, C. Wang, K. Xu, and B. W. Eichhorn, "Identifying the components of the solid electrolyte interphase in lithium-ion batteries," *Nature Chemistry*, vol. 11, no. 9, pp. 789–796, 9 2019.

[47] X. Xie, E. W. Clark Spotte-Smith, M. Wen, H. D. Patel, S. M. Blau, and K. A. Persson, "Data-driven prediction of formation mechanisms of lithium ethylene monocarbonate with an automated reaction network," *Journal of the American Chemical Society*, vol. 143, no. 33, pp. 13 245–13 258, 8 2021.

[48] G. V. Zhuang, K. Xu, H. Yang, T. R. Jow, and P. N. Ross, "Lithium ethylene dicarbonate identified as the primary product of chemical and electrochemical reduction of EC in 1.2 M $LiPF_6$/EC:EMC electrolyte," *The Journal of Physical Chemistry B*, vol. 109, no. 37, pp. 17 567–17 573, 9 2005.

[49] B. Simon, I. L. Moulineaux, and J. Boeuve, "Recharchable lithium electrochemical cell," 5 1997.

[50] D. Aurbach, K. Gamolsky, B. Markovsky, Y. Gofer, M. Schmidt, and U. Heider, "On the use of vinylene carbonate (VC) as an additive to electrolyte solutions for lithium-ion batteries," *Electrochimica Acta*, vol. 47, pp. 1423–1439, 2002. [Online]. Available: www.elsevier.com/locate/electacta

[51] S. K. Heiskanen, J. Kim, and B. L. Lucht, "Generation and evolution of the solid electrolyte interphase of lithium-ion batteries," *Joule*, vol. 3, no. 10, pp. 2322–2333, 10 2019.

[52] P. Guan, L. Liu, and X. Lin, "Simulation and experiment on solid electrolyte interphase (SEI) morphology evolution and lithium-ion diffusion," *Journal of The Electrochemical Society*, vol. 162, no. 9, pp. A1798–A1808, 6 2015.

[53] T. Liu, L. Lin, X. Bi, L. Tian, K. Yang, J. Liu, M. Li, Z. Chen, J. Lu, K. Amine, K. Xu, and F. Pan, "In situ quantification of interphasial chemistry in lithium-ion battery," *Nature Nanotechnology*, vol. 14, no. 1, pp. 50–56, 1 2019.

[54] M. Nie, D. Chalasani, D. P. Abraham, Y. Chen, A. Bose, and B. L. Lucht, "Lithium-ion battery graphite solid electrolyte interphase revealed by microscopy and spectroscopy," *Journal of Physical Chemistry C*, vol. 117, no. 3, pp. 1257–1267, 1 2013.

[55] F. A. Soto, Y. Ma, J. M. Martinez De La Hoz, J. M. Seminario, and P. B. Balbuena, "Formation and growth mechanisms of solid electrolyte interphase layers in rechargeable batteries," *Chemistry of Materials*, vol. 27, no. 23, pp. 7990–8000, 11 2015.

[56] F. Single, B. Horstmann, and A. Latz, "Dynamics and morphology of solid electrolyte interphase (SEI)," *Physical Chemistry Chemical Physics*, vol. 18, no. 27, pp. 17 810–17 814, 2016.

[57] ——, "Revealing SEI morphology: In-depth analysis of a modeling approach," *Journal of The Electrochemical Society*, vol. 164, no. 11, pp. E3132–E3145, 5 2017.

[58] R. D. Deshpande and D. M. Bernardi, "Modeling solid electrolyte interphase (SEI) fracture: Coupled mechanical/chemical degradation of the lithium-ion battery," *Journal of The Electrochemical Society*, vol. 164, no. 2, pp. A461–A474, 1 2017.

[59] M. Esmaeilpour, S. Jana, H. Li, M. Soleymanibrojeni, and W. Wenzel, "A solution-mediated pathway for the growth of the solid electrolyte interphase in lithium-ion batteries," *Advanced Energy Materials*, vol. 13, no. 14, 4 2023.

[60] F. Baakes, M. Lüthe, M. Gerasimov, V. Laue, F. Röder, P. B. Balbuena, and U. Krewer, "Unveiling the interaction of reactions and phase transition during thermal abuse of Li-ion batteries," *Journal of Power Sources*, vol. 522, 2 2022.

[61] X. Feng, D. Ren, X. He, and M. Ouyang, "Mitigating thermal runaway of lithium-ion batteries," *Joule*, vol. 4, no. 4, pp. 743–770, 4 2020.

[62] X. Feng, M. Ouyang, X. Liu, L. Lu, Y. Xia, and X. He, "Thermal runaway mechanism of lithium-ion battery for electric vehicles: A review," *Energy Storage Materials*, vol. 10, pp. 246–267, 1 2018.

[63] S. Solchenbach, G. Hong, A. T. S. Freiberg, R. Jung, and H. A. Gasteiger, "Electrolyte and SEI decomposition reactions of transition metal ions investigated by on-line electrochemical mass spectrometry," *Journal of The Electrochemical Society*, vol. 165, no. 14, pp. A3304–A3312, 2018.

[64] R. Spotnitz and J. Franklin, "Abuse behavior of high-power, lithium-ion cells," *Journal of Power Sources*, vol. 113, pp. 81–100, 2003.

[65] P. T. Coman, S. Mátéfi-Tempfli, C. T. Veje, and R. E. White, "Modeling vaporization, gas generation and venting in lithium-ion battery cells with a dimethyl carbonate electrolyte," *Journal of The Electrochemical Society*, vol. 164, no. 9, pp. A1858–A1865, 2017.

[66] R. C. Shurtz and J. C. Hewson, "Review—Materials science predictions of thermal runaway in layered metal-oxide cathodes: A review of thermodynamics," *Journal of The Electrochemical Society*, vol. 167, no. 9, p. 090543, 1 2020.

[67] D. Mishra, K. Shah, and A. Jain, "Investigation of the impact of flow of vented gas on propagation of thermal runaway in a lithium-ion battery pack," *Journal of The Electrochemical Society*, vol. 168, no. 6, p. 060555, 6 2021.

[68] G. Wang, D. Kong, P. Ping, X. He, H. Lv, H. Zhao, and W. Hong, "Modeling venting behavior of lithium-ion batteries during thermal runaway propagation by coupling CFD and thermal resistance network," *Applied Energy*, vol. 334, p. 120660, 3 2023.

[69] H. Maleki, G. Deng, A. Anani, and J. Howard, "Thermal stability studies of lithium-ion cells and components," *Journal of The Electrochemical Society*, vol. 146, no. 9, pp. 3224–3229, 9 1999.

[70] D. Ren, X. Liu, X. Feng, L. Lu, M. Ouyang, J. Li, and X. He, "Model-based thermal runaway prediction of lithium-ion batteries from kinetics analysis of cell components," *Applied Energy*, vol. 228, pp. 633–644, 10 2018.

[71] T. Kawamura, A. Kimura, M. Egashira, S. Okada, and J.-I. Yamaki, "Thermal stability of alkyl carbonate mixed-solvent electrolytes for lithium-ion cells," *Journal of Power Sources*, vol. 104, pp. 260–264, 2002.

[72] A. Veluchamy, C. H. Doh, D. H. Kim, J. H. Lee, H. M. Shin, B. S. Jin, H. S. Kim, and S. I. Moon, "Thermal analysis of Li_xCoO_2 cathode material of lithium-ion battery," *Journal of Power Sources*, vol. 189, no. 1, pp. 855–858, 4 2009.

[73] B. Lei, W. Zhao, C. Ziebert, N. Uhlmann, M. Rohde, and H. J. Seifert, "Experimental analysis of thermal runaway in 18650 cylindrical lithium-ion cells using an accelerating rate calorimeter," *Batteries*, vol. 3, no. 2, 6 2017.

[74] O. S. Mendoza-Hernandez, H. Ishikawa, Y. Nishikawa, Y. Maruyama, and M. Umeda, "Cathode material comparison of thermal runaway behavior of lithium-ion cells at different state of charges including over charge," *Journal of Power Sources*, vol. 280, pp. 499–504, 4 2015.

[75] M. Fleischhammer, T. Waldmann, G. Bisle, B. I. Hogg, and M. Wohlfahrt-Mehrens, "Interaction of cyclic ageing at high-rate and low temperatures and safety in lithium-ion batteries," *Journal of Power Sources*, vol. 274, pp. 432–439, 1 2015.

[76] M. Börner, A. Friesen, M. Grützke, Y. P. Stenzel, G. Brunklaus, J. Haetge, S. Nowak, F. M. Schappacher, and M. Winter, "Correlation of aging and thermal stability of commercial 18650-type lithium-ion batteries," *Journal of Power Sources*, vol. 342, pp. 382–392, 2017.

[77] C. M. Vendra, A. V. Shelke, J. E. Buston, J. Gill, D. Howard, E. Read, A. Abaza, B. Cooper, and J. X. Wen, "Numerical and experimental characterisation of high energy density 21700 lithium-ion battery fires," *Process Safety and Environmental Protection*, vol. 160, pp. 153–165, 4 2022.

[78] C.-Y. Jhu, Y.-W. Wang, C.-Y. Wen, and C.-M. Shu, "Thermal runaway potential of $LiCoO_2$ and $Li(Ni_{1/3}Co_{1/3}Mn_{1/3})O_2$ batteries determined with adiabatic calorimetry methodology," *Applied Energy*, vol. 100, pp. 127–131, 12 2012.

[79] M. Feinauer, A. A. Abd-El-Latif, P. Sichler, A. Aracil Regalado, M. Wohlfahrt-Mehrens, and T. Waldmann, "Change of safety by main aging mechanism – A multi-sensor accelerating rate calorimetry study with commercial lithium-ion pouch cells," *Journal of Power Sources*, vol. 570, p. 233046, 6 2023.

[80] T. Waldmann, J. B. Quinn, K. Richter, M. Kasper, A. Tost, A. Klein, and M. Wohlfahrt-Mehrens, "Electrochemical, post-mortem, and ARC analysis of lithium-ion cell safety in second-life applications," *Journal of The Electrochemical Society*, vol. 164, no. 13, pp. A3154–A3162, 2017.

[81] X. Feng, S. Zheng, D. Ren, X. He, L. Wang, H. Cui, X. Liu, C. Jin, F. Zhang, C. Xu, H. Hsu, S. Gao, T. Chen, Y. Li, T. Wang, H. Wang, M. Li, and M. Ouyang,

"Investigating the thermal runaway mechanisms of lithium-ion batteries based on thermal analysis database," *Applied Energy*, vol. 246, pp. 53–64, 7 2019.

[82] Y. Baba, S. Okada, and J.-I. Yamaki, "Thermal stability of Li_xCoO_2 cathode for lithium ion battery," *Solid State Ionics*, vol. 148, pp. 311–316, 2002. [Online]. Available: www.elsevier.com/locate/ssi

[83] H. Yang, G. V. Zhuang, and P. N. Ross, "Thermal stability of $LiPF_6$ salt and lithium-ion battery electrolytes containing $LiPF_6$," *Journal of Power Sources*, vol. 161, no. 1, pp. 573–579, 10 2006.

[84] A. Kriston, I. Adanouj, V. Ruiz, and A. Pfrang, "Quantification and simulation of thermal decomposition reactions of lithium-ion battery materials by simultaneous thermal analysis coupled with gas analysis," *Journal of Power Sources*, vol. 435, 9 2019.

[85] S. Solchenbach, M. Metzger, M. Egawa, H. Beyer, and H. A. Gasteiger, "Quantification of PF_5 and POF_3 from side reactions of $LiPF_6$ in lithium-ion batteries," *Journal of The Electrochemical Society*, vol. 165, no. 13, pp. A3022–A3028, 2018.

[86] M. He, "Elucidating interface reactions in lithium-ion batteries and supercapacitors by in situ gas analysis," Ph.D. dissertation, ETH Zürich, Zürich, 2016.

[87] C. Misiewicz, R. Lundström, I. Ahmed, M. J. Lacey, W. R. Brant, and E. J. Berg, "Online electrochemical mass spectrometry on large-format lithium-ion cells," *Journal of Power Sources*, vol. 554, p. 232318, 1 2023.

[88] L. Bläubaum, P. Röse, F. Baakes, and U. Krewer, "Impact of lithium-ion battery separators on gas evolution during temperature abuse," *Batteries & Supercaps*, p. e202300534, 2024.

[89] J. Diekmann, S. Doose, S. Weber, S. Münch, W. Haselrieder, and A. Kwade, "Development of a new procedure for nail penetration of lithium-ion cells to obtain meaningful and reproducible results," *Journal of The Electrochemical Society*, vol. 167, no. 9, p. 090504, 1 2020.

[90] I. Avdeev and M. Gilaki, "Structural analysis and experimental characterization of cylindrical lithium-ion battery cells subject to lateral impact," *Journal of Power Sources*, vol. 271, pp. 382–391, 12 2014.

[91] T. D. Hatchard, D. D. MacNeil, A. Basu, and J. R. Dahn, "Thermal model of cylindrical and prismatic lithium-ion cells," *Journal of The Electrochemical Society*, vol. 148, no. 7, p. A755, 2001.

[92] S. Doose, A. Hahn, M. Bredekamp, W. Haselrieder, and A. Kwade, "Scaling methodology to describe the capacity dependent responses during thermal runaway of lithium-ion batteries," *Batteries & Supercaps*, vol. 5, no. 7, 7 2022.

[93] V. Ruiz, A. Pfrang, A. Kriston, N. Omar, P. Van den Bossche, and L. Boon-Brett, "A review of international abuse testing standards and regulations for lithium-ion batteries in electric and hybrid electric vehicles," *Renewable and Sustainable Energy Reviews*, vol. 81, pp. 1427–1452, 1 2018.

[94] M. N. Richard and J. R. Dahn, "Part I: Accelerating rate calorimetry study on the thermal stability of lithium intercalated graphite in electrolyte I. experimental," *The Electrochemical Society*, vol. 146, p. 2068, 1999.

[95] D. D. MacNeil and J. R. Dann, "Test of reaction kinetics using both differential scanning and accelerating rate calorimetries as applied to the reaction of Li_xCoO_2 in non-aqueous electrolyte," *Journal of Physical Chemistry A*, vol. 105, no. 18, pp. 4430–4439, 5 2001.

[96] G. H. Kim, A. Pesaran, and R. Spotnitz, "A three-dimensional thermal abuse model for lithium-ion cells," *Journal of Power Sources*, vol. 170, no. 2, pp. 476–489, 7 2007.

[97] A. Melcher, C. Ziebert, M. Rohde, and H. J. Seifert, "Modeling and simulation of the thermal runaway behavior of cylindrical lithium-ion cells—computing of critical parameters," *Energies*, vol. 9, no. 4, 4 2016.

[98] S. Abada, G. Marlair, A. Lecocq, M. Petit, V. Sauvant-Moynot, and F. Huet, "Safety focused modeling of lithium-ion batteries: A review," *Journal of Power Sources*, vol. 306, pp. 178–192, 2 2016.

[99] M.-K. Tran, A. Mevawalla, A. Aziz, S. Panchal, Y. Xie, and M. Fowler, "A review of lithium-ion battery thermal runaway modeling and diagnosis approaches," *Processes*, vol. 10, no. 6, p. 1192, 6 2022.

[100] M. N. Richard and J. R. Dahn, "Predicting electrical and thermal abuse behaviours of practical lithium-ion cells from accelerating rate calorimeter studies on small samples in electrolyte," *Journal of Power Sources*, vol. 79, pp. 135–142, 1999.

[101] M. Zhang, L. Liu, A. Stefanopoulou, J. Siegel, L. Lu, X. He, and M. Ouyang, "Fusing phenomenon of lithium-ion battery internal short circuit," *Journal of The Electrochemical Society*, vol. 164, no. 12, pp. A2738–A2745, 9 2017.

[102] P. T. Coman, E. C. Darcy, C. T. Veje, and R. E. White, "Modelling lithium-ion cell thermal runaway triggered by an internal short circuit device using an efficiency factor

and Arrhenius formulations," *Journal of The Electrochemical Society*, vol. 164, no. 4, pp. A587–A593, 2017.

[103] P. T. Coman, S. Rayman, and R. E. White, "A lumped model of venting during thermal runaway in a cylindrical lithium Cobalt Oxide lithium-ion cell," *Journal of Power Sources*, vol. 307, pp. 56–62, 3 2016.

[104] J. P. Joule and W. Thomson, "Lxxvi. on the thermal effects experienced by air in rushing through small apertures," *The London, Edinburgh, and Dublin Philosophical Magazine and Journal of Science*, vol. 4, no. 28, pp. 481–492, 1852.

[105] P. J. Bugryniec, D. J. N. Davidson, and D. S. F. Brown, "Advanced abuse modelling of lithium-ion cells – A novel description of cell pressurisation and simmering reactions," *Journal of Power Sources*, vol. 474, p. 228396, 10 2020.

[106] J. Kim, A. Mallarapu, D. P. Finegan, and S. Santhanagopalan, "Modeling cell venting and gas-phase reactions in 18650 lithium-ion batteries during thermal runaway," *Journal of Power Sources*, vol. 489, 3 2021.

[107] G. Wang, D. Kong, P. Ping, J. Wen, X. He, H. Zhao, X. He, R. Peng, Y. Zhang, and X. Dai, "Revealing particle venting of lithium-ion batteries during thermal runaway: A multi-scale model toward multiphase process," *eTransportation*, vol. 16, p. 100237, 4 2023.

[108] P. T. Coman, E. C. Darcy, C. T. Veje, and R. E. White, "Numerical analysis of heat propagation in a battery pack using a novel technology for triggering thermal runaway," *Applied Energy*, vol. 203, pp. 189–200, 2017.

[109] N. Tanaka and W. G. Bessler, "Numerical investigation of kinetic mechanism for runaway thermo-electrochemistry in lithium-ion cells," *Solid State Ionics*, vol. 262, pp. 70–73, 9 2014.

[110] C. Kupper and W. G. Bessler, "Multi-scale thermo-electrochemical modeling of performance and aging of a $LiFePO_4$ /graphite lithium-ion cell," *Journal of The Electrochemical Society*, vol. 164, no. 2, pp. A304–A320, 2017.

[111] C. Kupper, S. Spitznagel, H. Döring, M. A. Danzer, C. Gutierrez, A. Kvasha, and W. G. Bessler, "Combined modeling and experimental study of the high-temperature behavior of a lithium-ion cell: Differential scanning calorimetry, accelerating rate calorimetry and external short circuit," *Electrochimica Acta*, vol. 306, pp. 209–219, 5 2019.

[112] A. Kriston, A. Podias, I. Adanouj, and A. Pfrang, "Analysis of the effect of thermal runaway initiation conditions on the severity of thermal runaway—numerical

simulation and machine learning study," *Journal of The Electrochemical Society*, vol. 167, no. 9, p. 090555, 1 2020.

[113] X. Feng, S. Zheng, X. He, L. Wang, Y. Wang, D. Ren, and M. Ouyang, "Time sequence map for interpreting the thermal runaway mechanism of lithium-ion batteries with $LiNi_xCo_yMn_zO_2$ Cathode," *Frontiers in Energy Research*, vol. 6, 11 2018.

[114] B. P. E. Clapeyron, "Mémoire sur la puissance motrice de la chaleu," *Journal de L'Ecole Royale Polytechnique*, vol. 14, pp. 153–190, 1934.

[115] J. D. Van der Waals, "De continuteit van den gas—en vloeistoftoestand," Ph.D. dissertation, Hoogeschool de Leiden, Leiden, 6 1873.

[116] G. Wilczek-Vera and J. H. Vera, "Understanding cubic equations of state: A search for the hidden clues of their success," *AIChE Journal*, vol. 61, no. 9, pp. 2824–2831, 9 2015.

[117] G. Soave, "Equilibrium constants from a modified Redkh-Kwong equation of state," *Chemical Engineering Science*, vol. 27, pp. 1197–1203, 1972.

[118] D.-Y. Peng and D. B. Robinson, "A new two-constant equation of state," *Industrial & Engineering Chemistry Fundamentals*, vol. 15, no. 1, pp. 59–64, 1976. [Online]. Available: https://pubs.acs.org/sharingguidelines

[119] J. S. Lopez-Echeverry, S. Reif-Acherman, and E. Araujo-Lopez, "Peng-Robinson equation of state: 40 years through cubics," *Fluid Phase Equilibria*, vol. 447, pp. 39–71, 9 2017.

[120] D. S. H. Wong and S. I. Sandler, "A theoretically correct mixing rule for cubic equations of state," *AIChE Journal*, vol. 38, no. 5, pp. 671–680, 1992.

[121] M.-J. Huron and J. Vidal, "New mixing rules in simple equations of state for representing vapour-liquid equilibria of strongly non-ideal mixtures," *Fluid Phase Equilibria*, vol. 3, no. 4, pp. 255–271, 1 1979.

[122] P. Coutsikos, N. S. Kalospiros, and D. P. Tassios, "Capabilities and limitations of the wong-sandler mixing rules," *Fluid Phase Equilibria*, vol. 108, no. 1-2, pp. 59–78, 1995.

[123] G. M. Kontogeorgis, X. Liang, A. Arya, and I. Tsivintzelis, "Equations of state in three centuries. Are we closer to arriving to a single model for all applications?" *Chemical Engineering Science: X*, vol. 7, 5 2020.

[124] W. Chapman, K. Gubbins, G. Jackson, and M. Radosz, "Saft: equation of state solution model for associating fluids," *Fluid Phase Equilibria*, vol. 52, pp. 31–38, 1989. [Online]. Available: https://www.sciencedirect.com/science/article/pii/0378381289803085

[125] W. G. Chapman, K. E. Gubbins, G. Jackson, and M. Radosz, "New reference equation of state for associating liquids," *Industrial & engineering chemistry research*, vol. 29, no. 8, pp. 1709–1721, 1990.

[126] M. S. Wertheim, "Fluids with highly directional attractive forces. II. Thermodynamic perturbation theory and integral equations," *Journal of Statistical Physics*, vol. 35, no. 2, 1984.

[127] ——, "Fluids with highly directional attractive forces. I. Statistical thermodynamics," *Journal of Statistical Physics*, vol. 35, 1984.

[128] M. Wertheim, "Fluids with highly directional attractive forces. iii. multiple attraction sites," *Journal of statistical physics*, vol. 42, no. 3-4, pp. 459–476, 1986.

[129] ——, "Fluids with highly directional attractive forces. iv. equilibrium polymerization," *Journal of statistical physics*, vol. 42, no. 3-4, pp. 477–492, 1986.

[130] G. M. Kontogeorgis, E. C. Voutsas, I. V. Yakoumis, and D. P. Tassios, "An equation of state for associating fluids," *Industrial & engineering chemistry research*, vol. 35, no. 11, pp. 4310–4318, 1996.

[131] J. Gross and G. Sadowski, "Application of perturbation theory to a hard-chain reference fluid: an equation of state for square-well chains," *Fluid Phase Equilibria*, vol. 168, pp. 183–199, 2000. [Online]. Available: www.elsevier.nlrlocaterfluid

[132] ——, "Perturbed-chain SAFT: An equation of state based on a perturbation theory for chain molecules," *Industrial and Engineering Chemistry Research*, vol. 40, no. 4, pp. 1244–1260, 2 2001.

[133] F. J. Blas and L. F. Vega, "Thermodynamic behaviour of homonuclear and heteronuclear Lennard-Jones chains with association sites from simulation and theory," *Molecular Physics*, vol. 92, no. 1, pp. 135–150, 1997.

[134] A. Galindo, S. J. Burton, G. Jackson, D. P. Visco Jr, and D. A. Kofke, "Improved models for the phase behaviour of hydrogen fluoride: chain and ring aggregates in the SAFT approach and the AEOS model," *Molecular Physics*, vol. 100, no. 14, p. 2259, 2002. [Online]. Available: http://www.tandf.co.uk/journals

[135] A. L. Lydersen, *Estimation of critical properties of organic compounds by the method of group contibutions*. Madison, WI: University of Wisconsin, 1955.

[136] K. G. Joback and R. C. Reid, "Estimation of pure-component properties from group-contributions," *Chemical Engineering Communications*, vol. 57, no. 1-6, pp. 233–243, 7 1987.

[137] A. J. Haslam, A. González-Pérez, S. Di Lecce, S. H. Khalit, F. A. Perdomo, S. Kournopoulos, M. Kohns, T. Lindeboom, M. Wehbe, S. Febra, G. Jackson, C. S. Adjiman, and A. Galindo, "Expanding the applications of the SAFT-γMie group-contribution equation of state: Prediction of thermodynamic properties and phase behavior of mixtures," *Journal of Chemical and Engineering Data*, vol. 65, no. 12, pp. 5862–5890, 12 2020.

[138] A. Lymperiadis, C. S. Adjiman, G. Jackson, and A. Galindo, "A generalisation of the SAFT-γ group contribution method for groups comprising multiple spherical segments," *Fluid Phase Equilibria*, vol. 274, no. 1-2, pp. 85–104, 12 2008.

[139] A. I. Papadopoulos, G. Shavalieva, S. Papadokonstantakis, P. Seferlis, F. A. Perdomo, A. Galindo, G. Jackson, and C. S. Adjiman, "An approach for simultaneous computer-aided molecular design with holistic sustainability assessment: Application to phase-change CO_2 capture solvents," *Computers & Chemical Engineering*, vol. 135, p. 106769, 4 2020.

[140] P. Kazepidis, A. I. Papadopoulos, P. Seferlis, F. A. Perdomo, A. Galindo, G. Jackson, and C. S. Adjiman, "Optimal design of post combustion CO_2 capture processes based on phase-change solvents," *Computer Aided Chemical Engineering*, vol. 46, pp. 463–468, 1 2019.

[141] M. Wehbe, A. J. Haslam, G. Jackson, and A. Galindo, "Phase behaviour and pH-solubility profile prediction of aqueous buffered solutions of ibuprofen and ketoprofen," *Fluid Phase Equilibria*, vol. 560, 9 2022.

[142] F. A. Perdomo, S. H. Khalit, E. J. Graham, F. Tzirakis, A. I. Papadopoulos, I. Tsivintzelis, P. Seferlis, C. S. Adjiman, G. Jackson, and A. Galindo, "A predictive group-contribution framework for the thermodynamic modelling of CO_2 absorption in cyclic amines, alkyl polyamines, alkanolamines and phase-change amines: New data and SAFT-γ Mie parameters," *Fluid Phase Equilibria*, vol. 566, 3 2023.

[143] F. Baakes, D. Witt, and U. Krewer, "Impact of electrolyte impurities and sei composition on battery safety," *Chemical Science*, vol. 14, pp. 13 783–13 798, 2023.

[144] M. Stich, M. Göttlinger, M. Kurniawan, U. Schmidt, and A. Bund, "Hydrolysis of lipf$_6$ in carbonate-based electrolytes for lithium-ion batteries and in aqueous media," *The Journal of Physical Chemistry C*, vol. 122, no. 16, pp. 8836–8842, 2018.

[145] S. E. Sloop, J. K. Pugh, S. Wang, J. B. Kerr, and K. Kinoshita, "Chemical reactivity of PF_5 and $LiPF_6$ in ethylene carbonate/dimethyl carbonate solutions," *Electrochemical and Solid-State Letters*, vol. 4, no. 4, 4 2001.

[146] K. Tasaki, K. Kanda, S. Nakamura, and M. Ue, "Decomposition of $LiPF_6$ and stability of PF_5 in lithium-ion battery electrolytes," *Journal of The Electrochemical Society*, vol. 150, no. 12, p. A1628, 2003.

[147] T. Kawamura, S. Okada, and J. i. Yamaki, "Decomposition reaction of $LiPF_6$-based electrolytes for lithium ion cells," *Journal of Power Sources*, vol. 156, no. 2, pp. 547–554, 6 2006.

[148] Y. Okamoto, "Ab initio calculations of thermal decomposition mechanism of $LiPF_6$-based electrolytes for lithium-ion batteries," *Journal of The Electrochemical Society*, vol. 160, no. 2, pp. A404–A409, 2013.

[149] S. J. An, J. Li, C. Daniel, D. Mohanty, S. Nagpure, and D. L. Wood, "The state of understanding of the lithium-ion-battery graphite solid electrolyte interphase (SEI) and its relationship to formation cycling," *Carbon*, vol. 105, pp. 52–76, 8 2016.

[150] D. Aurbach, I. Weissman, A. Zaban, and P. Dan, "On the role of water contamination in rechargeable lithium batteries," *Electrochimica Acta*, vol. 45, pp. 1135–1140, 1999. [Online]. Available: www.elsevier.nl/locate/electacta

[151] A. M. Andersson and K. Edström, "Chemical composition and morphology of the elevated temperature SEI on graphite," *Journal of The Electrochemical Society*, vol. 148, no. 10, p. A1100, 2001.

[152] A. T. Freiberg, J. Sicklinger, S. Solchenbach, and H. A. Gasteiger, "Li_2CO_3 decomposition in lithium-ion batteries induced by the electrochemical oxidation of the electrolyte and of electrolyte impurities," *Electrochimica Acta*, vol. 346, 6 2020.

[153] K. Kanamura, S. Shiraishi, and Z.-i. Takehara, "Electrochemical deposition of very smooth lithium using nonaqueous electrolytes containing hf," *Journal of the Electrochemical Society*, vol. 143, no. 7, p. 2187, 1996.

[154] W. D. Machin and F. C. Tompkins, "Kinetics of the reaction of water vapour with crystalline lithium hydride," *Transactions of the Faraday Society*, vol. 62, pp. 2205–2218, 1966.

[155] D. G. Kellerman, V. V. Karelina, V. S. Gorshkov, and Y. N. Blinovskov, "Investigation of thermal stability of $LiCoO_2$ and $Li_{1-x}CoO_2$," *Chemistry for Sustainable Development*, vol. 10, pp. 721–726, 2002.

[156] H. Arai, S. Okada, Y. Sakurai, and J.-I. Yamaki, "Thermal behavior of $LiNiO_2$ and the decomposition mechanism 12y 2," *Solid State Ionics*, vol. 109, pp. 295–302, 1998.

[157] D. P. Abraham, E. P. Roth, R. Kostecki, K. McCarthy, S. MacLaren, and D. H. Doughty, "Diagnostic examination of thermally abused high-power lithium-ion cells," *Journal of Power Sources*, vol. 161, no. 1, pp. 648–657, 10 2006.

[158] W. C. Chen, Y. W. Wang, and C. M. Shu, "Adiabatic calorimetry test of the reaction kinetics and self-heating model for 18650 lithium-ion cells in various states of charge," *Journal of Power Sources*, vol. 318, pp. 200–209, 6 2016.

[159] M. M. Kabir and D. E. Demirocak, "Degradation mechanisms in lithium-ion batteries: a state-of-the-art review," *International Journal of Energy Research*, vol. 41, no. 14, pp. 1963–1986, 11 2017.

[160] S. Wiemers-Meyer, S. Jeremias, M. Winter, and S. Nowak, "Influence of battery cell components and water on the thermal and chemical stability of $LiPF_6$ cased lithium-ion battery electrolytes," *Electrochimica Acta*, vol. 222, pp. 1267–1271, 12 2016.

[161] G. H. Hess, "Recherches thermochimiques," *Bulletin scientifique Académie impériale des sciences*, vol. 8, pp. 257–272, 1840.

[162] renata batteries, "36_M_ICP622540PMT," Itlingen, 8 2019.

[163] A. M. Colclasure and R. J. Kee, "Thermodynamically consistent modeling of elementary electrochemistry in lithium-ion batteries," *Electrochimica Acta*, vol. 55, no. 28, pp. 8960–8973, 12 2010.

[164] B. Rieger, S. Schlueter, S. V. Erhard, J. Schmalz, G. Reinhart, and A. Jossen, "Multi-scale investigation of thickness changes in a commercial pouch type lithium-ion battery," *Journal of Energy Storage*, vol. 6, pp. 213–221, 2016.

[165] S. Arrhenius, "Über die dissociationswärme und den einfluss der temperatur auf den dissociationsgrad der elektrolyte," *Zeitschrift für physikalische Chemie*, vol. 4, no. 1, pp. 96–116, 1889.

[166] H. Shin, J. Park, S. Han, A. M. Sastry, and W. Lu, "Component-/structure-dependent elasticity of solid electrolyte interphase layer in lithium-ion batteries: Experimental and computational studies," *Journal of Power Sources*, vol. 277, pp. 169–179, 3 2015.

[167] D. Bedrov, O. Borodin, and J. B. Hooper, "Li^+ transport and mechanical properties of model solid electrolyte interphases (SEI): Insight from atomistic molecular dynamics simulations," *The Journal of Physical Chemistry C*, vol. 121, no. 30, pp. 16 098–16 109, 8 2017.

[168] H. Ye, S. Gui, Z. Wang, J. Chen, Q. Liu, X. Zhang, P. Jia, Y. Tang, T. Yang, C. Du, L. Geng, H. Li, Q. Dai, Y. Tang, L. Zhang, H. Yang, and J. Huang, "In situ measurements of the mechanical properties of electrochemically deposited Li_2CO_3 and Li_2O nanorods," *ACS Applied Materials & Interfaces*, vol. 13, no. 37, pp. 44 479–44 487, 9 2021.

[169] C. Stetson, Y. Yin, C. S. Jiang, S. C. Decaluwe, M. Al-Jassim, N. R. Neale, C. Ban, and A. Burrell, "Temperature-dependent solubility of solid electrolyte interphase on silicon electrodes," *ACS Energy Letters*, vol. 4, no. 12, pp. 2770–2775, 12 2019.

[170] P. Atkins and J. de Paula, *Physical chemistry: Thermodynamics and kinetics*. Oxford: Oxford University Press, 2006.

[171] H. Maleki and J. N. Howard, "Role of the cathode and anode in heat generation of lithium-ion cells as a function of state of charge," *Journal of Power Sources*, vol. 137, no. 1, pp. 117–127, 10 2004.

[172] J. Dalton, "Essay IV. On the expansion of elastic fluids by heat," *Memoirs of the Literary and Philosophical Society of Manchester*, vol. 5, no. 2, pp. 595–602, 1802.

[173] A. D. McNaught and A. Wilkinson, "The IUPAC compendium of chemical terminology," in *The IUPAC Compendium of Chemical Terminology*, 2nd ed. Research Triangle Park, NC: International Union of Pure and Applied Chemistry (IUPAC), 2 2014.

[174] W. Henry, "Experiments on the quantity of gases absorbed by water at different temperatures, and under different pressure," *Philosophical Transactions Royal Society London*, vol. 93, pp. 29–42, 1803.

[175] K. H. Lee, E. H. Song, J. Y. Lee, B. H. Jung, and H. S. Lim, "Mechanism of gas build-up in a lithium-ion cell at elevated temperature," *Journal of Power Sources*, vol. 132, no. 1-2, pp. 201–205, 5 2004.

[176] V. Papaioannou, T. Lafitte, C. Avendaño, C. S. Adjiman, G. Jackson, E. A. Müller, and A. Galindo, "Group contribution methodology based on the statistical associating fluid theory for heteronuclear molecules formed from Mie segments," *The Journal of Chemical Physics*, vol. 140, no. 5, p. 054107, 2 2014.

[177] S. Dufal, V. Papaioannou, M. Sadeqzadeh, T. Pogiatzis, A. Chremos, C. S. Adjiman, G. Jackson, and A. Galindo, "Prediction of thermodynamic properties and phase behavior of fluids and mixtures with the SAFT-γ Mie group-contribution equation of state," *Journal of Chemical & Engineering Data*, vol. 59, no. 10, pp. 3272–3288, 10 2014.

[178] S. Dufal, T. Lafitte, A. J. Haslam, A. Galindo, G. N. Clark, C. Vega, and G. Jackson, "The A in SAFT: Developing the contribution of association to the Helmholtz free energy within a Wertheim TPT1 treatment of generic Mie fluids," *Molecular Physics*, vol. 113, no. 9-10, pp. 948–984, 5 2015.

[179] D. K. Eriksen, G. Lazarou, A. Galindo, G. Jackson, C. S. Adjiman, and A. J. Haslam, "Development of intermolecular potential models for electrolyte solutions using an electrolyte SAFT-VR Mie equation of state," *Molecular Physics*, vol. 114, no. 18, pp. 2724–2749, 9 2016.

[180] J. M. Schreckenberg, S. Dufal, A. J. Haslam, C. S. Adjiman, G. Jackson, and A. Galindo, "Modelling of the thermodynamic and solvation properties of electrolyte solutions with the statistical associating fluid theory for potentials of variable range," *Molecular Physics*, vol. 112, no. 17, pp. 2339–2364, 9 2014.

[181] G. Lazarou, "Development of the SAFT-γ Mie equation of state for predicting the thermodynamic behaviour of strong and weak electrolyte solutions," Ph.D. dissertation, Imperial College London, London, 9 2017.

[182] L. Blum, "Solution of a model for the solvent - electrolyte interactions in the mean spherical approximation," *The Journal of Chemical Physics*, vol. 61, no. 5, pp. 2129–2133, 9 1974.

[183] ——, "Mean spherical model for asymmetric electrolytes," *Molecular Physics*, vol. 30, no. 5, pp. 1529–1535, 11 1975.

[184] M. Born, "Volumen und Hydratationswärme der Ionen," *Zeitschrift für Physik*, vol. 1, no. 1, pp. 45–48, 2 1920.

[185] J. S. Rowlinson and F. L. Swinton, *Liquid and liquid mixtures*, 3rd ed. London: Butterworth & Co Ltd, 1982.

[186] T. Lafitte, A. Apostolakou, C. Avendaño, A. Galindo, C. S. Adjiman, E. A. Müller, and G. Jackson, "Accurate statistical associating fluid theory for chain molecules formed from Mie segments," *The Journal of Chemical Physics*, vol. 139, no. 15, p. 154504, 10 2013.

[187] G. H. Hudson and J. C. McCoubrey, "Intermolecular forces between unlike molecules. A more complete form of the combining rules," *Transactions of the Faraday Society*, vol. 56, p. 761, 1960.

[188] M. A. Rivas, S. M. Pereira, and T. P. Iglesias, "Relative permittivity of the mixtures (dimethyl or diethyl carbonate) + n-nonane from T = 288.15 K to T = 308.15 K," *Journal of Chemical Thermodynamics*, vol. 34, no. 11, pp. 1897–1907, 2002.

[189] C. G. Malmberg and A. A. Maryott, "Dielectric constant of water from 0°C to 100°C," *Journal of Research of the National Bureau of Standards*, vol. 56, no. I, 1956.

[190] R. Payne and I. E. Theodorou, "Dielectric properties and relaxation in ethylene carbonate and propylene carbonate," *The Journal of Physical Chemistry*, vol. 76, no. 20, pp. 2892–2900, 1972.

[191] Z. Feng, K. Higa, K. S. Han, and V. Srinivasan, "Evaluating transport properties and ionic dissociation of $LiPF_6$ in concentrated electrolyte," *Journal of The Electrochemical Society*, vol. 164, no. 12, pp. A2434–A2440, 2017.

[192] Y. Marcus and G. Hefter, "Ion pairing," *Chemical Reviews*, vol. 106, no. 11, pp. 4585–4621, 11 2006.

[193] B. Koo, H. Lee, S. Hwang, and H. Lee, "Ionic conduction and speciation in $LiPF_6$ and $LiBF_4$ dimethyl sulfoxide electrolytes: Comparison with propylene carbonate electrolytes," *Journal of Physical Chemistry C*, 3 2022.

[194] O. Borodin and G. D. Smith, "Quantum chemistry and molecular dynamics simulation study of dimethyl carbonate: Ethylene carbonate electrolytes doped with $LiPF_6$," *Journal of Physical Chemistry B*, vol. 113, no. 6, pp. 1763–1776, 2 2009.

[195] O. Borodin, M. Olguin, P. Ganesh, P. R. Kent, J. L. Allen, and W. A. Henderson, "Competitive lithium solvation of linear and cyclic carbonates from quantum chemistry," *Physical Chemistry Chemical Physics*, vol. 18, no. 1, pp. 164–175, 2016.

[196] K. Hayamizu, "Temperature dependence of self-diffusion coefficients of ions and solvents in ethylene carbonate, propylene carbonate, and diethyl carbonate single solutions and ethylene carbonate + diethyl carbonate binary solutions of $LiPF_6$ studied by NMR," *Journal of Chemical and Engineering Data*, vol. 57, no. 7, pp. 2012–2017, 7 2012.

[197] S. A. Krachkovskiy, J. D. Bazak, S. Fraser, I. C. Halalay, and G. R. Goward, "Determination of mass transfer parameters and ionic association of $LiPF_6$: Organic carbonates solutions," *Journal of The Electrochemical Society*, vol. 164, no. 4, pp. A912–A916, 2017.

[198] J. Self, N. T. Hahn, and K. A. Persson, "Solvation effects on the Dielectric constant of 1 M $LiPF_6$ in ethylene carbonate:ethyl methyl carbonate 3:7," *Energy and Environmental Materials*, 2023.

[199] G. Das, S. Hlushak, M. C. dos Ramos, and C. Mccabe, "Predicting the thermodynamic properties and dielectric behavior of electrolyte solutions using the SAFT-VR+DE equation of state," *AIChE Journal*, vol. 61, no. 9, pp. 3053–3072, 9 2015.

[200] N. Novak, G. M. Kontogeorgis, M. Castier, and I. G. Economou, "Extension of the eSAFT-VR Mie equation of state from aqueous to non-aqueous electrolyte solutions," *Fluid Phase Equilibria*, vol. 565, 2 2023.

[201] M. D. Olsen, G. M. Kontogeorgis, X. Liang, and N. von Solms, "Comparison of models for the relative static permittivity with the e-CPA equation of state," *Fluid Phase Equilibria*, vol. 565, 2 2023.

[202] H. Krienke and J. Barthel, "MSA models of ion association in electrolyte solutions," *Zeitschrift fur Physikalische Chemie*, vol. 204, pp. 71–83, 1998.

[203] Natick, "MATLAB," Massachusetts, 2023.

[204] N. Bjerrum, *Untersuchungen über Ionenassoziation*. AF Høst, 1926.

[205] M. L. Michelsen and J. M. Mollerup, *Thermodynamic models: Fundamentals & computational aspects*, 2nd ed. Tie-Line Publications, 2007.

[206] Process Systems Enterprise, "gPROMS Process Academic Teaching," pp. 1997–2023.

[207] A. Mejía, E. A. Muller, and G. Chaparro Maldonado, "Sgtpy: A python code for calculating the interfacial properties of fluids based on the square gradient theory using the saft-vr mie equation of state," *Journal of Chemical Information and Modeling*, vol. 61, no. 3, pp. 1244–1250, 2021.

[208] P. J. Walker, H.-W. Yew, and A. Riedemann, "Clapeyron. jl: An extensible, open-source fluid thermodynamics toolkit," *Industrial & Engineering Chemistry Research*, vol. 61, no. 20, pp. 7130–7153, 2022.

[209] J. Self, B. M. Wood, N. N. Rajput, and K. A. Persson, "The interplay between salt association and the dielectric properties of low permittivity electrolytes: The case of $LiPF_6$ and $LiAsF_6$ in dimethyl carbonate," *Journal of Physical Chemistry C*, vol. 122, no. 4, pp. 1990–1994, 2 2018.

[210] H. Lee, S. Hwang, M. Kim, K. Kwak, J. Lee, Y. K. Han, and H. Lee, "Why does dimethyl carbonate dissociate lithium salt better than other linear carbonates? Critical

role of polar conformers," *Journal of Physical Chemistry Letters*, vol. 11, no. 24, pp. 10 382–10 387, 12 2020.

[211] M. Castriota, E. Cazzanelli, I. Nicotera, L. Coppola, C. Oliviero, and G. A. Ranieri, "Temperature dependence of lithium-ion solvation in ethylene carbonate-$LiClO_4$ solutions," *Journal of Chemical Physics*, vol. 118, no. 12, pp. 5537–5541, 3 2003.

[212] G. Åvall, J. Wallenstein, G. Cheng, K. L. Gering, P. Johansson, and D. P. Abraham, "Highly concentrated electrolytes: Electrochemical and physicochemical characteristics of $LiPF_6$ in propylene carbonate solutions," *Journal of The Electrochemical Society*, vol. 168, no. 5, p. 050521, 5 2021.

[213] F. Röder, V. Laue, and U. Krewer, "Model-based multiscale analysis of film formation in lithium-ion batteries," *Batteries & Supercaps*, vol. 2, no. 3, pp. 248–265, 3 2019.

[214] P. Schön and U. Krewer, "Revealing the complex sulfur reduction mechanism using cyclic voltammetry simulation," *Electrochimica Acta*, vol. 373, p. 137523, 3 2021.

[215] D. Aurbach, A. Zaban, A. Schechter, Y. Ein-Eli, E. Zinigrad, and B. Markovsky, "The study of electrolyte solutions based on ethylene and diethyl carbonates for rechargeable lithium batteries," *Journal of the Electrochemical Society*, vol. 142, no. 9, pp. 2873–2882, 1995.

[216] M. Nie, D. P. Abraham, D. M. Seo, Y. Chen, A. Bose, and B. L. Lucht, "Role of solution structure in solid electrolyte interphase formation on graphite with $LiPF_6$ in propylene carbonate," *Journal of Physical Chemistry C*, vol. 117, no. 48, pp. 25 381–25 389, 12 2013.

[217] U. Heider, R. Oesten, and M. Jungnitz, "Challenge in manufacturing electrolyte solutions for lithium and lithium-ion batteries quality control and minimizing contamination level," *Journal of Power Sources*, vol. 81, pp. 119–122, 1999. [Online]. Available: www.elsevier.comrlocaterjpowsour

[218] X. Liu, S. I. Stoliarov, M. Denlinger, A. Masias, and K. Snyder, "Comprehensive calorimetry of the thermally-induced failure of a lithium-ion battery," *Journal of Power Sources*, vol. 280, pp. 516–525, 4 2015.

[219] S. Wilke, B. Schweitzer, S. Khateeb, and S. Al-Hallaj, "Preventing thermal runaway propagation in lithium-ion battery packs using a phase change composite material: An experimental study," *Journal of Power Sources*, vol. 340, pp. 51–59, 2 2017.

[220] J. Kalhoff, G. G. Eshetu, D. Bresser, and S. Passerini, "Safer electrolytes for lithium-ion batteries: state of the art and perspectives," *ChemSusChem*, vol. 8, no. 13, pp. 2154–2175, 2015.

[221] A. Kwade, W. Haselrieder, R. Leithoff, A. Modlinger, F. Dietrich, and K. Droeder, "Current status and challenges for automotive battery production technologies," *Nature Energy*, vol. 3, no. 4, pp. 290–300, 4 2018.

[222] U. Langklotz, M. Schneider, and A. Michaelis, "Water uptake of tape-cast cathodes for lithium-ion batteries," *Journal of Ceramic Science and Technology*, vol. 4, no. 2, pp. 69–76, 2013.

[223] L. Q. Zheng, S. J. Li, H. J. Lin, Y. Y. Miao, L. Zhu, and Z. J. Zhang, "Effects of water contamination on the electrical properties of 18650 lithium-ion batteries," *Russian Journal of Electrochemistry*, vol. 50, no. 9, pp. 904–907, 2014.

[224] R. M. Kasse, N. R. Geise, J. S. Ko, J. Nelson Weker, H.-G. Steinrück, and M. F. Toney, "Understanding additive controlled lithium morphology in lithium-metal batteries," *Journal of Materials Chemistry A*, vol. 8, no. 33, pp. 16 960–16 972, 2020.

[225] W. Weber, V. Kraft, M. Grützke, R. Wagner, M. Winter, and S. Nowak, "Identification of alkylated phosphates by gas chromatography-mass spectrometric investigations with different ionization principles of a thermally aged commercial lithium-ion battery electrolyte," *Journal of Chromatography A*, vol. 1394, pp. 128–136, 5 2015.

[226] F. Huttner, W. Haselrieder, and A. Kwade, "The influence of different post-drying procedures on remaining water content and physical and electrochemical properties of lithium-ion batteries," *Energy Technology*, vol. 8, no. 2, 2 2020.

[227] Sigma Aldrich, "Product specification: lithium hexafluorophosphate solution in ethlene carbonate and dimethyl carbonate," 2022.

[228] M. Gerasimov, F. A. Soto, J. Wagner, F. Baakes, N. Guo, F. Ospina-Acevedo, F. Röder, P. B. Balbuena, and U. Krewer, "Species distribution during solid electrolyte interphase formation on lithium using MD/DFT-parameterized kinetic Monte Carlo simulations," *The Journal of Physical Chemistry C*, vol. 127, no. 10, pp. 4872–4886, 3 2023.

[229] J. Wagner, D. Kuai, M. Gerasimov, F. Röder, P. Balbuena, and U. Krewer, "Knowledge-driven design of solid electrolyte interphases on lithium metal: Insights from multiscale modelling," *Nature Communication*, 2023.

[230] B. Lu, D. Cheng, B. Sreenarayanan, W. Li, B. Bhamwala, W. Bao, and Y. S. Meng, "Key parameters in determining the reactivity of lithium metal battery," *ACS Energy Letters*, vol. 8, no. 7, p. 3230–3238, 2023.

[231] B. S. Vishnugopi, M. T. Hasan, H. Zhou, and P. P. Mukherjee, "Interphases and electrode crosstalk dictate the thermal stability of solid-state batteries," *ACS Energy Letters*, vol. 8, no. 1, pp. 398–407, 2022.

[232] P. Röder, B. Stiaszny, J. C. Ziegler, N. Baba, P. Lagaly, and H. D. Wiemhöfer, "The impact of calendar aging on the thermal stability of a $LiMn_2O_4$-$Li(Ni_{1/3}Mn_{1/3}Co_{1/3})O_2$/graphite lithium-ion cell," *Journal of Power Sources*, vol. 268, pp. 315–325, 12 2014.

[233] C. Jayawardana, N. Rodrigo, B. Parimalam, and B. L. Lucht, "Role of electrolyte oxidation and difluorophosphoric acid generation in crossover and capacity fade in lithium-ion batteries," *ACS Energy Letters*, vol. 6, no. 11, pp. 3788–3792, 11 2021.

[234] A. W. Golubkov, D. Fuchs, J. Wagner, H. Wiltsche, C. Stangl, G. Fauler, G. Voitic, A. Thaler, and V. Hacker, "Thermal-runaway experiments on consumer lithium-ion batteries with metal-oxide and olivin-type cathodes," *RSC Advances*, vol. 4, no. 7, pp. 3633–3642, 2014.

[235] A. W. Golubkov, S. Scheikl, R. Planteu, G. Voitic, H. Wiltsche, C. Stangl, G. Fauler, A. Thaler, and V. Hacker, "Thermal runaway of commercial 18650 li-ion batteries with lfp and nca cathodes–impact of state of charge and overcharge," *Rsc Advances*, vol. 5, no. 70, pp. 57 171–57 186, 2015.

[236] C. Y. Jhu, Y. W. Wang, C. M. Shu, J. C. Chang, and H. C. Wu, "Thermal explosion hazards on 18650 lithium-ion batteries with a VSP2 adiabatic calorimeter," *Journal of Hazardous Materials*, vol. 192, no. 1, pp. 99–107, 8 2011.

[237] S. Dufal, T. Lafitte, A. Galindo, G. Jackson, and A. J. Haslam, "Developing intermolecular-potential models for use with the SAFT-VR Mie equation of state," *AIChE Journal*, vol. 61, no. 9, pp. 2891–2912, 9 2015.

[238] L. Chen, R. J. Zhu, Y. Fang, P. F. Yuan, L. Q. Cao, and Y. L. Tian, "Vapor-liquid equilibrium data for carbon dioxide+dimethyl carbonate binary system," *Wuli Huaxue Xuebao/ Acta Physico - Chimica Sinica*, vol. 29, no. 1, pp. 11–16, 2013.

[239] M. A. Saleh, S. Akhtar, M. S. Ahmed, and M. H. Uddin, "Density, excess molar volume, viscosity and thermodynamic activation of viscous flow of water + ethylene carbonate," *Physics and Chemistry of Liquids*, vol. 43, no. 4, pp. 367–377, 8 2005.

[240] V. D. Kiselev and A. V. Bolotov, "P-V-T parameters of propylene carbonate and cis-,trans-decahydronaphthalene in temperature and pressure ranges of 20–50°C and 1–1000 bar," *Russian Journal of Physical Chemistry A*, vol. 84, no. 4, pp. 593–597, 4 2010.

[241] S. A. Kozlova, V. N. Emel'yanenko, M. Georgieva, S. P. Verevkin, Y. Chernyak, B. Schäffner, and A. Börner, "Vapour pressure and enthalpy of vaporization of

aliphatic dialkyl carbonates," *Journal of Chemical Thermodynamics*, vol. 40, no. 7, pp. 1136–1140, 7 2008.

[242] W. Steele, R. Chirico, S. Knipmeyer, A. Nguyen, and N. Smith, "Thermodynamic properties and ideal-gas enthalpies of formation for dicyclohexyl sulfide, diethylenetriamine, di-n-octyl sulfide, dimethyl carbonate, piperazine, hexachloroprop-1-ene, tetrakis (dimethylamino) ethylene, n, n '-bis-(2-hydroxyethyl) ethylenediamine, and 1, 2, 4-triazolo [1, 5-a] pyrimidine," *Journal of Chemical & Engineering Data*, vol. 42, no. 6, pp. 1037–1052, 1997.

[243] F. Stehmann, P. Prziwara, C. Bradtmöller, M. Schoenitz, and S. Scholl, "Adsorption equilibria of dimethyl carbonate and ethyl methyl carbonate onto activated carbon," *Chemie-Ingenieur-Technik*, vol. 88, no. 3, pp. 327–335, 3 2016.

[244] V. Pokorný, V. Štejfa, M. Fulem, C. Červinka, and K. Růžička, "Vapor pressures and thermophysical properties of dimethyl carbonate, diethyl carbonate, and dipropyl carbonate," *Journal of Chemical and Engineering Data*, vol. 62, no. 10, pp. 3206–3215, 10 2017.

[245] S. P. Verevkin, A. V. Toktonov, Y. Chernyak, B. Schäffner, and A. Börner, "Vapour pressure and enthalpy of vaporization of cyclic alkylene carbonates," *Fluid Phase Equilibria*, vol. 268, no. 1-2, pp. 1–6, 6 2008.

[246] C. Hong, R. Wakslak, H. Finston, and V. Fried, "Some thermodynamic properties of systems containing propylene carbonate and ethylene carbonate," *Journal of Chemical and Engineering Data*, vol. 27, no. 2, pp. 146–148, 1982.

[247] X. Zhang, J. Zuo, and C. Jian, "Experimental isobaric vapor-liquid equilibrium for binary systems of ethyl methyl carbonate + methanol, + ethanol, + dimethyl carbonate, or + diethyl carbonate at 101.3 kPa," *Journal of Chemical and Engineering Data*, vol. 55, no. 11, pp. 4896–4902, 11 2010.

[248] R. Naejus, D. Lemordant, R. Coudert, and P. Willmann, "Excess thermodynamic properties of binary mixtures containing linear or cyclic carbonates as solvents at the temperatures 298.15 K and 315.15 K," *The Journal of Chemical Thermodynamics*, vol. 29, p. 15031515, 1997.

[249] M. Anouti, Y. R. Dougassa, C. Tessier, L. El Ouatani, and J. Jacquemin, "Low pressure carbon dioxide solubility in pure electrolyte solvents for lithium-ion batteries as a function of temperature. Measurement and prediction," *Journal of Chemical Thermodynamics*, vol. 50, pp. 71–79, 7 2012.

[250] F. Blanchard, B. Carré, F. Bonhomme, P. Biensan, and D. Lemordant, "Solubility of carbon dioxide in alkylcarbonates and lactones," *Canadian Journal of Chemistry*, vol. 81, no. 5, pp. 385–391, 5 2003.

[251] E. M. Terrado, J. I. Pardo, J. S. Urieta, and A. M. Mainar, "Solubilities of nonpolar gases in dimethyl carbonate and diethyl carbonate," *Journal of Chemical & Engineering Data*, vol. 50, no. 2, pp. 512–516, 2005.

[252] N. Xin, Y. Sun, C. J. Radke, and J. M. Prausnitz, "Osmotic and activity coefficients for five lithium salts in three non–aqueous solvents," *Journal of Chemical Thermodynamics*, vol. 132, pp. 83–92, 5 2019.

[253] Y. R. Dougassa, C. Tessier, L. El Ouatani, M. Anouti, and J. Jacquemin, "Low pressure carbon dioxide solubility in lithium-ion batteries based electrolytes as a function of temperature. Measurement and prediction," *Journal of Chemical Thermodynamics*, vol. 61, pp. 32–44, 2013.

[254] Y. R. Dougassa, J. Jacquemin, L. El Ouatani, C. Tessier, and M. Anouti, "Viscosity and carbon dioxide solubility for $LiPF_6$, LiTFSI, and LiFAP in alkyl carbonates: lithium salt nature and concentration effect," *Journal of Physical Chemistry B*, vol. 118, no. 14, pp. 3973–3980, 4 2014.

[255] A. Chremos, E. Forte, V. Papaioannou, A. Galindo, G. Jackson, and C. S. Adjiman, "Modelling the phase and chemical equilibria of aqueous solutions of alkanolamines and carbon dioxide using the SAFT-γ SW group contribution approach," *Fluid Phase Equilibria*, vol. 407, pp. 280–297, 1 2016.

[256] Y. F. Feng, C. Wang, J. N. Shen, and Y. J. He, "Kinetic resolution of thermal runaway for lithium-ion batteries: A Gaussian surrogate-assisted separate optimization approach," *Chemical Engineering Science*, vol. 277, 8 2023.

[257] W. Li, K. R. Crompton, C. Hacker, and J. K. Ostanek, "Comparison of current interrupt device and vent design for 18650 format lithium-ion battery caps," *Journal of Energy Storage*, vol. 32, 12 2020.

[258] L. Yuan, T. Dubaniewicz, I. Zlochower, R. Thomas, and N. Rayyan, "Experimental study on thermal runaway and vented gases of lithium-ion cells," *Process Safety and Environmental Protection*, vol. 144, pp. 186–192, 2020.

[259] S. Koch, A. Fill, and K. P. Birke, "Comprehensive gas analysis on large scale automotive lithium-ion cells in thermal runaway," *Journal of Power Sources*, vol. 398, pp. 106–112, 2018.

[260] O. De la Iglesia, A. M. Mainar, J. I. Pardo, and J. S. Urieta, "Solubilities of nonpolar gases in triethylene glycol dimethyl ether, tetraethylene glycol dimethyl ether, dimethyl carbonate, and diethyl carbonate at 298.15 k and 101.33 kpa partial pressure of gas," *Journal of Chemical & Engineering Data*, vol. 48, no. 3, pp. 657–661, 2003.

[261] F. J. Günter, J. Keilhofer, C. Rauch, S. Rössler, M. Schulz, W. Braunwarth, R. Gilles, R. Daub, and G. Reinhart, "Influence of pressure and temperature on the electrolyte filling of lithium-ion cells: Experiment, model and method," *Journal of Power Sources*, vol. 517, p. 230668, 2022.

[262] J. Ming, Z. Cao, Y. Wu, W. Wahyudi, W. Wang, X. Guo, L. Cavallo, J.-Y. Hwang, A. Shamim, L.-J. Li *et al.*, "New insight on the role of electrolyte additives in rechargeable lithium ion batteries," *ACS energy letters*, vol. 4, no. 11, pp. 2613–2622, 2019.

[263] Sigma Aldrich, "Product specification: Vinylene Carbonate," 2024.

[264] ——, "Product specification: Fluoroethylene carbonate," 2024.

[265] Institut für Arbeitsschutz der Deutschen Gesetzlichen Unfallversicherung, "GESTIS - Stoffdatenbank," 2020.

[266] F. A. Mier, S. M. Hill, J. Lamb, and M. J. Hargather, "Non-invasive internal pressure measurement of 18650 format lithium-ion batteries during thermal runaway," *Journal of Energy Storage*, vol. 51, 7 2022.

[267] M. S. Shaharun, H. Mukhtar, and B. K. Dutta, "Solubility of carbon monoxide and hydrogen in propylene carbonate and thermomorphic multicomponent hydroformylation solvent," *Chemical Engineering Science*, vol. 63, no. 11, pp. 3024–3035, 2008.

[268] N. Li, P. Ma, and S. Xia, "Determination of solubility of carbon monoxide in methanol-dimethyl carbonate under high pressure," *Shiyou Huagong*, vol. 34, no. 1, pp. 60–64, 2005.

[269] A. Behr, D. Obst, and C. Schulte, "Kinetik der isomerisierenden hydroformylierung von trans-4-octen," *Chemie Ingenieur Technik*, vol. 76, no. 7, pp. 904–910, 2004.

[270] O. Rivas and J. Prausnitz, "Sweetening of sour natural gases by mixed-solvent absorption: solubilities of ethane, carbon dioxide, and hydrogen sulfide in mixtures of physical and chemical solvents," *AIChE Journal*, vol. 25, no. 6, pp. 975–984, 1979.

[271] S. E. Sloop, J. B. Kerr, and K. Kinoshita, "The role of li-ion battery electrolyte reactivity in performance decline and self-discharge," *Journal of power sources*, vol. 119, pp. 330–337, 2003.

[272] B. Winter, C. Winter, T. Esper, J. Schilling, and A. Bardow, "SPT-NRTL: A physics-guided machine learning model to predict thermodynamically consistent activity coefficients," *Fluid Phase Equilibria*, vol. 568, p. 113731, 5 2023.

[273] J. G. Rittig, K. C. Felton, A. A. Lapkin, and A. Mitsos, "Gibbs-Duhem-informed neural networks for binary activity coefficient prediction," *Digital Discovery*, vol. 2, no. 6, pp. 1752–1767, 2023.

[274] V. Pokorný, V. Štejfa, M. Fulem, C. Červinka, and K. Růžička, "Vapor pressures and thermophysical properties of ethylene carbonate, propylene carbonate, γ-Valerolactone, and γ-Butyrolactone," *Journal of Chemical & Engineering Data*, vol. 62, no. 12, pp. 4174–4186, 12 2017.

[275] A. Butland and R. Maddison, "The specific heat of graphite: An evaluation of measurements," *Journal of Nuclear Materials*, vol. 49, no. 1, pp. 45–56, 1973.

[276] K. S. Gavritchev, G. A. Sharpataya, A. A. Smagin, E. N. Malyi, and V. A. Matyukha, "Calorimetric study of thermal decomposition of lithium hexafluorophosphate," *Journal of Thermal Analysis and Calorimetry*, vol. 73, pp. 71–83, 2003.

[277] S. O. Dang, "Modelling thermodynamic properties of intercalation compounds for lithium-ion batteries," Ph.D. dissertation, RWTH Aachen University, Jülich, 2015.

[278] P. Gotcu and H. J. Seifert, "Thermophysical properties of $LiCoO_2$-$LiMn_2O_4$ blended electrode materials for lithium-ion batteries," *Physical Chemistry Chemical Physics*, vol. 18, no. 15, pp. 10 550–10 562, 4 2016.

[279] M. S. Ding, "Liquid-solid phase equilibria and thermodynamic modeling for binary organic carbonates," *Journal of Chemical and Engineering Data*, vol. 49, no. 2, pp. 276–282, 3 2004.

[280] C. L. Yaws, *Chemical Properties Handbook: Physical, Thermodynamics, Environmental Transport, Safety & Health Related Properties for Organic & Inorganic Chemicals*. New York, N.Y.: McGraw- Hill Education LLC, 1998.

[281] H. Maleki, S. A. Hallaj, J. R. Selman, R. B. Dinwiddie, and H. Wang, "Thermal properties of lithium-ion battery and components," *Journal of The Electrochemical Society*, vol. 146, no. 3, pp. 947–954, 3 1999.

[282] P. Lindstrom, "NIST ChemistryWebBook," 1997.

[283] J. Chase, *NIST-JANAF thermochemical tables*. Woodbury, N.Y.: American Institute of Physics, 1998.

[284] J. E. Hurst and B. Keith Harrison, "Estimation of liquid and solid heat capacities using a modified Kopps rule," *Chemical Engineering Communications*, vol. 112, no. 1, pp. 21–30, 2 1992.

[285] J. W. Larson, "Thermodynamics of formation, hydrolysis and ionization of monofluorophosphorous acid," *Polyhedron*, vol. 10, no. 14, pp. 1695–1698, 1 1991.

[286] www.ddbst.com, "Dortmund Data Bank," 2020.

[287] C. G. Maier and K. K. Kelley, "An equation for the representation of high-temperature heat content data," *Journal of the American Chemical Society*, vol. 54, no. 8, pp. 3243–3246, 8 1932.

[288] C. L. Yaws, *Thermophysical Properties of Chemicals and Hydrocarbons*, 2nd ed. Elsevier Inc., 2014.

[289] G. Wypych, "Knovel solvents: a properties database: a comprehensive collection of health, safety, and physical property information for over 1100 different solvents," ChemTec Pub, New York, Tech. Rep., 2000.

[290] S. C. Chen, C. C. Wan, and Y. Y. Wang, "Thermal analysis of lithium-ion batteries," *Journal of Power Sources*, vol. 140, no. 1, pp. 111–124, 2005.

[291] Amsler & Frey AG, "Technisches Datenblatt PVDF Polyvinylfluorid," Amsler & Frey AG, Schinznach-Dorf, Tech. Rep., 8 2013.

[292] K. Batra and I. Sc, "Role of additives in linear low density polyethylene (lldpe) films," *Project Report (2013-14)/Department of chemistry/Indian institute of Technology KHaragpur/Kharagpur, west Bengal-721302*, 2014.

[293] A. Loges, S. Herberger, P. Seegert, and T. Wetzel, "A study on specific heat capacities of lithium-ion cell components and their influence on thermal management," *Journal of Power Sources*, vol. 336, pp. 341–350, 12 2016.

[294] M. Herrmann, "Packaging-materials review," in *AIP Conference Proceedings*, vol. 1597, no. 1. American Institute of Physics, 2014, pp. 121–133.

[295] L. C. Wilson, L. V. Jasperson, D. Vonniederhausern, N. F. Giles, and C. Ihmels, "DIPPR Project 851 - Thirty years of vapor-liquid critical point measurements and experimental technique development," *Journal of Chemical and Engineering Data*, vol. 63, no. 9, pp. 3408–3417, 9 2018.

[296] I. H. Bell, J. Wronski, S. Quoilin, and V. Lemort, "Pure and pseudo-pure fluid thermophysical property evaluation and the open-source thermophysical property library CoolProp," *Industrial & Engineering Chemistry Research*, vol. 53, no. 6, pp. 2498–2508, 2 2014.

[297] P. Gotcu-Freis, D. M. Cupid, M. Rohde, and H. J. Seifert, "New experimental heat capacity and enthalpy of formation of lithium cobalt oxide," *The Journal of Chemical Thermodynamics*, vol. 84, pp. 118–127, 5 2015.

[298] T. Abe and T. Koyama, "Thermodynamic modeling of the $LiCoO_2$–CoO_2 pseudo-binary system," *Calphad*, vol. 35, no. 2, pp. 209–218, 6 2011.

[299] M. Wang, A. Navrotsky, S. Venkatraman, and A. Manthiram, "Enthalpy of formation of $LiCoO_2$," *Journal of The Electrochemical Society*, vol. 152, no. 7, p. J82, 2005.

[300] M. S. Ding, K. Xu, S. Zhang, and T. R. Jow, "Liquid/solid phase diagrams of binary carbonates for lithium batteries part II," *Journal of The Electrochemical Society*, vol. 148, no. 4, p. A299, 2001.

[301] K.-H. Lee and S.-J. Park, "Thermo-physical properties, excess and deviation properties for a mixture of γ-butyrolactone with diethyl carbonate or propylene carbonate," *Korean Journal of Chemical Engineering*, vol. 35, no. 1, pp. 222–233, 1 2018.

[302] G. P. Cunningham, G. A. Vidulich, and R. L. Kay, "Several properties of acetonitrile-water, acetonitrile-methanol, and ethylene carbonate-water systems," *Journal of Chemical & Engineering Data*, vol. 12, no. 3, pp. 336–337, 7 1967.

[303] H. Y. Oh, J.-E. Gu, and S.-J. Park, "Solid-liquid equilibria and thermo-physical properties of liquid electrolyte systems for lithium-ion batteries," *Fluid Phase Equilibria*, vol. 473, pp. 138–144, 10 2018.

[304] S. Hess, M. Wohlfahrt-Mehrens, and M. Wachtler, "Flammability of lithium-ion battery electrolytes: Flash point and self-extinguishing time measurements," *Journal of The Electrochemical Society*, vol. 162, no. 2, pp. A3084–A3097, 2015.

[305] J. Neuhaus, E. von Harbou, and H. Hasse, "Physico-chemical properties of solutions of lithium bis(fluorosulfonyl)imide (LiFSI) in dimethyl carbonate, ethylene carbonate, and propylene carbonate," *Journal of Power Sources*, vol. 394, pp. 148–159, 8 2018.

[306] R. Kempa and W. H. Lee, "392. The dipole moments of some cyclic carbonates," *Journal of the Chemical Society (Resumed)*, p. 1936, 1958.

[307] R. Naejus, C. Damas, D. Lemordant, R. Coudert, and P. Willmann, "Excess thermodynamic properties of the ethylene carbonate–trifluoroethyl methyl carbonate and propylene carbonate–trifluoroethyl methyl carbonate systems at T = (298.15 or 315.15) K," *The Journal of Chemical Thermodynamics*, vol. 34, no. 6, pp. 795–806, 6 2002.

[308] Y. J. Fang and J. M. Qian, "Isobaric vapor-liquid equilibria of binary mixtures containing the carbonate group -OCOO," *Journal of Chemical and Engineering Data*, vol. 50, no. 2, pp. 340–343, 3 2005.

[309] H. L. Liu, G. Feng, and Y. Hu, "A modified PR equation," *Tianranqi Huagong*, vol. 1, no. 2, pp. 47–50, 1987.

[310] H. S. Booth and F. B. Dutton, "The fluorination of phosphoryl trichloride," *Journal of the American Chemical Society*, vol. 61, no. 10, pp. 2937–2940, 10 1939.

[311] B. E. Poling, J. M. Prausnitz, and J. P. O'Connel, *The Properties of Gases and Liquids*, 5th ed. New York: McGraw-Hill Education, 2001.

[312] M. Łencka and A. Anderko, "Modeling phase equilibria in mixtures containing hydrogen fluoride and halocarbons," *AIChE Journal*, vol. 39, no. 3, pp. 533–538, 3 1993.

[313] R. Privat, J.-N. Jaubert, and Y. Privat, "A simple and unified algorithm to solve fluid phase equilibria using either the gamma–phi or the phi–phi approach for binary and ternary mixtures," *Computers & Chemical Engineering*, vol. 50, pp. 139–151, 3 2013.

[314] M. S. Ding, "Excess Gibbs energy of mixing for organic carbonates from fitting of their binary phase diagrams with nonideal solution models," *Journal of Solution Chemistry*, vol. 34, no. 3, pp. 343–359, 3 2005.

[315] P. Kolář, H. Nakata, J. W. Shen, A. Tsuboi, H. Suzuki, and M. Ue, "Prediction of gas solubility in battery formulations," *Fluid Phase Equilibria*, vol. 228-229, pp. 59–66, 2 2005.

[316] J. de la Torre, A. Cháfer, A. Berna, and R. Muñoz, "Liquid-liquid equlibria of the system dimethyl carbonate + methanol + water at different temperatures," *Fluid Phase Equilibria*, vol. 247, no. 1-2, pp. 40–46, 9 2006.

[317] S. Dufal, T. Lafitte, A. J. Haslam, A. Galindo, G. N. Clark, C. Vega, and G. Jackson, "Corrigendum: The A in SAFT: developing the contribution of association to the Helmholtz free energy within a Wertheim TPT1 treatment of generic Mie fluids," *Molecular Physics*, vol. 113, no. 9-10, pp. 948–984, 5 2015.

[318] D. S. Hall, J. Self, and J. R. Dahn, "Dielectric constants for quantum chemistry and lithium-ion batteries: Solvent blends of ethylene carbonate and ethyl methyl carbonate," *Journal of Physical Chemistry C*, vol. 119, no. 39, pp. 22 322–22 330, 9 2015.

[319] R. P. Seward and E. C. Vieira, "The dielectric constants of ethylene carbonate and of solutions of ethylene carbonate in water, methanol, benzene and propylene carbonate," *The Journal of Physical Chemistry*, vol. 62, no. 1, pp. 127–128, 1958.

[320] H. Schwetlick, *Numerische Lösung nichtlinearer Gleichungen*, 346th ed. Berlin: Deutscher Verlag der Wissenschaften, 1979.

[321] K. Kwon, F. Kong, F. McLarnon, and J. W. Evans, "Characterization of the SEI on a carbon film electrode by combined EQCM and spectroscopic ellipsometry," *Journal of The Electrochemical Society*, vol. 150, no. 2, p. A229, 2003.

[322] C. H. Shomate, "A method for evaluating and correlating thermodynamic data," *The Journal of Physical Chemistry*, vol. 58, no. 4, pp. 368–372, 4 1954.

[323] V. V. Avdeev, A. P. Savchenkova, L. A. Monyakina, I. V. Nikol'skaya, and A. V. Khvostov, "Intercalation reactions and carbide formation in graphite-lithium system," *Journal of Physics and Chemistry of Solids*, vol. 57, no. 6-8, pp. 947–949, 6 1996.

[324] National Center for Biotechnology Information, "PubChem compound summary for CID 61681, difluorophosphoric acid," 6 2023.

[325] Y. Suehiro, M. Nakajima, K. Yamada, and M. Uematsu, "Critical parameters of {xCO2+ (1- x) CHF3} for x=(1.0000, 0.7496, 0.5013, and 0.2522)," *The Journal of Chemical Thermodynamics*, vol. 28, no. 10, pp. 1153–1164, 1996.

[326] F. A. Perdomo, S. H. Khalit, C. S. Adjiman, A. Galindo, and G. Jackson, "Description of the thermodynamic properties and fluid-phase behavior of aqueous solutions of linear, branched, and cyclic amines," *AIChE Journal*, vol. 67, no. 3, p. e17194, 2021.

[327] G. L. Gutsev, "A theoretical study on the structure and stability of the PFn and PFn- series n=1-6," *The Journal of Chemical Physics*, vol. 98, no. 1, pp. 444–452, 1993.

[328] K. Bica, M. Deetlefs, C. Schröder, and K. R. Seddon, "Polarisabilities of alkylimidazolium ionic liquids," *Physical Chemistry Chemical Physics*, vol. 15, p. 2703, 2013. [Online]. Available: www.rsc.org/pccp

[329] V. Papaioannou, F. Calado, T. Lafitte, S. Dufal, M. Sadeqzadeh, G. Jackson, C. S. Adjiman, and A. Galindo, "Application of the saft-γ mie group contribution equation of state to fluids of relevance to the oil and gas industry," *Fluid Phase Equilibria*, vol. 416, pp. 104–119, 2016.

List of Figure

List of Tables

List of Abbreviations and Symbols

Formula Symbols

$\%AAD$	Percentage average absolute deviation	%
$\%AD$	Percentage absolute deviation	%
AAD	Average absolute deviation	—
AD	Absolute deviation	—
$\Delta \underline{G}_r$	Gibbs free energy of reaction	$J\,mol^{-1}$
$\Delta \underline{H}_r$	Enthalpy of reaction	$J\,mol^{-1}$
$\Delta \underline{H}_{vap}$	Enthalpy of vaporisation	$J\,mol^{-1}$
$\Delta \underline{S}_r$	Entropy of reaction	$J\,K^{-1}\,mol^{-1}$
$\underline{C}_p$	Isobaric specific heat capacity	$J\,mol^{-1}\,K^{-1}$
A	Area, Helmholtz free energy	m^2, J
a	Activity, Attractive parameter in cubic equations of state	—, $Pa\,m^6\,mol^{-2}$
a_s	Specific surface area	m^{-1}
b	Co-volume parameter in cubic equations of state	$m^3\,mol^{-1}$
C	Concentration	$mol\,m^{-3}$
c_1, c_2	Constants for cubic equations of state	—
C_p	Isobaric total heat capacity	$J\,K^{-1}$
c_p	Isobaric mass specific heat capacity	$J\,g^{-1}\,K^{-1}$
D	Dielectric constant	—
E_A	Activation energy	$J\,mol^{-1}$
H	Henry's coefficient	Pa^{-1}
h	Height	m
I	Ionisation potential	eV
K, K_A	Bonding volume, Equilibrium, resp. association constant	m^3,—
k_0	Frequency factor	$mol\,s^{-1}$,$mol\,m\,s^{-1}$

l	Length	m
N	Total number of points	—
n	Molar amount	mol
p	Pressure	Pa
P_{n}	Coupling term related to effective charge	—
r	Center-center distance, radius	m
r	Reaction rate	$\mathrm{mol\,s^{-1}}$
T	Temperature	K
T_{b}	Boiling temperature	K
T_{c}	Critical temperature	K
T_{d}	Dew temperature	K
T_{r}	Reduced temperature	—
V	Volume	$\mathrm{m^3}$
v	Molar volume	$\mathrm{m^3\,mol^{-1}}$
w	Width	m
X	Experimental values	—
x	Liquid molar fraction	—
Y	Simulation values	—
y	Vapour molar fraction	—
Z	Compressibility factor	—
z	Global molar fraction, charge	—
α	Degree of salt dissociation	—
$\alpha(T_{\mathrm{r}})$	Temperature dependency of attractive parameter in cubic EoS	—
α^0	Electronic polarisability	$\mathrm{m^3}$
Δ	Packing fraction	—
Γ	Screening length	m
γ'_0	Activity coefficient of ion-pair	—
$\gamma'_{\pm}$	Mean activity coefficient of ions	—
ε	Potential well, volume fraction	J, —
κ	Debye shielding length coefficient	$\mathrm{m^{-1}}$
λ^y	y=a,r, attractive, repulsive exponents	—

μ	Chemical potential, mean value	$\mathrm{J\,mol^{-1}}$, —
ν	Stoiciometric coefficient	—
ρ	Density, number density	$\mathrm{kg\,m^{-3}}$,$\mathrm{m^{-3}}$
σ	Interaction distance, standard deviation	m, —
ϕ	Fugacity coefficient	—
Ω	Set, Coupling term related to packing fraction	—
ω	Acentric factor	—

Indices

g	Species in gas phase
i	Species
j	Reaction
k	SAFT segment
l	Species in liquid phase, SAFT segment
s	Species in solid phase
u	Species in reaction j

γ	Species in gas phase in case of double sum
μ	Solid electrolyte interphase species
σ	Solvent species

Constants

ε_0	Permittivity of the vacuum, $8.8541878128 \cdot 10^{-12}$	$\mathrm{F\,m^{-1}}$
e	Elementary charge, $1.60217663 \cdot 10^{-19}$	C
F	Faraday's constant, 96485.33212	$\mathrm{C\,mol^{-1}}$
h	Planck's constant, $6.62607015 \cdot 10^{-34}$	J s
k_B	Boltzmann's constant, $1.380649 \cdot 10^{-23}$	$\mathrm{J\,K^{-1}}$
N_A	Avogadro's constant, $6.0221476 \cdot 10^{23}$	$\mathrm{mol^{-1}}$
R	Molar gas constant, 8.314462	$\mathrm{J\,K^{-1}\,mol^{-1}}$

Subscripts

$1, 2, 3, \ldots$	Numbering of constants
+,-,±	Cation, anion, mean-ionic
A	Association
a	Site on SAFT segment k
An	Anode
association	Association term in Helmholtz free energy
b	Backwards reaction, Site on SAFT segment l
bat	Battery
Born	Born term in Helmholtz free energy
c	Critical
Cat	Cathode
chain	Chain term in Helmholtz free energy
DCS	Double coated sheets
El	Electrolyte
f	Forwards reaction
G	Set of gaseous species
ion	Ion term in Helmholtz free energy
monomer	Monomer term in Helmholtz free energy
PT	Phase transition
r	Reaction
RE	Set of all reactions
S	Set of solid species
SCS	Single coated sheets
SEI	Solid electrolyte interphase
Solv	Set of solvent species
tot	Total
U	Set of all species taking part in reaction j

Superscripts

$\ominus$	IUPAC reference state
',""	Liquid and gaseous state
a	Attractive term
fix	Fixed polar molecules
HB	Hydrogen bonding
max	Maximum solubility
Mie	Mie potential
polar	Polar molecules
r	Repulsive term
Res	Residual

Abbreviations

AM	Active material
ARC	Accelerated rate calorimetry
BC	Buthylene carbonate
CID	Current interruption device
DEC	Diethyl carbonate
DMC	Dimethyl carbonate
DPC	Dipropyl carbonate
DSC	Differential scanning calorimetry
EC	Ethylene carbonate
EMC	Ethyl methyl carbonate
EoS	Equation of state
EV	Electric vehicle
GC	Group contribution
HWS	Heat-Wait-Seek
ICEV	Internal combustion engine vehicle
IUPAC	International union of pure and applied chemistry
LEDC	Lithium ethylene dicarbonate
MS	Mass spectrometry

MSA	Mean sphere approximation
OEMS	Online electrochemical mass spectrometry
PC	Propylene carbonate
PR	Peng-Robinson
SAFT	Statistical associating fluid theory
SEI	Solid electrolyte interphase
SRK	Soave-Redlich-Kwong
TGA	Thermogravimetric analysis
VC	Vinylene carbonate
VdW	Van-der-Waals
VLE	Vapour-liquid equilibrium

A Additional model equations[1]

The following chapter entails additional model equations that have, due to space restrictions, not been included in the main body of the manuscript. First, the reference volume calculations are presented. This is followed by a description of how the initial conditions are calculated. Thereafter, the thermodynamic models utilised within the scope of this thesis to obtain a proper set of physical parameters are described. Ultimately, a detailed description of the SAFT-γ Mie EoS is given.

A.1 Reference volumes

The calculation of the reference volumes of the electrolyte V_{El}, the active material in the anode $V_{\mathrm{AM,An}}$, the active material in the cathode $V_{\mathrm{AM,Cat}}$ and the SEI volume V_{SEI}, respectively, is necessary to calculate the concentrations needed for the reaction kinetics.

The electrolyte volume V_{El} is calculated by the density ρ and the molar mass M of both electrolyte solvents:

$$V_{\mathrm{El}} = \sum_{\sigma}^{|\Omega_{\mathrm{Solv}}|} \frac{n_{\sigma}^{'} \cdot M_{\sigma}}{\rho_{\sigma}} \tag{A.1}$$

The volume of both active materials, $V_{\mathrm{AM,An}}$ and $V_{\mathrm{AM,Cat}}$, is determined by the coated areas A, the number of sheets used in the battery $n_{\mathrm{DCS/SCS}}$, the given volume fraction of the active materials ε and their thickness d. All needed parameters are listed in Table B.1.

$$V_{\mathrm{AM,An}} = (2 \cdot n_{\mathrm{DCS,An}} \cdot A_{\mathrm{Cell}}) \cdot \varepsilon_{\mathrm{AM,An}} \cdot d_{\mathrm{An}}, \tag{A.2}$$

[1] Parts of this chapter have been published as own contributions in Baakes, F., Lüthe M., Gerasimov, M., Laue, V., Röder, F., Balbuena, P., Krewer, U., "Unveiling the interaction of reactions and phase transition during thermal abuse of Li-ion batteries", Journal of Power Sources, DOI:10.1016/j.jpowsour.2021.230881, CC BY 4.0 [60].

$$V_{\mathrm{AM,Cat}} = ((2 \cdot n_{\mathrm{DCS,Cat}} \cdot A_{\mathrm{Cell}}) + n_{\mathrm{SCS,Cat}} \cdot A_{\mathrm{Cell}})) \cdot \varepsilon_{\mathrm{AM,Cat}} \cdot d_{\mathrm{Cat}}. \tag{A.3}$$

The SEI volume V_{SEI} is calculated analogously to the electrolyte volume based on the molar amounts of each SEI component:

$$V_{\mathrm{SEI}} = \sum_{\mu}^{|\Omega_{\mathrm{SEI}}|} \frac{n_\mu \cdot M_\mu}{\rho_\mu}. \tag{A.4}$$

A.2 Initial conditions

This section covers the calculation of initial molar amounts of the solvent components n_{EC} and n_{EMC} as well as SEI components n_{LEDC}, $n_{\mathrm{Li_2CO_3}}$, n_{LiOH}, $n_{\mathrm{Li_2O}}$, and n_{LiF}.

The following equation illustrates how to calculate the initial electrolyte volume based on the structural data of the battery, which can be found in Table B.1:

$$\begin{aligned} V_{\mathrm{El}} = &\left(\left((2 \cdot n_{\mathrm{DCS,Cat}} \cdot A_{\mathrm{Cell}}) + n_{\mathrm{SCS,Cat}} \cdot A_{\mathrm{Cell}}) \right) \cdot \varepsilon_{\mathrm{El,Cat}} \cdot d_{\mathrm{Cat}} \right) \\ &+ \left((2 \cdot n_{\mathrm{DCS,An}} \cdot A_{\mathrm{Cell}}) \cdot \varepsilon_{\mathrm{El,An}} \cdot d_{\mathrm{An}} \right) \\ &+ \left((2 \cdot n_{\mathrm{DCS,An}} \cdot A_{\mathrm{Cell}}) \cdot \varepsilon_{\mathrm{El,Sep}} \cdot d_{\mathrm{Sep}} \right) \end{aligned} \tag{A.5}$$

Based on this volume, the initial amount of each component can be calculated based on the assumed volume fractions and rearranging Equation A.1. Please note that this also assumes that the solvent components are in the liquid state only and no gas volume is present.

For the calculation of the initial SEI volume, a planar surface on the anode particles is assumed, such that it can be calculated from the anodes specific surface area a_{s} and the SEI thickness d_{SEI} as described in Equations A.6 & A.7:

$$a_{\mathrm{s,An}} = \frac{\varepsilon_{\mathrm{AM,An}} \cdot 3}{r_{\mathrm{An}}}, \tag{A.6}$$

$$V_{\mathrm{SEI}} = a_{\mathrm{s,An}} \cdot V_{\mathrm{AM,An}} \cdot d_{\mathrm{SEI}}. \tag{A.7}$$

Analogously to the solvent species, the initial molar amounts of each SEI component can be calculated based on assumed volume fractions by rearranging Equation A.4.

For the calculation of initial amounts of HF, H_2O, PF_5, POF_3, and HPO_2F_2 parts per million are utilised:

$$\mathrm{ppm} = \frac{\frac{n \cdot M}{\rho} \cdot 10^6}{V_{\mathrm{El}}}, \tag{A.8}$$

where the mass M is the molar mass, and ρ the density. Again rearranging Equation A.8 for n gives the needed initial values in molar quantity.

The initial concentration of lithium in each electrode is calculated as follows:

$$C_{\mathrm{Li},0,\mathrm{An/Cat}} = C_{\mathrm{max,\,An/Cat}} \cdot \Big(z_{0,\mathrm{An/Cat}} + SOC \cdot (z_{1,\mathrm{An/Cat}} - z_{0,\mathrm{An/Cat}}) \Big), \tag{A.9}$$

here the maximum concentration of each active material has been calculated as:

$$C_{\mathrm{max,\,An/Cat}} = \frac{\frac{V_{\mathrm{An/Cat}} \cdot \rho_{\mathrm{An/Cat}}}{M_{\mathrm{An/Cat}}}}{V_{\mathrm{An/Cat}}} = \frac{\rho_{\mathrm{An/Cat}}}{M_{\mathrm{An/Cat}}}. \tag{A.10}$$

Additionally, *SOC* refers to a number between 0 and 1 corresponding to the battery's state of charge. Further, $z_{1,\mathrm{An/Cat}}$ and $z_{0,\mathrm{An/Cat}}$ refer to the degree of lithium intercalation or insertion in the anode or cathode active material at SOC 1 or 0, respectively.

A.3 Thermodynamic calculations

For various species, different thermodynamic models have been employed to determine the caloric properties (molar heat capacity, change of molar enthalpy and enthalpy of formation) as well as liquid and vapour density. So, this section aims to present all used auxiliary equations and is structured as follows. First, a short comment on general underlying assumptions is given. This is followed by presenting the various models for caloric properties, such as heat capacity and the temperature dependence of enthalpy. Next, the density calculations include the Peng-Robinson EoS with some modifications. Thereafter, the vapour-liquid equilibrium model used in Chapter 4 and the solubility model are displayed.

A.3.1 General assumptions

If no pressure-dependent equations have been available, it has been generally assumed that all equations by the different authors describe the isobaric molar or mass-specific heat capacity at the chosen standard pressure $p^{\ominus}$ = 1 bar. This assumption has been made in Chapters 4 and 5 describing the corresponding species and their state of matter:

- **EC_s & EC_l :** [274],
- **C :** [275],
- **$LiPF_6$:**[276],
- **Li_xCoO_2 :** [277] and [278],
- **EMC_l :** [279],
- **EC_g& EMC_g :** [280],
- **LiC_6 :** [281].

The influence of pressure on the isobaric molar heat capacity is generally considered negligible regarding solids and liquids. For consistency reasons, data from the [282] have been preferred. Molar mass values of $LiCoO_2$, LiC_6 and $(CH_2OCO_2Li)_2$ are calculated by summing up the molar mass of the atoms forming the species. The same reference states for all elements to determine the standard enthalpy of formation as in the [283]. The standard enthalpy of formation of LiC_6 has been calculated by correcting the known enthalpy of formation at 455 K using the implemented model for enthalpy change. Table B.2 shows all species properties at standard conditions $p^{\ominus} = 100\,000\,\mathrm{Pa}$ and $T^{\ominus} = 298.15\,\mathrm{K}$.

A.3.2 Heat capacity and change in molar enthalpy

The following subsection will exhibit the models used for heat capacity calculations. First, the Shomate equation will be presented as it is used for most species. After this, the models for species where the Shomate equation has not been available will be given. These range from simple constant heat capacity models to some modifications of the Mayer-Kelley type equation.

A.3.2.1 Shomate equation

The Shomate equation is the standard method to calculate the isobaric heat capacity and change in molar enthalpy put forth by the NIST Chemistry Webbook [282]. The equation is given with:

$$\underline{C}_{\mathrm{p}^{\ominus},i} = A_i + B_i \cdot \left(\frac{T}{1000}\right) + C_i \cdot \left(\frac{T}{1000}\right)^2 + D_i \cdot \left(\frac{T}{1000}\right)^3 + \frac{E_i}{\left(\frac{T}{1000}\right)^2}. \tag{A.11}$$

Integration of Equation A.11 gives the temperature dependency of molar enthalpy as follows:

$$\Delta\underline{H}_i^{\ominus\rightarrow T} = \left(A_i \cdot \left(\frac{T}{1000}\right) + B_i \cdot \frac{\left(\frac{T}{1000}\right)^2}{2} + C_i \cdot \frac{\left(\frac{T}{1000}\right)^3}{3} + D_i \cdot \frac{\left(\frac{T}{1000}\right)^4}{4} + \frac{E_i}{\left(\frac{T}{1000}\right)} + F_i - H_i\right). \tag{A.12}$$

$A_i, B_i, C_i, D_i, E_i, F_i, H_i$ Parameters of the Shomate equations

Parameters of all relevant Shomate Equations have been taken from NIST Chemistry Webbook and have been modified in cases of suspected mismatches. Table A.1 presents all utilised values and modifications.

Table A.1: Parameters for Shomate equation.

Species	State	A_i $\frac{J}{molK}$	B_i $\frac{J}{molK^2}$	C_i $\frac{J}{molK^3}$	D_i $\frac{J}{molK^4}$	E_i $\frac{JK}{mol}$	F_i $\frac{J}{mol}$	H_i $\frac{J}{mol}$	Temp. Range K
Li	solid	169.552	−882.711	1977.438	−1487.312	−1.609 635	−31.248 25	0	298 - 453.69
Li	liquid	32.46972	−2.635975	−6.327128	4.230359	0.005 686	−7.117 319	0 *	453.69 - 700
P	solid	16.45576	43.28892	−58.73876	25.60646	−0.086 728	−6.657 121	0	298 - 317.3
P	liquid	26.32602	1.041373	−6.12136	1.094033	2.995 196	−7.234 262	0 **	317.3 - 1180.008
Co	solid	10.9943	54.375	−55.5132	25.817	0.164 533	−4.7033	0	298 - 700
H_2	gas	33.066178	−11.363417	11.432816	−2.772874	−0.158 558	−9.980 797	0	298 - 1000
F_2	gas	31.4451	8.413831	−2.77885	0.218104	−0.211 175	−10.4326	0	298 - 6000
O_2	gas	31.32234	−20.23531	57.86644	−36.50624	−0.007 374	−8.903 471	0	100 - 700
HF	gas	30.11693	−3.246612	2.868116	0.457914	−0.024 861	−281.4912	−272.5462	298 - 1000
POF_3	gas	40.13209	152.4223	−133.0863	41.85757	−0.539 184	−1273.71	−1254.25	298 - 1100
PF_5	gas	55.27064	187.0637	−171.7833	56.05807	−1.108 38	−1621.518	−1594.409	298 - 1100
H_2O	liquid	−203.606	1523.29	−3196.413	2474.455	3.855 326	−256.5478	−285.8304	298 - 372.78
H_2O	gas	30.092	6.832514	6.793435	−2.53448	0.082 139	−250.881	−285.8304 ***	372.78 - 1700
CO_2	gas	24.99735	55.18696	−33.69137	7.948387	−0.136 638	−403.6075	−393.5224	298 - 1200
C_2H_4	gas	−6.38788	184.4019	−112.9718	28.49593	0.315 54	48.173 32	52.46694	298 - 1200
LiF	solid	41.75837	18.7111	0.693674	−0.992621	−0.487 055	−631.8342	−616.9308	298 - 1121.3
Li_2O	solid	68.6971	5.467149	23.18308	−9.495631	−1.602 44	−625.0352	−598.7304	298 - 1600
Li_2CO_3	solid	68.3323	146.639	−162.573	248.026	−0.702 297	−1244.29	−1216.04	298 - 683.15 ****
Co_3O_4	solid	177.0953	−100.4361	185.7792	−49.04861	−3.483 951	−971.5415	−910.02	298 - 1500

* value of Nist Chemistry Webbook 2.380002 corrected to 0
** value of Nist Chemistry Webbook 0.615002 corrected to 0
*** value of Nist Chemistry Webbook -241.8264 corrected to -285.8304
**** value of Nist Chemistry Webbook of upper-temperature limit 683.00 corrected to 683.15

A.3.2.2 Constant heat capacity — LiC_6, LEDC, HPO_2F_2

For LiC_6, LEDC, and HPO_2F_2, none of the more accurate mathematical descriptions for the caloric properties have been available. Therefore constant molar heat capacities have been assumed. Furthermore, the lack of any caloric data for LEDC has necessitated an approximation by a modified Kopp's rule by [284]. For HPO_2F_2, the constant heat is assumed to be similar to its mono fluoro counterpart and is taken from Larson et al. [285]. The heat capacity is thus given as:

$$\underline{C}_{\mathrm{p}^{\ominus},i} = const, \tag{A.13}$$

the temperature dependence for the molar enthalpy $\Delta\underline{H}_i^{\ominus\rightarrow T}$ is given with:

$$\Delta\underline{H}_i^{\ominus\rightarrow T} = \underline{C}_{\mathrm{p}^{\ominus},i} \cdot \left(T - T^{\ominus}\right). \tag{A.14}$$

$\underline{C}_{\mathrm{p}^{\ominus},i}$ / $\frac{\mathrm{J}}{\mathrm{mol\,K}}$ Molar heat capacity at constant pressure of species i
$\Delta\underline{H}_i^{\ominus\rightarrow T}$ / $\frac{\mathrm{kJ}}{\mathrm{mol}}$ Molar enthalpy change of species i

A.3.2.3 Estimation of liquid and solid heat capacities — LEDC

The lack of data on the thermodynamic properties of LEDC has necessitated using the modified (Neumann-)Kopp rule by [284] to estimate the molar heat capacity at standard conditions. Equation A.15 shows the correlation for the estimation of liquid and solid heat capacities:

$$\underline{C}_{\mathrm{p}^{\ominus},i} = \left(\sum_{i=1}^{n_i} C_e \cdot N_{ei}\right) + C_{\mathrm{Misc}} \cdot N_{\mathrm{Misc},i}. \tag{A.15}$$

$\underline{C}_{\mathrm{p}^{\ominus},i}$ / $\frac{\mathrm{J}}{\mathrm{mol\,K}}$ Estimated molar heat capacity at $T^{\ominus}$ = 298 K of the species i
C_e / $\frac{\mathrm{J}}{\mathrm{mol\,K}}$ Constant associated with each element e
N_{ei} / - Number of occurrences of element e in the species i
C_{Misc} / $\frac{\mathrm{J}}{\mathrm{mol\,K}}$ Constant associated with elements not having a specified constant
$N_{\mathrm{Misc},i}$ / - Number of elements e not having a specified constant in the species i
n_i / - Number of different elements in species i for which there are specific constants.

The corresponding coefficients are listed in Table A.2.

Table A.2: Coefficients for solid and liquid species used in correlation by [284]

Element	H	Li	Be	B	C	N	O	F	Na	Mg	Al	Si	S	Cl	K	Ca	Misc
solid C_e	7.56	23.25	12.47	10.10	10.89	18.74	13.42	26.16	26.19	22.69	18.07	17.00	12.36	24.69	28.78	28.25	26.63
liquid C_e	9.20	...	...	...	13.08	30.19	16.00	19.47	...	...	...	...	32.05	31.91	...	...	26.19

Element	Ti	V	Mn	Fe	Co	Ni	Cu	Br	Sr	Zr	Mo	I	Ba	W	Hg	Pb
solid C_e	27.24	29.36	28.06	29.08	25.71	25.46	26.92	25.36	28.41	26.82	29.44	25.29	32.37	30.87	27.87	31.60
liquid C_e	...	...	...	...	...	...	...	37.23	...	...	...	...	...	...	...	...

To asses the accuracy of this approach, the %AD between the molar heat capacity at standard conditions estimated with the correlation by [284] and available reference data from thermodynamic databases and publications has been calculated.

The %AD is lower than 20 %, except for $LiPF_6$. Especially the marginal deviation of 1.47 % for Li_2CO_3 renders the chosen approach viable to estimate the molar heat capacity at standard conditions of LEDC.

Table A.3: Estimated molar heat capacity at standard conditions ($T^{\ominus}$ = 298.15 K, $p^{\ominus} = 10^5$ Pa) for LEDC and comparison of estimations by the mod. NKR by [284] to reference data for selected species

species	$\underline{C}_{p^{\ominus},i}$ at $T^{\ominus}$ estimated by mod. NKR[284] $\frac{J}{mol\,K}$	$\underline{C}_{p^{\ominus},i}$ at $T^{\ominus}$ reference data $\frac{J}{mol\,K}$	%AD %
$C_3H_4O_3$	103.17	117.44 [286]	12.15
$LiPF_6$	206.84	151.1 [276]	36.89
$Li_{0.977}CoO_2$	75.27	71.52 [278]	5.24
LiF	49.41	41.815 [283]	18.16
Li_2O	59.92	54.087 [283]	10.80
Li_2CO_3	97.65	96.232 [283]	1.47
Co_3O_4	130.81	123.051 [283]	6.31
$(CH_2OCO_2Li)_2$ (LEDC)	200.82		

A.3.2.4 Maier-Kelley type equations — $LiPF_6$ and $LiCoO_2$

Another often employed model equation for the isobaric heat capacity is the Maier-Kelley type. Here, two modifications of the equations, originally published by [287], were employed.

A.3.2.4.1 $LiPF_6$ The equations to describe the molar heat capacity and molar enthalpy change of $LiPF_6$ are based on the results of [276]:

$$\underline{C}_{p^{\ominus},LiPF_6} = a + b \cdot T - c \cdot \left(\frac{1}{T^2}\right) + d \cdot T^2 + e \cdot T^3 + f \cdot T^4 \tag{A.16}$$

a,b,c,d,e,f Specific parameters of the modified Maier-Kelley type equation by [276]

Table A.4: Parameter sets for the Maier-Kelley equations to model $LiPF_6$ as described by[276]

a	b	c	d	e	f	Temp. Range
$\frac{J}{mol\,K}$	$\frac{J}{mol\,K^2}$	$\frac{J\,K}{mol}$	$\frac{J}{mol\,K^3}$	$\frac{J}{mol\,K^4}$	$\frac{J}{mol\,K^5}$	K
113.98	0.22	2122892	$-5.35 \cdot 10^{-4}$	$2.60 \cdot 10^{6}$	$-3.33 \cdot 10^{-9}$	298–410

A.3.2.4.2 Li_xCoO_2 In the publications by [277] and [278], the identical Maier-Kelley type equation (Equation A.17) has been used to describe the molar heat capacity of lithium cobalt oxide Li_xCoO_2:

$$\underline{C}_{p^{\ominus},Li_xCoO_2} = a_1 + a_2 \cdot T + a_3 \cdot T^{-2}, \tag{A.17}$$

the change in molar enthalpy can again be calculated by integration as in:

$$\Delta\underline{H}^{\ominus\rightarrow T}_{Li_xCoO_2} = a_1 \cdot \left(T - T^{\ominus}\right) + a_2 \cdot \left(\frac{T^2 - T^{\ominus 2}}{2}\right) - a_2 \cdot \left(\frac{1}{T^{\ominus}} - \frac{1}{T}\right) \tag{A.18}$$

a_1, a_2, a_3 Specific parameters of the modified Maier-Kelley type equation

To consider the delithiation of the cathode caused by the simulated chemical reactions, the thermodynamic properties have to be made dependent on the respective chemical composition of the active cathode material (Li_xCoO_2) at each timestep. This has been achieved by inserting Li/Co-ratio (x) dependent parameters $a_1(x)$, $a_2(x)$, $a_3(x)$ into the Eqs. A.17 and A.18:

$$\underline{C}_{\mathrm{p}^\ominus,\mathrm{Li}_x\mathrm{CoO}_2} = a_1(x) + a_2(x)\cdot T + a_3(x)\cdot T^{-2} \tag{A.19}$$

$$\Delta\underline{H}^{\ominus\rightarrow T}_{\mathrm{Li}_x\mathrm{CoO}_2} = a_1(x)\cdot\left(T - T^\ominus\right) + a_2(x)\cdot\left(\frac{T^2 - T^{\ominus 2}}{2}\right) - a_2(x)\cdot\left(\frac{1}{T^\ominus} - \frac{1}{T}\right) \tag{A.20}$$

The publication by [278] provides measurements of molar heat capacity of Li_xCoO_2 for x = 0.977. A set of parameters (a_1, a_2, a_3) has been fitted to the measurements in the temperature range from 240 K to 603 K.
These parameters have been correlated with measurements of the molar heat capacity of $Li_{0.977}CoO_2$. The publication by [277] provides two sets of parameters (a_1,a_2,a_3) for x = $\{0.5, 0.67\}$. These are correlated with the molar heat capacity of $Li_{0.5/0.67}CoO_2$ derived from DFT calculations.
All of these correlated parameter sets and the corresponding coefficients of determination are listed in Tab. A.5.

Table A.5: Parameter sets for the Maier-Kelley equations described by [278] and [277] with respective Li/Co-ratios.

x	a_1	a_2	a_3	Temp. Range	Ref
-	$\frac{\mathrm{J}}{\mathrm{mol\,K}}$	$\frac{\mathrm{J}}{\mathrm{mol\,K^2}}$	$\frac{\mathrm{JK}}{\mathrm{mol}}$	K	
0.977	85.1	$2.42587\cdot10^{-2}$	$-1.80728\cdot10^{6}$	240–603.2	[278]
0.67	84.7	$0.98\cdot10^{-2}$	$-1.37\cdot10^{6}$	250–600	[277]
0.5	75.1	$2.24\cdot10^{-2}$	$-1.37\cdot10^{6}$	250–600	[277]

Piece-wise linear interpolation between the above-listed parameters is used to obtain mathematical expressions for $a_1(x)$, $a_2(x)$, $a_3(x)$. Figure A.1 compares the employed model against available simulative and experimental data.

For Li/Co-ratios lower than 0.5, the parameters are extrapolated by the corresponding linear interpolation.

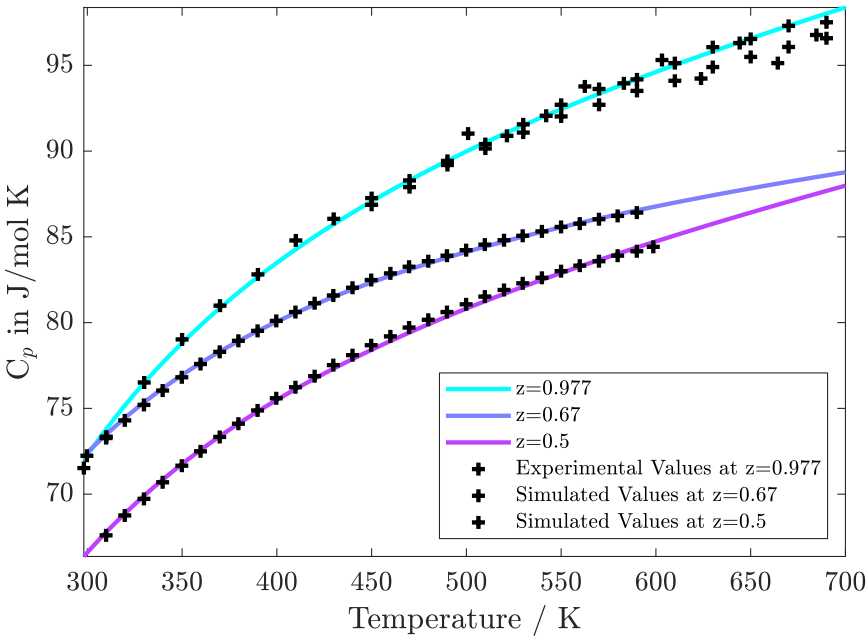

Figure A.1: Comparison of the correlated second-degree polynomial for Li_xCoO_2 utilised in Chapter 4 and 5 with the results published by Dang et al. [277] and Gotcu-Freis et al. [278]

A.3.2.5 Equation by Butland and Madison — Carbon (C)

The equations describing the molar heat capacity and the molar enthalpy change of carbon in the simulation are derived from the results of [275]. Their publication focuses on the heat capacity of graphite, which represents the reference state for Carbon. [275] describe a fitted curve (Equation A.21) of the (mass) specific heat capacity at constant pressure $c_{\mathrm{p}^{\ominus},\mathrm{C}}$ in $\frac{\mathrm{cal}}{\mathrm{g\,K}}$ valid from 250 K up to 3000 K:

$$c_{\mathrm{p}^{\ominus},\mathrm{C}} = A + B \cdot T + \frac{C}{T} + \frac{D}{T^2} + \frac{E}{T^3} + \frac{F}{T^4} \tag{A.21}$$

molar heat capacity at constant pressure of Carbon $\underline{C}_{\mathrm{p}^{\ominus},\mathrm{C}}$ in $\frac{\mathrm{J}}{\mathrm{g\,K}}$ is described by:

$$\underline{C}_{\mathrm{p}^{\ominus},\mathrm{C}} = M_{\mathrm{C}} \cdot f_{conv.} \cdot \left(A + B \cdot T + \frac{C}{T} + \frac{D}{T^2} + \frac{E}{T^3} + \frac{F}{T^4} \right) \tag{A.22}$$

A, B, C, D, E, F	Specific parameters for equations based on [275]
$M_{\mathrm{C}} = 12.0107\ \frac{\mathrm{g}}{\mathrm{mol}}$	molar mass of Carbon
$f_{\mathrm{conv.}} = 4.184 \times 10^4\ \frac{\mathrm{J\,g}}{\mathrm{cal\,kg}}$	conversion factor as stated in [283]

Table A.6: Parameters of Butland and Madison equation[275]

A $\frac{\mathrm{cal}}{\mathrm{g\,K}}$	B $\frac{\mathrm{cal}}{\mathrm{g\,K^2}}$	C $\frac{\mathrm{cal}}{\mathrm{g}}$	D $\frac{\mathrm{cal\,K}}{\mathrm{g}}$	E $\frac{\mathrm{cal\,K^2}}{\mathrm{g}}$	F $\frac{\mathrm{cal\,K^3}}{\mathrm{g}}$	valid Temp. Range
0.538657	9.11129×10^{-6}	−90.2725	−43449.3	1.59309×10^7	-1.43688×10^9	250–3000

A.3.2.6 Equation by Pokorný et al. — Liquid and solid EC

The equation provided by Pokorný et al. [274], and terms derived from it are used to calculate the relevant caloric properties of solid and liquid EC. The following Equation A.23 is given by [274] to determine the molar heat capacity at constant pressure for multiple solid or liquid substances.

$$\underline{C}_{\mathrm{p}^{\ominus},i} = R \cdot \sum_{j=0}^{n} A_{ij+1,i} \cdot \left(\frac{T}{100} \right)^{j} \tag{A.23}$$

$A_{1,i}, A_{2,i}, A_{3,i}, A_{4,i}$ Specific parameters of the equation by [274]

Table A.7: Values of the parameters for solid and liquid EC in the equation described by [274]

	$A_{1,\mathrm{EC_{s/l}}}$ $\left(\frac{\mathrm{J}}{\mathrm{mol\,K}}\right)$	$A_{2,\mathrm{EC_{s/l}}}$ $\left(\frac{\mathrm{J}}{\mathrm{mol\,K^2}}\right)$	$A_{3,\mathrm{EC_{s/l}}}$ $\left(\frac{\mathrm{J}}{\mathrm{mol\,K^3}}\right)$	valid Temp. Range K
solid (s)	9.16145	−4.18175	2.04450	262–308
liquid (l)	8.52925	3.26969	−0.212330	293–466

A.3.2.7 Equation by Ding et al. — Liquid EMC

The equation provided by [279], and terms derived from it are used to calculate the relevant caloric properties of liquid EMC. By correcting the expression by [279] with the molar mass of EMC Equation A.24 has been obtained to determine the molar heat capacity at constant pressure:

$$\underline{C}_{\mathrm{p}^{\ominus},\mathrm{EMC_l}} = M_{\mathrm{EMC}} \cdot \left(a_0 + a_1 \cdot \left(\frac{T}{1000} \right) + a_2 \cdot \left(\frac{T}{1000} \right)^2 + a_3 \cdot \left(\frac{T}{1000} \right)^3 \right) \tag{A.24}$$

a_0, a_1, a_2, a_3 Parameters specific for liquid EMC given by [279] (see Tab. B.2)

$M_{\mathrm{EMC}} = 104.1045 \ \frac{\mathrm{g}}{\mathrm{mol}}$ molar mass of EMC

Table A.8: Values of the parameters for liquid EMC in the equation described by [279]

$a_{0,\mathrm{EMC_l}}$ $\left(\frac{\mathrm{J}}{\mathrm{mol\,K}}\right)$	$a_{1,\mathrm{EMC_l}}$ $\left(\frac{\mathrm{J}}{\mathrm{mol\,K}}\right)$	$a_{2,\mathrm{EMC_l}}$ $\left(\frac{\mathrm{J}}{\mathrm{mol\,K^2}}\right)$	$a_{3,\mathrm{EMC_l}}$ $\left(\frac{\mathrm{J}}{\mathrm{mol\,K^3}}\right)$	valid Temp. Range (K)
1.0943	2.2044	0	0	280–400

A.3.2.8 Equations by Yaws et al. — EC and EMC

Several Equations from [280] are utilised by the simulation to calculate thermophysical properties. The following Equation A.25 is given by [288] to determine the molar heat capacity at constant pressure for gaseous substances:

$$\underline{C}_{\mathrm{p}^{\ominus},i} = A_i + B_i \cdot T + C_i \cdot T^2 + D_i \cdot T^3 + E_i \cdot T^4 + F_i \cdot T^5 + G_i \cdot T^6, \tag{A.25}$$

the respective integration to obtain the change in molar enthalpy is then as follows:

$$\begin{aligned}\Delta\underline{H}_i^{\ominus\rightarrow T} =& \Delta\underline{H}_{\mathrm{vap},i} + \Delta\underline{H}_{i_{\mathrm{s,l}}}^{\ominus\rightarrow T_{\mathrm{b},i}} + A_i \cdot \left(T - T_{b,i}\right) + \\ & B_i \cdot \left(\frac{T^2 - {T_{\mathrm{b},i}}^2}{2}\right) + C_i \cdot \left(\frac{T^3 - {T_{\mathrm{b},i}}^3}{3}\right) + D_i \cdot \left(\frac{T^4 - {T_{\mathrm{b},i}}^4}{4}\right) + \\ & E_i \cdot \left(\frac{T^5 - {T_{\mathrm{b},i}}^5}{5}\right) + F_i \cdot \left(\frac{T^6 - {T_{\mathrm{b},i}}^6}{6}\right) + G_i \cdot \left(\frac{T^7 - {T_{\mathrm{b},i}}^7}{7}\right)\end{aligned} \tag{A.26}$$

The given parameters are defined as:

$A_i, B_i, C_i, D_i, E_i, F_i, G_i$	Species i specific parameters provided by [280]
$T_{\mathrm{b},i}(\mathrm{p}^{\ominus})$ / K :	Boiling temperature of substance i at $p^{\ominus} = 1\,\mathrm{bar}$
$\Delta\underline{H}_{\mathrm{vap},i}(T_{\mathrm{b}})$ / $\frac{\mathrm{J}}{\mathrm{mol}}$:	Molar enthalpy of vaporisation of substance i at boiling temperature T_{b}
$\Delta\underline{H}_{i_{\mathrm{l}}}^{\ominus\rightarrow T_{\mathrm{b},i}}$ / $\frac{\mathrm{J}}{\mathrm{mol}}$:	Molar enthalpy change of liquid substance i from $T^{\ominus}$ to $T_{\mathrm{b},i}$ at $p^{\ominus} = 1\,\mathrm{bar}$

The parameters provided by [280] have been used for gaseous EC. For gaseous EMC, the parameters (A_{EMC} to G_{EMC}) have been fitted to data of the molar heat capacity from [289].

A.3.2.9 Heat capacity calculations for inert materials

The heat capacity of the entire battery is the sum of the individual heat capacities of all components (see Equation A.27). Furthermore, inert components like the current collector and the pouch cell have been considered. Exemplary the heat capacity of the aluminium current is determined by:

$$C_{\mathrm{p,Al}} = c_{\mathrm{p,Al}} \cdot \rho_{\mathrm{Al}} \cdot V_{\mathrm{Al}}, \tag{A.27}$$

Table A.9: Values of the parameters for gaseous EC and gaseous EMC in the equation described by [280]

		EC	EMC
A_i	$\frac{\mathrm{J}}{\mathrm{mol\,K}}$	79.99101664	33.5333
B_i	$\frac{\mathrm{J}}{\mathrm{mol\,K^2}}$	-0.462426097	0.326515
C_i	$\frac{\mathrm{J}}{\mathrm{mol\,K^3}}$	0.002745562	-0.0000681751
D_i	$\frac{\mathrm{J}}{\mathrm{mol\,K^4}}$	$-5.21078 \cdot 10^{-6}$	$-3.74767 \cdot 10^{-8}$
E_i	$\frac{\mathrm{J}}{\mathrm{mol\,K^5}}$	$4.88306 \cdot 10^{-9}$	$-1.92466 \cdot 10^{-12}$
F_i	$\frac{\mathrm{J}}{\mathrm{mol\,K^6}}$	$-2.27373 \cdot 10^{-12}$	$1.451 \cdot 10^{-15}$
G_i	$\frac{\mathrm{J}}{\mathrm{mol\,K^7}}$	$4.18731 \cdot 10^{-16}$	$-4.25976 \cdot 10^{-19}$
valid Temp. Range	K	298.15–600	301.49–600

V_{Al} represents the total volume of aluminum inside the battery. The volumes need to be approximated:

$$V_{\mathrm{Al}} = A_{\mathrm{Cell}} \cdot n_{\mathrm{DCS,Cat}} \cdot d_{\mathrm{DCS,Cat}} + A_{\mathrm{Cell}} \cdot n_{\mathrm{SCS,Cat}} \cdot d_{\mathrm{SCS,Cat}} \tag{A.28}$$

$$V_{\mathrm{Cu}} = A_{\mathrm{Cell}} \cdot n_{\mathrm{DCS,An}} \cdot d_{\mathrm{DCS,An}} \tag{A.29}$$

$$V_{\mathrm{Pouch\,foil}} = 2 \cdot A_{\mathrm{Cell}} \cdot d_{\mathrm{Pouch\,foil}} + 2 \cdot (d_{\mathrm{Bat}} \cdot w_{\mathrm{Bat}}) \cdot d_{\mathrm{Pouch\,foil}} \tag{A.30}$$

$$V_{\mathrm{PVDF}} = \varepsilon_{\mathrm{PVDF}} \cdot V_{\mathrm{An}} + \varepsilon_{\mathrm{PVDF}} \cdot V_{\mathrm{Cat}} \tag{A.31}$$

The thickness of the battery pouch foil is determined by the difference between the thickness of the entire battery and the accumulated thickness of all internal components:

$$\begin{aligned} d_{\mathrm{Pouch\,foil}} = d_{\mathrm{Cell}} - (&n_{\mathrm{DCS,An}} \cdot d_{\mathrm{DCS,Cu}} + n_{\mathrm{DCS,An}} \cdot 2 \cdot (d_{\mathrm{An}} + d_{\mathrm{Sep}}) \\ &+ n_{\mathrm{DCS,Cat}} \cdot d_{\mathrm{DCS,Al}} + n_{\mathrm{DCS,Cat}} \cdot 2 \cdot d_{\mathrm{Cat}} + n_{\mathrm{SCS,Cat}} \cdot d_{\mathrm{SCS,Al}}) \end{aligned} \tag{A.32}$$

The entire battery mass is computed by adding up the mass of each component:

$$m_{\mathrm{Cell}} = \sum_{i}^{|SP|} n_i \cdot M_i + V_{\mathrm{Al}} \cdot \rho_{\mathrm{Al}} + V_{\mathrm{Cu}} \cdot \rho_{\mathrm{Cu}} + V_{\mathrm{Pouch\,foil}} \cdot \rho_{\mathrm{Pouch\,foil}} + V_{\mathrm{PVDF}} \cdot \rho_{\mathrm{PVDF}} \tag{A.33}$$

Table A.10: Specific heat capacity and density of the relevant inert materials.

Parameter	Aluminum	Copper	PE	Pouch foil	Separator	PVDF
c_p / J kg^{-1} K^{-1}	903 [290]	385[290]	-	1273 *	1978 [290]	1200 [291]
ρ / kg m^{-3}	2702[290]	8933[290]	900 [292]	1494 [293]	1008 [290]	1770 [291]

* Calculated as the mixture of 33 % aluminum and 67 % PE as given in a 3 layer pouch foil [294]

A.3.2.10 Enthalpy of vaporisation — EC, EMC, DMC

The enthalpy of vaporisation has been calculated for all relevant species (EC, EMC, DMC) based on the equation stated by Yaws' Critical Property Data for Chemical Engineers and Chemists:

$$\Delta \underline{H}_{\mathrm{vap},i} = 1000 \cdot A_i \cdot \left(1 - \frac{T}{T_{\mathrm{c},i}}\right)^{n_i} \tag{A.34}$$

A_i, n_i Parameter of the equation by [280] for species i

$T_{\mathrm{c},i}$ /K Critical temperature of species i

The critical Temperatures T_c and the sources can be taken from the table A.16. The Parameters A and n for each species have been derived by the authors individually.

EC: The published measurements of the enthalpies of vaporisation in the range from 310.3 K to 369.5 K by [245] have been used to fit the equation parameters of EC.

EMC / DMC: Because of a severe lack of usable data regarding EMC, an established model of the close chemical analogue DMC has been utilised. The Parameter n has been fitted to data generated by the Helmholtz energy equation of the state of DMC in the range from 298.15 K to 519 K implemented in the CoolProp Library. Then the parameter A has been fitted to the known value of the enthalpy of EMC vaporisation.

A.3.2.11 Standard enthalpy of formation — Li_xCoO_2

Compared to most other species, the standard enthalpy of formation for Li_xCoO_2 depends on the degree of intercalation. Thus, a second-degree polynomial expression, see Equation A.35,

Table A.11: Parameter values to describe the enthalpy of vaporisation for EC, EMC and DMC.

	A_i	$T_{c,i}$	n_i	valid Temp. Range
	$\frac{J}{mol}$	K	-	K
EC	72.1349	786 [295]	0.359691	298.15–786
EMC	43.2451	560.75 [247]	0.250254	298.15–560.75
DMC	44.2645	557 [296]	0.250254	298.15–557

has been constructed by Gotcu-Freis et al. [297]. Figure A.2 show the comparison of the model equation against simulated data by Abe et al. [298] and experimental data by Gotcu-Freis et al. [297] as well as Wang et al. [299].

$$\Delta \underline{H}^{\ominus}_{f,Li_xCoO_2} = -280445 - 479287 \cdot x + 81323.9 \cdot x^2 \tag{A.35}$$

Table A.12: Deviation between data by [299] or [278] respectively of the fitted curve described by [298]

x	$AD\left(\Delta \underline{H}^{\ominus}_{f,Li_xCoO_2}\right)$	$\%AD\left(\Delta \underline{H}^{\ominus}_{f,Li_xCoO_2}\right)$
—	$\frac{kJK}{mol}$	%
1.00	1.202	0.18
0.977	1.978	0.29
0.93	1.635	0.25
0.88	4.060	0.64
0.80	6.297	1.04
0.75	11.446	1.96
0.47	18.035	3.84
$\sum/n$	6.379	1.17

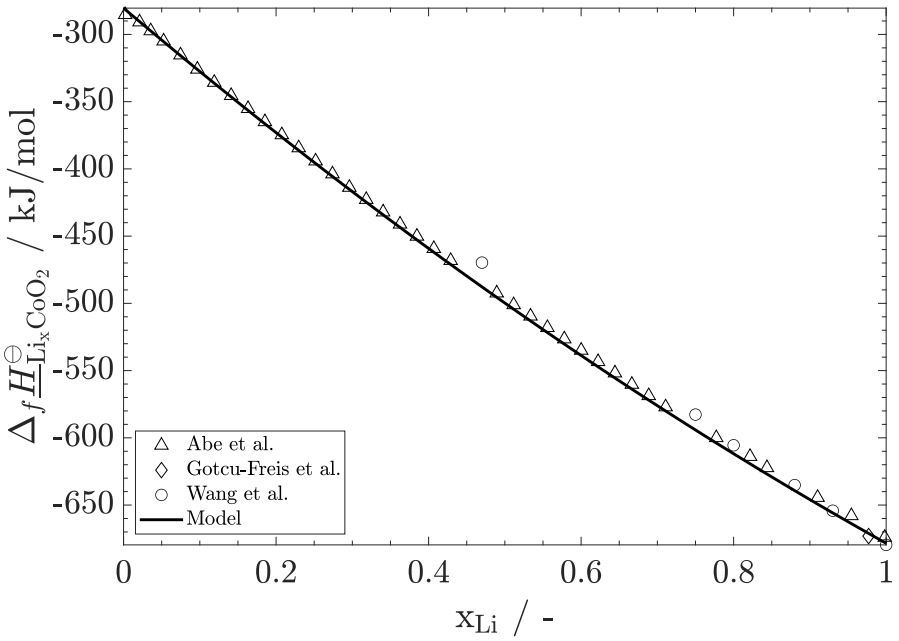

Figure A.2: Comparison of the correlated second-degree polynomial, solid black line, utilised in this work with the results published by [298], upward triangles, and measurements by [299], circles, and [297], diamonds.

A.3.3 Densities

The employed models to calculate the densities for various species will be presented. Starting with empirical equations for liquid density calculation and proceeding with the Peng-Robinson equation and some modifications.

A.3.3.1 Density of liquids — Liquid EC

The density of pure liquid EC has been determined by the equation provided by [288]. This approach has been preferred to utilising the Peng-Robinson equation of state because of the known weakness in cubic equations of state related to the deviation between predicted liquid density values and experimental ones [119].
The parameter for Equation A.36 has been fitted to density data from multiple sources. The pressure dependent effect on liquid density is neglected[2]. Missing data, a similar approach for EMC has not been possible.

$$\rho_i = 1000 \cdot A_i \cdot B_i^{-\left(1-\frac{T}{T_{c,i}}\right)^{n_i}}; \tag{A.36}$$

A_i, B_i, n_i Parameter of the density equation by [280] for species i
ρ_i / $\frac{\text{kg}}{\text{m}^3}$ Density of the liquid state of pure species i

Table A.13: Values of the parameters for liquid EC in the equation described by [280]

A_{EC}	B_{EC}	$T_{c,EC}$	n_{EC}	valid Temp. Range
$\frac{\text{g}}{\text{m}^3}$	–	K	–	K
0.348012	0.207718	786 [295]	0.323643	309.55–790

[2] Differences between measurements at 1 atm = 101 325 Pa and at 1 bar = 100 000 Pa are neglected

Table A.14: Density data for liquid EC and %AD of the fitted function (Equation A.36)

Temperature T K	Density $\rho_{l,EC}$ $\frac{kg}{m^3}$	%AD($\rho_{l,EC}$) %	Temperature T K	Density $\rho_{l,EC}$ $\frac{kg}{m^3}$	%AD($\rho_{l,EC}$) %
298.15	1.321 [300]	1.296	313.2	1.321 [301]	0.072
	1.338 [302]	0.009	318.15	1.311 [239]	0.235
	1.35 [253]	0.880		1.316 [303]	0.146
312.15	1.322 [286]	0.052	318.2	1.316 [301]	0.150
	1.33 [304]	0.653	323.15	1.305 [305]	0.233
313.15	1.316 [239]	0.313	323.2	1.31 [301]	0.155
	1.32 [305]	0.009	328.15	1.3 [239]	0.152
	1.321 [306]	0.067	333.15	1.294 [305]	0.146
	1.322 [307]	0.143			

A.3.3.2 Density of gases and liquids: PR EoS — POF_3,PF_5, EMC, EC

The Peng-Robinson equation of state [118] has been used to determine the densities in the liquid or gaseous state for certain pure substances:

$$p = \frac{RT}{\underline{V}_i - b_i} - \frac{a_i\ \alpha_i(T)}{(\underline{V}_i \cdot (\underline{V}_i + b_i) + b_i \cdot (\underline{V}_i - b_i)} \tag{A.37}$$

$$a_i = 0.45724 \cdot \frac{(RT_{\mathrm{c},i})^2}{p_{\mathrm{c},i}} \quad b_i = 0.07780 \cdot \frac{RT_{\mathrm{c},i}}{p_{\mathrm{c},i}} \tag{A.38}$$

In addition to the α function, improved by Peng and Robinson themselves in 1978 [119], the α function specific to EC by Fang et al. [308] (developed from the expression of Liu et al. [309]) has also been implemented. Rearranging Equation A.37 gives a polynomial expression

Table A.15: α functions utilised for the PR EoS.

Peng-Robinson (1978) [119]	$\alpha_i(T) = \left(1 + \kappa_i \cdot \left(1 - \sqrt{T_{\mathrm{r},i}}\right)\right)^2$
Utilized for	$\kappa_i = 0.37464 + 1.54226 \cdot \omega_i - 0.26992 \cdot {\omega_i}^2$, $\omega_i \leq 0.491$
EMC, POF_3, PF_5	$\kappa_i = 0.379642 + 1.48503 \cdot \omega_i - 0.164423 \cdot {\omega_i}^2 + 0.016666 \cdot \omega^3$, $\omega_i > 0.491$
Liu-Feng-Hu (1987) [308, 309]	$\alpha_i(T) = 1 + (1 - T_{\mathrm{r},i}) \cdot \left(m_k + \frac{n_i}{{T_{\mathrm{r},i}}^2}\right)$
Utilized for EC	

Reduced temperature: $T_\mathrm{r} = \dfrac{T}{T_\mathrm{c}}$

[116] (Equation A.39):

$$\underline{V}_i^3 + \underline{V}_i^2 \cdot \left(b_i - \frac{RT}{p}\right) + \underline{V}_i \cdot \left(-3b_i^2 + \frac{a_i\ \alpha_i(T) - 2b_i\ RT}{p}\right) + \left(-b_i^3 + \frac{a_i\ \alpha_i(T) - b_i^2\ RT}{p}\right) = 0 \tag{A.39}$$

For conditions below the critical point, the lowest and highest roots of Equation A.39 represent the molar volumes of the liquid and the gas phase. The density of both phases can be calculated by Equation A.41. The assumed isobaric conditions ($p^{\ominus}$=10^5 Pa) entail that none of the

species modelled by the Peng-Robinson equation of state reaches a supercritical state during the simulation.

$$\rho_{\mathrm{g},i} = \frac{M_i}{\underline{V}_{\mathrm{g},i}} \text{ , } \underline{V}_{\mathrm{g},i}\text{: root with highest value of Equation A.39} \tag{A.40}$$

$$\rho_{\mathrm{l},i} = \frac{M_i}{\underline{V}_{\mathrm{l},i}} \text{ , } \underline{V}_{\mathrm{l},i}\text{: root with lowest value of Equation A.39} \tag{A.41}$$

Table A.16: Parameters for density calculation with PR EOS: Critical parameters (T_c & p_c), acentric factors (ω), boiling temperatures $T_{\mathrm{b},1\,\mathrm{atm}}$ at 1 atm and parameters (n & m) for the EC specific α function

Species	T_c	p_c	ω	$T_{\mathrm{b},1\,\mathrm{atm}}$	n	m
	K	MPa	-	K	-	-
$C_3H_4O_3$ (EC)	786 [295]	5.28 [295]	-	521.5906 **	0.1553 [308]	0.8101 [308]
$C_4H_8O_3$ (EMC)	560.75 [247]	3.839 [247]	0.429 321 *	380.8529 **	-	-
PF_5	295.7 [280]	3.72 [280]	0.170 694 [280]	188.3 [282]	-	-
POF_3	346.45 [310]	4.235 [310]	0.426 689 *	233.35 [310]	-	-

* Estimated based on Poling [311]
** Calculated by solving: $p_\mathrm{vap}(T_\mathrm{b}) = 1$ atm, see Equation A.55 for EC and Equation A.54 for EMC

A.3.3.2.1 Estimation of acentric factors — EMC and POF_3 To estimate the acentric factor of EMC and POF_3, the procedure described in Properties of Gases and Liquids by [311] is used:

$$T_{\mathrm{br},i} = \frac{T_{\mathrm{vap},i}}{T_{\mathrm{c},i}}, \quad \tau_i = 1 - T_{\mathrm{br},i} \tag{A.42}$$

$$\begin{aligned} f_i^{(0)} &= \frac{\left(-5.97616 \cdot \tau_i + 1.29874 \cdot \tau_i^{1.5} - 0.60394 \cdot \tau_i^{2.5} - 1.06841 \cdot tau_i^5\right)}{T_{\mathrm{br},i}} \\ f_i^{(1)} &= \frac{\left(-5.03365 \cdot \tau_i + 1.11505 \cdot \tau_i^{1.5} - 5.41217 \cdot \tau_i^{2.5} - 7.46628 \cdot \tau_i^5\right)}{T_{\mathrm{br},i}} \end{aligned} \tag{A.43}$$

$$\omega_i = -\frac{\ln\left(\frac{p_{\mathrm{c},i}}{101\,325\,\mathrm{Pa}}\right) + f_i^{(0)}}{f_i^{(1)}} \tag{A.44}$$

$T_{\mathrm{c},i,1\,\mathrm{atm}}$ / K Critical temperature of species i

$p_{\mathrm{c},i}$ / Pa Critical pressure of substance i

$T_{\mathrm{br},i}, \tau_i, f_i^{(0)}, f_i^{(1)}$ Substance-specific parameters for the equations from [311]

ω_i Estimated acentric factor of species i

Table A.17: Necessary data and estimated acentric factors ω given by approach in [311] for POF_3 and EMC

Species	$T_{\mathrm{b},i,1\,\mathrm{atm}}$	$T_{\mathrm{c},i}$	$p_{\mathrm{c},i}$	ω_i
EMC	381.05 K [247]	560.75 K [247]	3.839 MPa [247]	0.429321
POF_3	233.35 K [310]	346.45 K [310]	4.235 MPa [310]	0.426689

A.3.3.3 Density of gases: EoS by Łenka et al. — HF

The equation of state by Łenka et al. [312] has been employed to determine the density of gaseous HF. The compressibility factor Z is decomposed into a physical (Z^{ph}) and a chemical (Z^{ch}) contribution:

$$Z = Z^{\mathrm{ph}} + Z^{\mathrm{ch}} - 1 = \frac{p\underline{V}}{RT} \tag{A.45}$$

Physical contribution, Peng-Robinson equation of state:

$$Z^{\mathrm{ph}} = \frac{\underline{V}}{\underline{V}-b} - \frac{a(T)\underline{V}}{R\cdot T\cdot[\underline{V}\,(\underline{V}+b)+b\,(\underline{V}-b)]}, \tag{A.46}$$

with

$$a(T) = 10^6 \cdot \left(0.7187 + 0.2734 \cdot \exp\left(-0.6232\left(\frac{T}{100} - 4.02\right)^2\right)\right) \tag{A.47}$$

in $\mathrm{bar\,cm/mol^2}$ and

$$b = 9.69\,\mathrm{cm^3/mol} \tag{A.48}$$

Chemical contribution:

$$Z^{\mathrm{ch}}_{\mathrm{pure}} = F(q) = \frac{1+\sum_{k=1}^{8} a_k q^k}{(1+q)^8}, \quad q = \frac{RTK}{\underline{V}} \tag{A.49}$$

$$\ln K = \frac{-\Delta\underline{H}^0 + \Delta\underline{C}^0_{\mathrm{p}} T_0}{RT} + \frac{1}{R}\left(\Delta\underline{S}^0 - \Delta\underline{C}^0_{\mathrm{p}} - \Delta\underline{C}^0_{\mathrm{p}} \ln T_0\right) + \frac{\Delta\underline{C}^0_{\mathrm{p}}}{R}\ln T, \tag{A.50}$$

with $\Delta\underline{H}^0 = -35\,069\,\mathrm{J\,mol^{-1}}$, $\Delta\underline{S}^0 = -133.67\,\mathrm{J\,mol^{-1}\,K^{-1}}$ and $\Delta\underline{C}^0_{\mathrm{p}} = 52.68\,\mathrm{J\,mol^{-1}\,K^{-1}}$.

Table A.18: Parameters for the chemical contribution of the equation of state by Łenka et al. [312]

a_1	a_2	a_3	a_4	a_5	a_6	a_7	a_8
7.8291	−27.5821	113.5793	−88.229	55.9557	−2.9443	1.6500	0.109 27

Merging and rearranging Equation A.45 to Equation A.50 leads to a polynomial expression. The highest root of this expression represents the molar volume of the gaseous HF:

$$\rho_{\mathrm{g,HF}} = \frac{M_{\mathrm{HF}}}{\underline{V}_{\mathrm{g,HF}}}\,,\ \underline{V}_{\mathrm{g,HF}} \tag{A.51}$$

A.3.4 Simple vapour-liquid equilibria and solubility

This chapter summarises the needed definitions and all used equations and parameters for calculating the phase equilibria, including their derivation and transition heat.

For the VLE calculation, the method of Privat et al. [313] was used. The gas phase is assumed to be ideal:

$$\phi_{\mathrm{EC}} = \frac{z_{\mathrm{EC}} \cdot p}{p_{\mathrm{sat,EC}}}, \tag{A.52}$$

$$\phi_{\mathrm{EMC}} = \frac{(1 - z_{\mathrm{EC}}) \cdot p}{p_{\mathrm{sat,EMC}}}. \tag{A.53}$$

Here, ϕ refers to the individual fugacity coefficient for each solvent within the gas phase. The Antoine-Equation, see Equation A.54, and the Cox-Equation, see Equation A.55, have been used to describe the relation between vapour pressure and temperature for pure substances EC, EMC and DMC. They are given as follows:

$$\log(p_{\mathrm{vap}}) = A - \frac{B}{T + C}, \tag{A.54}$$

$$\ln \frac{p_{\mathrm{vap}}}{p^0} = \left(1 - \frac{T^0}{T}\right) \exp\left(\sum_{i=0}^{n} A_i \cdot T^i\right). \tag{A.55}$$

Where p_{vap} represents the vapour pressure, A, B, and C represent equation-specific parameters and p^0 and T^0 represent a certain reference pressure and temperature, respectively. The parameters are provided by Zhang et. al. [247] and Prokorný et al. [244, 274], see Table A.19. Models for the activity coefficient in liquid-phase have been taken from Ding [314]:

$$\gamma_{\mathrm{EC,\ EC\text{-}DMC}} = \exp\left(\frac{x_{\mathrm{DMC}}^2 (a_0 + 2 \cdot a_1 x_{\mathrm{EC}})}{RT}\right), \tag{A.56}$$

$$\gamma_{\mathrm{DMC,\ EC\text{-}DMC}} = \exp\left(\frac{x_{\mathrm{EC}}^2 (a_0 + 2 \cdot a_1 x_{\mathrm{EC}})}{RT}\right), \tag{A.57}$$

$$\gamma_{\mathrm{EC,\ EC\text{-}EMC}} = \exp\left(\frac{x_{\mathrm{EMC}}^2 (a_0 + 2 \cdot a_1 x_{\mathrm{EC}} + 3 \cdot a_2 x_{\mathrm{EC}}^2)}{RT}\right), \tag{A.58}$$

$$\gamma_{\mathrm{EMC,\ EC\text{-}EMC}} = \exp\left(\frac{x_{\mathrm{EC}}^2 (a_0 + 2 \cdot (a_1 - a_2) x_{\mathrm{EC}} + 3 \cdot a_2 \cdot x_{\mathrm{EC}}^2)}{RT}\right). \tag{A.59}$$

Table A.19: Model parameters used for the calculation of the phase equilibria using Equations A.54,A.55,A.56,A.57,A.58, and A.59

Species	A_1	$A_2 \cdot 10^3$	$A_3 \cdot 10^6$	T_0 / K	p_0 / Pa
EC[274]	3.354356	-0.7637676	0.5033676	309.13	12.78
DMC[244]	3.164781	-1.606787	1.477391	278.16	2358
	A	B	C		
EMC[247]	6.4308	1466.437	-49.461	-	-
Mixture	a_0	a_1	a_2		
DMC-EC [314]	2126.0	-944.19	0	-	-
EMC-EC [314]	2595.6	1053.7	-2121.2	-	-

No reference data has been available to validate the EC-EMC phase diagram used for the calculations in this work. Therefore the approach has been validated by calculating the phase equilibrium of a mixture EC-DMC for which data has been available, see Fig. A.3.

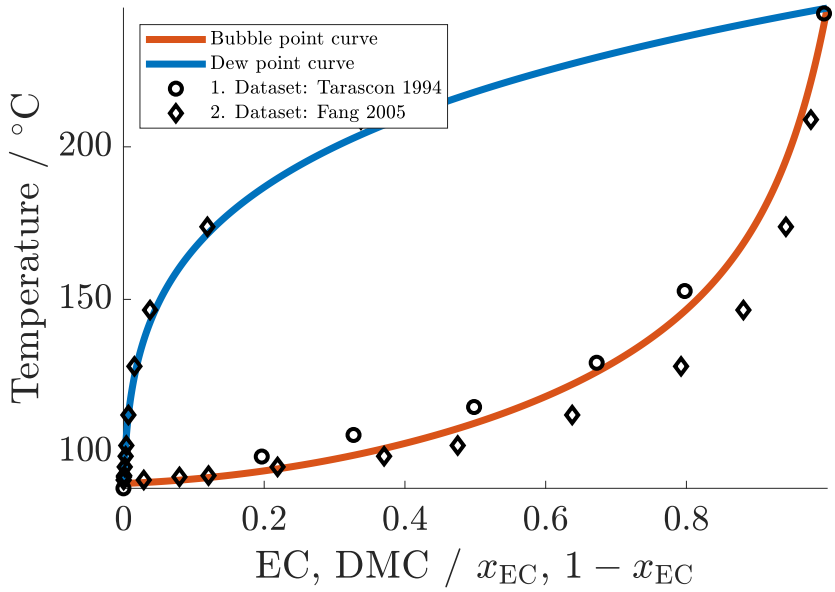

Figure A.3: Simulation of the phase diagram of EC-DMC at 101.3 kPa including measurement data from Fang et al. and Tarascon et al. [6, 308] for validation.

A.3.4.1 Numerical validation

The fraction of gas and liquid phases can be calculated at any timestep using the equilibrium data. To determine the vaporisation heat, the time derivative needs to be approximated. Therefore the artificial states, η''_{EC}, η''_{EMC}, are introduced in order to enable the numerical differentiation:

$$\sum_{\sigma}^{|\Omega_{\mathrm{Solv}}|} \frac{\mathrm{d}\eta''_{\sigma}}{\mathrm{d}t} = \frac{n''_{\sigma} - \eta''_{\sigma}}{10^{-|n''_{\sigma} - \eta''_{\sigma}| \cdot C}}. \tag{A.60}$$

Here C is an arbitrarily chosen constant, $C = 50000$ in this study. The percentage absolute deviation %AD calculated in Equation 3.53: Besides a major %AD at the beginning of boiling (91.4 % for both solvents), the %AAD over the entire simulated timespan is 0.3 % for EC and 0.01 % for EMC.

A.3.4.2 Solubility model

The solubility model is subdued to the following assumptions:

- All gas species stay completely dissolved until reaching their solubility limit in each solvent
- Liquid-liquid interactions between the solvents or dissolved species, as well as the used conductive salt, do not affect the solubility of gas species

As a source of temperature-dependent Henry coefficients, the results by Kolar et al. have been taken [315]. They used a predictive Soave-Redlich-Kwong equation of state combined with the Non-Random-Two-Liquid expression for activity coefficients for predicting solubilities of several gases in organic carbonates between 283 K and 363 K and pressures below 1 MPa. The prediction model correlates well with known gas solubility data over the entire temperature range. Unfortunately, only for some gases were data available in literature. Thus further assumptions have been unavoidable:

- All gas solubilities in EMC have been approximated by solubilities in DMC since it is also a linear carbonate
- In cases the solubility of a gas in EC has not been modelled, PC has been used since it is also a cyclic carbonate

- None of the renowned sources or thermodynamic databases could provide any information about the solubility of the considered fluorine species (HF, PF_5, POF_3) in relevant carbonates. Therefore, based on the simulations by Kolar et al. [315], CO has been chosen for EC and N_2 for EMC to represent the solubility characteristics of the fluorine species. This has been done since the polarization of these substances is the closest to each other, and no better approximation has been available. Here, future research on the solubility of fluorinated species in common battery electrolyte solvents such as EC, DMC and EMC could be of significant value.
- For water, a maximal solubility of 10 weight-% is assumed in both solvents based on the publication of de la Torre et al. [316], under the assumption that water solubility in linear and cyclic carbonates is roughly the same.

Temperature-dependent second-degree polynomials were correlated to the predictions by [315] to determine the necessary Henry coefficients:

$$H_\sigma = 10^5 \cdot \left(A_{\sigma i} \cdot T^2 + B_{\sigma i} \cdot T + C_{\sigma i}\right) \tag{A.61}$$

Avoiding extrapolation at temperatures exceeding 363 K, the maximum temperature examined by [315], the Henry coefficients remain unaltered at the values at 363 K. The coefficients used for the specific species are listed in Table A.20.

Table A.20: Parameters used for the calculation of the Henry coefficients calculated with Equation A.61

Species	A		B		C	
	EC	EMC	EC	EMC	EC	EMC
O_2	-0.0545916	0.0006	42.6335	0.9818	-5148.51	-248.97
CO_2	0.0142415	0.0049272	-5.85594	-2.11479	608.341	232.114
C_2H_4	0.00555133	0.00058081	-0.27055	0.981763	-202.571	-248.972
HF, POF_3, PF_5	-0.105488	-0.0858892	89.0442	60.6321	-13378.3	-8376.09

A.4 SAFT model equations[3]

As described in Section 3.3.1 is the total Helmholtz free energy A simply the sum of all its contributions. Following the individual contributions will be presented.

The first part A^{ideal} depicts the contribution given by an ideal gas and is calculated as:

$$\frac{A^{\text{ideal}}}{Nk_{\text{B}}T} = \left(\sum_{i=1}^{N_{\text{C}}} x_i \ln\left(\rho_i \Lambda_i^3\right) \right) - 1, \tag{A.62}$$

here, x_i is the mole fraction of given component i. ρ_i computes the number density as $\rho_i = N_i/V$, where N_i is the number of molecules i and V is the total volume. Further is k_{B} the Boltzmann constant, N the total number of molecules and T the absolute temperature. Λ_i describes the thermal de Broglie wavelength with $\Lambda_i = \frac{h}{2\pi m_i k_{\text{B}} T}$ with h being the Planck constant and m_i the mass of component i.

In the next step, the contribution of the segment interaction based on a Mie potential is computed as:

$$\frac{A^{\text{monomer}}}{Nk_{\text{B}}T} = \frac{A^{\text{HS}}}{Nk_{\text{B}}T} + \frac{A^1}{Nk_{\text{B}}T} + \frac{A^2}{Nk_{\text{B}}T} + \frac{A^3}{Nk_{\text{B}}T} \tag{A.63}$$

here, the monomer contribution is further divided into the hard sphere contribution A^{HS}, the first order expansion term A^1 describing the mean attractive energy, the second order expansion term A^2 constituting the energy fluctuations and the third order term A^3. The latter has been introduced for a better representation of the critical point [186]. The hard sphere contribution is based on the free energy of a reference system with temperature-dependent diameter d_{kk}. It is computed as the sum of contributions of each segment as:

$$\frac{A^{\text{HS}}}{Nk_{\text{B}}T} = \left(\sum_{i=1}^{N_{\text{C}}} x_i \sum_{k=1}^{N_{\text{G}}} \nu_{k,i} \nu_k^* S_k \right) a^{\text{HS}}, \tag{A.64}$$

where N_{G} is the total number of groups, $\nu_{k,i}$ counts the occurrences of group k in component i, ν_k^* is the number of identical segments in group k, S_k is the shape factor accounting for the proportion of segment k in a molecule, and a^{HS} is the dimensionless contribution to the hard-sphere free energy part of each segment. The latter is then computed as:

[3] The following model description has been chiefly adapted from Haslam et al. [137]

$$a^{\mathrm{HS}} = \frac{6}{\pi\rho_{\mathrm{s}}}\left[\left(\frac{\zeta_2^3}{\zeta_3^2}-\zeta_0\right)\ln(1-\zeta_3)+3\left(\frac{\zeta_1\zeta_2}{1-\zeta_3}\right)+\frac{\zeta_2^3}{\zeta_3(1-\zeta^3)^2}\right] \tag{A.65}$$

here, ρ_{s} is the segment density and ζ_m, with $m = 1,2,3$ the moment densities, see Table A.21. The expansion contributions are calculated following the same procedure:

$$\frac{A_{\mathrm{q}}}{Nk_{\mathrm{B}}T} = \left(\frac{1}{k_{\mathrm{B}}T}\right)^q\left(\sum_{i=1}^{N_{\mathrm{C}}}x_i\sum_{k=1}^{N_{\mathrm{G}}}\nu_{k,i}\nu_k^*S_k\right)a_{\mathrm{q}}, q = 1,2,3. \tag{A.66}$$

Whereas the dimensionless segment contribution is then calculated as follows:

$$a_{\mathrm{q}} = \sum_{k=1}^{N_{\mathrm{G}}}\sum_{l=1}^{N_{\mathrm{G}}}x_{s,k}x_{s,l}a_{q,kl}, q = 1,2,3. \tag{A.67}$$

The individual pair-wise $a_{q,kl}$ is calculated by Lafitte et al. [186].

The chain contribution A^{chain} to the total free energy can be obtained as:

$$\frac{A^{\mathrm{chain}}}{Nk_{\mathrm{B}}T} = -\sum_{i=1}^{N_{\mathrm{C}}}x_i\left(\sum_{k=1}^{N_{\mathrm{G}}}\nu_{k,i}\nu_k^*S_k-1\right)\ln g_{\mathrm{Mie}}^{ii}(\bar{\sigma}_{ii};\zeta_x), \tag{A.68}$$

where $g_{ii}^{Mie}(\bar{\sigma}_{ii};\zeta_x)$ is the value of the radial distribution function (RDF) of the hypothetical one-fluid Mie system at a packing fraction ζ_x evaluated at the effective diameter $\bar{\sigma}_{ii}$, see Table A.21. An accurate estimate of the contact value of the RDF for a Mie fluid can be obtained employing a second-order expansion which is explained in detail in the original SAFT-γ Mie publication by Papaioannou et al. [176].

The association contribution $A^{\mathrm{association}}$, which makes the SAFT theory stand out from classical cubic EoS, is computed as:

$$\frac{A^{\mathrm{association}}}{Nk_{\mathrm{B}}T} = \sum_{i=1}^{N_{\mathrm{C}}}x_i\sum_{k=1}^{N_{\mathrm{G}}}\nu_{k,i}\sum_{a=1}^{N_{\mathrm{ST},k}}n_{k,a}\left(\ln X_{i,k,a}+\frac{1-X_{i,k,a}}{2}\right), \tag{A.69}$$

here $X_{i,k,a}$ refers to the fraction of non bonded sites of type a in segment k and component i given with

$$X_{i,k,a} = \left[1 + \rho \sum_{j=1}^{N_C} x_j \sum_{l=1}^{N_G} \nu_{j,l} \sum_{b=1}^{N_{ST,l}} n_{l,b} X_{j,l,b} \Delta_{ij,kl,ab} \right]^{-1}. \tag{A.70}$$

The strength of association is expressed as $\Delta_{ij,kl,ab} = F_{kl,ab} K_{kl,ab} I_{ij,kl,ab}$, where $F_{kl,ab}$ equates to the association energy as:

$$F_{kl,ab} = \exp \varepsilon^{HB}_{kl,ab} / k_B T - 1, \tag{A.71}$$

and $I_{ij,kl,ab}$ gives the temperature density correlation with:

$$I_{ij,kl,ab} = \sum_{p=0}^{10} \sum_{q=0}^{10-p} c_{pq} (\rho_s \sigma_x^3)^p \left(\frac{k_B T}{\bar{\varepsilon}_{ij}} \right). \tag{A.72}$$

The coefficients c_{pq} can be extracted from Dufal et al. [178] and the corresponding Corrigendum [317]. Equations for σ_x^3 and $\bar{\varepsilon}_{ij}$ can again be found in Table A.21.

The influence of electrically charged particles on the free energy can be summarised in two terms. The first term A^{Born} contemplating the formation of a spherical cavity with diameter $\sigma_{Born,kk}$ is given with:

$$A^{Born} = -\frac{e^2}{4\pi\varepsilon_0} \left(1 - \frac{1}{D} \right) \sum_{i=k}^{N_{ion}} N_k Z_k^2 \sigma_{Born,kk}, \tag{A.73}$$

also called Born term and can be calculated based on a Born cycle as demonstrated by Schreckenberg et al. [180]. Here, e is the elementary charge, ε_0 the permittivity of the vacuum, D the relative permittivity or Dielectric constant of the solvent and N_i and Z_i are the number and charge of ion i, respectively.

The second contribution A_{ion} is equated as:

$$A^{ion} = \frac{U_{MSA}}{N k_B T} + \frac{\Gamma^3}{3\pi\rho}, \tag{A.74}$$

where U_{MSA} is the potential energy calculated from the mean sphere approximation and is given with:

$$\frac{U_{\mathrm{MSA}}}{Nk_{\mathrm{B}}T} = -\frac{e^2}{(4\pi\varepsilon_0)\rho k_{\mathrm{B}}TD}\Gamma\rho\sum_{k=1}^{N_{\mathrm{ion}}}\left(x_k z_k^2\frac{1}{1+\Gamma\sigma_{kk}}\right)+\frac{\pi}{2}\Delta\Omega P_n^2, \tag{A.75}$$

here P_n, Δ and Ω are intermediate functions already introduced in Section 3.3.3. The ion screening length Γ has also been introduced in Section 3.3.3. However, compared to the MSA PM approach for ion association here Γ_0 as the starting point for its iterative computation is given with half the Debye length κ [180]:

$$\Gamma_0 = \frac{\kappa}{2} = 0.5\sqrt{\frac{e^2}{4D\varepsilon_0 V k_{\mathrm{B}}T}\sum_{k=1}^{N_{\mathrm{ion}}} n_k z_k^2}. \tag{A.76}$$

Table A.21: Constitutive equations within the SAFT-γ Mie framework.

Name	Equation	Number
Number density of segment s	$\rho_{\mathrm{s}} = \rho\left(\sum_{i=1}^{N_{\mathrm{C}}} x_i \sum_{k=1}^{N_{\mathrm{G}}} \nu_{k,i}\nu_k^* S_k\right)$	(A.77)
Moment densities	$\zeta_m = \frac{\pi\rho_{\mathrm{s}}}{3}\sum_{k=1}^{N_{\mathrm{G}}} x_{s,k} d_{kk}^m$	(A.78)
Fraction of a type k like group in the mixture	$x_{s,k} = \frac{\sum_{i=1}^{N_{\mathrm{C}}} x_i \nu_{k,i}\nu_k^* S_k}{\sum_{j=1}^{N_{\mathrm{C}}} x_j \sum_{l=1}^{N_{\mathrm{C}}} \nu_{l,j}\nu_l^* S_l}$	(A.79)
Effective segment diameter	$\bar{\sigma}_{ii}^3 = \sum_{k=1}^{N_{\mathrm{G}}}\sum_{l=1}^{N_{\mathrm{G}}} z_{k,i} z_{l,i}\sigma_{kl}^3$	(A.80)
Effective hard-sphere diameter	$\bar{d}_{ii}^3 = \sum_{k=1}^{N_{\mathrm{G}}}\sum_{l=1}^{N_{\mathrm{G}}} z_{k,i} z_{l,i} d_{kl}^3$	(A.81)
Fraction of group k in molecule i	$z_{k,i} = \frac{\nu_{k,i}\nu_k^* S_k}{\sum_{l=1}^{N_{\mathrm{G}}} \nu_{l,i}\nu_l^* S_l}$	(A.82)
Average interaction energy	$\bar{\varepsilon}_{ii} = \sum_{k=1}^{N_{\mathrm{G}}}\sum_{l=1}^{N_{\mathrm{G}}} z_{k,i} z_{l,i}\varepsilon_{kl}$	(A.83)
Average interaction length exponents	$\bar{\lambda}_{ii} = \sum_{k=1}^{N_{\mathrm{G}}}\sum_{l=1}^{N_{\mathrm{G}}} z_{k,i} z_{l,i}\lambda_{kl}$	(A.84)
Packing fraction of a hypothetical fluid	$\zeta_x = \frac{\pi}{6}\rho_{\mathrm{s}}\sum_{k=1}^{N_{\mathrm{G}}}\sum_{l=1}^{N_{\mathrm{G}}} d_{kl}^3$	(A.85)
Average interaction diameter	$\sigma_x^3 = \sum_{k=1}^{N_{\mathrm{G}}}\sum_{l=1}^{N_{\mathrm{G}}} x_{s,k} x_{s,l}\sigma_{kl}^3$	(A.86)

A.4.1 Dielectric constant of solvents

The SAFT-γ Mie model is capable of representing solvent ion mixtures. To do so, the dielectric constant D has to be known for all non-ionic species. This is done using the simple expression: $D = 1 + \rho_{\mathrm{solv}} d$ as adapted by Schreckenberg et al. [180]. Here, ρ_{solv} refers to the liquid molar density of the solvent or the solvent mixture, and d is a newly introduced variable covering the temperature dependency as follows:

$$d = d_{\mathrm{V}} \left(\frac{d_{\mathrm{T}}}{T} - 1 \right). \tag{A.87}$$

The necessary parameters d_{V} and d_{T} have been obtained by regressing against experimental data or, in the case of CO_2, have been taken from the original publication [180]. The regression has been performed in MATLAB [203] using the particle swarm algorithm embedded in MATLABs particle swarm solver. The swarm size has been chosen as 1000. The obtained parameters are listed in Table A.22, and the corresponding graphical representation can be found in Figure A.4. To get the dielectric constant of a given mixture, a linear mixing rule as:

$$y_{\mathrm{mix}} = \sum_{i=1} \sum_{j=1} x_i x_j y_{ij}, \tag{A.88}$$

is applied. Here, y_{mix} stands for either the dielectric parameter d or the density of given solvent mixtures ρ. y_{ij} is computed as the arithmetic mean of the pure parameters as in $y_{ij\ldots} = \frac{y_{ii}+y_{jj}+\ldots}{n_{\mathrm{comp}}}$, where n_{comp} represents the total number of solvent components. The mixing rule can be extended to multi-component mixtures by adding additional sums.

Table A.22: Parameters to simulate the dielectric constant D of each solvent.

Solvent	d_{V} / dm^3 mol^{-1}	d_{T} / K
EC	3.1571	900
PC	2.052	1148
DMC	-0.183	0
DEC	-0.2262	0
EMC	-0.2675	0
CO_2 [180]	-0.025	0
$LiPF_6$	-16.0	0
Fixed molecules	0	0

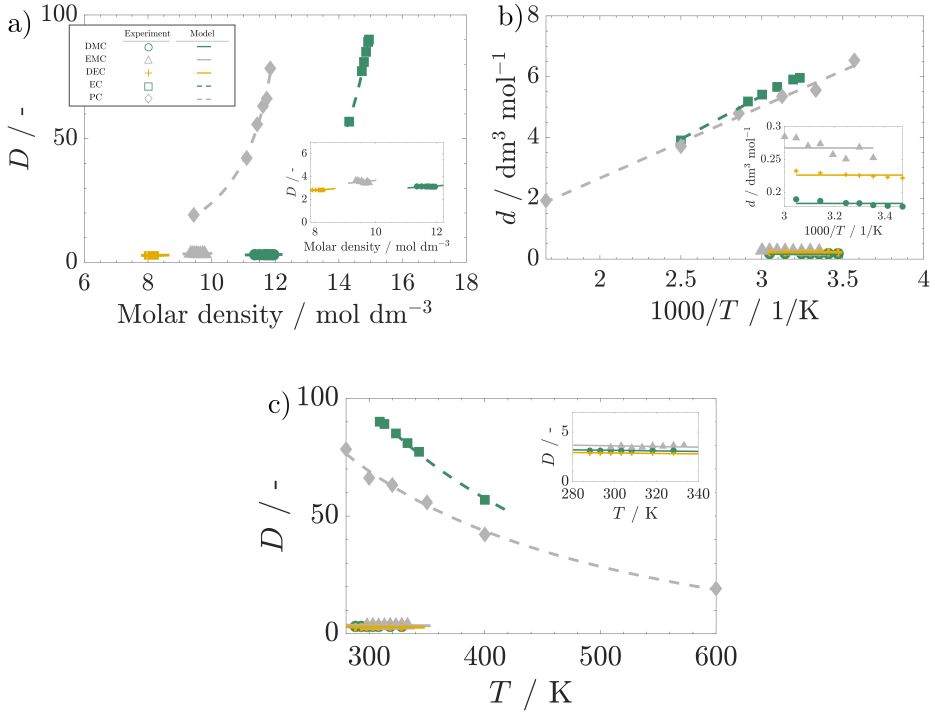

Figure A.4: Comparison of simple model expression with pure species experimental data for a) the dielectric constant D over molar volume, b) its volume reduced form d over temperature, and c) the Dielectric constant D over temperature for DMC [188], EMC [318], DEC [188], EC [190, 319] and PC [190].

A.5 Numerical methods

A.5.1 Euler-Tschebyschow Procedure

The Euler-Tschebyschow procedure is a modification of Newton's method to find the roots of a function efficiently [320]:

1. **Initial setup:** Start with a function $f(x)$ and its derivative $f'(x)$. Pick an initial guess x_0.
2. **Newton's step:** Calculate the a Newton's step as: $s(x_0) = \frac{f(x_0)}{f'(x_0)}$.
3. **Tschebyschow (quadratic) correction:** Calculate the quadractic correction term as: $t(x_0) = \frac{f'(x_0)s^2}{f''(x_0)}$.
4. **Perform step:** $x_1 = x_0 + s(x_0) + t(x_0)$

5. **Iterate:** Repeat steps 2 and 3 until the solution has converged to within the desired tolerance.

A.5.2 Direct Substitution Method

The Direct Substitution Method is a simple and commonly applied iterative method for solving equations [320]:

1. **Setup:** Rewrite the equation in the form $x = g(x)$.
2. **Initial guess:** Choose an initial guess x_0 for the root.
3. **Perform step:** Substitute x_0 into the right-hand side of the equation to find a new approximation $x_1 = g(x_0)$.
4. **Iterate:** Repeat the substitution process to find $x_{n+1} = g(x_n)$, for $n = 0, 1, 2, 3, \ldots$ until the solution has converged to within the desired tolerance.

B Supporting details Chapter 4[1]

The following chapter contains the additional results and parameters corresponding to the study regarding the interaction of phase transition and reactions during thermal abuse of Li-ion batteries presented in Chapter 4. First, additional results for the produced heats are shown. This is followed by listing all necessary model parameters in table format.

B.1 Additional results

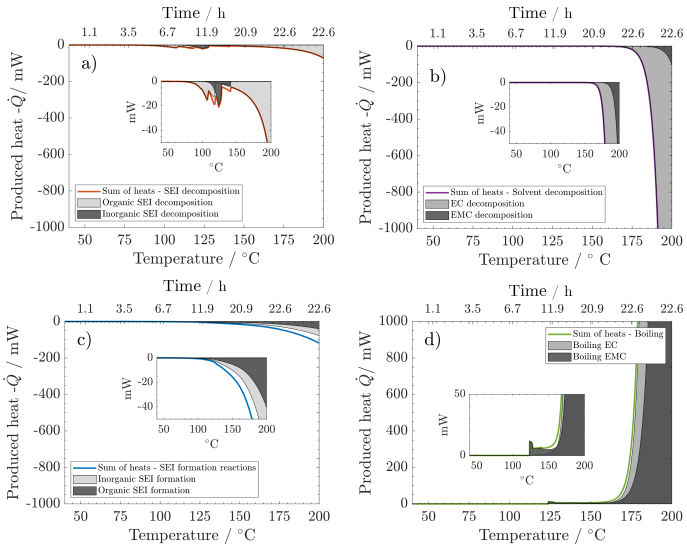

Figure B.1: Individual contribution to a) SEI formation, b) solvent decomposition, c) SEI decomposition and d) solvent boiling for the case with boiling.

[1] Parts of this chapter have been published as own contributions in Baakes, F., Lüthe M., Gerasimov, M., Laue, V., Röder, F., Balbuena, P., Krewer, U., "Unveiling the interaction of reactions and phase transition during thermal abuse of Li-ion batteries", Journal of Power Sources, DOI:10.1016/j.jpowsour.2021.230881, CC BY 4.0 [60].

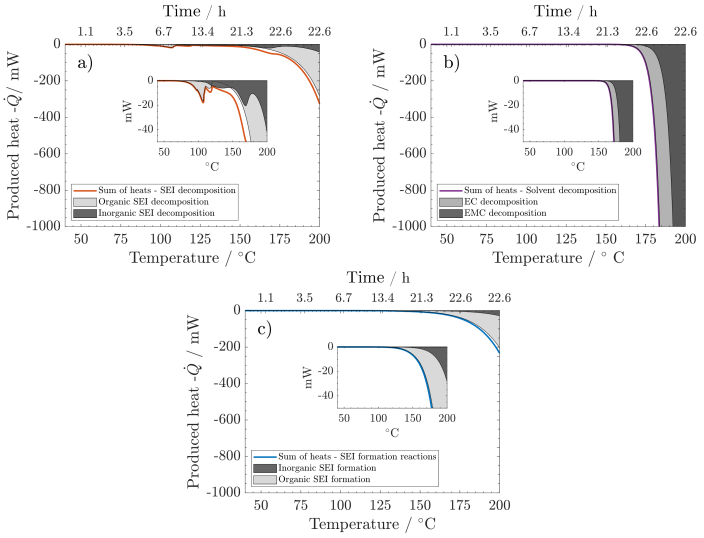

Figure B.2: Individual contribution to a) SEI formation, b) solvent decomposition, c) SEI decomposition and for the case without boiling.

B.2 Supporting tables

In Table B.3, the kinetic parameters (k_0 and E_A) obtained for both scenarios parameterised in Chapter 4 are listed.

Table B.1: Structural battery parameters.

Parameter	Symbol	Value	
Battery thickness	d_{Cell}	6.5	mm [162]
Battery length	l_{Cell}	42.5	mm [162]
Battery width	w_{Cell}	25.7	mm [162]
Cell area	A_{Cell}	1097	mm^2 *
Volume fraction AM anode	$\varepsilon_{\text{AM, An}}$	0.62	- [164]
Volume fraction AM cathode	$\varepsilon_{\text{AM, Cat}}$	0.61	- [164]
Volume fraction electrolyte anode	$\varepsilon_{\text{El, An}}$	0.32	- [164]
Volume fraction electrolyte separator	$\varepsilon_{\text{El, Sep}}$	0.5	- [164]
Volume fraction electrolyte cathode	$\varepsilon_{\text{El, Cat}}$	0.33	- [164]
Volume fraction PVDF	$\varepsilon_{\text{PVDF}}$	0.06	- *
Particle radius anode	r_{An}	1	µm [163]
Particle radius cathode	r_{Cat}	1	µm [163]
Thickness anode	d_{An}	77	µm [164]
Thickness separator	d_{Sep}	25	µm [164]
Thickness cathode	d_{Cat}	68	µm [164]
Volume cell	$V_{\text{Cell,0}}$	7.1	mL *
Volume copper	V_{Cu}	0.19	mL *
Volume aluminum	V_{Al}	0.37	mL *
Volume PVDF	V_{PVDF}	0.32	mL *
Volume pouch foil	$V_{\text{Pouch foil}}$	0.95	mL *
Volume AM anode	$V_{\text{AM, An}}$	1.77	mL *
Volume AM cathode	$V_{\text{AM, Cat}}$	1.54	mL *
Volume SEI	$V_{\text{SEI,0}}$	0.16	mL *
Volume electrolyte	$V_{\text{El,,0}}$	1.54	mL *
Specific surface area anode	$a_{\text{s, An}}$	1860000	$\text{m}^2\,\text{m}^{-3}$ *
Specific surface area cathode	$a_{\text{s, Cat}}$	1830000	$\text{m}^2\,\text{m}^{-3}$ *
Number of double coated sheets anode	$n_{\text{DCS, An}}$	17	- [164]
Number of double coated sheets cathode	$n_{\text{DCS, Cat}}$	16	- [164]
Number of single coated sheets cathode	$n_{\text{SCS, Cat}}$	2	- [164]
Thickness aluminum single coated sheets	$d_{\text{SCS, Al.}}$	50	µm [164]
Thickness aluminum double coated	$d_{\text{DCS, Al.}}$	15	µm [164]
Thickness copper double coated	$d_{\text{DCS, Cu.}}$	10	µm [164]
Thickness pouch foil	$d_{\text{Pouch foil}}$	346	µm *
Intercalation fraction 100 % SOC anode	$z_{1,\text{An}}$	0.676	- [163]
Intercalation fraction 0 % SOC anode	$z_{0,\text{An}}$	0.181	- [163]
Intercalation fraction 100 % SOC cathode	$z_{1,\text{Cat}}$	0.442	- [163]
Intercalation fraction 0 % SOC cathode	$z_{0,\text{Cat}}$	0.986	- [163]
Maximal concentration AM anode	$C_{\text{max, An.}}$	20530	$\text{mol}\,\text{m}^{-3}$ *
Maximal concentration AM cathode	$C_{\text{max, Cat}}$	31827	$\text{mol}\,\text{m}^{-3}$ *
Concentration conductive salt	C_{LiPF_6}	1200	$\text{mol}\,\text{m}^{-3}$ *
SEI thickness	d_{SEI}	50	nm
Battery heat capacity	$C_{\text{p, Cell}}$	9.43	$\text{J}\,\text{K}^{-1}$ *
Battery mass	m_{Cell}	11.12	g *

* Calculated.

Table B.2: Table of all species listed with their density, molar heat capacity, formation enthalpy, and entropy at standard state and molar mass. The first reference indicates the publication of the model, if available, and the following refer to the data used to validate the model if available .

Species	$\rho^{\ominus}$	$\underline{C}_p^{\ominus}$	$\Delta\underline{H}_f^{\ominus}$	$\underline{S}^{\ominus}$	M
	$\mathrm{kg\,m^{-3}}$	$\cdot 10^{-3}\ \mathrm{kJ\,mol^{-1}\,K^{-1}}$	$\mathrm{kJ\,mol^{-1}}$	$\mathrm{J\,mol^{-1}\,K^{-1}}$	$\cdot 10^{-3}\ \mathrm{kg\,mol^{-1}}$
$(CH_2OCO_2Li)_2$	1300 [321]	200.82 *, [284]	-1370.00 [110]	88.8 [110]	161.95 **, [282]
Li_2CO_3	2110 [265]	96.27 [282, 322]	-1216.04 [282]	90.31 [282]	73.89 [282]
Li_2O	2013 [282]	54.10 [282, 322]	-598.73 [282]	37.85 [282]	29.88 [282]
LiOH	1450 [282]	49.57 [282, 322]	-484.93 [282]	42.81 [282]	23.94 [282]
LiF	2640 [265]	41.89 [282, 283, 322]	-616.93 [282]	35.73 [282]	25.94 [282]
$LiPF_6$	1500 [265]	151.15 [276, 287]	-2296.00 [276]	160.82 [276]	151.91 [276]
LiC_6	1622 [69]	49.22 [69]	-3.9170 [323]	—	79.01 **, [282]
Li_zCoO_2	3115 [69]	66.37 ***, [278, 287, 299]	-499.76 ***, [277, 278, 299]	—	97.87 **, [282]
Co_3O_4	6110 [265]	123.17 [282, 283, 322]	-910.02 [282]	114.44 [282]	240.80 [282]
C_2H_4	1.14 [296]	43.13 [283, 296]	52.47 [296]	219.32 [282]	28.10 [282]
H_2	0.0813 [296]	28.83 [283, 296]	0 [296]	107.71 [296]	2.0159 [282]
CO_2	1.78 [296]	37.44 [283, 296]	-393.52 [282]	213.79 [282]	44.01 [282]
O_2	1.29 [296]	29.43 [283, 296]	0.00 [282]	205.15 [282]	32.00 [282]
H_2O	997 [296]	75.33 [283, 296]	-285.83 [282]	69.95 [282]	18.02 [282]
HF	0.83 [312]	29.14 [282, 283, 322]	-272.55 [282]	173.78 [282]	20.01 [282]
PF_5	5.13 [118]	84.79 [282, 283, 322]	-1594.41 [282]	300.80 [282]	125.97 [282]
POF_3	4.26 [118]	68.79 [282, 283, 322]	-1254.25 [282]	285.41 [282]	103.97 [282]
HPO_2F_2	1583.26 [324]	145.04 [285]	-971.00 [285]	193.2 [285]	101.98 [282]
$C_3H_4O_3$	1333 [280, 308]	123.62 [274]	-590.90 [282]	132.54 [282]	88.06 [282]
$C_4H_8O_3$	1060 [118, 280]	175.15 [280]	-645.73 [282]	—	104.10 [282]

* Estimated with modified Kopps rule.
** Calculated from its elements.
*** Modified heat capacity and formation enthalpy model to address different intercalated mole fractions. For this value, the intercalation is $z = 0.5$.

Table B.3: The kinetic parameters k_0 and E_A are listed below for the scenarios with vaporisation and without vaporisation.

Parameter	With vaporisation	Without vaporisation
$E_{A,OSD}$ / kJ mol^{-1}	149.3	148.3
$E_{A,ISD}$ / kJ mol^{-1}	216.3	166
$E_{A,ISP}$ / kJ mol^{-1}	70	135.2
$E_{A,OSP}$ / kJ mol^{-1}	69	124.4
$E_{A,CSD}$ / kJ mol^{-1}	113	48.6
$E_{A,PFD}$ / kJ mol^{-1}	335	192
$E_{A,ECD}$ / kJ mol^{-1}	450	450
$E_{A,EMCD}$ / kJ mol^{-1}	470	470
$E_{A,CD}$ / kJ mol^{-1}	473.8	473.8
$k_{0,OSD}$ / mol s^{-1}	$1{\cdot}10^{14}$	$1{\cdot}10^{14}$
$k_{0,ISD}$ / mol s^{-1}	$1.5{\cdot}10^{32}$	$1.5{\cdot}10^{23}$
$k_{0,ISP}$ / mol m s^{-1}	$7.2{\cdot}10^{-8}$	$7.2{\cdot}10^{-4}$
$k_{0,OSP}$ / mol m s^{-1}	$5.3{\cdot}10^{-8}$	$5.3{\cdot}10^{-4}$
$k_{0,CSD}$ / mol s^{-1}	8	8
$k_{0,PFD}$ / mol s^{-1}	$1{\cdot}10^{42}$	$1{\cdot}10^{23}$
$k_{0,ECD}$ / mol s^{-1}	$1{\cdot}10^{49}$	$1{\cdot}10^{49}$
$k_{0,EMCD}$ / mol s^{-1}	$1{\cdot}10^{52}$	$1{\cdot}10^{52}$
$k_{0,CD}$ / mol s^{-1}	$1.1{\cdot}10^{50}$	$1.1{\cdot}10^{50}$

C Supporting details Chapter 5[1]

The following chapter contains the additional results and parameters corresponding to the study sensitivity of thermal abuse of Li-ion batteries to SEI properties and impurities presented in Chapter 5. First, the procedures to estimate initial values of $LiPF_6$ decomposition products as well as the SEI compounds are presented. This is followed by additional results regarding the produced heats and concentration profiles. Eventually, necessary model parameters are listed in table format.

C.1 Additional results

C.1.1 Estimation of initial values of $LiPF_6$ decomposition products

In the following, the results including a visualisation for the procedure of identifying proper initial values for the decomposition products of $LiPF_6$ are shown.

In Figure C.1, the initial mixing of the electrolyte is shown. The very first process occurring is the equilibration of $LiPF_6$ with PF_5 and LiF. This process happens extremely fast. Afterwards, PF_5 and POF_3 decompose with the water within the solvent. After 60 days, the H_2O concentration dropped under 10 ppm, and the HF concentration rose over 50 ppm. This is in very good agreement with the $<$15 ppm H_2O and $<$ 50 ppm HF reported by electrolyte producers [227].

Figure C.2 shows the same system after adding 1000 ppm or 70 mM of H_2O as an impurity. The results resemble those of the experimental study conducted by Stich et al. [144], which was used to parameterise the reactions shown in Figure C.2 b). Experimental points, are shown as stars, crosses, and circles, referring to HF, H_2O, and HPO_2F_2, respectively.

[1] Parts of this chapter have been published as own contributions in Baakes, F., Witt, D., Krewer, U., "Impact of electrolyte impurities and SEI composition on battery safety", Chemical Science, DOI:10.1039/D3SC04186G, CC BY 3.0 [143].

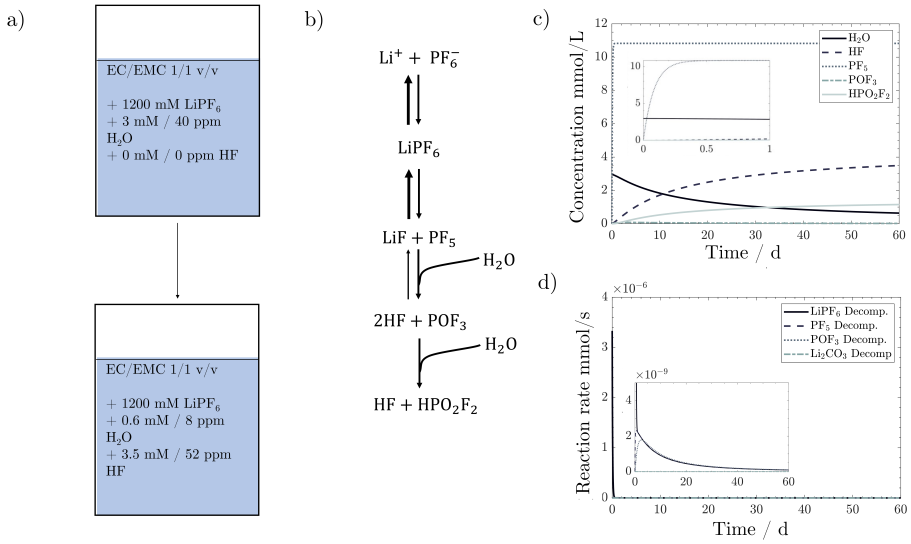

Figure C.1: Calendaric ageing of the electrolyte after initial mixing with a) initial and final values after 60 days for $LiPF_6$, H_2O and HF,. b) the considered reaction scheme. c) the concentration progression and d) the reaction rates.

In Figure C.3, the change occurring in the "formation and conditioning" period is shown, and the simulation including Li_2CO_3 is compared to the experimental results of Stich et al. [144] where no Li_2CO_3 was present. Due to very fast reaction of Li_2CO_3 with HF, the HF level almost immediately drops to 0. Further, due to the presence of H_2O, the depletion is slowed down and the concentration of HPO_2F_2 is drastically increased. Based on the strong difference between the electrolyte composition before and after assembly and formation, we conclude that it is advised to conduct studies on electrolyte ageing always in a true battery environment, if the goal is to compare electrolyte composition of a fresh cell with aged cells.

C.1.2 Estimation of initial SEI composition

In the following, the calculations for the initial SEI composition are presented. In their study, Liu et al. [53] measured a maximum SEI weight of 3250 ng. 1750 ng are attributed to LEDC based on the slope of 80 $\Delta g/\Delta C$ mass change per charge. Here, the value has to be multiplied by two since two electrons are transferred to produce LEDC. The resulting 160 $\Delta g/\Delta C$ are very close to molar mass of 162 g/mol for LEDC. In the first discharge, the overall weight is reduced to 2400 ng. Here, the re-oxidation of LEDC is assumed to take place following the reaction: $(CH_2OCOLi)_2) \longrightarrow Li_2O + 2\,CO_2 + C_2H_4 + O_2$. This results into a weight loss of

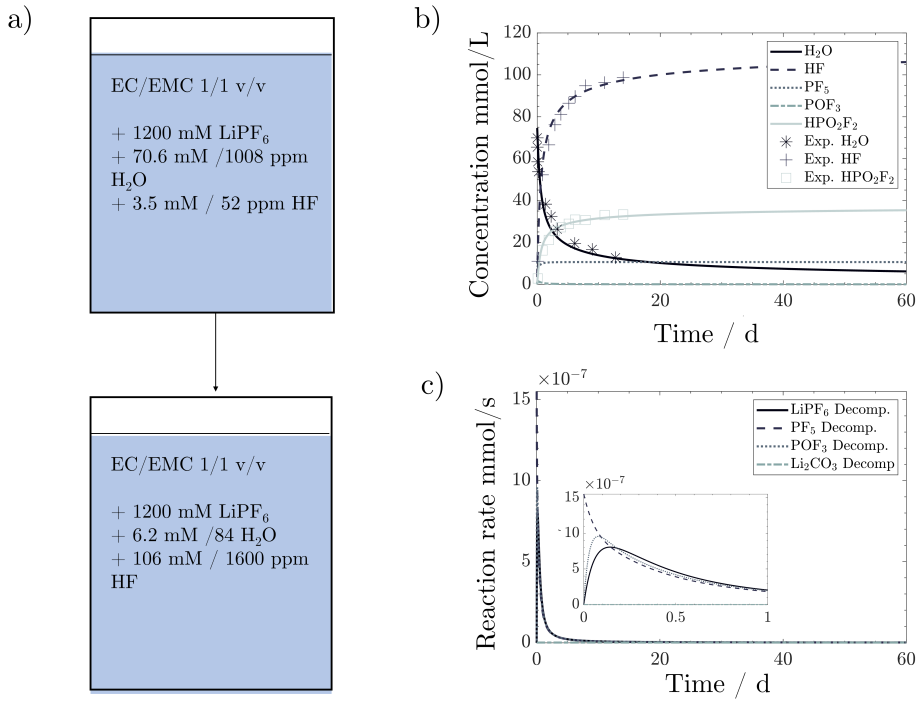

Figure C.2: Calendaric ageing of electrolyte after adding 1000 ppm of water to initial electrolyte mixture with a) initial and final values after 60 days for $LiPF_6$, H_2O and HF, b) the concentration progression with experimental values taken from Stich et al. [144] c) the reaction rates.

850 ng. Considering a 1.22 ratio of weight of the gaseous products to LEDC, a loss of 1040 ng LEDC is estimated and a production of roughly 200 ng Li_2O. Considering the overall mass of the SEI of 2400 ng and 700 ng of LEDC and 200 ng of Li_2O, translates to 32 wt-% LEDC and 8 wt-% Li_2O. Further, 350 ng LiF production translates to 14 wt-% of SEI content. This corresponds to 45 vol-%, 8 vol-% and 12 vol-% for LEDC, Li_2O and LiF, respectively. The amount of LiOH is calculated based on the assumption that all H_2O present in the anode after drying will react to LiOH. For the reference case, this gives 0.6 vol-% LiOH. Li_2O and the sum of LiF and LiOH are rounded to to 10 vol-% each. Eventually, the last 33 vol-% are assumed to consist of Li_2CO_3. Please note that these estimations give only a rough idea of the order of magnitude for the SEI composition. Also note that these are the values before the "formation and conditioning" procedure, described above, will be performed. Thus, the initial compositions listed in Table C.2 are slightly different to the ones described here

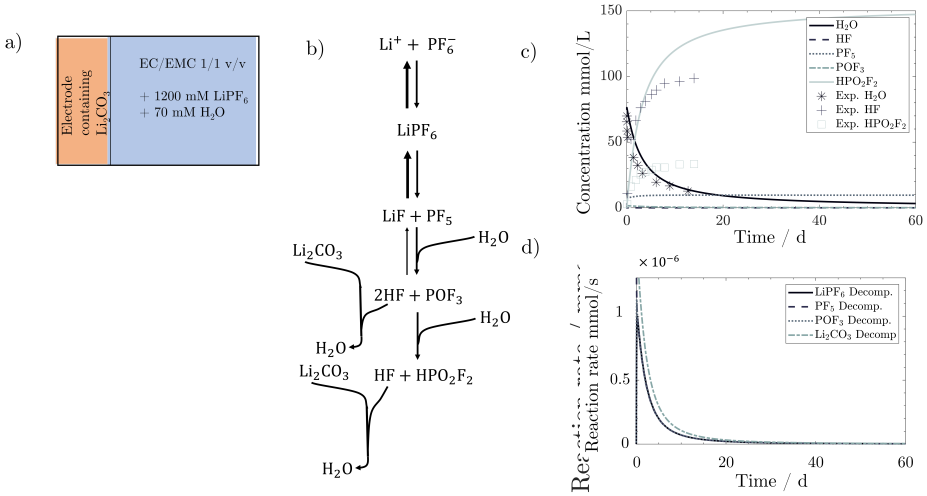

Figure C.3: Simulation of impact of cell assembly, formation and subsequent 60 days calendaric ageing on battery composition with a) sketch of the simulated setup, b) the considered reaction scheme, and c) the concentration progression with experimental values taken from Stich et al. [144] comparison to reactions without Li_2CO_3, and d) the reaction rates.

C.1.3 Additional heat and concentration progressions

Figure C.4 a) shows the produced heats of the formation reactions of LEDC, Li_2CO_3 and LiOH. Note that LiOH does not occur to a notably extent since the water concentration is too low and most of it has been consumed before substantial formation could take place. Figure C.4 b shows the produced heats of cathode, EC and EMC decomposition.

Figure C.5, Figure C.6, and Figure C.7 show the comprehensive comparison for the SEI composition variation, the SEI thickness variation and the water impurity variation, respectively.

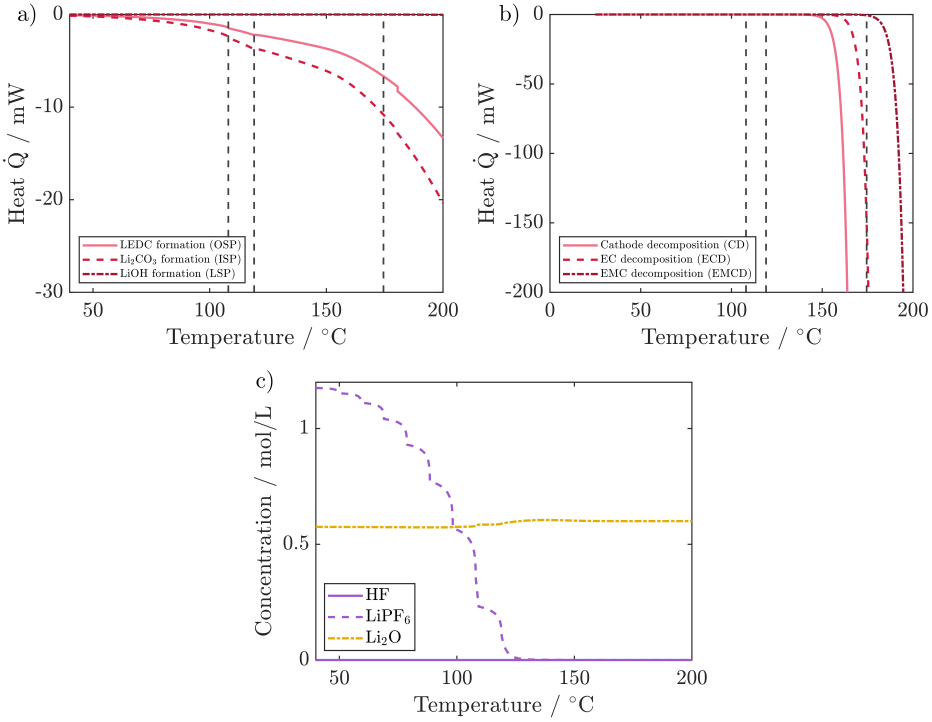

Figure C.4: Changes during accelerated rate calorimetry simulation for the reference case (45 vol-% LEDC, 260 ppm H_2O, 50 nm thick SEI): produced heats from a) SEI forming reaction: LEDC, Li_2CO_3, and LiOH, and from b) cathode decomposition, EC decomposition, and EMC decomposition as well as c) additional concentrations of HF, $LiPF_6$ and Li_2O.

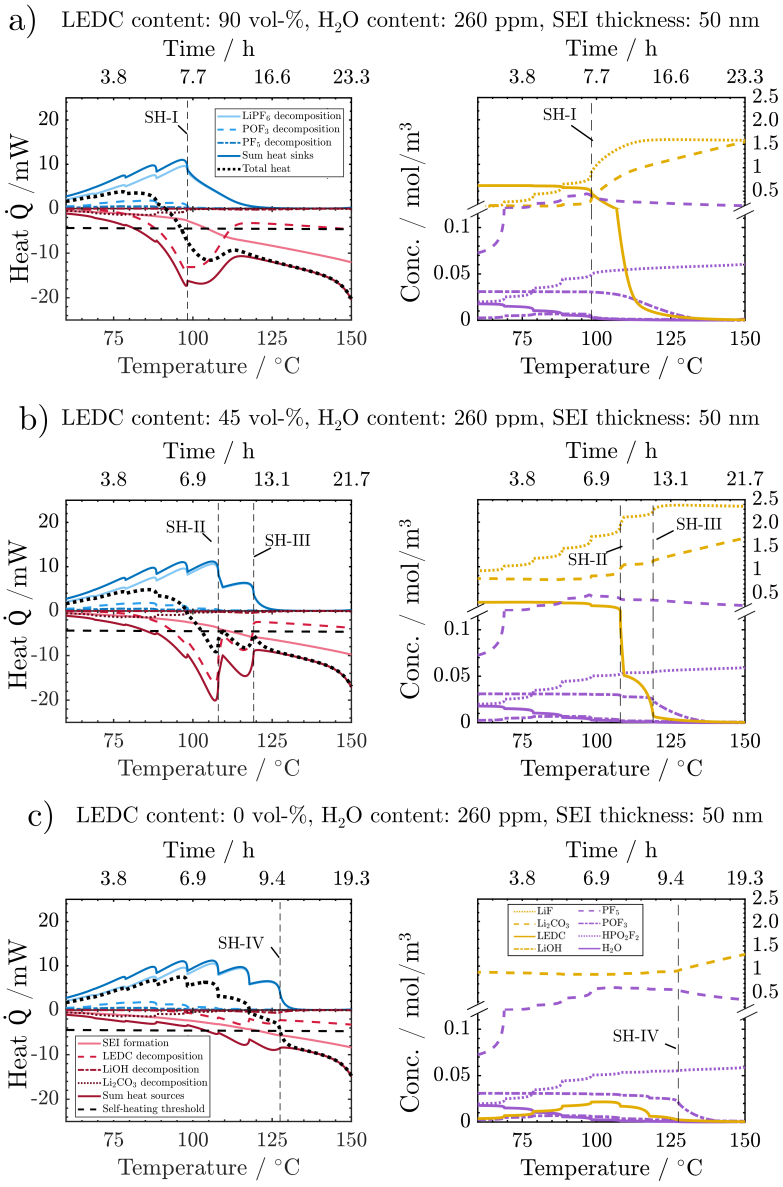

Figure C.5: Comprehensive comparison of progression of heat sinks and sources and concentration for the high LEDC (a), the reference (b), and the low LEDC case (c).

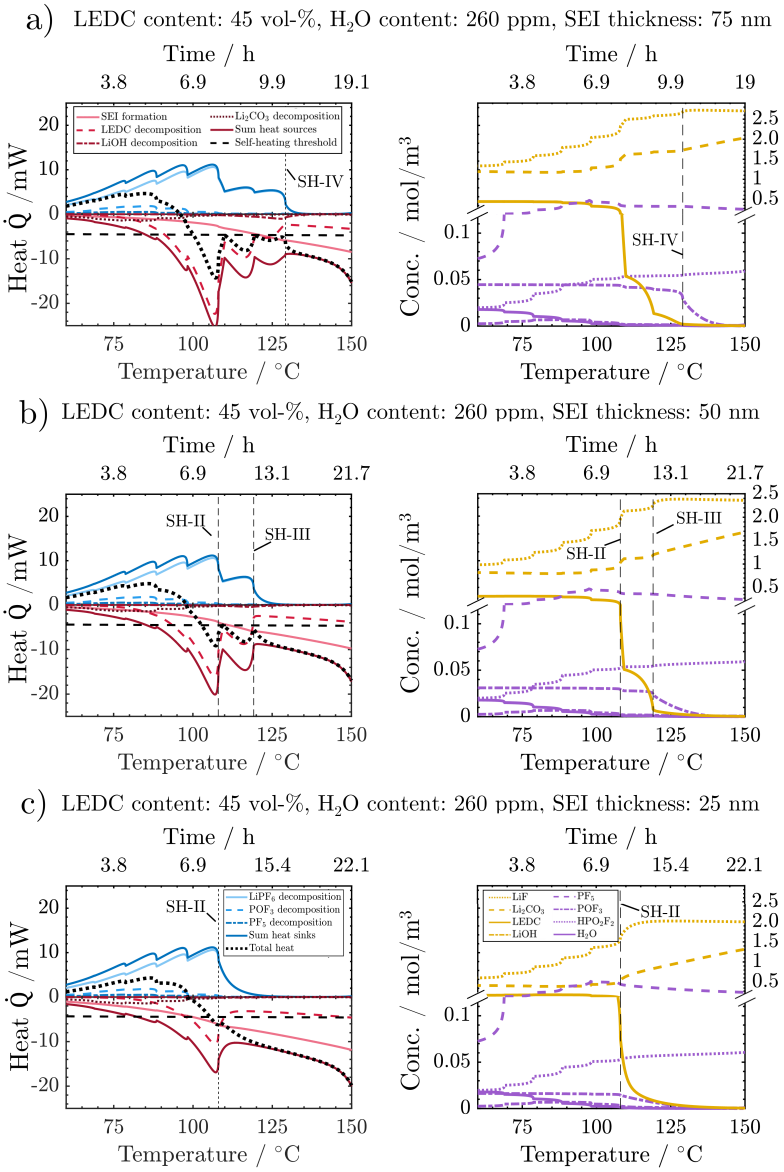

Figure C.6: Comprehensive comparison of progression of heat sinks and sources and concentration for the thick SEI (a), the reference (b), and the thin SEI case (c).

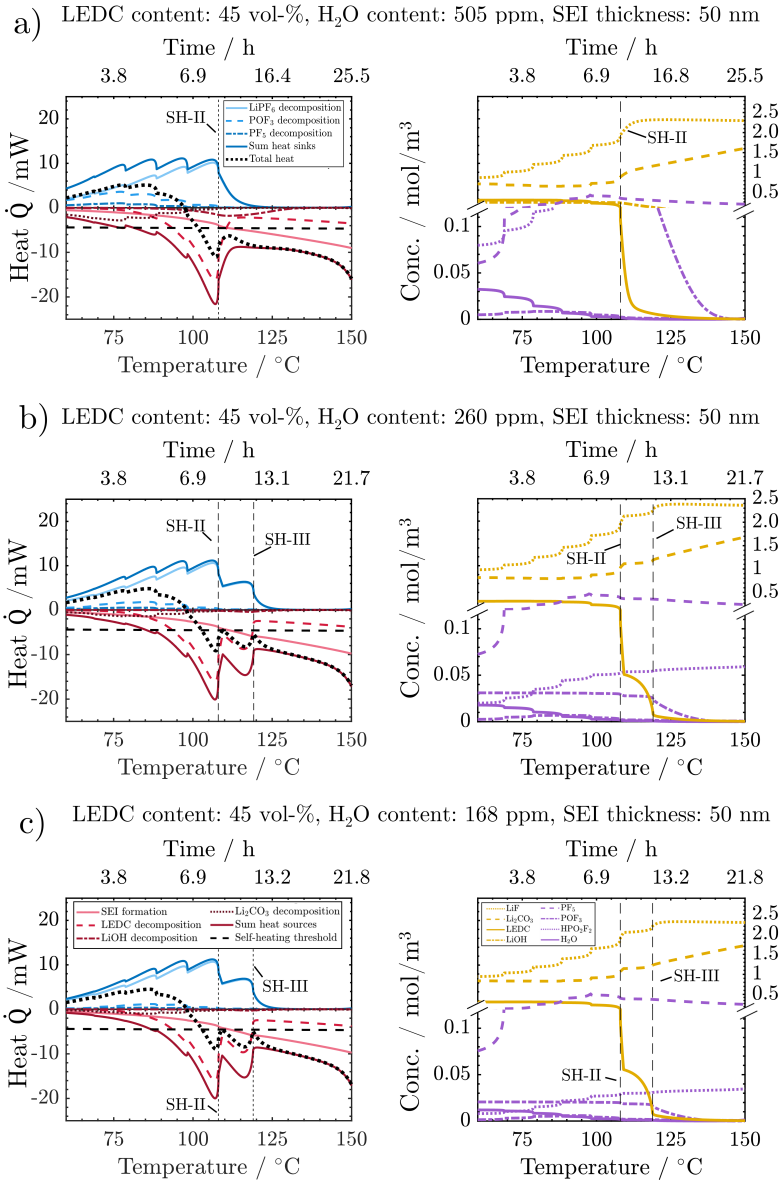

Figure C.7: Comprehensive comparison of progression of heat sinks and sources and concentration for the high water contamination (a), the reference (b), and the low water contamination case (c).

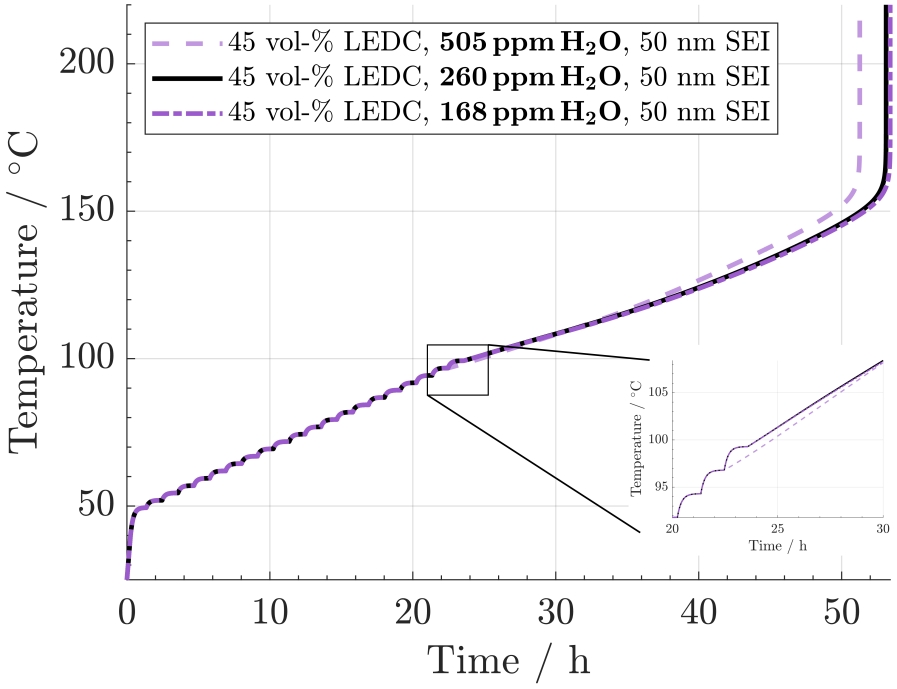

Figure C.8: Simulation of the H_2O impurity variation ARC measurements with a 2.5 °C temperature step.

C.2 Supporting tables

Table C.1: Initial molar amounts (n_i (t=0)) for all considered species, states of each species and reference volume for concentration calculation for the reference case (45 vol-% LEDC, 260 ppm H_2O, 50 nm thick SEI).

Species	States /Sets	n_i (t=0) in mmol	Reference volume
$(CH_2OCO_2Li)_2$ (LEDC)	Solid/ Ω_S, Ω_{SEI}	0.5976	$V_{SEI} + V_{AM,An}$
Li_2CO_3	Solid/ Ω_S, Ω_{SEI}	1.5946	$V_{SEI} + V_{AM,An}$
LiOH	Solid/ Ω_S, Ω_{SEI}	0.0601	$V_{SEI} + V_{AM,An}$
Li_2O	Solid/ Ω_S, Ω_{SEI}	1.1143	$V_{SEI} + V_{AM,An}$
LiF	Solid/ Ω_S, Ω_{SEI}	1.7359	$V_{SEI} + V_{AM,An}$
$LiPF_6$	Liquid/ Ω_L	2.6035	V_{El}
PF_5	Liquid, Gas/ Ω_L, Ω_G	0.0232	V_{El}
POF_3	Liquid, Gas/ Ω_L, Ω_G	0.0016	V_{El}
HPO_2F_2	Liquid/ Ω_L	0.0381	V_{El}
H_2O	Liquid, Gas/ Ω_L, Ω_G	0.0424	V_{El}
HF	Liquid, Gas/ Ω_L, Ω_G	0	V_{El}
CO_2	Liquid, Gas/ Ω_L, Ω_G	0	V_{El}
O_2	Liquid, Gas/ Ω_L, Ω_G	0	V_{El}
H_2	Liquid, Gas/ Ω_L, Ω_G	0	V_{El}
Li_xCoO_2	Solid/ Ω_S	27.3571	$V_{AM,Cat}$
Co_3O_4	Solid/ Ω_S	0	$V_{AM,Cat}$
LiC_6	Solid/ Ω_S	24.6048	$V_{AM,An}$
$C_3H_4O_3$ (EC)	Liquid/ Ω_L	16.8104	V_{El}
$C_4H_8O_3$ (EMC)	Liquid/ Ω_L	10.2377	V_{El}

Table C.2: Values for initial conditions for SEI composition and $LiPF_6$ decomposition products for all simulated variations. d_{SEI} denotes SEI thickness, ε the volume-fraction inside the SEI, and C_{xy} the concentration in the electrolyte.

Cases	d_{SEI}	ε_{LEDC}	$\varepsilon_{Li_2CO_3}$	ε_{LiF}	ε_{Li_2O}	ε_{LiOH}	C_{H_2O}	C_{HF}	C_{PF_5}	C_{POF_3}	$C_{HPO_2F_2}$	C_{LiPF_6}
Unit	nm	vol-%	vol-%	vol-%	vol-%	vol-%	ppm	ppm	ppm	ppm	ppm	ppm
R/OS/W	50	91	0	4	0	5	503	0	879	116	5358	133367
R/OS/D	50	90	9.2	0.4	0	0.4	168	0	1016	37	536	135084
R/IS/W	50	0	36	29	30	5	504	0	880	95	5348	128966
R/IS/D	50	0	39.6	30	30	0.4	168	0	1017	30	537	135092
TkS/R/W	75	45	32	8	10	5	505	0	880	95	5334	128983
TkS/R/D	75	45	34.6	10	10	0.4	168	0	1016	30	535	135093
TnS/R/W	25	46	26	13	10	5	504	0	880	95	5342	128975
TnS/R/D	25	45	34.6	10	10	0.4	168	0	1016	30	538	135091
TkS/OS/R	75	90.2	8.6	0	0.6	0.6	260	0	992	55	1319	134083
TkS/IS/R	75	0	39.4	30	30	0.6	259	0	992	46	1303	134113
TnS/OS/R	25	90.6	7	1.8	0	0.6	259	0	992	55	1319	134083
TnS/IS/R	25	0	38	31.4	30	0.6	259	0	991	46	1310	134106
TkS/OS/W	75	90.8	1.8	2.4	0	5	503	0	880	116	5363	129921
TkS/OS/D	75	90	9.2	0.4	0	0.4	168	0	1017	37	540	135079
TkS/IS/W	75	0	37	28	30	5	504	0	880	95	5349	128964
TkS/IS/D	75	0	39.6	30	30	0.4	168	0	1016	30	538	135091
TnS/OS/W	25	91	0	5	0	5	299	725	977	31	3946	130750
TnS/OS/D	25	90.2	8.6	0	0.8	0.4	168	0	1017	37	540	135082
TnS/IS/W	25	0	31	34	30	5	505	0	880	95	5344	128972
TnS/IS/D	25	0	39.1	30.1	30.4	0.4	168	0	1017	30	538	135093

R=Reference depending on position, i.e., SEI thickness, SEI composition or humidity
TkS = Thick SEI, TnS = Thin SEI, IS = Inorganic SEI, OS = Organic SEI, W = Wet, D = Dry

Table C.3: Kinetic parameters $k_{0,j}$, and $E_{A,j}$ for all reactions obtained by parameterising the model with the experiments of Stich et al. [144] and Maleki et al. [69].

Reaction	Frequency factor, $k_{0,j}$ / mol s^{-1}	Activation energy, $E_{A,j}$ / kJ mol^{-1}
$LiPF_6 \rightleftharpoons LiF + PF_5$	18	53
$PF_5 + H_2O \rightleftharpoons 2\,HF + POF_3$	35	35
$POF_3 + H_2O \longrightarrow HF + HPO_2F_2$	27.5	37.5
$2\,LiC_6 + 2\,C_3H_4O_3$(EC) $\longrightarrow$ $(CH_2OCO_2Li)_2 + C_2H_4 + 2\,C_6$	$3.2 \cdot 10^{-11}$ *	42
$2\,LiC_6 + C_3H_4O_3$(EC) $\longrightarrow Li_2CO_3 +$ $C_2H_4 + 2\,C_6$	$3.2 \cdot 10^{-11}$ *	42
$LiC_6 + H_2O \longrightarrow LiOH + 0.5\,H_2 + C_6$	$3.2 \cdot 10^{-11}$ *	42
$(CH_2OCO_2Li)_2 \longrightarrow Li_2CO_3 + C_2H_4 +$ $CO_2 + 0.5\,O_2$	$1 \cdot 10^{14}$	148
$Li_2CO_3 + 2\,HF \longrightarrow 2\,LiF + H_2O + CO_2$	$8 \cdot 10^{14}$	65
$LiC_6 + LiOH \longrightarrow Li_2O + 0.5\,H_2 + C_6$	350	126
$LizCoO_2 \longrightarrow zLiCoO_2 + (1\text{-}z)/_3\,O_2 +$ $(1\text{-}z)/_3\,Co_3O_4$	10^{47} **	480 **
$3.5\,O_2 + C_4H_8O_3$(EMC) $\longrightarrow 4\,CO_2 +$ $4\,H_2O$	$2.5 \cdot 10^{53}$ **	470 **
$2.5\,O_2 + C_3H_4O_3$(EC) $\longrightarrow 3\,CO_2 +$ $2\,H_2O$	$2.5 \cdot 10^{53}$ **	470 **

* mol m s^{-1}

** Only with these high activation energy and frequency factor values could the reaction behaviour be reproduced with power-law kinetics. A change from power law to other reaction exponents could solve this in the future

D Supporting details Chapter 6

The following chapter contains the additional results and parameters corresponding to the study of pressure evolution during the thermal abuse of Li-ion batteries presented in Chapter 6. First, the SAFT-γ Mie model is compared to experimental data to evaluate its accuracy. This is followed by tables containing all necessary model parameters. Eventually, the calculated deviations between model and experimental data are presented in table format.

D.1 Model accuracy

In order to accurately model thermodynamic properties and vapour-liquid phase equilibria of liquid electrolyte mixtures used in Li-ion batteries, several groups present in the respective molecules have to be introduced to the SAFT-γ Mie approach. First, the linear and cyclic carbonate groups, denoted as OCOO and cyOCOO, respectively are introduced. Combinations of these with groups already implemented in the SAFT-γ Mie approach, such as CH_2, CH_3 and cyCH form the linear and cyclic carbonates employed in Li-ion battery electrolytes. The linear carbonates included in the current work are dimethyl carbonate (DMC), ethyl methyl carbonate (EMC), diethyl carbonate (DEC) and dipropyl carbonate (DPC). They differ solely in the length of chains, consisting of CH_2 and CH_3 groups, attached to OCOO. The cyclic carbonates are ethylene carbonate (EC), propylene carbonate (PC) and butylene carbonate (BC). Also they only differ in the chain length. A graphical representation of all modelled species as well as their group structure can be found in Figure 6.2 in the main manuscript. The missing like and unlike group interactions are estimated from pure and binary experimental data.

In Figure D.1, the comparison between the simulated and experimental dependency of pure-compound properties on temperature is shown: these comprise liquid density (D.1a), vapour pressure (D.1b) and enthalpy of vaporisation (D.1c). The data is represented with an outstanding accuracy of a %AAD of 0.3% for density, 7.36% for vapour pressure, and 0.8% for enthalpy of vaporisation. The %AAD for individual substances is listed in Table D.4 in Section D.2. The apparent high deviations of DEC and DPC, with a %AAD of around 15% are explained by the generally low vapour pressure value compared to the linear carbonates with a short chain length, i.e. DMC and EMC. Further, are these substances not used in the parameter estimation

procedure as they are not commonly used as in liquid battery electrolyte. Therefore, they serve as a model validation only. The deviation of $< 20\%$ shows a good agreement between the experiment and the employed SAFT-γ Mie model. The obtained interaction energies and repulsive exponents for the linear carbonate group OCOO and cyclic carbonate group cyOCOO are $\varepsilon_{\mathrm{OCOO-OCOO}}/k_{\mathrm{B}} = 268.51\,\mathrm{K}$, $\lambda^{\mathrm{r}}_{\mathrm{OCOO-OCOO}} = 10.351$, $\varepsilon_{\mathrm{cyOCOO-cyOCOO}}/k_{\mathrm{B}} = 652.18\,\mathrm{K}$, and $\lambda^{\mathrm{r}}_{\mathrm{cyOCOO-cyOCOO}} = 11.882$, which are in a typical range. The interaction energy of OCOO compares well to other unpolar and linear groups reported in Haslam et al. [137] such as CH_3 and CO_2. In contrast, the cyclic carbonate group interaction aligns with more polar groups like COO or cyclic groups like cyCH, cyCH$_2$ and the like.

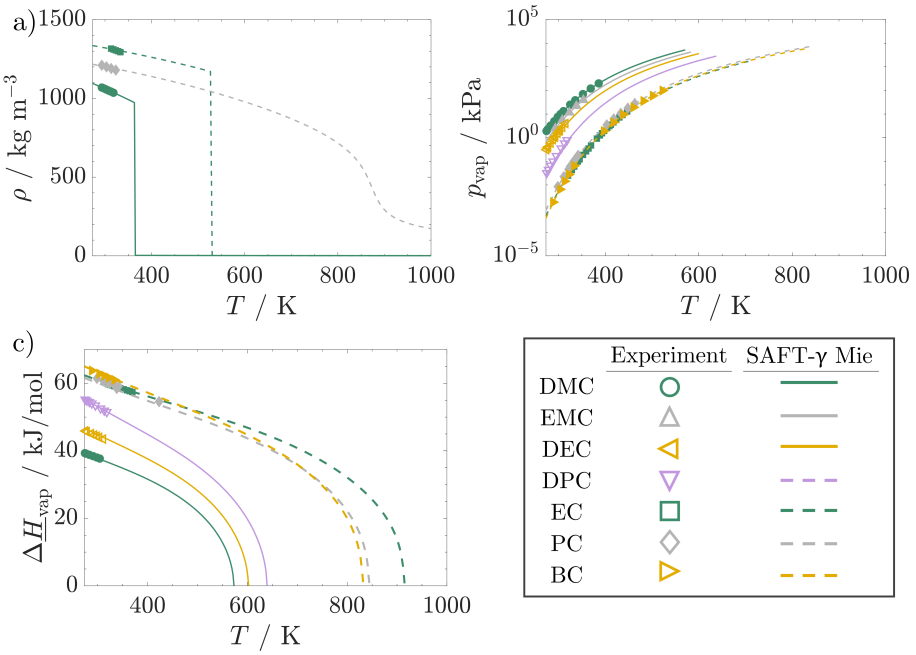

Figure D.1: Comparison of thermodynamic properties of pure compounds calculated by the SAFT-γ Mie model with experimental data for linear and cyclic carbonates: a) liquid density [238–240], b) vapour Pressure [241–246] and c) enthalpy of vaporisation [241, 245, 246]. Experimental data used in the estimation of the group-interaction parameters are represented with filled symbols, and those not used are represented with open symbols.

In Figure D.2 the comparison of the established model to binary mixture data is presented. An excellent agreement with an overall %AAD of 1.38% could be obtained here. Interestingly,

no interaction between the electron-donating e sites from the OCOO group with the electron-accepting H sites of the cyOCOO group seems to occur. This is deduced from the fact that including these interactions does not improve the data description further. This phenomenon can be explained by the high interaction potential $(\varepsilon^{\mathrm{HB}}_{kl,ab}/k_{\mathrm{B}}) = 1159.54$ K of the electron donor site in cyOCOO with its own electron acceptor site H. Any other interaction energy with the electron acceptor site H cyOCOO would have to be in the same order of magnitude to obtain any significant effect. The individual %AADs for separate experiments and mixtures can be found in Table D.5 in Section D.2.

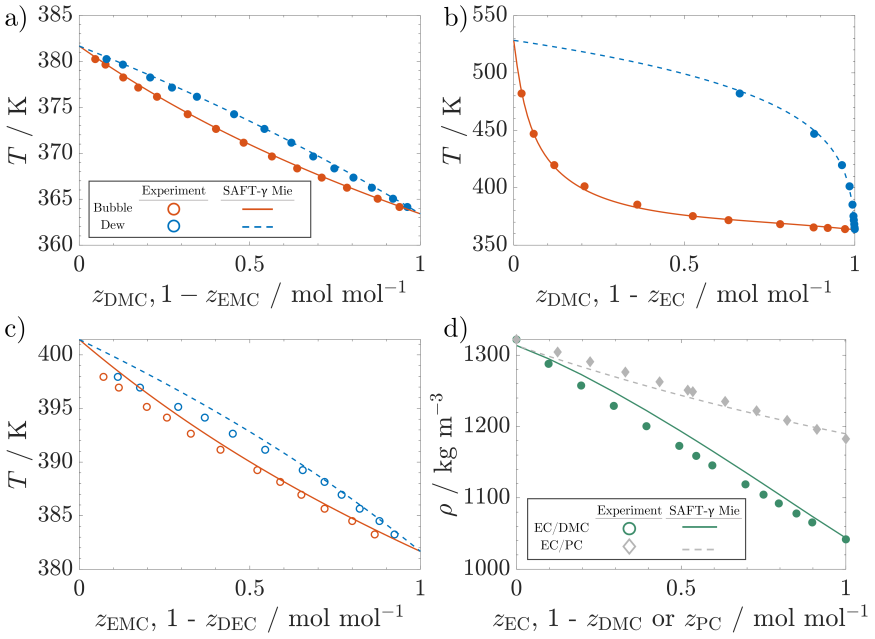

Figure D.2: Comparison of thermodynamic properties of binary mixtures calculated by the SAFT-γ Mie model with experimental data of linear and cyclic carbonates: a) vapour-liquid data of EMC/DMC at 101.1 kPa [247],b) vapour-liquid data of EC/DMC at 101.1 kPa [308], c) vapour-liquid data of EMC/DEC at 101.1 kPa [247], d) liquid density data of EC/DMC and EC/PC at 313.15 K and at 101.1 kPa [248]. Experimental data used in the estimation of the group-interaction parameters are represented with filled symbols, and those not used are represented with open symbols.

Since studying the pressure evolution during a thermal event in Li-ion batteries is the main goal of this work gaseous species are also included in this analysis. It was decided to use CO_2 and Ar for a first evaluation. CO_2 is, aside CO and H_2 among the most common degradation gases that were measured after a thermal event in Li-ion batteries [234, 258, 259]. Ar on the

other hand is typically used as an inert gas during cell assembly and, thus, is in direct contact with liquid battery electrolytes.

Figure D.3 further contemplates the gas solubility of CO_2 in linear carbonates (D.3a), cyclic carbonates (D.3b) and a binary mixture of DMC/EC (D.3c) as well as the gas solubility of Ar in linear carbonates (D.3d). The visual agreement between the experimental data and the simulated one is excellent. Exceptions are the solubility of CO_2 in DEC and in the binary mixture of DMC/EC. Please note that here also, no interaction between the association sites of cyOCOO and CO_2 is observed, and this interaction can be neglected. The deviation for DEC can be explained by the discrepancy in the pure components' vapour pressure. However, there is no clear explanation for the inconsistency in the DMC/EC mixture. A possible explanation could be that the experiment was performed at 303 K which is close to the critical temperature of CO_2 with 304 K [325]. Difficulties of the SAFT EoS to simultaneously represent systems close to and far from the critical point could therefore also be the reason for this deviation. The overall %AAD for CO_2 solubility is 16.87%. The high value contradicts the curves in Figure D.3. The cause of this lies exclusively in the characteristics of the way the %AAD is calculated. Using the solute as the denominator inherently leads to high relative deviations, even for low absolute solubility values. Also the AAD values for CO_2 are given in Table D.6. The solubility of Ar in the linear carbonates DMC and DEC is satisfactory. The model, however, is not capable to capture the endothermic dissolution enthalpy of Ar in the linear carbonates. The average %AAD for solubility of Ar in linear carbonates is 3.63%.

The last species that has to be considered for a full battery electrolyte is the conductive salt $LiPF_6$. In the following, the experiments that allow for the deduction of interaction parameters of $LiPF_6$ are shown in Figure D.4.

All unlike interaction energies involving ion interaction have been calculated based on the combining rule introduced in [180]. Exceptions to this are the interactions of both ions with both carbonate groups OCOO and cyOCOO as well as CO_2. These have been adjusted to represent the experimental data of vapour pressure for DMC/$LiPF_6$ and CO_2 solubilities in mixtures of DMC/$LiPF_6$, EMC/$LiPF_6$ and PC/$LiPF_6$, as can be seen in Figure D.4 a) and d).

Experimental data for the change in the dielectric constant of DMC with increasing salt concentration (Figure D.4 b), and liquid density for mixtures of $LiPF_6$ with DMC, EMC and EC (Figure D.4 c), are predicted using the chosen parameters. With the employed model for ion association, it is possible to represent and reproduce the given data with a %AAD over all experiments involving the salt interaction of 2.23%. Individual %AADs for each experiment are listed in Table D.7. For an initial estimate, using the same assumptions but performing the calculations sequentially, this is quite remarkable. Please note that a relatively low number

of associated ions can explain the deviation in the vapour pressure of Figure D.4 a). Considering also solvent separated ion-pairs in the ion association model could solve this in the future. Alternative approaches to this have recently been published by Olsen et al. [201] where the contribution of ion association on the free energy has explicitly been included in a cubic plus association EoS. Therewith, the authors could quantitatively reproduce the change in the dielectric constant of water for several salts.

The %AAD over all 632 evaluated experimental points, including the predicted values, is 5.10%. Hence, a valid parameter set to study pressure evolution in Li-ion batteries has successfully been obtained.

Figure D.5 shows the percentage absolute deviations, %AD for all performed studies. Information about the respective figure showing the original study as well as the chosen references used for each study is indicated in the figure caption.

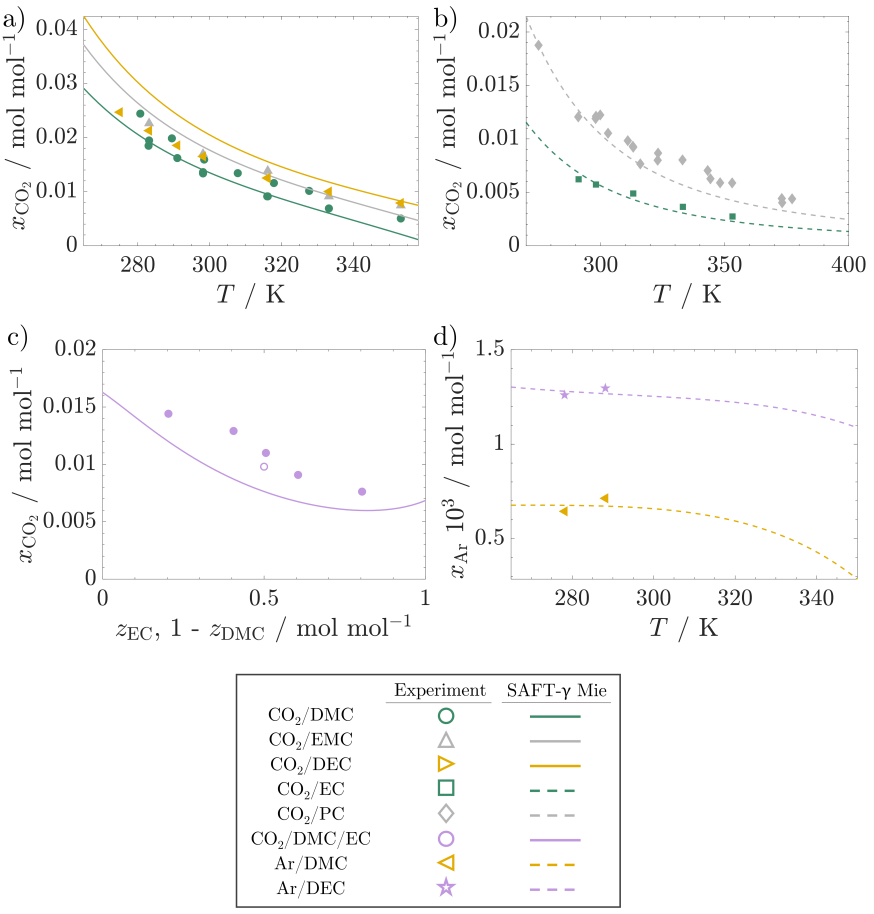

Figure D.3: Comparison of thermodynamic properties of gas solubility calculated by the SAFT-γ Mie model with experimental data for CO_2 and Ar in linear and cyclic carbonates a) linear carbonates at 101.1 kPa [249], b) cyclic carbonates and 101.1 kPa [249], c) EC/DMC mixture at 291 K and 101.1 kPa [250], d) Ar solubility at 101.1 kPa in DMC and DEC [251] Experimental data used in the estimation of the group-interaction parameters are represented with filled symbols, and those not used are represented with open symbols.

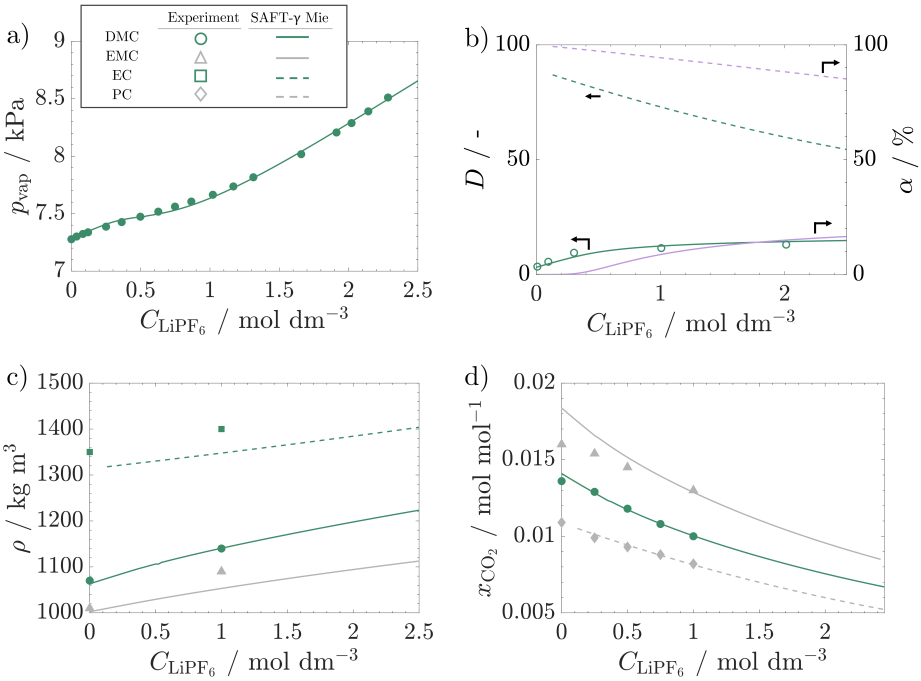

Figure D.4: Comparison of thermodynamic properties of the influence of $LiPF_6$ calculated by the SAFT-γ Mie model with experimental data for CO_2, linear and cyclic carbonates: a) vapour pressure of DMC at 298.15 K [252], b) dielectric constant and degree of dissociation at 298.15 K of DMC [210] and EC, c) liquid density of DMC and EC at 298.15 K and 101.1 kPa [253], and d) CO_2 solubility at 298.15 K and 101.1 kPa in DMC, EMC and PC [254]. Experimental data used in the estimation of the group-interaction parameters are represented with filled symbols, and those not used are represented with open symbols.

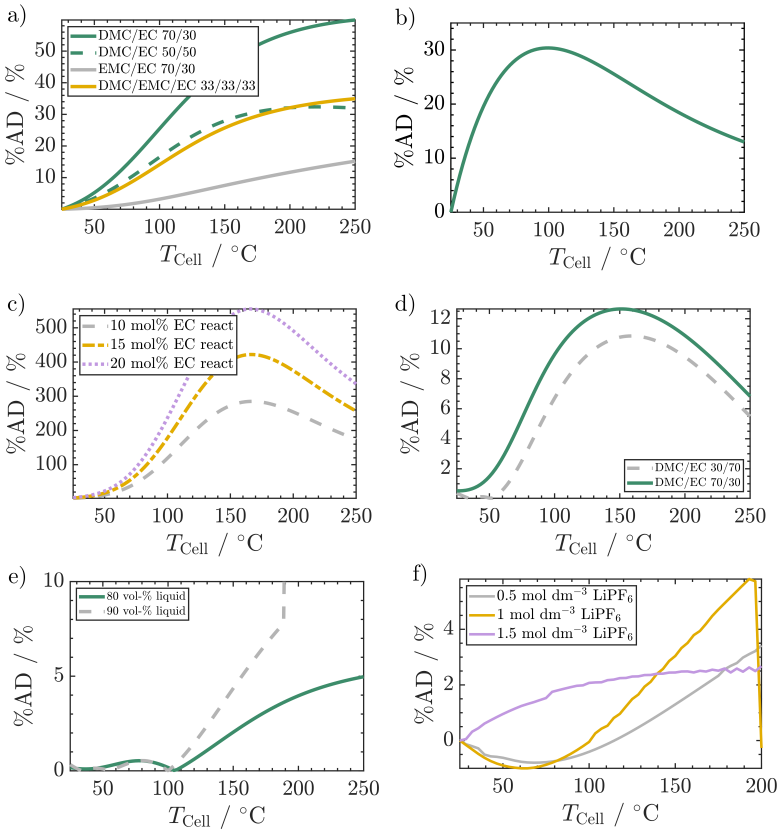

Figure D.5: Shown are the %ADs for a) solvent composition analysis with EMC/EC 50/50 as the reference, b) the solubility analysis calculated with CO_2/DMC/EC case as reference, c) the reactivity analysis with the no reaction case as reference, d) the composition dependent reactivity analysis with the DMC/EC 50/50 as reference, e) the liquid volume fraction including constant reaction with the 70 vol-% liquid case as reference, f) the conductive salt analysis with the the 0 mol dm^{-3} $LiPF_6$ case as reference.

D.2 Supporting tables

Table D.1: Self-interaction parameters. Either taken from literature or developed in the current work.

k	group	ν_k^*	S_k	σ_{kk}/Å	$\sigma_{kk}^{\mathrm{Born}}$/Å	$\lambda_{kk}^{\mathrm{r}}$	$\lambda_{kk}^{\mathrm{a}}$	$(\varepsilon_{kk}/k_{\mathrm{B}})$/K	$n_{\mathrm{H},k}$	$n_{\mathrm{e},k}$	charge	I/ eV	$\alpha/(10^{24}\mathrm{cm}^3)$	ref
1	CH_3	1	0.5726	4.0772	-	15.050	6.0000	256.77	-	-	-	-	-	[176]
2	CH_2	1	0.2293	4.8801	-	19.871	6.0000	473.39	-	-	-	-	-	[176]
3	$cyCH_2$	1	0.2475	4.7852	-	20.386	6.0000	477.36	-	-	-	-	-	[177]
4	cyCH	1	0.0961	5.4116	-	8.0000	6.0000	699.92	-	-	-	-	-	[326]
5	OCOO	2	0.8569	2.8924	-	10.351	6.0000	268.55	-	6	-	-	-	†
6	cyOCOO	1	1.0000	3.7823	-	11.882	6.0000	652.18	1	6	-	-	-	†
7	Li^+	1	1.0000	1.8000	2.632	12.000	6.0000	6.1036	-	-	+1	75.64	0.0029	[179]
8	$PF_6{}^-$	1	1.0000	5.0800	5.334	12.000	6.0000	24.322	-	-	-1	7.33	4.18	†,[327, 328]
9	$LiPF_6$	1	1.0000	6.8800	-	12.000	6.0000	384.22	-	-	-	-	-	†
10	CO_2	2	0.8468	3.0500	-	26.480	5.0550	207.89	-	-	-	-	-	[329]
11	Ar	1	1.0000	3.4038	-	12.0850	6.0000	117.84	-	-	-	-	-	[237]

† indicates that the corresponding model parameters have been developed in the presented work.

Table D.2: Unlike-interaction parameters. Either taken from literature or developed in the current work. Interactions that have been calculated using combining rules are indicated by CR.

k	l	group k	group l	(ε_{kl}/k_B)/K	λ^r_{kl}	ref	k	l	group k	group l	(ε_{kl}/k_B)/K	λ^r_{kl}	ref
1	2	CH_3	CH_2	350.77	CR	[176]	4	6	cyCH	cyOCOO	386.23	CR	†
1	3	CH_3	$cyCH_2$	355.95	CR	[177]	4	7	cyCH	Li^+	42.260	CR	†
1	4	CH_3	cyCH	690.17	CR	[326]	4	8	cyCH	$PF_6{}^-$	130.28	CR	†
1	5	CH_3	OCOO	317.06	CR	†	4	9	cyCH	$LiPF_6$	CR	CR	†
1	6	CH_3	cyOCOO	405.44	CR	†	4	10	cyCH	CO_2	294.99	CR	[142]
1	7	CH_3	Li^+	31.020	CR	†	4	11	cyCH	Ar	CR	CR	†
1	8	CH_3	$PF_6{}^-$	77.610	CR	†	5	6	OCOO	cyOCOO	100.00	9.5000	†
1	9	CH_3	$LiPF_6$	CR	CR	†	5	7	OCOO	Li^+	37.240	CR	†
1	10	CH_3	CO_2	205.70	CR	[329]	5	8	OCOO	$PF_6{}^-$	71.870	CR	†
1	11	CH_3	Ar	127.90	CR	†	5	9	OCOO	$LiPF_6$	CR	CR	†
2	3	CH_2	$cyCH_2$	469.67	CR	[177]	5	10	OCOO	CO_2	279.61	CR	†
2	4	CH_2	cyCH	522.57	CR	[326]	5	11	OCOO	Ar	210.47	CR	†
2	5	CH_2	OCOO	305.61	CR	†	6	7	cyOCOO	Li^+	43.550	CR	†
2	6	CH_2	cyOCOO	513.92	CR	†	6	8	cyOCOO	$PF_6{}^-$	103.92	CR	†
2	7	CH_2	Li^+	CR	CR	†	6	9	cyOCOO	$LiPF_6$	CR	CR	†
2	8	CH_2	$PF_6{}^-$	CR	CR	†	6	10	cyOCOO	CO_2	281.75	9.0000	†
2	9	CH_2	$LiPF_6$	CR	CR	†	6	11	cyOCOO	Ar	CR	CR	†
2	10	CH_2	CO_2	276.45	CR	[329]	7	8	Li^+	$PF_6{}^-$	3.2000	CR	†
2	11	CH_2	Ar	208.74	CR	†	7	9	Li^+	$LiPF_6$	42.260	CR	†
3	4	$cyCH_2$	cyCH	321.71	CR	[326]	7	10	Li^+	CO_2	15.130	CR	†
3	5	$cyCH_2$	OCOO	781.89	9.0000	†	7	11	Li^+	Ar	CR	CR	†
3	6	$cyCH_2$	cyOCOO	654.48	CR	†	8	9	$PF_6{}^-$	$LiPF_6$	90.980	CR	†
3	7	$cyCH_2$	Li^+	38.230	CR	†	8	10	$PF_6{}^-$	CO_2	20.560	CR	†
3	8	$cyCH_2$	$PF_6{}^-$	107.61	CR	†	8	11	$PF_6{}^-$	Ar	CR	CR	†
3	9	$cyCH_2$	$LiPF_6$	CR	CR	†	9	10	$LiPF_6$	CO_2	140.130	CR	†
3	10	$cyCH_2$	CO_2	269.68	CR	[142]	9	11	$LiPF_6$	Ar	CR	CR	†
3	11	$cyCH_2$	Ar	CR	CR	†	10	11	CO_2	Ar	CR	CR	†
4	5	cyCH	OCOO	933.84	CR	†							

† indicates that the corresponding model parameters have been developed in the presented work.

Table D.3: Association interaction parameters.

k	l	group k	site a in group k	group l	site b in group l	$(\varepsilon^{HB}_{kl,ab}/k_B)$/K	$K_{kl,ab}$/Å^3
6	6	cyOCOO	H	cyOCOO	e	1159.5	10.000

Table D.4: Percentage average absolute deviations (%AAD) of the liquid density (ρ_{liq}), vapour pressure (p_{vap}) and enthalpy of vaporisation ($\Delta\underline{H}_{vap}$) for the pure species of DMC, EMC, DEC, DPC, EC, PC and BC. n indicates the number of data points.

	ρ_{liq}					
	n	T_{range} / K	p_{range} / MPa	AAD / kg m^{-3}	%AAD / %	Ref.
DMC	6	274.20–397.48	—	0.934	0.080	[238]
EC	5	313.15–333.15	—	3.808	0.293	[239]
PC	20	293.15–323.15	5–25	4.443	0.371	[240]
Σ	31	—	—	3.662	0.304	—
	p_{vap}					
	n	T_{range} / K	p_{range} / MPa	AAD / Pa	%AAD / %	Ref.
DMC	34	274.20–397.48	—	384.9	2.105	[241, 242]
EMC	13	293.15–353.15	—	219.3	2.133	[243]
DEC	44	238.15–315.20	—	191.0	16.42	[241, 244]
DPC	31	238.15-318.20	—	27.58	15.84	[241, 244]
EC	64	320.30–449.01	—	614.6	6.711	[245, 246]
PC	34	298.40–473.15	—	4142	2.536	[245, 246]
BC	34	288.60–522.74	—	140.2	1.636	[245]
Σ	254	—	—	291.92	7.420	—
	$\Delta\underline{H}_{vap}$					
	n	T_{range} / K	p_{range} / MPa	AAD / J mol^{-1}	%AAD / %	Ref.
DMC	16	274.20–304.10	—	138.4	0.361	[241]
DEC	37	273.10–315.20	—	599.2	1.338	[241]
DPC	23	273.90–318.20	—	24.23	0.051	[241]
EC	25	320.30–369.50	—	128.7	0.219	[245, 246]
PC	24	298.40–443.00	—	1116	1.884	[245, 246]
BC	15	288.60–343.80	—	221.2	0.356	[245]
Σ	140	—	—	418.2	0.802	—
Σ	425	—	—	—	4.723	—

Table D.5: Percentage average absolute deviations (%AAD) of the bubble and dew temperature liquid density (T_{bub}, T_{dew}) as well as liquid density (ρ_{liq}) for the mixtures DMC/EMC, EMC/DEC, DMC EC, and PC/EC. n indicates the number of data points.

	T_{bub}						
	n	T_{range} / K	p_{range} / MPa	$z_{1,\,range}$	AAD / K	%AAD / %	Ref.
DMC/EMC	14	—	0.101	0.080–0.962	0.151	0.041	[247]
EMC/DEC	12	—	0.101	0.113–0.942	0.734	0.187	[247]
DMC/EC	11	—	0.101	0.023–0.971	1.115	0.281	[308]
∑	37	—	—	—	0.627	0.161	—
	T_{dew}						
	n	T_{range} / K	p_{range} / MPa	$z_{1,\,range}$	AAD / K	%AAD / %	Ref.
DMC/EMC	14	—	0.101	0.08–0.962	0.174	0.047	[247]
EMC/DEC	12	—	0.101	0.113–0.942	0.811	0.206	[247]
DMC/EC	11	—	0.101	0.663–0.999	1.430	0.354	[308]
∑	37	—	—	—	0.754	0.191	—
	ρ						
	n	T_{range} / K	p_{range} / MPa	$z_{1,\,range}$	AAD / kg m^{-3}	%AAD / %	Ref.
DMC/EC	14	313.15	0.101	0.000–1.000	14.38	1.234	[248]
PC/EC	12	313.15	0.101	0.000–1.000	65.72	5.264	[248]
∑	26	—	—	—	38.08	3.094	—
∑	100	—	—	—	—	0.935	—

Table D.6: Percentage average absolute deviations (%AAD) and average absolute deviations (AAD) for the solubility of CO_2 (x_{CO_2}) and Ar (x_{Ar}) in the pure species DMC, EMC, DEC, EC, PC and a binary mixture of DMC/EC. n indicates the number of data points.

	x_{CO_2}						
	n	T_{range} / K	p_{range} / MPa	$z_{1,\,range}$	AAD mol mol^{-1}	%AAD / %	Ref.
DMC	15	280.70–353.15	0.101	—	0.0016	13.596	[249]
EMC	5	283.15–353.15	0.101	—	0.0013	10.046	[249]
DEC	9	275.00–353.15	0.101	—	0.0043	24.797	[249]
EC	5	291.15–353.15	0.101	—	0.0004	11.201	[249]
PC	20	275.00–377.15	0.101	—	0.0012	16.712	[249]
DMC/EC	5	291.00	0.101	0.204–0.804	0.0028	25.527	[250]
∑	59	—	—	—	0.0018	16.868	-
	x_{Ar}						
	n	T_{range} / K	p_{range} / MPa	$z_{1,\,range}$	AAD mol mol^{-1} 10^5	%AAD / %	Ref.
DMC	2	278.15–288.15	0.101	—	3.6565	5.3626	[251]
DEC	2	278.15–288.15	0.101	—	2.4471	1.9101	[251]
∑	4	—	—	—	3.0518	3.6363	-
∑	63	—	—	—	0.0017	16.0279	-

Table D.7: Percentage average absolute deviations (%AAD) of the vapour pressure (p_{vap}), dielectric constant (D), liquid density (ρ_{liq}), and CO_2 solubility of mixtures $LiPF_6$/DMC, $LiPF_6$/EMC, $LiPF_6$/EC, $LiPF_6$/PC. n indicates the number of data points.

	p_{vap}						
	n	T_{range} / K	p_{range} / MPa	$C_{LiPF_6,\ range}$ / mol dm^{-3}	AAD / Pa	%AAD / %	Ref.
DMC	19	298.15	0.101	0.000–2.530	13.88	0.178	[252]
Σ	19	—	—	—	13.88	0.178	—
	D						
	n	T_{range} / K	p_{range} / MPa	$C_{LiPF_6,\ range}$ / mol dm^{-3}	AAD	%AAD / %	Ref.
DMC	5	298.15	—	0.000–2.000	1.027	11.65	[210]
Σ	5	—	—	—	1.027	11.65	—
	ρ						
	n	T_{range} / K	p_{range} / MPa	$C_{LiPF_6,\ range}$ / mol dm^{-3}	AAD / kg m^{-3}	%AAD / %	Ref.
DMC	2	298.15	0.101	0.000–1.000	3.661	0.341	[253]
EMC	2	298.15	0.101	0.000–1.000	22.24	2.068	[253]
EC	2	298.15	0.101	0.000–1.000	44.36	3.217	[253]
Σ	6	—	—	—	23.42	1.875	—
	x_{CO_2}						
	n	T_{range} / K	p_{range} / MPa	$C_{LiPF_6,\ range}$ / mol dm^{-3}	AAD mol mol^{-1}	%AAD / %	Ref.
DMC	5	298.15	0.101	0.000–1.000	0.000137	1.054	[254]
EMC	4	298.15	0.101	0.000–1.000	0.001100	6.996	[254]
PC	5	298.15	0.101	0.000–1.000	0.000096	1.027	[254]
Σ	14	—	—	—	0.000397	2.742	—
Σ	44	—	—	—	—	2.531	—